



HAL
open science

Functional printing: from the study of printed layers to the prototyping of flexible devices

Daniele Sette

► **To cite this version:**

Daniele Sette. Functional printing: from the study of printed layers to the prototyping of flexible devices. Materials. Université de Grenoble, 2014. English. NNT : 2014GRENI065 . tel-01152867

HAL Id: tel-01152867

<https://theses.hal.science/tel-01152867>

Submitted on 18 May 2015

HAL is a multi-disciplinary open access archive for the deposit and dissemination of scientific research documents, whether they are published or not. The documents may come from teaching and research institutions in France or abroad, or from public or private research centers.

L'archive ouverte pluridisciplinaire **HAL**, est destinée au dépôt et à la diffusion de documents scientifiques de niveau recherche, publiés ou non, émanant des établissements d'enseignement et de recherche français ou étrangers, des laboratoires publics ou privés.

THÈSE

Pour obtenir le grade de

DOCTEUR DE L'UNIVERSITÉ DE GRENOBLE

Spécialité : **Matériaux, Mécanique, Génie Civil, Electrochimie**

Arrêté ministériel : 7 août 2006

Présentée par

Daniele SETTE

Thèse dirigée par **Anne BLAYO**,
Co-encadrée par **Christophe POULAIN**

préparée au sein du **Commissariat à l'Energie Atomique et aux Energies Alternatives – CEA** et du **Laboratoire du Génie des Procédés Papetiers – LGP2**

dans l'**École Doctorale Ingénierie – Matériaux, Mécanique, Energétique, Environnement, Procédés, Production (I-MEP2)**.

Functional printing: From the study of printed layers to the prototyping of flexible devices

Thèse soutenue publiquement le **11 décembre 2014**,
devant le jury composé de :

Mme Panagiota MORFOULI

Professeur, Grenoble INP – PHELMA, Présidente de jury

M. Reinhard R. BAUMANN

Professeur, Chemnitz University of Technology, Rapporteur

M. Yvan BONNASSIEUX

Professeur, Ecole Polytechnique, Palaiseau, Rapporteur

M. Mohamed SAADAoui

Chargé de Recherche, Ecole des Mines de Saint-Etienne, Examineur

Mme Anne BLAYO

Enseignant-Chercheur, Grenoble INP – PAGORA, Directrice de Thèse

M. Christophe POULAIN

Ingénieur-Chercheur, CEA Grenoble, Encadrant de Thèse





By Schulz

Remerciements

Bien que placées au début, ce sont les dernières que j'écris dans ce manuscrit. Elles sont pour vous tous, qui m'avez accompagné, guidé, soutenu, et supporté aussi, pendant ces dernières années...

Tout d'abord je tiens à remercier le Département des Composants Silicium du CEA, Leti et le Laboratoire du Génie des Procédés Papetiers pour m'avoir accueilli et fourni tous les supports, humains et matériels, nécessaires au bon déroulement de mes travaux de recherche. Merci à tous ceux qui ont participé de près ou de loin à ces travaux! *Au moins comme ça je suis sûr de n'avoir oublié personne...*

Anne, Christophe, je pense que nous avons formé une belle équipe! Nos réunions dans le calme et le soleil du campus me manqueront. Ces moments ont été un vrai plus de votre encadrement, toujours riches en conseils, encouragements, disponibilité et bonne humeur. Vous avez été des encadrants exemplaires à mon sens, et je garderai précieusement vos enseignements. La page de la thèse se tourne, mais cette relation que nous avons construite continue, et je vous en suis reconnaissant. Merci!

D'autre part, je souhaite exprimer une sincère gratitude à l'ensemble des membres du jury pour l'intérêt porté à ce travail de thèse en acceptant de l'évaluer. Un grand merci au Professeur Panagiota Morfouli (Grenoble INP) d'avoir présidé ce jury, aux Professeurs Reinhard R. Baumann (Technische Universität Chemnitz) et Yvan Bonnassieux (Ecole Polytechnique) d'avoir rapporté et corrigé cette thèse. De même, je remercie Mohamed Saadaoui, Chargé de Recherche (Ecole des Mines de Saint Etienne), d'avoir examiné mon travail et participé à ce jury.

Aussi, un grand merci aux partenaires du Projet I2Flex, sans qui ces travaux n'auraient pas vu le jour! J'espère que de nouvelles occasions se présentent pour renouveler cette belle réussite.

Je voudrais maintenant et plus particulièrement diriger mes pensées envers ceux que j'ai sollicités, du début à la fin de cette thèse: Frédéric Souchon pour son premier accueil et son énergie, Denis Mercier pour ses idées et son ingéniosité, David Bouchu pour les longues heures passée derrière le MEB, Marcel Audoin pour ses problèmes mais surtout ses solutions, Florence Sonnerat pour son aide avec mes mesures RF, Solange Garrais pour les mesures d'angle de goutte, Vincent Mandrillon pour son aide mécanique passionnée, Frédéric-Xavier Gaillard pour sa créativité, Emmanuel Defay pour nos travaux sur le BST et son enthousiasme, Patrick Brunet-Manquat pour ses tiroirs cachés! Et encore une fois, merci à vous tous qui m'avez aidé et dédié un peu de votre temps.

Une pensée émue pour tous mes collègues et amis du LCFC, Denis, Philippe, Romain, Patrick, Antoine, Pierre et Pierre-Louis, Frédéric, Marcel, Hélène, Stéphane, Robert, Vincent, Kevin, David, Gérard... pour les moments partagés autour d'un repas ou d'un bon café! A Didier Bloch, chef de laboratoire, j'adresse un grand merci pour son accueil au LCFC. Je n'oublierai pas ta passion pour l'énergie ainsi que ta disponibilité. Estelle, tu as été d'un soutien et d'une aide formidable, tout au long de ces années. Merci de ton dévouement, ta force et ta gentillesse. Enfin, je n'oublie pas mes compagnons de bureau, qui ont dû supporter mon humour douteux... Un grand merci à vous, amis stagiaires, thésards et CDD : David M., Alexis, Alexandra, Simon, Marie, Florence, Jennifer, Sébastien, Guillaume, Laurent, ... Je vous dis à très bientôt à tous!

Une pensée pour mes chers amis du CEA Jérémie et François, merci pour ces moments de détente, ces heures de squash, ces échanges... Et pour vous également, Gaël et Camille, Guillaume et Elena, mes compagnons de jeunesse, d'aventure et de la vie!

E infine ci siete voi, Mamma e Papà, Anna-Luce, Emilia e Giacomo, Nonna Giovanna e Nonno Daniele, a cui penso ogni giorno, Ernesto, Nonno Nicola e tutta la famiglia! Non ho parole per ringraziarvi per tutto ciò che mi date, giorno dopo giorno. Vi voglio bene a tutti!

Marine, ces dernières lignes sont pour toi, et elles sont encore toutes à écrire, car ce n'est qu'un début!
Merci de ta patience et de la sérénité que tu m'apportes au quotidien.

Table of Contents

<u>Scientific publications</u>	5
<u>Abbreviations and Symbols</u>	7
<u>General Introduction</u>	9
I. CONTEXT OF THE THESIS	12
II. OPPORTUNITIES OF FUNCTIONAL PRINTING	12
III. OBJECTIVES OF THE THESIS	13
<u>Chapter 1: Printed functional layers: from fabrication to properties</u>	15
INTRODUCTION	17
I. OVERVIEW OF PRINTING PROCESSES FOR PRINTED ELECTRONICS	18
I.1. CONTACT PRINTING PROCESSES	18
I.2. NON-CONTACT AND DIRECT-WRITING PROCESSES	21
I.3. COMPARISON OF PRINTING PROCESSES CHARACTERISTICS	25
II. INKJET PRINTING FOR PRINTED ELECTRONICS	26
II.1. PIEZOELECTRIC DOD INKJET PRINTING PROCESS	26
II.2. PRINTING EQUIPMENT	31
II.3. TECHNOLOGY OF A LAB PRINTER: DIMATIX DMP2831	32
II.4. SUMMARY	35
III. FROM INKS TO FUNCTIONAL LAYERS	36
III.1. FUNCTIONAL MATERIALS FOR PRINTED ELECTRONICS	36
III.2. CONDUCTIVE NANOPARTICLES INKS	37
III.3. SUMMARY	40
IV. SINTERING AND GRAIN GROWTH	41
IV.1. NANOPARTICLES SIZE EFFECTS	41
IV.2. SINTERING	42
IV.3. GRAIN GROWTH	43
IV.4. ANNEALING METHODS	45
IV.5. SUMMARY	51
V. ELECTRONIC TRANSPORT IN THIN FILMS	52
V.1. BULK METALS	52
V.2. THIN FILMS METALS	53

VI. MECHANICAL CHARACTERIZATION OF THIN FILMS	56
VI.1. NANOINDENTATION	56
VI.2. ELASTIC PROPERTIES.....	60
VI.3. PLASTIC PROPERTIES	62
CONCLUSION	64
<u>Chapter 2: Characterization of inkjet printed silver layers</u>	65
INTRODUCTION	67
I. SAMPLE PREPARATION	68
I.1. SILVER INK	68
I.2. SUBSTRATE	71
I.3. PRINTING CONDITIONS.....	71
II. ANALYSIS OF THE MICROSTRUCTURE	73
II.1. CHARACTERIZATION METHODS	73
II.2. IMAGE PROCESSING	74
II.3. GRAIN MORPHOLOGY	79
II.4. POROSITY	85
II.5. THICKNESS	90
II.6. SUMMARY	91
III. ELECTRICAL PROPERTIES	92
III.1. ELECTRICAL RESISTIVITY	92
III.2. TEMPERATURE COEFFICIENT OF RESISTANCE	96
III.3. SUMMARY	101
IV. MECHANICAL PROPERTIES	102
IV.1. CALIBRATION.....	102
IV.2. ELASTIC PROPERTIES	103
IV.3. PLASTIC PROPERTIES	106
IV.4. SUMMARY	107
CONCLUSION	108
<u>Chapter 3: Prototyping of Printed Flexible Devices</u>	109
INTRODUCTION	111
I. OPTIMIZATION OF PRINTING CONDITIONS	113
I.1. FLEXIBLE POLYIMIDE SUBSTRATE	113
I.2. OPTIMIZATION OF THE PRINTED PATTERN	113
I.3. DRYING AND ANNEALING.....	116
I.4. SUMMARY	116

II. 17 GHZ BAND-PASS FILTER	117
II.1. STATE-OF-THE-ART.....	117
II.2. FILTER DESIGN	117
II.3. FABRICATION DETAILS	118
II.4. FREQUENCY RESPONSE OF THE FILTER	119
II.5. CONCLUSION.....	121
III. MICRO PIRANI GAUGE.....	122
III.1. STATE-OF-THE-ART.....	122
III.2. PRINTED MICRO PIRANI DESIGN	122
III.3. FABRICATION DETAILS	122
III.4. TEST BENCH	123
III.5. EXPERIMENTAL RESULTS.....	124
III.6. DISCUSSION	126
III.7. CONCLUSION.....	127
IV. MEMBRANE SWITCH.....	128
IV.1. STATE-OF-THE-ART.....	128
IV.2. MEMBRANE SWITCH FABRICATION	128
IV.3. EXPERIMENTAL PROCEDURE.....	131
IV.4. EXPERIMENTAL RESULTS.....	132
IV.5. MEMBRANE SWITCH CHARACTERIZATION	132
IV.6. ELECTRICAL CONTACT	134
IV.7. LIFT MEMBRANE SWITCH	135
IV.8. CONCLUSION.....	136
V. PRINTED BARIUM STRONTIUM TITANATE CAPACITORS.....	137
V.1. STATE-OF-THE-ART.....	137
V.2. EXPERIMENTAL PROCEDURE.....	137
V.3. RESULTS	140
V.4. DISCUSSION	142
V.5. CONCLUSION.....	143
CONCLUSION.....	144
<u>General Conclusion & Perspectives.....</u>	<u>145</u>
<u>References.....</u>	<u>151</u>
<u>Annexes</u>	<u>167</u>
<u>Résumé</u>	<u>173</u>

Scientific publications

Journals

1. **D. Sette**, C. Poulain, A. Blayo, D. Mercier, 2013. *Design and Inkjet Printing of a Bandpass Filter in the GHz Range*. Journal of Print and Media Technology Research, 2(2013)4, pp. 219-226.
2. **D. Sette**, V. Kovacova, E. Defay. *Printed Barium Strontium Titanate Capacitors*. Submitted to Thin Solid Films in December 2014.

Oral communications in International Conferences

1. **D. Sette**, D. Mercier, P. Brunet-Manquat, C. Poulain, A. Blayo, 2013. *Micro Pirani pressure sensor fabricated by inkjet printing of silver nanoparticles*. Transducers Eurosensors XXVII: The 17th International Conference on Solid-State Sensors, Actuators and Microsystems, (Barcelona, Spain).
doi:10.1109/Transducers.2013.6627134.
2. **D. Sette**, C. Poulain, A. Yakoub, M. Saadaoui, B. Dubois, A. Blayo, 2013. *Study of the Electrical Contact in a Fully Inkjet Printed Membrane Switch*. 59th IEEE HOLM Conference on Electrical Contacts (Newport RI, USA).
doi:10.1109/HOLM.2013.6651427.

Paul and Dee-Dee Slade 2013 **Young Investigator Award** at the 59th IEEE HOLM Conference on Electrical Contacts.
3. **D. Sette**, C. Poulain, A. Blayo, D. Mercier, 2013. *Design and Inkjet Printing of RF devices in the GHz Range*. 40th International conference of IARIGAI (Chemnitz, Germany).

3rd best conference presentation at the 40th International conference of IARIGAI, Advances in Printing and Media Technology, 2013.
4. **D. Sette**, C. Poulain, V. Mandrillon, A. Blayo, 2014. *Influence of the Annealing Temperature on the Properties of Inkjet Printed Porous Silver Layers*, E-MRS 2014 Spring Meeting (Lille, France).

Young Scientist Award at the E-MRS Spring 2014 Meeting, Symposium DD: Functional Materials and Devices for Organic Electronics.
5. **D. Sette**, C. Poulain, A. Blayo, 2014. *Temperature Coefficient of Resistance of Inkjet Printed Silver Nanoparticles*. 41st International conference of IARIGAI (Swansea, UK).

2nd best conference presentation at the 41st International conference of IARIGAI, Advances in Printing and Media Technology, 2014.

Posters communications in International Conferences

1. **D. Sette**, A. Blayo, C. Poulain, D. Mercier, 2013. *Silver nanoparticle inkjet printed 17 GHz filter*. IEEE International Microwave Symposium (Seattle WA, USA). doi:10.1109/MWSYM.2013.6697350.
2. J. Ailuno, L. Rapp, **D. Sette**, A.P. Alloncle, C. Poulain, Ph. Delaporte, 2013. *Laser-induced forward transfer of silver nanoparticles paste for membrane switch printing on flexible substrates*. E-MRS 2013 Spring Meeting (Strasbourg, France).
3. J. Ailuno, L. Rapp, C. Constantinescu, A.P. Alloncle, Ph. Delaporte, **D. Sette**, C. Poulain, 2013. *A laser transfer technique for passive and active components printing*. 5th International Conference and Exhibition for the Organic and Printed Electronics Industry, LOPE-C (Munich, Germany).

Patents

Two pending patents at CEA, Leti.

Abbreviations

AFM	Atomic Force Microscopy
BST	Barium Strontium Titanate
CVD	Chemical Vapor Deposition
CIJ	Continuous Inkjet
DoD	Drop-on-Demand
DUT	Device Under Test
FE-SEM	Field Effect Scanning Electron Microscopy
FIB	Focused Ion Beam
IR	Infrared
LCP	Liquid Crystal Polymer
LCVD	Laser Chemical Vapor Deposition
LED	Light Emitting Diode
LEEP	Laser Enhanced Electroless Plating
LF	Low Frequency
LIFT	Laser Induced Forward Transfer
MEMS	Micro Electro Mechanical Systems
MIM	Metal-Insulator-Metal
MOCVD	Metal-organic Chemical Vapor Deposition
MWCNT	Multi Wall Carbon Nanotubes
NPs	Nanoparticles
OECT	Organic Electro-Chemical Transistor
OLED	Organic Light Emitting Diode
OTFT	Organic Thin Film Transistor
PEDOT:PSS	Poly(3,4-ethylenedioxythiophene):Polystyrene sulfonate
PEN	Polyethylene naphthalate
PET	Polyethylene Terephthalate
PI	Polyimide
PLD	Pulsed Laser Deposition
PTFE	Polytetrafluoroethylene
PVP	Polyvinylpyrrolidone
PZT	Lead Zirconium Titanate
RF	Radio Frequency
RFID	Radio-Frequency Identification
ROI	Region Of Interest
SEM	Scanning Electron Microscope
SU-8	Epoxy-based negative photoresist
TFT	Thin Film Transistor
TEOS	Tetraethyl orthosilicate
TPV	Through Polymer Via
TSV	Through Silicon Via
XRD	X-Ray Diffraction

Symbols

A or A_c	Contact area
a	Nozzle characteristic dimension
α	Temperature Coefficient of Resistance
C	Circularity or Capacitance
D or d	Grain diameter
d_x	Drop spacing in X direction
d_y	Drop spacing in Y direction
e	Electron charge
E	Electrical field or Young's modulus
E_F	Fermi's energy
ϵ	Dielectric constant / Permittivity
ϕ	Porosity
G	Thermal conductance
H	Hardness
h or h_c	Indentation depth
\hbar	Reduced Planck's constant
η	Viscosity
J	Current density
k_F	Fermi's vector
L	Length
λ_0	Mean free path in bulk material at 25°C
m_e	Electron mass
N	Charge carrier density
ν	Droplet velocity or Poisson's ratio
Oh	Ohnesorge Number
R	Reflection coefficient at grain boundaries of Mayadas-Shatzkes or Resistance
Re	Reynolds Number
p	Specular parameter of Fuchs-Sondheimer
P	Load or Pressure
r or a	Contact radius
R_a	Average roughness
R_{RMS}	Root Mean Square roughness
ρ	Density or Electrical resistivity
S	Contact Stiffness or Section
σ	Surface tension or Electrical conductivity
t	Thickness or Time
T	Temperature
τ	Relaxation time (average time between two scattering events)
v_F	Fermi's velocity
We	Weber number
Z	Inverse of the Ohnesorge Number

General Introduction

The 20th century is without any doubt under the strong footprint of the development of electronics. Since the invention of the first transistor at Bell Labs in 1947, there has been a huge evolution of technologies for the manufacturing of electronic components. The challenges were and still are: miniaturization, integration and energy consumption.

The fabrication of electronic devices requires the patterning of all type of materials (conductive, semi-conductive, and dielectric). With the recent event of new fields of applications such as large area and flexible electronics, standard processes of silicon technologies have shown their limits. Indeed, the cost of silicon devices increases because of a high cost per unit area of silicon substrates (Hutchings, 2012). Meanwhile, thanks to their ability to pattern large surfaces on low-cost (compared to silicon) and flexible substrates, printing technologies have experienced a revolution. Conventional printing techniques for paper-based media are being adapted to functional materials. Hence, to achieve printed functionalities beyond conventional, printing and material sciences are inevitably connecting each other (Gunde, 2012).

However, it is important to keep in mind that functional printing must not aim to replace nor to compete with standard silicon patterning techniques. It should stand aside and offer complementary technological solutions, in particular for applications that are not area-constrained.

I. Context of the thesis

This thesis was carried out at *CEA, Leti* in Grenoble in collaboration with the *Laboratoire Génie des Procédés Papetiers (LGP2)* from *Grenoble INP-Pagora*. *Leti* is an applied research institute focused on creating value and innovation through technology transfer to its industrial partners. It specializes in micro and nanotechnologies and their applications, from wireless devices and systems, to biology, healthcare and photonics. In this framework, a strong knowledge and know-how in material science and characterization of MEMS devices (radio-frequency, sensors, and actuators) has been developed in the Laboratory of Characterization and Reliability of Components (LCFC) over the last decade. The LGP2 is an academic research laboratory historically focused on paper-based materials and printing processes. More recently, its activity diversified towards biomaterials and bioproducts. Moreover, the background knowledge in surface treatment and ink formulation has led to advanced research in the functionalization of surfaces and printable materials to produce smart objects with high added value.

This thesis came along with the **I2Flex project**, standing for Printed Integration on Flexible substrates, in partnership with major industrial actors such as *Gemalto* and *STMicroelectronics* as well as smaller companies (*ASK, SANSystems, STID, Smart Packaging Solution*) and academic institutes, the *Center of Microelectronics in Provence (Mines de Saint-Etienne)* and the laboratory of *Lasers, Plasma and Photonic Processes (CNRS, LP3, Luminy)*. The objective of this project was to qualify and develop printing fabrication processes for the hybrid integration on plastic and paper substrates of silicon chips and printed interconnections and components. The innovative facets of I2Flex lie in the assessment of the potential of inkjet printing for industrial production through the study of the fabrication process, a deep analysis of the printed materials properties, the design and fabrication of passive and planar components and the investigation of their reliability.

II. Opportunities of functional printing

Printing processes have reached a level of maturity that offers an alternative to lithography for the fabrication of large area electronic components with minimum dimensions above 10 μm . The growing interest in printing processes for electronics manufacturing is usually driven by the idea of a low-cost technique. Subramanian *et al.* (2008) have proposed an accurate analysis of this industrial expectation:

i. Printing does not mean low-cost

Indeed, highly depreciated lithographic equipment are available and their industrial maturity competes with the young age of functional printing technologies. However, the large experience in conventional printing may speed-up their industrial development.

ii. Printing reduces process complexity

Printing is a fully additive patterning technique that allows the deposition of a material only where it is required. When compared to photolithographic patterning, fabrication steps are at least divided by a factor of 2. Moreover, printing processes require materials in the form of an ink or a paste, as a consequence, vacuum and clean room environments are no longer mandatory.

Flexible electronics using printing processes is a field of technology with great expectations in terms of market and business. A recent forecast from *Yole Développement* (February 2014) indicates that flexible and printed electronics market is likely to be close to one billion dollar by 2020, with a 27% Compound Annual Growth Rate (CAGR). In particular, as depicted in Figure I.1, functional printing will represent 89% of this market.

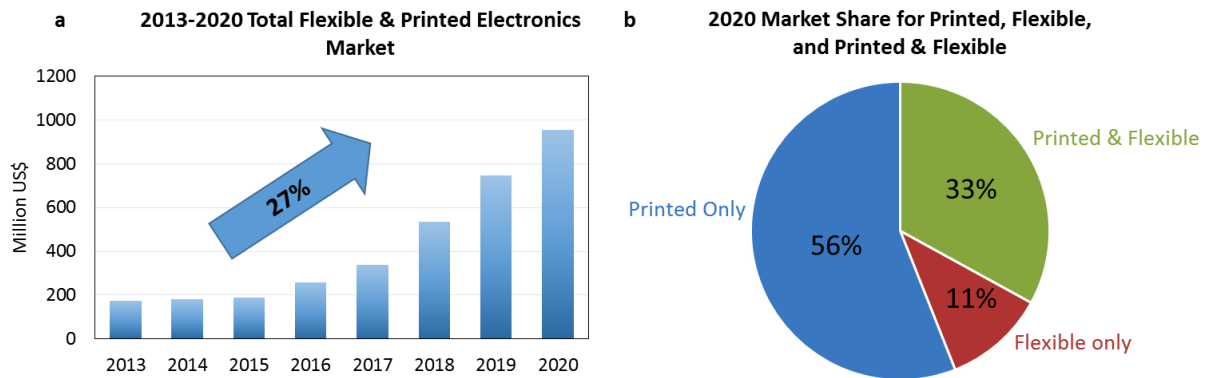


Figure I.1. a) 2013-2020 Flexible & Printed Electronics Market. b) 2020 Market Share for Printed, Flexible, and Printed and Flexible. Adapted from *Materials & Equipment for Printed and Flexible Electronics*, Yole Développement, 2014.

Therefore, there seems to be large industrial opportunities to seize in several fields of applications. If the flexible electronics market is strongly supported by the organic electronic materials for photovoltaics, displays and lighting, there are other fast growing domains such as sensors, e-paper and smart textiles. As a consequence, applied research institutes such as *Leti*, with a strong technological background have a large interest to explore the potential of this emerging market.

III. Objectives of the thesis

Among the several existing technologies for printed electronics, the interest was drawn towards drop-on-demand processes. Inkjet printing is a non-contact and digital technique that allows patterning features from 10 μm up to several centimeters. The digital source makes it independent regarding the volume to manufacture, and especially well-suited to prototyping and small-series fabrication.

In the past ten years, extensive efforts have been achieved for the formulation of electrically functional inks. Reviewing data from the literature shows that a broad electrical resistivity range has been covered ($10^{-7} - 10^{12} \Omega \cdot \text{m}$). Because of the potential of inkjet printing for the manufacturing of electrical interconnections, electrodes and antennas, inks based on conductive materials received much attention. Lots of research was conducted on metal nanoparticles-based inks (silver, gold, copper, and aluminum) as they offer low electrical resistivity close to the bulk material value. Moreover, colloidal suspensions of nanoparticles allow obtaining up to 60 wt% of active materials without hindering the printing process and its capabilities. Finally, nanoparticles exhibit enhanced size effects that reduce their melting temperatures and activation energy for sintering. Indeed, when printing metallic nanoparticles a post-printing thermal treatment is usually required not only to eliminate the ink vehicle but also to ensure contact between the nanoparticles and obtain a continuous medium for electronic transport. Nanoparticles inks are thus compatible with polymer substrates. Silver nanoparticles inks are undoubtedly the most widespread on the market of conductive printable materials. Self-formulation with specific features is commonly achieved at laboratory scale and many commercial references are nowadays available. Silver nanoparticles inks were thus selected and will be thoroughly investigated in this thesis. The present manuscript is organized in three chapters.

The first chapter is a literature review that introduces how conventional printing techniques are being adapted to functional inks and in what application fields they would most likely develop. A special

attention will be given to piezoelectric drop-on-demand inkjet printing. The printing process is detailed from ink ejection to impact and drying on the substrate. The key parameters involved in the conformal printing of a digital pattern, namely printing conditions and ink/substrate interactions are highlighted. As stated, layers printed with nanoparticles inks require thermal energy to become conductive. The annealing process, which can be achieved in several ways using convective, radiative and electromagnetic heat sources, induces severe modifications of the printed layers microstructure, which is polycrystalline and porous. Finally, to analyze the properties of these layers, theoretical models of electronic transport are presented as well as the nanoindentation method for mechanical characterization.

The second chapter is focused on the characterization of silver layers printed with a commercial silver nanoparticles ink. Test patterns are printed on SiO₂/Si substrates selected for their stability to thermal variations up to 300°C. The annealing is realized in oven and the evolution of the layers properties is investigated as a function of the annealing conditions. The microstructure is explored and morphological parameters such as roughness, grain size and porosity are measured. The electrical resistivity and the temperature coefficient of resistance of the silver layers is then analyzed. Moreover, the nanoindentation measurements allow the extraction of the mechanical parameters such as Young's modulus and hardness. In this chapter, the measured morphological parameters are employed to understand both electrical and mechanical properties of the silver layers. Besides, the correlation of the measurements with theoretical models supports the experimental methods that were developed.

In the last chapter, the knowledge of the printed silver layers assets and the optimization of the printing process lead to the design, fabrication and characterization of flexible electronic devices: a 17 GHz band-pass filter printed on polyimide, a flexible vacuum micro-sensor working on the Pirani principle, and a 250 μm thick membrane switch for keyboards. Finally, all-printed tunable capacitors were realized by stacking Barium Strontium Titanate (dielectric) and silver (electrode) printed layers. These prototypes exhibit performances near the state-of-the-art and suggest new opportunities for printing technologies.

The experience developed during this thesis on the inkjet printing of silver nanoparticles in the silicon environment of *Leti* offers promising perspectives that will be discussed in a concluding chapter.

Chapter 1

Printed Functional Layers: From Fabrication to Properties

Introduction

In the 20th century industrial printing techniques have been extensively developed for edition and packaging. In the last decades, the same printing processes are experiencing a fast technological development for flexible and functional applications. On one hand, roll-to-roll printing processes are a potential alternative manufacturing process to evaporation and metal-organic chemical vapor deposition (MOCVD) for large manufacturing volume and large area electronics applications (RFID antennas, photovoltaics, OLEDs-based displays). On the other hand, digital printing processes such as inkjet and spray offer new market opportunities for fast prototyping, low volume manufacturing (on demand), and patterning of 3D objects.

This introductory chapter is dedicated to a general description of the state-of-the-art printing techniques for the deposition of functional layers. We start by a review of the main printing processes employed for printed electronics, and a particular attention will be given to drop-on-demand inkjet printing.

The process flow for fabricating functional layers with inkjet printing is detailed from ink formulation and properties to post-printing treatments. In this thesis, a special interest is granted to silver nanoparticles inks for patterning conductive layers. Nanoparticles colloidal suspensions have to be stabilized by the addition of carbon chains. To obtain a conductive layer, a post-printing thermal treatment is required, not only to dry the layers but also to burn organic compounds and ensure contact between nanoparticles.

The resulting polycrystalline microstructure of the printed silver layers strongly depends on the annealing conditions. But above all, it defines both their electrical and mechanical properties. To understand and analyze the experimental results that will be presented in chapters 2 and 3, a theoretical approach on electron transport in polycrystalline media and a method to characterize thin films mechanical properties are finally proposed.

I. Overview of printing processes for printed electronics

The printing process flow can be divided in three main steps (Figure 1.1): ink formulation and fabrication, deposition and post-printing treatment.

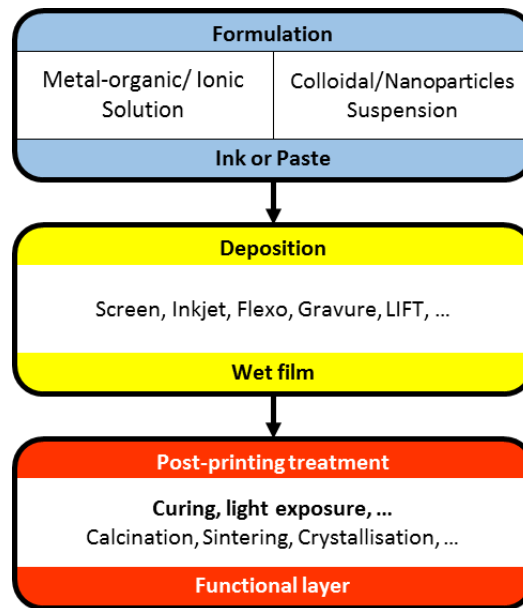


Figure 1.1. Printing process flow. Adapted from Pasquarelli (2011).

If all printing processes have a similar process flow, they usually differ in their ink requirements (viscosity, surface tension), their capabilities (resolution, printing speed) and their working principle. An overview of the main printing techniques that are employed for electronics manufacturing is proposed. They can be split in two families, namely contact and non-contact printing, coming from the mechanical contact between the ink delivery system and the substrate.

I.1. Contact printing processes

a) Offset lithography

In offset lithography, the pattern to print is supported by a plate functionalized with a patterned hydrophobic photopolymer thin layer (Figure 1.2.a). The plate, mounted on a cylinder, is wetted with a water-based dampening solution that is repulsed by the hydrophobic polymer. Then, the plate is inked with a hydrophobic and viscous ink (5-100 Pa.s) that fixes onto the patterned polymer. A blanket cylinder, usually of rubber, receives the patterned ink from the plate which is then transferred to the printing substrate (Figure 1.2.b).

Offset lithography is a printing technique commonly employed for prints from a few thousands up to several hundreds of thousands with high image quality. Its main limits originate from the degradation of the photopolymer plate.

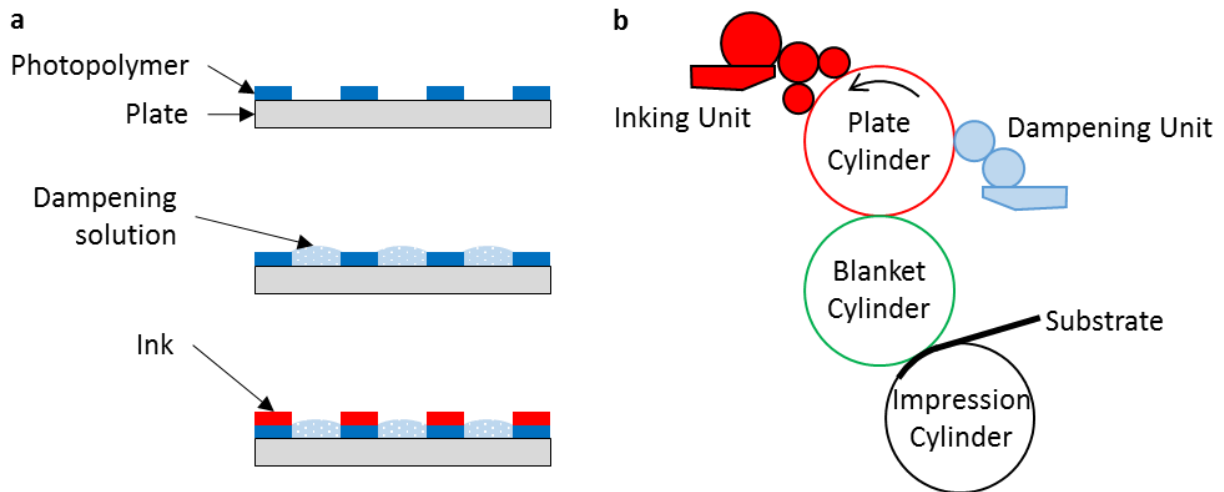


Figure 1.2. a) Inking process of a plate for offset lithography. b) Offset lithography printing. Adapted from Kipphan (2001).

For printed electronics applications, offset lithography main limitation arises from the aqueous dampening solution that might affect the functional materials (Blayo, 2005). This issue can be overcome by replacing the dampening solution by a silicone layer (“waterless” offset plate).

Offset techniques have been employed for printing conductive patterns such as silver electrodes for humidity sensor (Harrey, 2002) and conductive polymer layers (Reuter, 2007).

b) Flexography

Flexography printing is a relief- based printing method where a polymer is patterned with the features to print (plate cylinder). The anilox roller is the key element that characterizes this technology: it controls the quantity of ink that is transferred to the plate cylinder. The substrate receives the patterned ink by mechanical pressure between the plate and the impression cylinder (Figure 1.3). Flexographic inks can be water-based, solvent-based or UV-curable with relatively low viscosity (0.01 – 0.5 Pa.s).

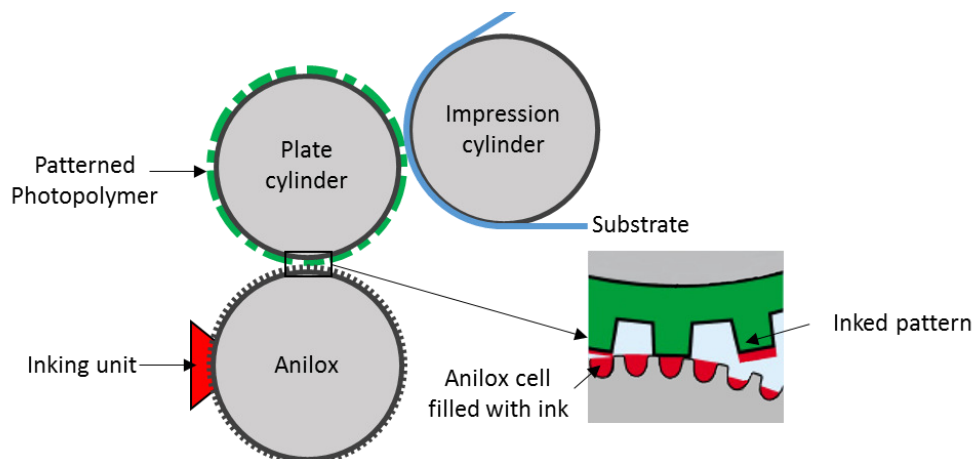


Figure 1.3. Flexographic printing process. Adapted from Kipphan (2001).

The anilox roller is a cylinder engraved with a matrix of cells allowing a fast and constant transfer of the ink to the plate cylinder. The shape and dimensions of the cells will be selected according to the substrate and ink properties.

The quality of flexographic printing highly depends on the settings of the equipment and in particular the pressure applied to the substrate. Indeed, the relief polymer may be squashed, inducing irregularities of the printed pattern. It is mostly used for packaging, bags and paperboards on short to medium runs.

Silver nanoparticles inks were printed with flexography to study inline photonic sintering (Hösel, 2012). Also, Yu *et al.* (2012) have printed silver electrodes for all-printed polymer solar cells.

c) Gravure printing

In gravure printing, the printing patterns are engraved in a metallic cylinder that soaks into an ink reservoir. A doctor blade allows removing the ink excess. The ink remaining in the engraved cells is finally transferred to the substrate under mechanical pressure. Gravure printing inks have low viscosity (0.01 – 0.05 Pa.s) and can be water or solvent-based.

Gravure printing is a high-speed roll-to-roll printing process well-adapted for long-runs (>500,000 units) with high printing quality.

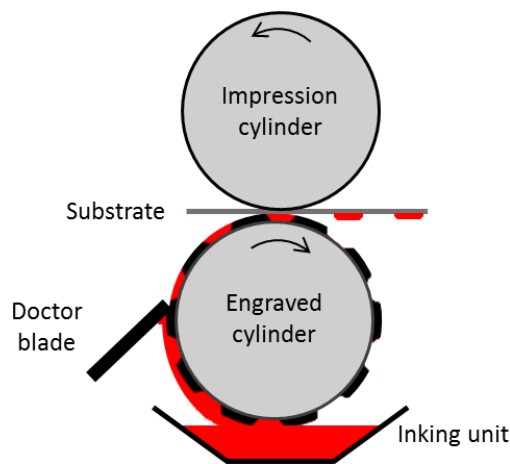


Figure 1.4. Gravure printing process. Adapted from Kipphan (2001).

Gravure printing main limitation for printed electronics is the applied mechanical pressure that might damage non-flexible and non-compressible substrates. Silver nanoparticles inks were gravure printed on a PET Melinex substrate (Sung, 2010) as well as on glass (Hrehorova, 2011).

d) Screen printing

Screen printing is a large area printing method based on the stencil principle: a viscous ink (0.1 – 10 Pa.s) is forced through a patterned solid mask by the means of mechanical pressure applied by a squeegee (Figure 1.5).

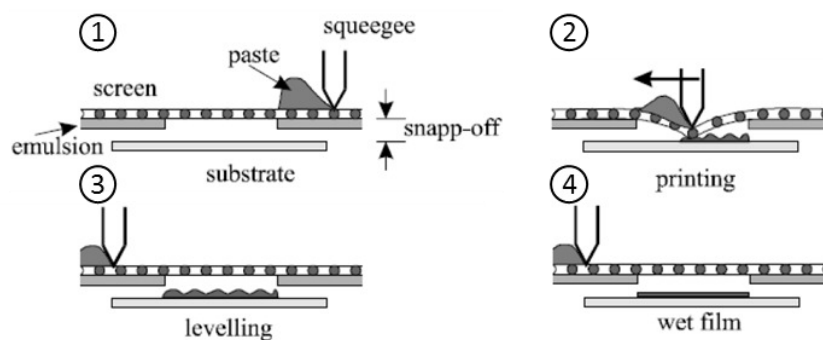


Figure 1.5. Screen printing process. Adapted from Burgelman (1998).

The main limitations of screen-printing are the printing speed and the lower resolution compared to most printing techniques. However, screen printing is very well-suited for printed electronics manufacturing due to its ability to produce thick layers from paste-like materials. It allows depositing and stacking several layers including dielectric materials.

Screen printing process is already deployed in industrial fabrication of printed electronics thanks to its maturity. As an example, ISORG¹ fabricates organic photodiodes by screen printing of organic photopolymers on flexible substrates such as PEN and PET. Also, Krebs *et al.* (2009) demonstrated the fabrication of large polymer solar cells by a full screen printing process (several square meters). Zinc/Manganese oxide batteries were recently screen printed on paper substrates by Madej *et al.* (2014). Among consumer applications, the most common are RFID tags and membrane switches used in remote controls and calculators. Also, screen printing is used in OLED displays manufacturing.

1.2. Non-contact and Direct-Writing processes

Non-contact printing processes differentiate from contact printing on two major points. The first is that the ink delivery system does not physically touch the substrate, allowing to print on a wide variety of objects that can also be 3D shaped. The second is their ability to transpose digital information through a computer-controlled translation stage, which moves a print head that patterns materials with controlled architecture and composition (Tekin, 2008).

Non-contact, and in general direct-writing technologies distinguish from photolithography patterning processes and contact printing as they allow depositing a controlled quantity of matter with a predefined shape without any pre-patterned hard mask. As a consequence, with direct-writing processes, several fabrication steps are avoided. Hon (2008) proposed the classification of direct-writing techniques in Figure 1.6.

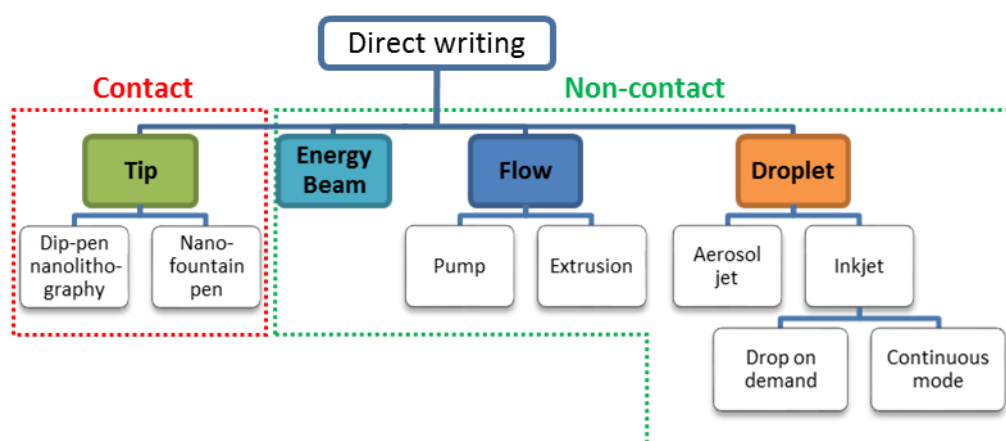


Figure 1.6. Classification of direct-writing methods. Adapted from Hon (2008).

Tip-based direct-writing techniques have emerged thanks to the normalization of Atomic Force Microscopy (AFM, cf. Annex 2). Several nano-patterning methods allow the manipulation of single molecules such as proteins, polymers and enzymes using AFM tools (Piner, 1999). Tip-based

¹ ISORG is a start-up from CEA, LITEN based in Grenoble. It develops and manufactures organic photo-detectors and imaging sensors.

techniques, even if classified as direct-writing, will not be detailed in this thesis as the patterning dimensions are about three orders of magnitude lower than ink-based printing techniques.

a) Energy beam - LIFT

Highly energetic beams like laser and focused ion beam can be used to deposit thin films and pattern 2D and 3D structures. There are several methods, especially laser-based for this purpose. In this non-exhaustive list we shall quote: laser chemical vapor deposition (LCVD), laser enhanced electroless plating (LEEP), laser induced forward transfer (LIFT).

LIFT consists in ablating a small part (a pixel) of a thin film deposited on a transparent substrate and transferring it to a receiving substrate placed in closed proximity. The pixel ablation is realized by a pulsed laser irradiation. The working principle of LIFT is illustrated in Figure 1.7.

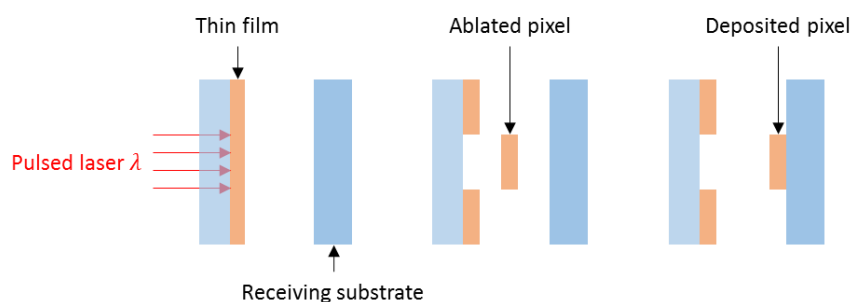


Figure 1.7. Working principle of Laser Induced Forward Transfer (LIFT).

Since its first demonstration by Bohandy *et al.* (1986), LIFT, that can be operated in room atmosphere, has been extensively studied for the deposition and direct-writing of all kinds of materials under different phases: solids (Adrian, 1987), liquids (Colina, 2006), and powders (Pimenov, 1995).

In addition to metals, LIFT has been successfully applied for laboratory-scale deposition of oxides (Sakata, 2005) and fragile materials such as biomolecules (Dinca, 2008), cells (Hopp, 2005) and DNA (Colina, 2005). Current trends led to the demonstration of the transfer of multilayered structures for organic thin films transistors (OTFTs) (Constantinescu, 2014).

The Laboratory of Lasers, Plasmas and Photonic process (LP3) in Marseille (France) has developed a strong knowledge and know-how in LIFT deposition techniques. LP3 was a partner of the I2Flex project in which a membrane switch was designed and fabricated. These results will be presented in chapter 3.IV.

b) Flow-based direct-writing

Flow-based processes allow a precise micro-dispensing of liquids through the application of a mechanical pressure on a reservoir with an output tip (syringe). This method differs from inkjet and aerosol technologies as the output is a continuous flow between the nozzle and the substrate. Thanks to the mechanical actuation system for the micro-dispensing, the range of fluid viscosities is broad (0.005 to 1000 Pa.s) (Hon, 2008). In parallel, the volume of fluid that can be delivered lies between dozens of nanoliters down to picoliters.

c) Spray printing

In spray or aerosol printing, a pneumatic atomizer creates an aerosol from the fluid to be jetted which is then carried to the ejection nozzle. The working principle of an M3D Optomec aerosol printer is illustrated in Figure 1.8. The ink is placed into an atomizer which creates a dense aerosol with droplets

between 1 and 5 μm . The aerosol is carried by a N_2 gas flow to a nozzle where it is focused and ejected towards the substrate.

This process uses low viscosity inks (1-2500 mPa.s) that can be particles suspensions, polymers and adhesives. This non-contact printing method enables printing over steps and curved surfaces with features as small as 10 μm . Aerosol direct-writing has found several applications in the field of electronics manufacturing. As an example, collector lines for silicon solar cells were aerosol printed using high silver load inks (> 70 wt%) (Hörteis, 2007).

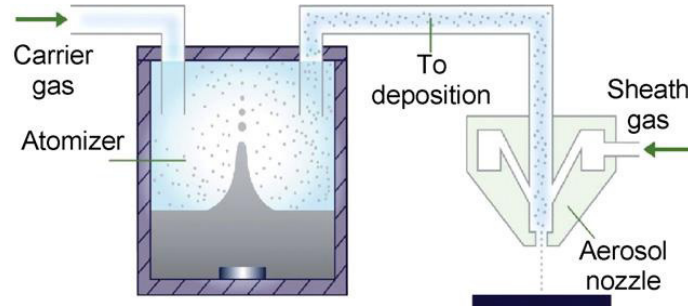


Figure 1.8. Printing by spraying (Hon, 2008).

d) Inkjet printing

Inkjet printing consists in the ejection of controlled volume droplets of ink from a chamber through a nozzle. The ink droplets that move at several meters per second reach the substrate at target positions, defined by a numerical file, to form a patterned layer.

Inkjet printing process can be divided in two families, namely Continuous Inkjet Printing (CIJ) and Drop-on-Demand printing (DoD). As illustrated in the roadmap of inkjet technology (Figure 1.9), there are several methods of actuation for droplet ejection.

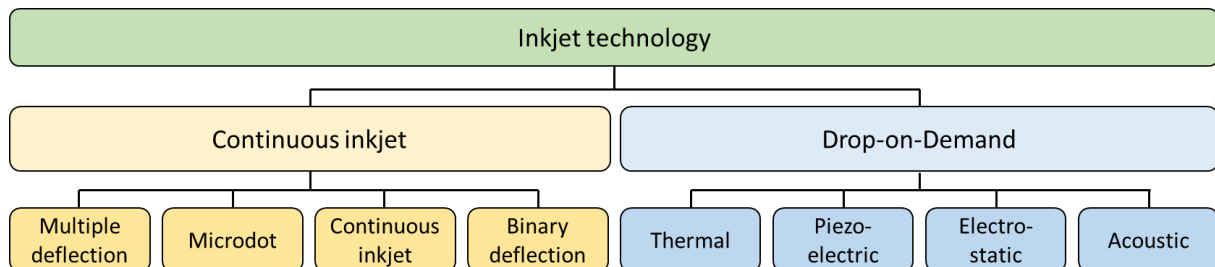


Figure 1.9. Roadmap of inkjet printing technology. Adapted from Le (1998).

i) Continuous inkjet printing

In continuous inkjet technology, a drop generator delivers a fluid from a reservoir to a nozzle that ejects a continuous stream of droplets at high frequency (50 – 175 kHz) (Figure 1.10). In a binary deflection system once the filament breaks, droplets travel through an electrode that selectively charges them with an electrical pulse. Then the droplets are deflected by a high electrostatic field:

- Charged droplets are deflected to a gutter for ink reflooding;
- Uncharged droplets are unaffected by the electrical field and go straight onto the substrate.

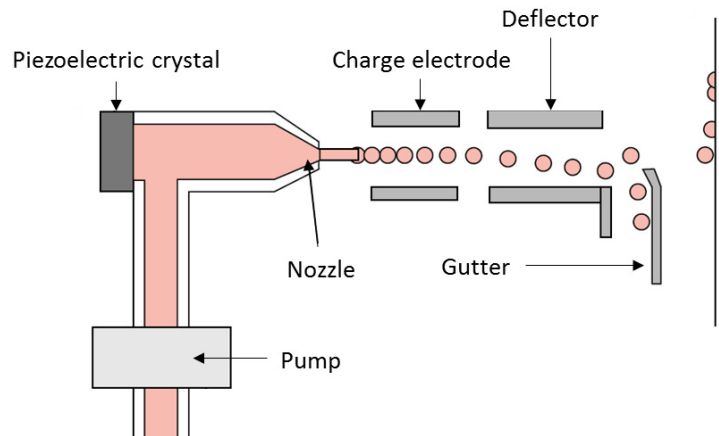


Figure 1.10. Continuous inkjet. Adapted from Kipphan (2001).

In a multiple deflection system, droplets are charged at different levels and then deflected onto the substrate by the electrostatic field with a different angle of impact while uncharged droplets are reflowed.

The high ejection frequency allows a rapid printing, suitable for industrial coding of products and packages. Moreover, thanks to the high droplet speed (in the order of $50 \text{ m}\cdot\text{s}^{-1}$), CIJ is well-suited to large distances (several mm) between the print head and the substrate as well as the use of volatile solvents inks (fast drying). Finally, the continuous ink flow prevents nozzles from clogging.

The main limitations of CIJ printing are a relatively low printing quality and the ink type, which must be electrically chargeable (Kipphan, 2001).

ii) Drop-on-Demand

Drop-on-demand technology (DoD) differs from CIJ as droplets are ejected from the nozzle only when required. As a consequence, nor droplet selection (electrical charging) neither ink reflowing are needed. DoD technology is based on the ability of the ejection system to create droplets with a similar volume at a constant frequency.

There are several actuation methods, the most popular used in the droplet formation process are thermal and piezoelectric.

- Thermal actuation (Figure 1.11): a heating element located near the nozzle generates a vapor bubble inducing an increase of volume in the pressure chamber. The exceeding volume leads to the ink droplet ejection. In this method, chamber volume is constant whereas ink is thermally dilated.
- Piezoelectric actuation (Figure 1.12): a piezoelectric element located near the nozzle deforms the chamber wall inducing the ejection of the ink droplet through the nozzle. Chamber volume decreases under a mechanical deformation whereas ink volume is constant, if considered incompressible.

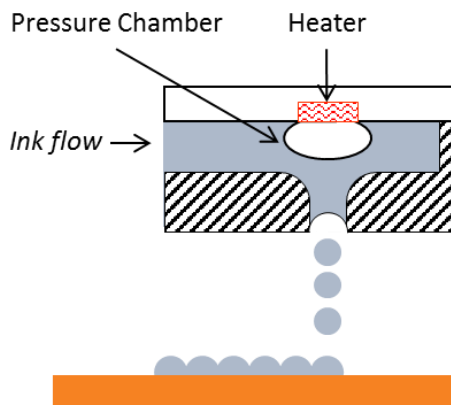


Figure 1.11. Thermal inkjet.

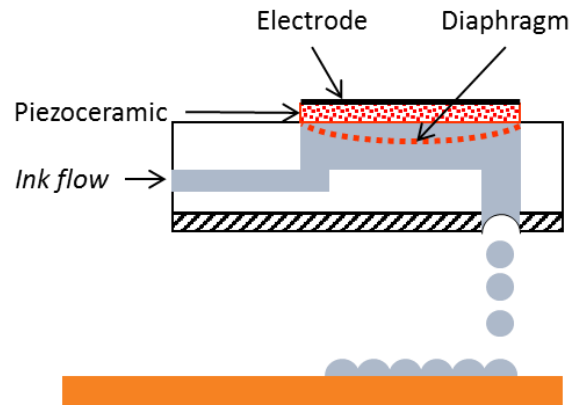


Figure 1.12. Piezoelectric inkjet.

In this thesis, a Dimatix DMP2831 piezoelectric inkjet printer was used (cf. paragraph II.3). Hence, we have focused on the requirements of piezoelectric inkjet printing, which is mostly employed in printed electronics.

iii) Inkjet inks

For inkjet printing, viscosity and surface tension of the ink are crucial parameters. Ink viscosity is low, in the order of 1-30 mPa.s, necessary for the piezoelectric chamber to be refilled at high frequency (several kHz). Surface tension is around 30 mJ.m⁻² allowing the droplet formation. Viscosity and surface tension are temperature dependent and advanced jetting technology may include a localized heating system for tuning ink properties just before ejection. Inkjet inks for conventional applications (edition and packaging) contain either pigments or soluble dyes. Their vehicle may be water-based, solvent-based, hot-melt or UV-curable. In the particular case of colloidal suspensions inks, additives are used to prevent particles agglomeration and precipitation.

1.3. Comparison of printing processes characteristics

The main characteristics of printing processes for printed electronics are presented in Table 1.1.

Table 1.1. Main characteristics of printing processes.

Printing method	Ink viscosity (Pa.s)	Min. Thickness (μm)	Min. size (μm)	Registration ² (μm)	Throughput (m ² /s)	Resolution (μm)
Offset	5 – 100	0.5 – 2	10 – 50	> 10	3 – 30	10 – 60
Flexography	0.01 – 0.5	0.4 – 8	80	< 200	3 – 30	10 – 50
Gravure	0.01 – 0.2	0.1 – 12	75	> 20	3 – 60	10 – 50
Screen	0.1 – 50	3 – 100	20 – 100	> 25	2 – 3	30 – 100
LIFT	0.001 – ∞	0.1 – 10	2 – 100	> 1	–	10
Spray	0.001 – 2.5	0.01 – 1	10 – 50	> 1	–	10
Inkjet	0.001 – 0.03	0.01 – 1	5 – 50	> 1	0.01 – 0.5	10 – 100

Inkjet printing technology was chosen in the framework of the I2Flex project for its many assets. Indeed it is a digital process that does not require manufacturing of hard masks. Moreover, it offers among the best capabilities in terms of resolution and the lowest achievable thicknesses, which is of major interest in the fabrication of electronic devices. Finally, if inkjet is not the most suited printing technique for large scale production, it is very well adapted for lab-scale studies and device prototyping.

²Registration: capability of a printing system to superimpose different ink layers. In microelectronic lithography the term alignment is employed.

II. Inkjet printing for printed electronics

Drop-on-Demand inkjet printing market had experienced a major impulse in the 1980's, when consumer and office inkjet printers appeared on the market. Canon and Hewlett Packard (HP) were leaders with thermally actuated nozzles. In the 1990's, the development of inkjet technologies continues, in particular for color printing. Thermal actuation performances are improved by Canon and HP while piezoelectric actuation is fast-growing, especially for non-aqueous inks.

Inkjet print heads, both thermal and piezoelectric, are amongst the first MEMS consumer products. Today, despite the diversification of MEMS components (sensors, RF, bolometers, etc.), inkjet print heads keep a constant share of the MEMS market (Figure 1.13).

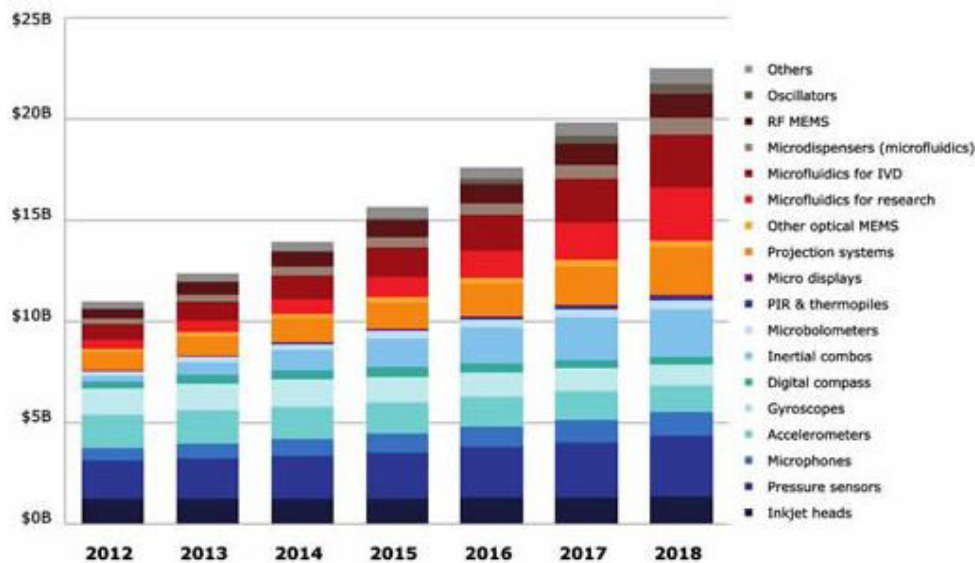


Figure 1.13. 2012-2018 MEMS market forecast by devices.
(Source: Status of the MEMS Industry report, July 2013, Yole Développement).

II.1. Piezoelectric DoD inkjet printing process

Successful inkjet printing of a pattern relies on the equilibrium between the characteristics of the printer, the physico-chemical and rheological properties of the ink, and the substrate surface properties.

Inkjet printing can be separated in three main steps, namely the droplet formation, the impact on the substrate and the drying of the ink. Each step strongly depends on the physico-chemical properties and dimensions of the involved elements, namely the printing system, the ink and the substrate.

a) Droplet ejection

The process of inkjet printing involves the ejection of a controlled quantity of a fluid stored in a reservoir through a nozzle. In the case of piezoelectric actuation, pressure waves (acoustic) resulting from the voltage applied to the piezoelectric ceramic propagate through a cavity pushing the fluid outwards (Figure 1.14).

A droplet is ejected when the amount of transferred kinetic energy is larger than the surface energy of the ink meniscus (Tekin, 2008). This transferred kinetic energy defines the droplet velocity. Moreover, the initial velocity of the droplet, in the order of several m/s, must overcome the friction with ambient air.

A large amount of research has been pursued in the design of piezoelectric and thermal heads as well as in the understanding of the droplet formation process (Bogy, 1984; Yang, 2006; Wijshoff, 2010).

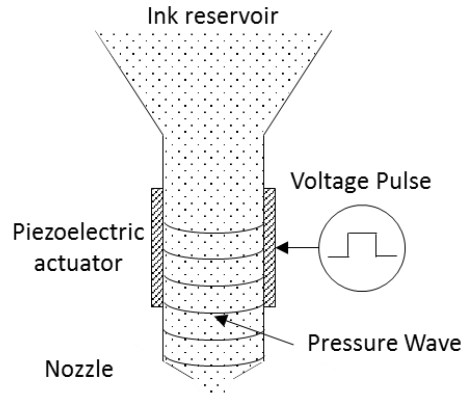


Figure 1.14. Schematic of the actuation of a piezoelectric inkjet nozzle. Adapted from Wu (2004).

With piezoelectric actuation, droplet size and ejection speed can be controlled by the actuation voltage and frequency. Reis *et al.* (2005) have demonstrated that the droplet volume and velocity are linearly dependent on the driving voltage of the piezoelectric, as illustrated in Figure 1.15. Reis *et al.* have also shown that the droplet volume follows a periodic behavior with pulse width and frequency.

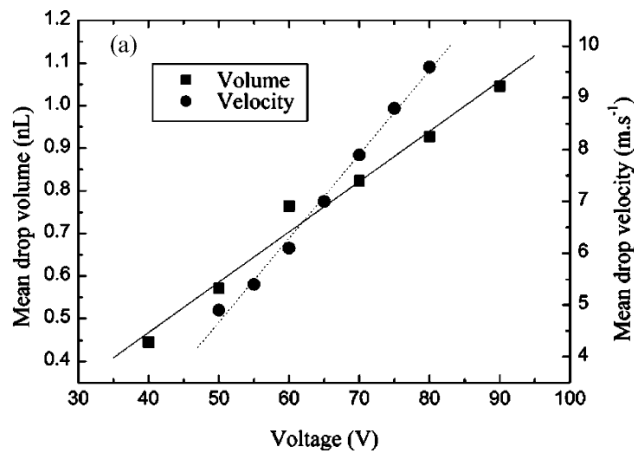


Figure 1.15. Influence of driving voltage on ejected droplet volume and velocity (Reis, 2005).

The droplet formation mechanisms depend on the propagation of the acoustic waves in the fluid-filled chamber. Wave propagation is not only influenced by the chamber dimensions (Bogy, 1984) but also by the ink physico-chemical properties.

These mechanisms can be described by the Navier-Stokes equation. Based on Fromm's results (1984), one of the most employed methods is to characterize droplets behavior through dimensionless numbers used in fluid mechanics. In the following equations (1. 1), (1. 2), and (1. 3) v, ρ, σ, η, a are the droplet velocity ($m.s^{-1}$), density ($kg.m^{-3}$), surface tension ($J.m^{-2}$), viscosity ($Pa.s$) and the characteristic dimension of the nozzle (m), respectively.

- Reynolds number Re (1. 1) is defined as the ratio of inertial forces to viscous forces. It characterizes the flow regime of a fluid. Laminar flows correspond to low Re whereas high Re correspond to turbulent flows.

$$Re = \frac{va\rho}{\eta} \quad (1. 1)$$

- Weber number We (1. 2) is defined as the balance between inertial and capillary forces. It is used to characterize fluid flow at the interface between two fluids and also in the study of drop formation mechanisms where a liquid interacts with the surrounding atmosphere.

$$We = \frac{v^2 a \rho}{\sigma} \quad (1. 2)$$

- Ohnesorge number Oh (1. 3) is defined as the ratio of the square root of We to Re . It relates viscous forces to inertial and surface tension forces. The Ohnesorge number is independent from the droplet velocity.

$$Oh = \frac{\sqrt{We}}{Re} = \frac{\eta}{\sqrt{a \rho \sigma}} \quad (1. 3)$$

Fromm (1984) demonstrated that the inverse of the Ohnesorge number, commonly noted Z , must be higher than 2 in order to obtain stable droplet ejection. Experimental studies and numerical simulations by Reis and Derby (2000) showed that stable droplet ejection can be achieved in the range $1 < Z < 10$.

In 2009, Jang *et al.* redefined the printability range to $4 < Z < 14$ by monitoring droplet formation dynamics. They considered characteristics such as single droplet formability, positional accuracy and maximum allowable jetting frequency.

- When $Z < 4$, long-living filaments are to be expected worsening minimum stand-off distance, positional accuracy, and maximum jetting frequency (Figure 1.16.a).
- For $Z > 14$, droplets experience a rapid elongation and rupture of the filament generating satellite droplets (Figure 1.16.b).

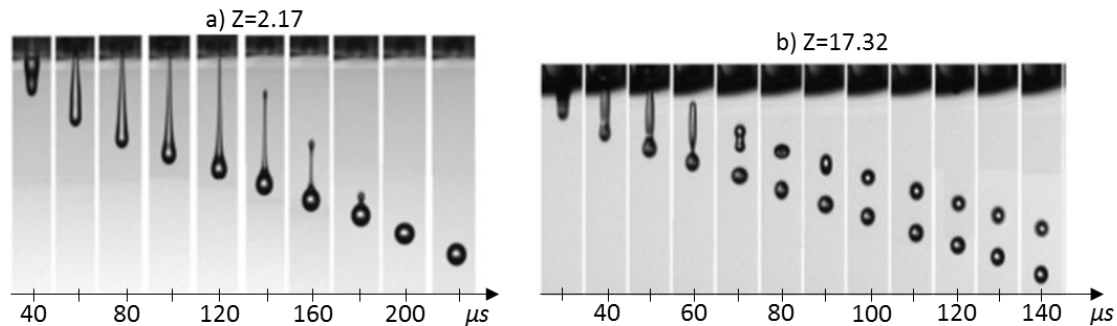


Figure 1.16. Droplet formation sequence for a fluid with a) $Z=2.17$ and b) $Z=17.32$. Adapted from Jang (2009).

Most piezoelectric inkjet print heads allow adjusting the nozzles temperature to tune viscosity and surface tension and hence Z number of the ink right before ejection.

b) Droplet impact

Once the droplet is created, the next step is its impact on the substrate. This is largely reported in literature with experimental observations and mathematical modeling. For example, Park *et al.* (2003) identified four stages in the impact process of a single drop on a smooth surface at room temperature through an experimental and theoretical study (Figure 1.17). These stages depend on the fluid properties and its interactions with the substrate. They can be characterized by the spreading ratio S_r , defined as the ratio of the droplet-substrate interface diameter to the initial droplet diameter.

- Stage 1: impact, the drop is spherical just before the impact. $S_r = 1$.
- Stage 2: spreading, the interface between the droplet and the substrate increases to a maximum value. $S_r = S_{r\ maximum} > 1$.
- Stage 3: retracting and rebounding, the fluid reaches its maximum retraction characterized by a minimum spreading ratio, a series of oscillations follow dampened by viscous dissipation. $S_r = S_{r\ minimum}$.
- Stage 4: equilibrium, the kinetic energy of the drop is totally dissipated. $S_r = S_{r\ final}$.

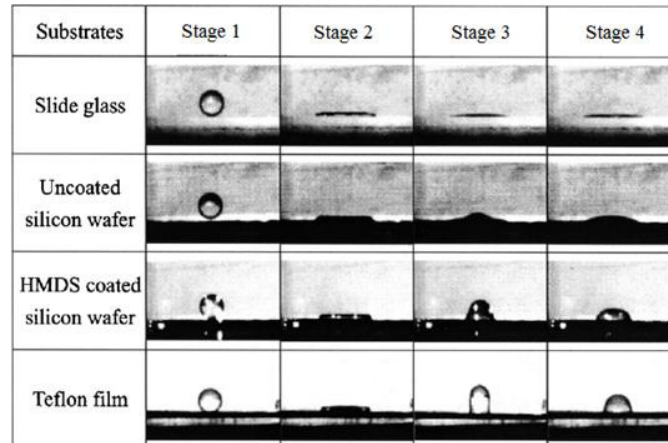


Figure 1.17. Spreading and retracting of a water droplet on smooth surfaces (Park, 2003).

The parameters that were identified to influence the impact process of inkjet droplets are:

- Ink: density, viscosity, elasticity and surface tension;
- Droplet: velocity and size;
- Substrate surface: roughness, surface energy, chemical homogeneity, planarity.

A thorough study of the impact process of inkjet droplets on smooth and non-porous substrates was carried out by Jung (2011) who concluded that the surface tension of the ink and the wettability of the surface have a key role in determining the drops final diameter.

When inkjet printing on porous substrates such as paper, other phenomena occur at the droplet impact. Indeed, because of the strong capillary forces originating from the substrate porosity ink vehicle is adsorbed and or absorbed, causing the separation of the ink functional materials and the solvent.

The properties of the “ink – substrate” system determine adhesion and wettability of the final printed layer. In the fabrication process, a proper binding of the ink to the substrate guarantees high printing quality (optical density, bright colors, sharpness). In the field of printed electronics, the expected properties of the printed layers are even more critical: pattern continuity, water resistance, mechanical properties (adhesion, shear, delamination, and flexibility). In addition, depending on the end-use of the printed layers, other characteristics might be expected: electrical conductivity, carriers mobility, permittivity, etc.

The interactions between ink and substrate have also a strong influence on the resolution of the patterns, the pitch between lines (ink spreading) and the reproducibility (substrate chemical and structural homogeneity).

In inkjet printing, because of its non-contact working principle, the dynamics of ink settling on the substrate is substantially different from other printing processes. As an example, in roll-to-roll printing

ink is transferred to the substrate under mechanical pressure, while for screen printing the highly viscous ink receives both kinetic energy and pressure from the squeegee.

Figure 1.18 illustrates the phenomena that may occur after droplet impact. It must be noted that these phenomena simultaneously occur and that the timescale gives an order of magnitude of the duration of each step (Kettle, 2010).

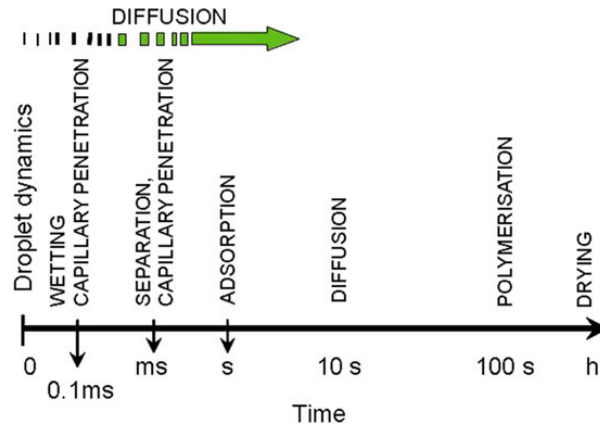


Figure 1.18. Presumed interaction phenomena of ink setting and their relevant onset timescales in porous media (coated paper). Kettle (2010).

In order to improve the substrate printability, either physical or chemical surface treatments can be realized. Physical treatments are used to temporarily change the surface energy of the substrate or clean the surface from ambient pollution like moisture and dusts (plasma and Corona treatment). Chemical treatments allow surface cleaning (chemical bath) and also chemical functionalization (e.g. tune hydrophobicity with a polymeric coating).

A general condition to fulfill in inkjet printing is that the ink surface tension must be lower than the surface energy of the substrate: $\sigma_{ink} < \sigma_{substrate}$.

c) Ink drying

The last step in the formation of an inkjet printed layer is the drying of the ink. In this process, the ink changes of physical state from liquid to solid. The ink solvent is evaporated while the ink functional materials (pigments, polymers, solid particles, molecules, etc.) remain on the substrate surface.

It was experimentally and theoretically demonstrated that the evaporation of the solvent of a colloidal droplet on a substrate can lead to a multiplicity of patterns as shown in Figure 1.19 (Bhardwaj, 2009). As a consequence, the drying process of printed films influences their morphology and the distribution of functional materials.

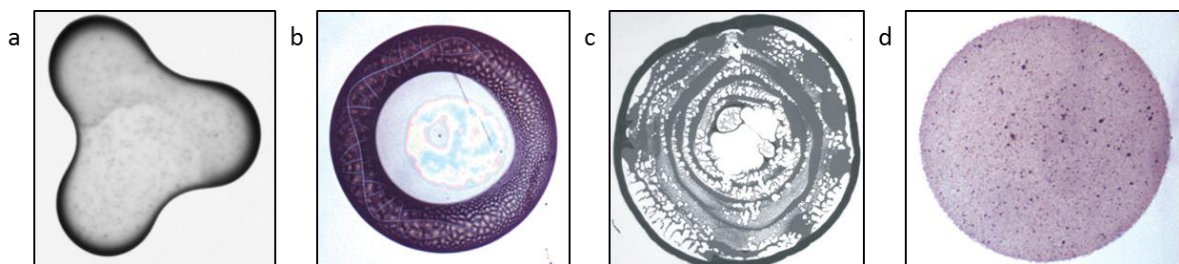


Figure 1.19. Deposits obtained after drying of colloidal drops. a) Coffee droplet (Deegan, 1997).
 b) Aqueous drop containing polystyrene spheres on titanium (Sommer, 2004).
 c) Aqueous drop containing 1 μ m polystyrene microspheres on glass (Bhardwaj, 2009).
 d) Aqueous drop containing hydroxyapatite particles on titanium (Sommer, 2004).

Deegan *et al.* (1997, 2000) have in particular studied the so-called “coffee-ring” effect which describes the preferential deposit of particles at the edges of a drying droplet (Figure 1.19.a). This phenomenon is caused by the higher evaporation rate at the edges than at the center that induces a convective flow.

The effect of the evaporation flows on the silver nanoparticles was observed on single droplets printed on silicon substrate. Figure 1.20 shows a splat of a silver NPs ink droplet printed on a silicon substrate. Here, the M-shape profile of the splat is characteristic of the coffee-ring phenomenon.

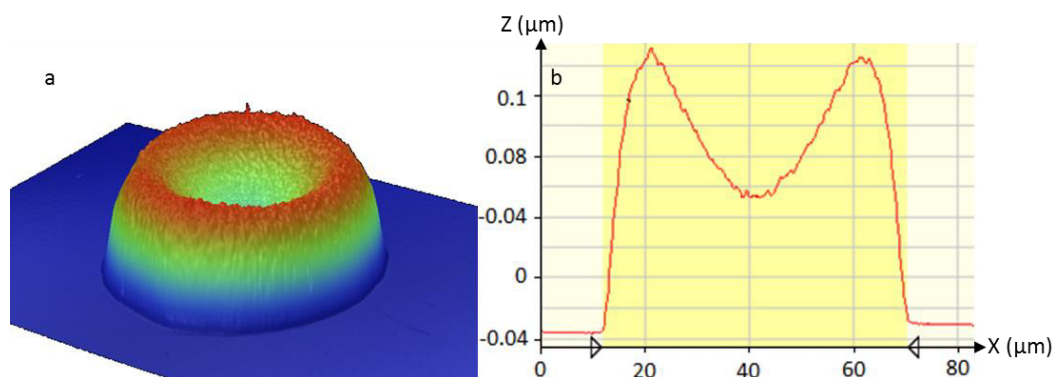


Figure 1.20. Splat of a silver ink droplet observed by optical interferometry. a) 3D view and b) profile.

Hu *et al.* (2006) have shown that Marangoni flow, i.e. surface tension driven flow, reverses the coffee-ring effect as it is directed in the opposite direction of the convective evaporation flow. Marangoni flows can be enhanced by adding a minor co-solvent with high boiling temperature and low surface tension (Lim, 2008).

II.2. Printing equipment

In the last decade, the rise of printed electronics led to the development of inkjet printing equipment with improved capabilities for the deposition of functional materials. Several manufacturers propose inkjet printers for the development of industrial production. Among these, one can cite Ceradrop and Impika (France), Fujifilm Dimatix (USA), Unijet (South Korea), PixDrop (Germany).

These printers can be equipped with several print heads (simultaneous printing of different materials), but they are limited by a sheet-feeding. Moreover, because post-printing treatment is not always integrated, manual or automatic transfer from the printers towards an annealing line is usually required.

To overcome these limitations, prototypes are being developed by the cooperation between academic laboratories and industry. As an example, at the *Center of Microelectronics in Provence* (CMP), a prototype printer *JetPac* has been developed in collaboration with Impika. It is equipped with several piezoelectric print heads, in-line modules allowing surface pre-printing treatment (atmospheric plasma torch) and post-printing treatment (UV lamp and microwave). An automatic conveyer moves the substrates between the different modules. *The JetPac was used to print patterns for the prototyping of a membrane switch that will be presented in chapter 3.IV.*

Another interesting and innovative test station³ has been developed at Chemnitz University of Technology where an inkjet Xaar 1001 system is integrated into a gravure printing system LaboMAN.

³Last accessed 09/15/2014 from <https://www.tu-chemnitz.de/mb/DigiTech/equipment.php>

Such a printing configuration allows not only the personalization of gravure printed structures but also the study of droplet flight and landing behavior on moving substrates.

II.3. Technology of a lab printer: Dimatix DMP2831

In this thesis the very popular⁴ laboratory-scale Dimatix DMP2831 inkjet printer was used for sample preparation. The Dimatix (Figure 1.21) is a drop-on-demand piezoelectric printer composed of four main parts.

- Print Carriage: it holds and moves the cartridge (ink tank and nozzles). The print carriage moves over the substrate in a single X direction. A fiducial camera is mounted on this carriage, allowing pattern alignment and observation of the printed patterns.
- Chuck: it is a stainless steel plate that holds by suction the substrate during printing. The chuck moves along a single direction Y, perpendicular to the print carriage displacement. A tilt angle can be applied to compensate misalignment with features on the substrate. The stand-off distance (distance between the nozzles and the top of the substrate) can be adjusted between 0.250 and 1.500 mm.
- Drop Watcher: it is a stroboscopic camera that allows observing droplets ejection in real-time while modifying the ejection parameters. A gutter is placed under the nozzles to collect ejected droplets during the settings of the ejection parameters.
- Cleaning station: it consists of a cleaning pad where the cartridge can be cleaned with different operations (spit, purge and blot). Cartridge cleaning can be programmed before, during and after printing.

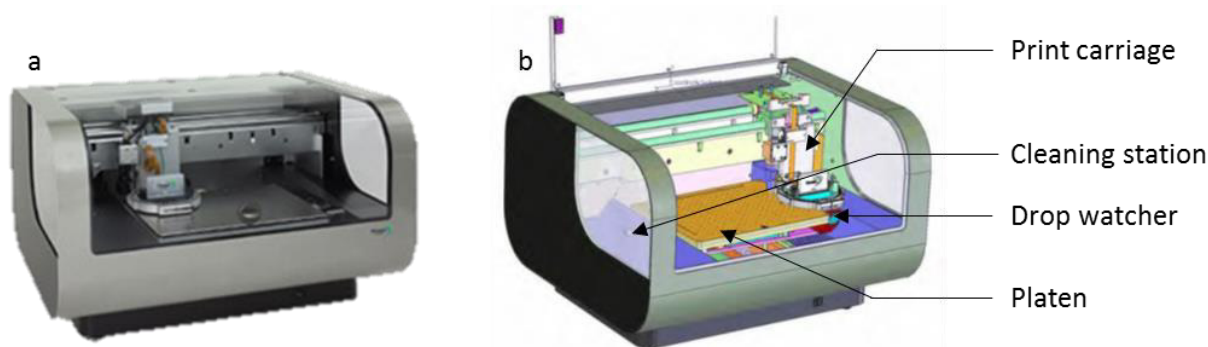


Figure 1.21. Dimatix DMP2831 inkjet printer. a) Picture. b) Schematic and parts.

The user manual of the printer is complete and lots of information are provided on the functioning and the capabilities of the printer. However, we report details on three main settings of the printer, namely the digital source patterns, the piezoelectric actuation of the print head, and the drop spacing (pattern resolution).

a) Digital source patterns

The input patterns to print with the Dimatix can be realized in two ways:

- Using the embedded design software where one can define geometrical shapes by entering the pixels coordinates. This method is useful to print simple patterns (lines, single dots,

⁴466 results on Google Scholar for the keywords « Dimatix DMP 2831 » on September, 15th 2014.

squares, and rectangles), however when it comes to more complex shapes (triangles, circles, coils, serpentes, etc.) pattern definition can be long and tedious.

- ii. Using binary bitmap (.bmp) files. *This method was mainly employed in this thesis. Patterns were firstly generated with a vectorial design software (CleWin4), and then saved as bitmap files. Finally pattern resolution in dpi (dot per inches) or pixels per centimeters (pix/cm) was adjusted using Adobe Photoshop CS5.*

b) Piezoelectric actuation

The print head of the Dimatix is composed of 16 aligned nozzles that have piezoelectric actuation and that can be heated up to 70°C. Each nozzle piezo-actuator can be individually set in order to achieve the same ejection conditions (compensate manufacturing differences from one actuator to another).

The actuation of the piezoelectric actuator goes through two steps: the setting of the voltage waveform and the setting of the maximum voltage applied. A typical actuation cycle is illustrated in Figure 1.22.

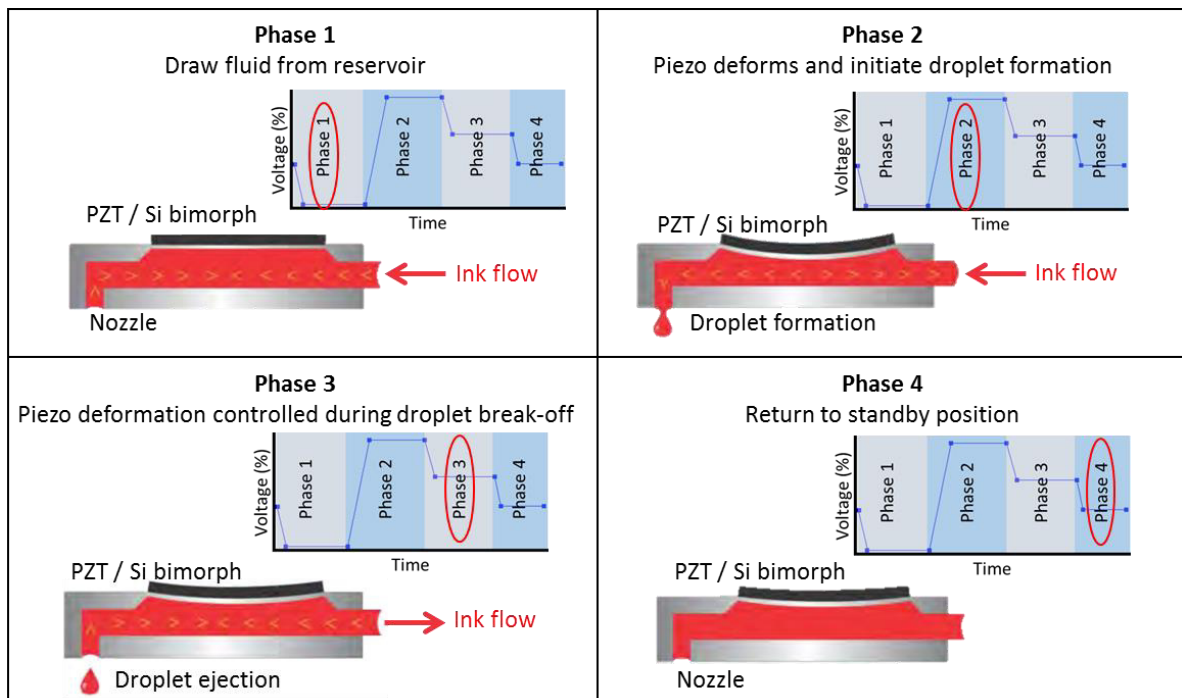


Figure 1.22. The four phases of the piezoelectric actuator of the Dimatix nozzles. Adapted from (Dimatix DMP2831 User manual, n.d.).

In the actuation cycle illustrated in Figure 1.22 the voltage waveform has four stages. On the Dimatix printer several parameters of the waveform can be modified, namely the duration, the slew rate, the number of phases.

The shape of the actuating waveform of the piezoelectric has a strong influence on the droplet ejection process. It controls the droplet dimensions and velocity as well as the ejection frequency. Because of the small dimensions of the nozzle orifices ($< 50\mu\text{m}$), the risk of clogging is high (Basaran, 2002). As a consequence, to improve the printing resolution and ejection stability it is beneficial to produce droplets smaller than the orifices (Chen, 2002; Gan, 2009).

c) Drop spacing

The drop spacing is defined as the distance between the centers of two adjacent droplets. On this printer, the drop spacing must be equal both on X and Y directions.

The drop spacing d_x in X direction is set by the print carriage speed v_c and the droplet ejection frequency f_e (1. 4).

$$d_x = \frac{v_c}{f_e} \quad (1. 4)$$

On the Dimatix printer, the drop spacing is defined by the angle (*sabre angle*) between the X direction (axe of displacement of the print carriage) and the axe of the nozzles, which are regularly spaced by 254 μm . As illustrated in Figure 1.23, an angle of 90° corresponds to the maximum achievable drop spacing (254 μm). Decreasing the drop spacing corresponds to increasing the pattern resolution, hence the quantity of ink deposited.

The drop spacing d_y in Y direction is set by the controlled displacement of the platen, but also by the sabre angle α_s (1. 5).

$$d_y = 254 * \sin(\alpha_s) \quad (1. 5)$$

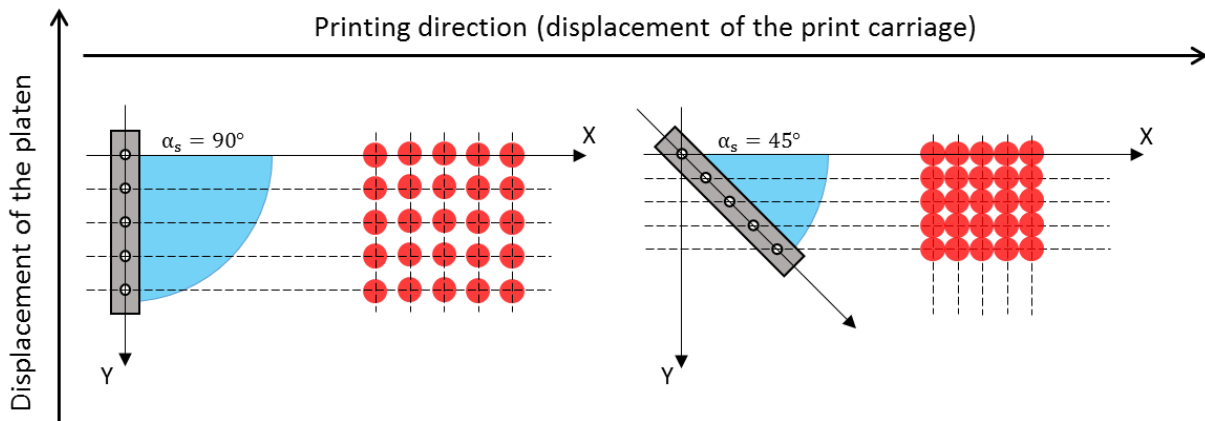


Figure 1.23. Setting of the drop spacing on the Dimatix DMP2831 printer.

Depending on the interaction of the ink with the substrate, if the resolution is too low the droplets may not overlap (Figure 1.24.a); while if the resolution is too high, over-spreading of the ink might occur causing the loss of the pattern shape (Figure 1.24.d).

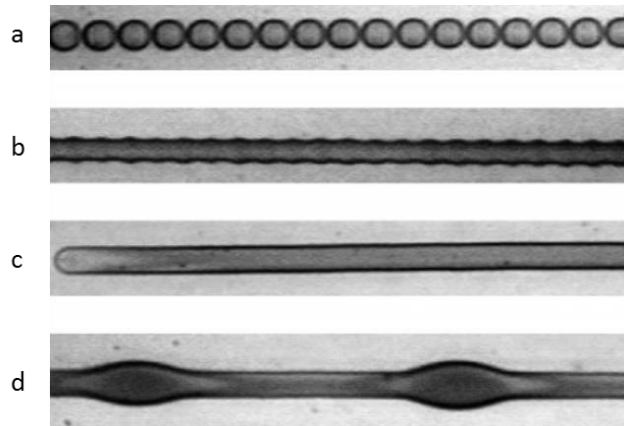


Figure 1.24. PEDOT-PSS printed line behaviors: a) separated droplets, b) scalloped, c) uniform, d) bulging. Drop spacing decreases from left to right. Adapted from Soltman (2008).

The method for setting the drop spacing on the Dimatix has the advantage of being simple. However, the sabre angle is set manually and several iterations might be required to obtain accurate settings. Moreover, a perfect synchronization of the ejection between nozzles is required to conform to the pixels arrangements. This synchronization is done by the driving computer of the printer for a given sabre angle. Even a slight discrepancy of the sabre angle will cause a misalignment between pixels in X and Y directions.

The consequence of this discrepancy was regularly experienced when printing with the Dimatix. It is characterized by uniform pattern edges on the printing direction and scalloped edges on the perpendicular direction (Figure 1.25).

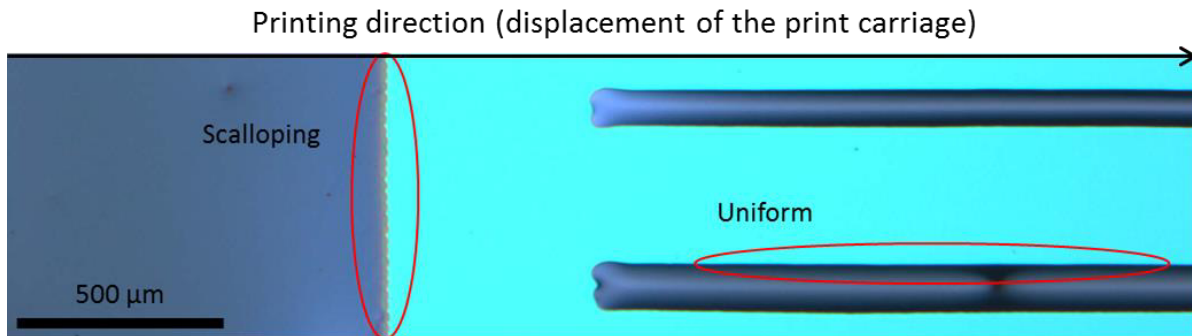


Figure 1.25. Uniform and scalloped edges because of discrepancies in the setting of the Dimatix sabre angle.

II.4. Summary

The Dimatix DMP2831 printer is a versatile tool very adequate for laboratory scale use. The main issues encountered during this thesis were nozzles clogging and droplets mis-jetting. Such failures of the printer usually cause killer defects on the printed patterns. Increasing the cleaning cycle frequency reduces the risk of such issues but also increases the printing time and the ink consumption. In conclusion, the Dimatix printer is the perfect tool for testing inks and ejection conditions as cartridges and print heads are affordable and disposable. If it is not suited for production, it can eventually be used for fast prototyping and small series. The main characteristics of the Dimatix DMP2831 printer are summarized in Table 1.2.

Table 1.2. Main characteristics of the Dimatix DMP2831 printer.

Cartridge	Reservoir Volume	1.5 ml
	Nozzles	16 (single row), 254 μm spacing
	Droplet volume	1 pl or 10 pl (depending on print head)
	Temperature	Heating up to 70°C
Ink	Viscosity	2-30 mPa.s
	Surface tension	28 and 33 mJ.m ⁻²
	Particles dimensions	< 200 nm
Mechanical parts	Printable surface	210 mm x 315 mm
	Repeatability	$\pm 25 \mu\text{m}$
	Temperature	Heating up to 60°C

III. From inks to functional layers

The fast development of printed electronics is partly driven by the advances in chemistry and ink formulation that made available a large spectrum of printable materials. Functional inks for printed electronics are developed with a common feature: low temperature processing, indeed such a characteristic is required for the fabrication of electronic components on flexible and low-cost substrates.

This paragraph focuses on the type of materials that are today available for inkjet printed electronics, which include metals, dielectrics, and semiconductors. Details on silver nanoparticles inks will be developed.

III.1. Functional materials for printed electronics

The literature provides lots of studies on the formulation, inkjet deposition, and characterization of functional materials for printed electronics. Table 1.3 presents a non-exhaustive list of materials that have been processed with inkjet technology for the fabrication of both functional layers and electronic components. Only one reference was selected, but usually others can be found in scientific press, patents, and commercial products.

Table 1.3. Review of functional materials for inkjet printing technology.

Nature	Material	Reference	Comments
Metals	Ag NPs	Kim, 2005	$\rho = 3.2\mu\Omega.cm @200^\circ C$
	Ag metal organic	Dearden, 2005	Transparent ink
	Cu NPs	Park, 2007	$\rho = 17.2\mu\Omega.cm @325^\circ C$ in vacuum
	Cu salt	Li, 2009	Printed reducing agent NaBH ₄ on paper
	Au NPs	Chung, 2004	Laser annealing
Ceramics	Al ₂ O ₃	Seerden, 2001	Hot-melt ink
	ZrO ₂	Ebert, 2009	3D inkjet printing, dental prostheses
	Si ₃ N ₄	Cappi, 2008	Gearwheels
	PZT	Bhatti, 2001	Micro-pillars
Dielectrics	BST metal organic	Kaydanova, 2007	RF tunable circuits
	Ion-gel [EMIM][TFSI] ⁵ and PS-PEO-PS ⁶	Cho, 2008	Dielectric gate for OTFT (10 kHz)
Polymers	SU-8 and PVP	Cook, 2013	MIM RF capacitors
	PEDOT:PSS (SemiC.)	Blaudeck, 2012	Channel of OECTs
	Polypyrrole (SemiC.)	Liu, 2005	All-polymer FETs
	Polyaniline (Cond.)	Crowley, 2008	Ammonia gas sensor
	PVK ⁷ (luminescent)	Hebner, 1998	OLEDs
Carbon	Carbon black	Loffredo, 2009	Chemical sensor
	MWCNTs	Denneulin, 2009	Conductive patterns
	MWCNTs	Gohier, 2011	Infrared sensor
	Graphene	Torrisi, 2012	TFTs

⁵[EMIM][TFSI]: 1-ethyl-3-methylimidazolium bis(trifluoromethylsulfonyl)imide

⁶PS-PEO-PS: poly(styrene-block-ethylene oxide-block-styrene)

⁷PVK: polyvinylcarbazol

III.2. Conductive nanoparticles inks

Conductive nanoparticles inks must fulfill typical requirements of inkjet printing process such as printability, high resolution, shelf-life, adhesion to substrate, viscosity, and surface tension. Moreover, other features are required:

- Colloidal stability: prevent agglomeration and precipitation.
- Nanoparticles dimensions: below 100 nm.
- Low temperature post-printing treatment (< 300°C).
- High metal loading: up to 60 wt%.
- Provide high electrical conductivity ($>10^4 \Omega \cdot m$)

In this paragraph, we introduce the main steps of the fabrication of nanoparticles inks, namely the preparation of the nanoparticles and their stabilization.

a) Metallic nanoparticles synthesis

There are two main methods for the synthesis of metallic nanoparticles (Kamyshny, 2011):

➤ Top-down or physical methods:

Bulk metals or microscopic structures are processed to reach nanoscale with highly energetic procedures: rapid condensation of metal vapor phases and laser ablation.

Metal vapor is obtained by thermal heating or plasma excitation of metal plates. An inert gas conveys the vapor phase onto a solid substrate or directly into a liquid containing stabilizing agents allowing the nanoparticles to be stored without aggregating. Copper and silver nanoparticles have been manufactured using this method (Kimura, 2000) in the size range of 10 nm.

Laser ablation allows dispersing bulk metals directly into organic or aqueous media (Heinglein, 1993; Mafune, 2000) with a larger range of nanoparticles dimensions (up to 80 nm).

➤ Bottom-up or chemical methods:

Bottom-up synthesis of nanoparticles is mainly performed through chemical reaction between metallic ions and molecules and a reducing agent (oxido-reduction reaction). This method usually takes place in a liquid environment and allows preparing nanoparticles with controlled features: size, crystalline orientation, and morphology. The main challenge lies in the realization of a homogeneous population of nanoparticles.

Lee *et al.* (2011) measured statistical distribution of three different morphologies of silver nanoplates synthesized by reduction of silver nitrate. Nanodisk, triangular and long nanoplates were obtained, with mean size between 100 and 200 nanometers and large variation both in the counting of the different morphologies and in their size were observed (Figure 1.26).

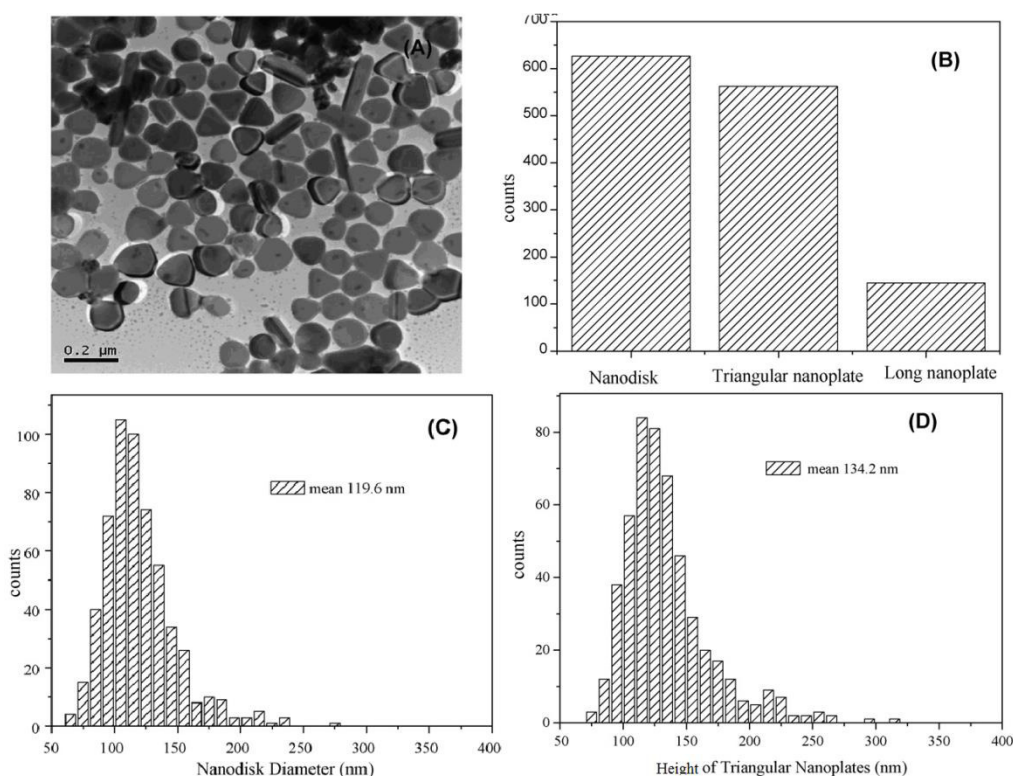


Figure 1.26. TEM image size distribution of nanoplates as ink particles: (A) TEM images, (B) statistical amount, (C) mean diameter of nanodisks, (D) mean height of triangular (Lee, 2011).

b) Stabilization of metallic nanoparticles

Conductive inks based on metallic nanoparticles must be stable colloidal dispersions in order to increase shelf-life, prevent agglomeration and precipitation. Because of Brownian motion, nanoparticles are submitted to frequent collisions. There are two basic interactions (Shi, 2002):

- When attraction dominates, nanoparticles agglomerate and the entire dispersion may coalesce;
- When repulsion dominates, the system will be stable and remain in a dispersed state.

Because of long range attractive forces between particles of the same element, it is necessary to provide long range repulsive interactions in order to maintain the colloidal stability (Shi, 2002). Two major mechanisms have been identified to achieve stable dispersions.

➤ Electrostatic stabilization

Long range attractive force is mainly due to Van der Waals and London interactions, whose range in colloids is around 10 nm. A proper way to counter this interaction is to provide nanoparticles with Coulombic repulsion. This can be done with ionic groups that are adsorbed at the nanoparticles surfaces creating a charged layer, which is itself covered by a second layer of ions of opposite sign to maintain electro-neutrality. Hence, nanoparticles are surrounded by an overall neutral double ionic barrier. The mutual repulsion of these double-barrier surrounding particles provides stability. The main difficulties encountered in electrostatic stabilization are:

- The dissolution of electrolytes in polar solvents;
- Increasing the electrolyte concentration improves the double-barrier quality, but high ionic concentration is difficult to obtain and may affect other properties of the ink.

To overcome the issues of electrostatic stabilization in the formulation of nanoparticles inks, polymeric stabilization can be achieved.

➤ Polymeric stabilization

Long polymer chains can reach dimensions in the order of Van der Waals and London interactions length. As a consequence, if the chains can generate repulsion they result in the stabilization of the colloidal dispersions.

Polymeric stabilization can be realized by two different mechanisms:

- steric stabilization (Figure 1.27.a) is realized by attaching long polymer chains to the nanoparticle surface;
- depletion stabilization (Figure 1.27.b) is realized by long polymer chains that are free in the solution.

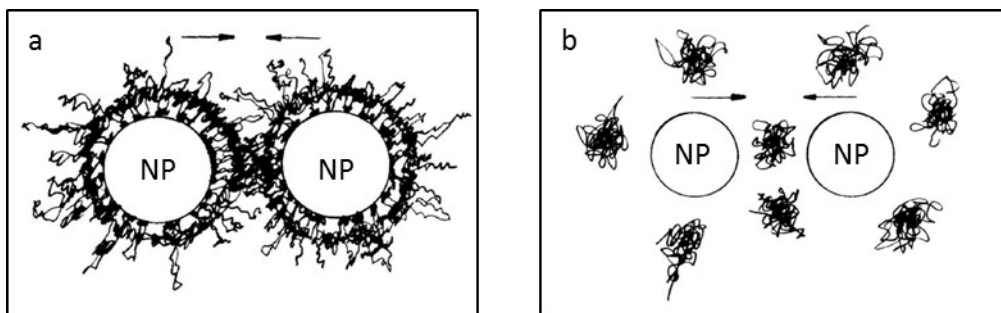


Figure 1.27. Schematic view of a) Steric and b) depletion stabilization. Adapted from Shi (2002).

Effective stabilizers for metal nanoparticles colloidal dispersions are amphiphilic polymers with both hydrophobic and hydrophilic groups. These molecules can bind to the nanoparticles surface creating a repulsive coating (Kamysny, 2011).

Polyvinyl pyrrolidone (PVP) is frequently used as a stabilizer of silver (Kapoor, 1998; Kim, 2005; Zhang, 2011) and copper nanoparticles (Park, 2007; Cheon, 2012). The literature concerning the stabilization of metal nanoparticles for printed electronics applications is very rich.

c) Silver nanoparticles inks

Silver well-known chemistry led to a wide range of commercial inks, not only for inkjet but also for offset, flexography, gravure and screen printing. In Table 1.4 are reported some commercial silver inks for inkjet printing and their main characteristics from the suppliers' datasheets.

In the framework of this thesis, ink formulation was not realized and mainly commercial inks from SunChemical were employed.

Table 1.4. Composition and properties of commercial silver nanoparticles inks for inkjet printing.

Supplier and Reference	Diameter (nm)	Weight percentage	Ink vehicles	Viscosity (mPa.s)	Surface tension (mJ.m ⁻²)
Harima NPS-JL	5-12	52-57	Tetradecane, naphthene	8-15	-
SunChemical EMD5714	30	40%	Ethanol, ethylene glycol	10-13	27-31
Cabot CCI-300	60-80	20%	Alcohol-based	11-15	30-33
ANP DGP-40LT-15C	10	30-35	TGME	10-17	35-38
Novacentrix Metalon JS-B35P	55	15	Water-based	6	31
Politronica InkA-C10	5-20	20-22	Bidistilled water, ethanol	16.5-19	55-58

III.3. Summary

Several studies are being conducted to replace silver by less noble materials such as copper and aluminum. However, fast oxidation of both these metals is a major issue for printing highly conductive patterns. As a consequence, in the synthesis and the formulation of colloidal suspensions of Al and Cu nanoparticles, an optimal protection is crucial not only against agglomeration but also oxidation.

The necessity of a thermal treatment on printed nanoparticles layers has been already stated in the previous paragraphs. In the following, the mechanisms that occur during thermal treatment as well as the annealing methods employed in printed electronics are presented.

IV. Sintering and grain growth

Metal nanoparticles inks require a post-printing treatment: it brings thermal energy to the system to evaporate the solvent and break the polymeric stabilizers which strongly deteriorate the electrical conductivity. However, the major requirement to achieve high electrical conductivity is nanoparticles coalescence and eventually size growth.

In this paragraph, we firstly present the enhanced behavior of nanoparticles (<100 nm) with respect to larger particles when provided with thermal energy. Then the mechanisms that drives sintering and grain growth are briefly introduced. Finally the main methods to sinter printed nanoparticles layers are described.

IV.1. Nanoparticles size effects

The physical properties of nanoparticles deviate from those of the same bulk material as a result of their reduced dimensions. They exhibit remarkable electronic and structural properties such as quantum size effect (Halperin, 1986) and high reactivity. The latter is due to an excess of internal energy of surface atoms:

- They have a higher degree of freedom;
- They have stressed covalent bonds because of high surface curvature;
- They are weakly bound and less constrained in their thermal motion.

Moreover, it is well-established that the melting temperature of metallic nanoparticles decreases with decreasing dimensions (Buffat, 1976; Qi, 2005). Several theoretical models have been proposed to fit the experimental data (Buffat, 1976; Jiang, 2003), but the understanding of surface interactions, the arrangement of atoms and their diffusion is a challenge for theory (Schmid, 1998). Nonetheless, the general tendency of these models tells that the lowering of the melting temperature is related to the high surface-to-volume ratio of the nanoparticle.

Buffat and Borel (1976) were among the firsts to measure the dependency of gold nanoparticles melting temperature with their dimensions (Figure 1.28). This feature of nanoparticles is of major interest in printed and flexible electronics as the microstructure of the printed layers can be modified and controlled at temperatures compatible with organic substrates.

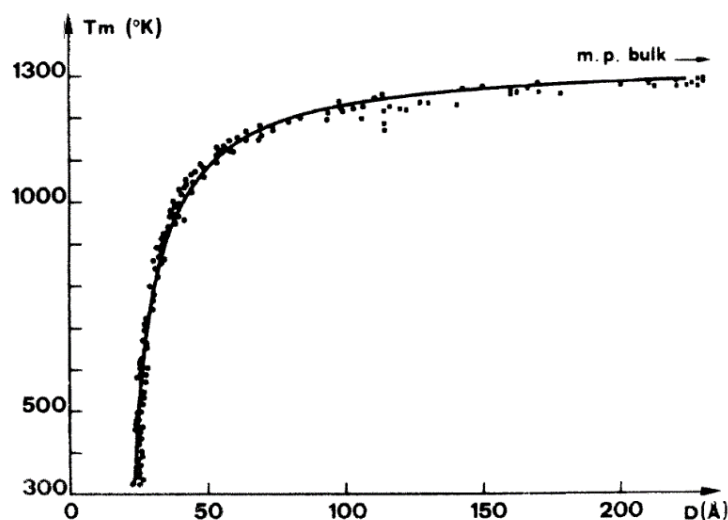


Figure 1.28. Experimental and theoretical values of the melting-point temperature of gold particles (Buffat, 1976).

IV.2. Sintering

Sintering describes the process of coalescence and packing of a powder (particles) into a solid using thermal energy (Figure 1.29). Historically, it is the most popular method for the fabrication of bulk ceramics bodies. In the field of powder metallurgy, sintering allows controlling the grain size and the packing density. The description of sintering mechanisms requires understanding the movement of particles grain boundaries when thermal energy is provided.

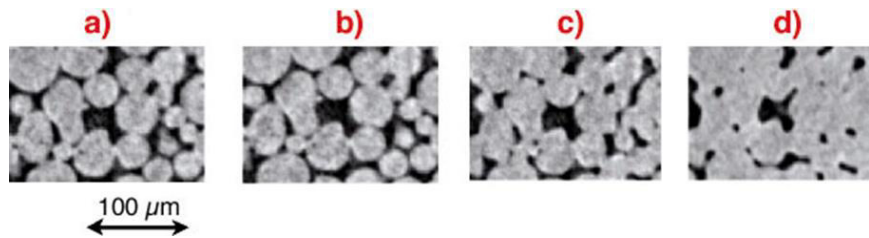


Figure 1.29. Illustration of the sintering process on Cu particles. a) Before sintering. b) After sintering at 1000°C. c) and d) after sintering at 1050°C (Lame, 2003).

The simplest way to describe sintering in two dimensions is with spherical particles of the same diameter. During sintering particles coalesce and their contact area increases from a single point to a line, called a grain boundary (Figure 1.30). The solid body formed after sintering will contain pores that are a structural element of the body and usually behave like grains of a different material (two phase body).

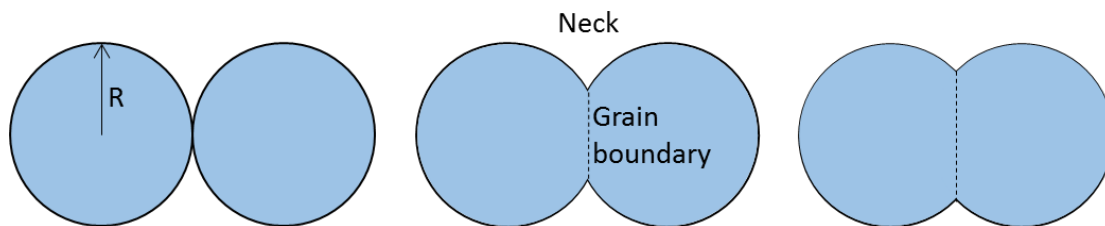


Figure 1.30. Coalescence of two spherical particles.

During sintering atoms are transported following various mechanisms that are given in Table 1.5. These transport mechanisms can be classified as:

- **Non-densifying:** the body density is slightly modified. Activation energy is lower and they usually dominate in low temperature range;
- **Densifying:** the body density is submitted to high variations and shrinkage usually occurs. Activation energy is higher and densifying mechanisms appear at higher temperatures.

Table 1.5. Mechanisms and transport in sintering (Carter, 2013).

Mechanism	Origin of the mechanism
<i>Non-densifying</i>	
Surface diffusion	Surface
Volume diffusion	Surface
Evaporation – Condensation	Surface
<i>Densifying</i>	
Volume diffusion	Grain boundaries
Grain boundaries diffusion	Grain boundaries

As sintering of nanoparticles proceeds, a simultaneous phenomenon occurs: grain growth. Indeed, during sintering, some grains will grow consuming others, essentially through Ostwald ripening process.

IV.3. Grain growth

Grain growth phenomenon in printed silver layers has been extensively observed in the literature (Kim, 2005; Kamyshny, 2011). It influences and often determines the microstructure of thin films because of the large driving forces available, arising from three main sources of energy: grain boundary, energy of the film surfaces and strain energy (Carel, 1995).

Grain growth mechanisms have been studied for many years and two growth modes have been identified as leading: normal and abnormal growth.

a) Normal growth

Normal grain growth is a mechanism where the average grain size d changes with time when provided with thermal energy. A common law to describe normal grain growth kinetics in bulk materials is given by equation (1. 6) (Atkinson, 1988; Thompson, 1996).

$$d^n - d_0^n = K * t \quad (1. 6)$$

where d_0 is the mean grain size at time $t = 0$, and K is a constant depending on the annealing temperature T and the activation energy of the grain boundary diffusion.

As illustrated in Figure 1.31 (Frost, 1988), in normal grain growth some grains shrink and others grow resulting in an increase of the average grain size, corresponding to a reduction of the total grain boundary area. As a consequence, the energy of the system is reduced because of the global decrease of the free energy of grain boundaries. Normal grain growth is characterized by a monomodal size distribution because of the isotropic and uniform growth in the film.

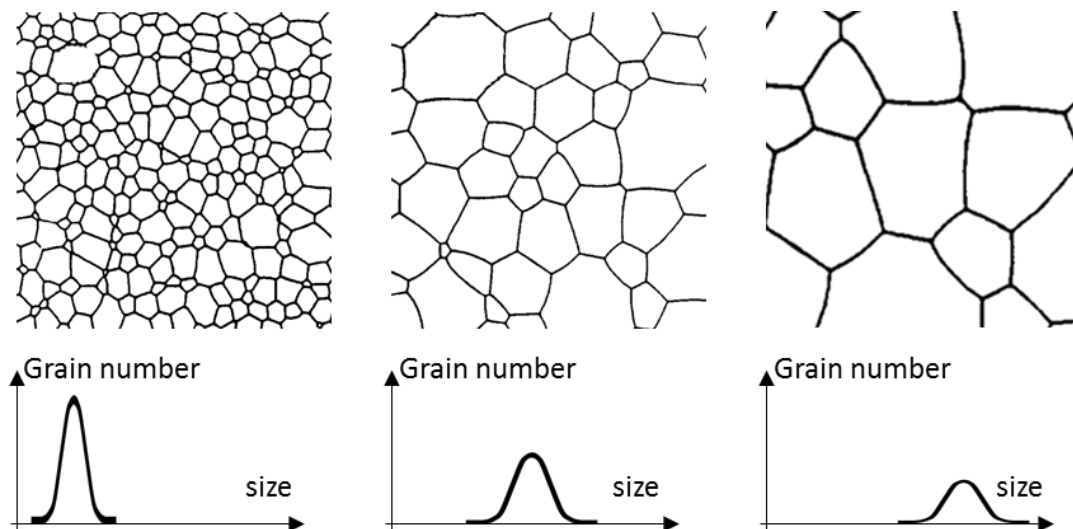


Figure 1.31. Top view of a thin film undergoing normal grain growth. Large grains tend to grow larger and small grains tend to disappear, thus average grain size increases over time. Adapted from Frost (1988).

b) Abnormal growth

Besides, it has been observed that other grain growth mechanisms can occur along with normal grain growth. This usually results in the event of other grains populations. In thin films, it was shown that when grain size is comparable to film thickness normal grain growth is interrupted while a few grains grow at a much higher rate (Palmer, 1987). As a consequence, the grain size distribution becomes bimodal (Figure 1.32). This phenomenon is commonly referred to as abnormal or secondary, growth.

In 1996, Thompson and Carel (1996) have identified two conditions that favor abnormal growth:

- Phenomena leading to grain boundary drag usually prevent steady state growth (or even lead to complete grain growth stagnation);
- There are almost always driving forces that favor the growth of subpopulations of grains with specific crystalline orientation and prevent steady state behavior until all favored grains are eliminated.

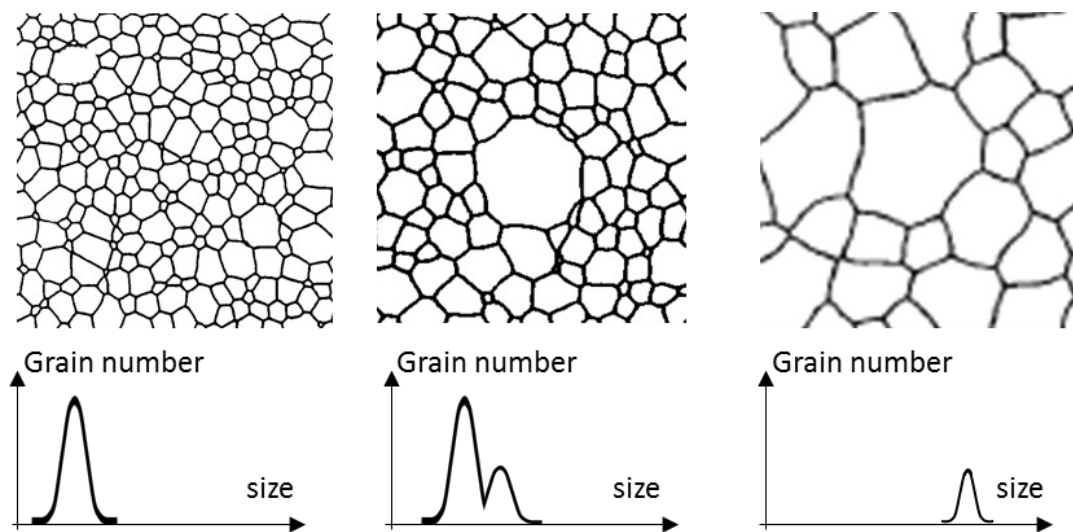


Figure 1.32. Top view of a thin film undergoing abnormal grain growth. A few large grains appear leading to a bimodal distribution of the grain size until the population becomes uniform again. Adapted from Frost (1988).

The driving forces in abnormal grain growth are more dependent on the reduction of surface energy anisotropy than on the reduction of grain boundaries energies (Thompson, 1987). One of the main sources of such anisotropy is the crystallographic orientation: some directions are more stable, meaning less energetic, than others. Table 1.6 summarizes the main characteristics of normal and abnormal grain growth.

Table 1.6. Comparison of grain growth mechanisms

	Normal growth	Abnormal growth
Grain size distribution	Monomodal	Bimodal
Grain size	↗	↗
Grain Number	↘	↘
Driving force	Grain boundary energy	Surface energy anisotropy
When?	Always	Grain size \approx film thickness

IV.4. Annealing methods

Sintering of ceramic and metallic powders is usually realized at high temperature under mechanical pressure (Carter, 2013). In the field of printed electronics, the maximum allowed temperature for sintering the deposited nano-materials is usually limited by the substrates (paper, polymer) or by the underlying patterns. In this paragraph, a review of the most employed methods for annealing nanoparticles printed layers is presented.

a) Thermal annealing

Thermal annealing, one of the most common methods, consists in heating the printed patterns and substrate altogether in an oven. Several studies have been carried out on metallic inks with annealing temperatures below 200°C (Kim, 2005; Lee, 2005). Lowering the annealing temperature has been achieved by optimizing the ink formulation and in particular by using short carbon chains as stabilizers, which can burn-out at lower temperature (Kamyshny, 2014).

Thermal annealing in ovens allows reaching electrical conductivities on silver tracks that exceed 50% of the bulk material value for temperatures below 30% of the bulk melting temperature. Electrical conductivity values given for commercial inks are usually obtained with this method.

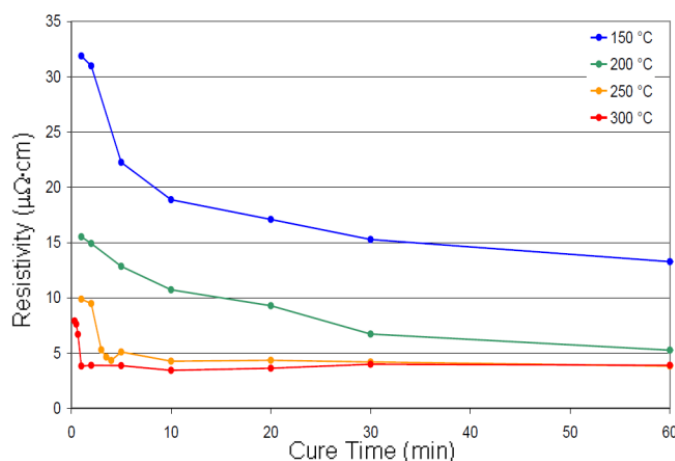


Figure 1.33. Electrical performance of Cabot silver nanoparticles ink CCI-30 printed on Kapton and annealed in oven under air. (Cabot CCI-300, n.d.).

Figure 1.33 clearly indicates that electrical resistivity decreases with the annealing temperature and time. Depending on the annealing temperature, it tends to a limit value higher than the bulk resistivity. Bulk resistivity of silver material is difficult to achieve because of the printed layer microstructure and thickness.

Figure 1.34 shows the evolution of the microstructure of a silver layer inkjet printed on glass substrate with the annealing temperature (Denneulin, 2011). Strong modifications can be observed, in particular grain growth.

A thorough characterization of the microstructure evolution with the annealing temperature of printed silver layers will be presented in chapter 2.

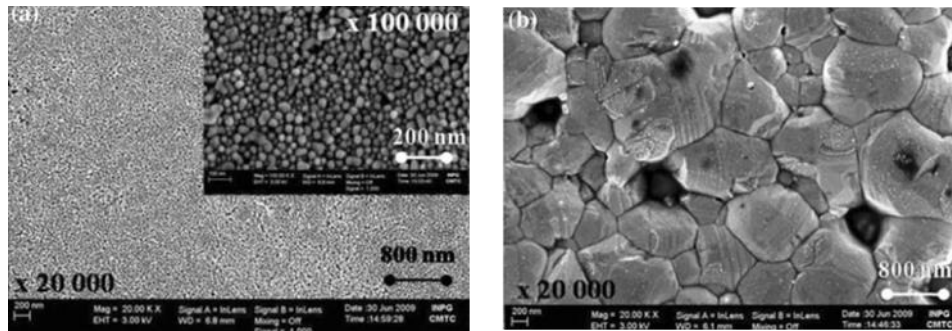


Figure 1.34. a) SEM image of silver ink as printed and b) Annealed silver ink at 400°C for 60 min. (Denneulin, 2011).

Regarding the adhesion of the printed layers on their substrates, Joo and Baldwin (2010) have shown that it mainly depends on the substrates hardness and the annealing temperature. In the particular case of organic substrates, if the annealing temperature is slightly above the glass transition temperature, a drastic improvement of the adhesion was observed while increasing again the annealing temperature led to a lack of adhesion.

If thermal annealing is an easy to implement technique and allows reaching high electrical conductivity, it has two major drawbacks:

- The annealing time is usually long (from minutes to hours), and thus hard to implement in industrial applications;
- Both the printed layer and the substrate are submitted to heating.

The substrates, in particular for low cost and large area electronics limit the maximum annealing temperature. In most cases, these substrates cannot withstand temperatures above 180°C except for polyimides. Also, these substrates usually have thermal coefficients of expansion much different than the printed nanoparticles. As a consequence, when cooling the printed system, large mechanical strains might occur causing failure mechanisms (cracks, delamination, stripping).

b) Photonic annealing

Photonic annealing consists in exposing the printed layers to a light source that can be either continuous or pulsed, and monochromatic (laser) or wide-spectrum. These techniques allow obtaining very high temperatures (up to 1000°C) on very short times (from microseconds to seconds).

➤ Laser annealing

Lasers are highly energetic and monochromatic beams that can be used either in continuous or pulsed mode to heat the printed pattern. Thanks to the different light absorption rates of metal nanoparticles, ink vehicles (solvent and additives) and substrate, monochromatic laser can be used to selectively sinter the printed layers.

As dispersing agents and solvents separate metallic nanoparticles, they must be burned-out during the annealing process. However, absorption rate may decrease when such species have disappeared and thus more power will be required to sinter the remaining materials on the substrate (Kumpulainen, 2011). Many studies of laser sintering of metallic nanoparticles inks can be found in the literature. Among the first results, Bieri *et al.* (2003) have selectively sintered gold nanoparticles printed lines with an argon-ion laser at 488 nm during 1 ms. In Table 1.7 is reported the comparison between continuous and pulsed laser sintering on inkjet printed silver tracks.

Table 1.7. Continuous vs. Pulsed wave laser sintering (Kumpulainen, 2011).

	Continuous wave laser sintering	Pulsed wave laser sintering
Covering	Large spot, diameter can be controlled with the working distance	Small spot, scanning pattern required to optimize energy dissipation
Adhesion	Poor at temperatures < 150°C, skinning	Poor, skinning
Resistivity	High with one pass at temperatures < 150°C	Lower
Multiple passes	Lower electrical resistivity, better adhesion, no skinning, smoother surface	Better control on the solvent evaporation
Structure	Smaller grains, higher porosity	Larger grains, lower porosity, micro cracks

In laser annealing, many parameters are available to optimize the sintering of metallic nanoparticles:

- laser equipment: wavelength, power density, pulses length (from picoseconds to continuous);
- irradiation: exposure area, scanning speed, number of passes.

The main drawback of laser annealing lies in the relatively small area of exposure (up to a dozen of square centimeters) and the high cost of the equipment. However, the selectivity of this method offers the possibility of obtaining highly conductive patterns without damaging the substrate.

Ko *et al.* (2005, 2007) have also shown that laser annealing can be used to selectively anneal printed metallic layers followed by the removal of the ink which was not exposed (Figure 1.35). In this way, the limited resolution of inkjet printing was overcome leading to high resolution patterns with line width as low as 6 μm .

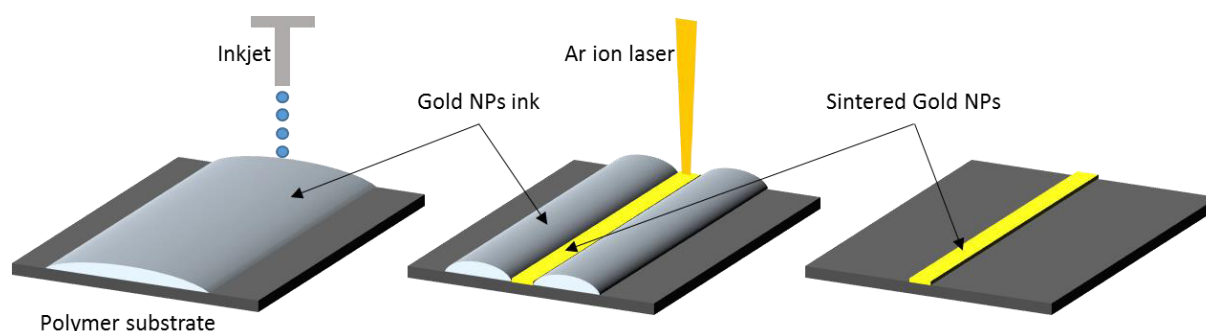


Figure 1.35. Principle of selective laser sintering of inkjet printed gold nanoparticles ink for high resolution patterning. Adapted from Ko (2007).

➤ Intense pulsed light annealing

This annealing process is based on the observation that light absorption can generate heat by dissipation of non-radiative energy and exothermic photochemical reactions. In nanostructured materials, the heat generated by photothermal phenomena is confined within the individual nanostructure. The heat transfer to neighboring nanostructures and environment being slow, it leads to a localized and rapid temperature increase within the nanostructures (Yung, 2010).

Intense pulsed light annealing is usually achieved by xenon lamps, which radiate light mainly in the visible spectrum (Figure 1.36). If this technique was firstly developed for copper inks to prevent oxidation during the annealing, it was demonstrated that it also works on silver (Kang, 2011).

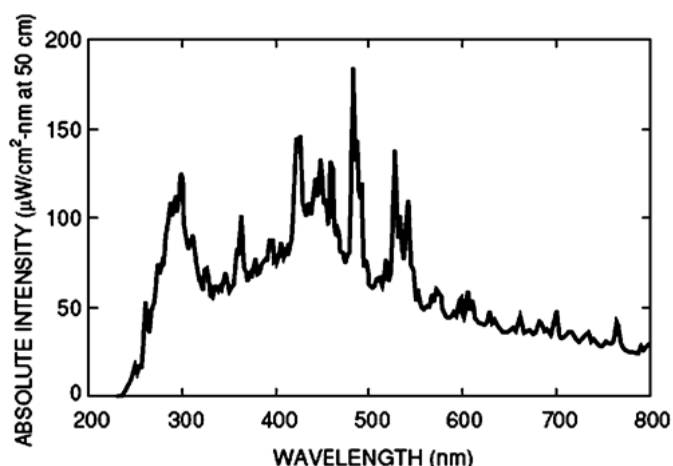


Figure 1.36. Spectral Distribution of a xenon flash lamp. (Kim, 2009).

Compared to laser sintering, intense pulsed light annealing allows exposing large area with both high power densities and uniform energy distribution. As with lasers, exposure time is very short, lower than one second while cost and maintenance of the equipment is much lower.

Technological advances are ongoing to improve the adjustability of xenon flashes to improve the annealing process. The materials characteristics and the corresponding settings of the lamps are given in Table 1.8.

Table 1.8. Xenon flash annealing, materials characteristics and corresponding process settings. (Akhavan, 2014).

Materials Characteristics (ink and substrates)	Xenon Lamps settings
Thermal and physical properties	Pulse power, amplitude
Film, ink thickness	Pulse duration
Particles morphology	Impinging wavelengths
Substrate composition and thickness	Number of pulses
Barriers or intermediate layers	Speed of pulses

Yung *et al.* (2010) demonstrated that the resistivity of printed silver inks stabilized by polyvinyl pyrrolidone (PVP) dramatically decreases after the first flashing and stabilizes around the second to third flash. Such a technique has been tested on substrates with different thermal conductivities and the lowest resistivity (around $6\mu\Omega\cdot\text{cm}$) was obtained on PET and PI. Patterns printed and sintered on photographic paper presented cracks and higher resistivity. From SEM images presented in this paper, it can be seen that the top of the sintered layers is much denser than the bottom, in contact with the substrate (Figure 1.37). Anisotropy in mechanical and electrical properties of the layer might occur because of such structural deviations, and substrate adhesion might be hindered.

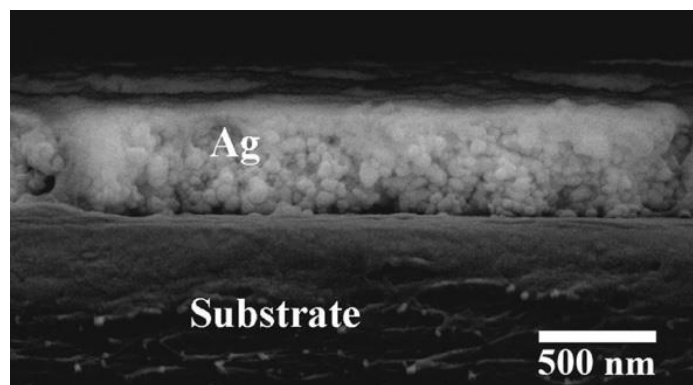


Figure 1.37. SEM image of the cross-section of one typical track on PI substrate (Yung, 2010).

This photonic annealing method is particularly well-suited for processing large areas on temperature sensitive organic substrates. If irradiation settings are still to be optimized, intense pulsed light annealing has a very high potential for industrial applications in printed electronics post-treatment. As an example, Novacentrix (USA) has recently mounted its PulseForge xenon system on an experimental roll-to-roll printer at the *Welsh Center for Printing and Coating* (WCPC).

➤ Other photonic annealing methods

Other methods have been successfully employed for the annealing of printed inks, in particular infrared (IR) radiations. One can cite the work of Denneulin (2011), where long-wave IR radiation with wavelengths between 8 and 15 μm have been used to sinter silver nanoparticles printed both on glass and paper substrates. Also, near infrared (NIR) in the range 700 to 2500 nm demonstrated to be very effective to rapidly sinter (few seconds) silver nanoparticles applied on PET substrates by slot-die coating without damaging the substrate (Cherrington, 2011).

c) Microwave annealing

Microwave heating fulfills most of the industrial requirements for the sintering of metallic nanoparticles: fast, simple, cost-effective, selective. Roy *et al.* (1999) proved that nanoparticles powder can absorb microwaves energy to be sintered.

Microwaves are electromagnetic radiations in the range of gigahertz. The oscillation of the electrical field excites dipolar or ionized materials which consequently align with the electrical field. The exposed material oscillations and the electrical fluctuations induce heat generation due to energy losses coming from molecular friction and dielectric losses. Microwaves produce a fast, uniform and volumetric heating (Perelaer, 2006).

Metals can be sintered with microwaves despite their small penetration depth. At 2.54 GHz, for silver, gold and copper the penetration depth is between 1.3 and 1.6 μm . Thus, the dimensions of the sintered materials in perpendicular direction to the incidence of the microwaves has to be in this range (Cauchois, 2014). Inkjet printed layers of metal nanoparticles inks usually fulfill this condition and are thus well-suited to this annealing method. Moreover, polymer substrates at temperatures below the glass transition temperature are almost transparent to microwave radiations (Perelaer, 2006).

Perelaer (2006) measured resistivity values as low as 30 $\mu\Omega\cdot\text{cm}$ on inkjet printed silver tracks by dividing by 20 the annealing time compared to conventional oven annealing. Cauchois *et al.* (2012) have measured silver bulk conductivities on inkjet printed silver layers annealed with Hybrid Variable Frequency Microwave (HVFM).

d) Electrical annealing

Electrical annealing consists in applying a voltage on a pattern and uses thermal dissipation due to a high initial resistivity to generate the heat necessary for the sintering process. Allen *et al.* (2008, 2011) achieved electrical sintering on printed silver ink reaching half the conductivity of bulk silver.

This technique has the advantages of being fast (voltage pulse of few μs), and allowing an in situ monitoring of the sintering quality (real-time resistance measurement). However, because of the high current densities involved in the process, a reliable and stable electrical contact between the printed layers and current supply probes is required.

e) Built-in self-sintering

Grouchko *et al.* (2011) have established a self-sintering mechanism of silver nanoparticles which is triggered during the drying of the printed pattern by a spontaneous chemical reaction, reaching up to 41% of bulk silver conductivity.

The principle of self-sintering is presented in Figure 1.38. During drying of the printed pattern, the concentration of a sintering agent (NaCl in this case) present in the ink vehicle increases and destabilizes the polymeric coating around nanoparticles. Then the sintering agent binds to the nanoparticles surface and leads to their coalescence.

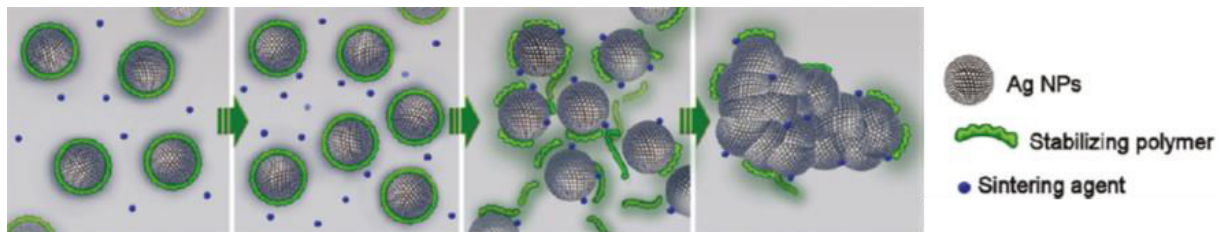


Figure 1.38. Schematic illustration of the stabilizer detachment, which leads to the NP sintering (Grouchko, 2011).

f) Plasma sintering

Plasma is often considered as the fourth possible state of matter, the others being solid, liquid, and gas. It consists in an ionized, electrically neutral, and disordered state of matter. Plasma is a highly energetic state of matter by far the most common in the universe (stars).

The ionic character of plasma makes it electrically conductive and inversely to gases, plasma can be manipulated and shaped with electromagnetic fields. As a consequence, several technological tools were developed to artificially create plasmas. Today, plasmas are extensively employed in manufacturing for surface energy manipulation, etching in microelectronics, and metal cutting.

Reinhold *et al.* (2009) have evaluated low-pressure argon plasma exposure as a selective method for the sintering of inkjet printed silver nanoparticles inks on polymer and glass substrates. In Figure 1.39 is plotted the electrical resistivity measured for plasma and thermal annealing versus time. Values down to three times the bulk silver resistivity were obtained. The electrical resistivity measured on polymer substrates was higher. The substrates thermal conductivity seem to play a major role in the annealing process as their temperature during plasma exposure does not evolve in the same way: glass reaches higher temperatures than polymer substrates.

This study of argon plasma annealing also revealed that the thickness of the printed layer is an important parameter as sintering did not occur for layer thicknesses higher than the penetration depth of the plasma.

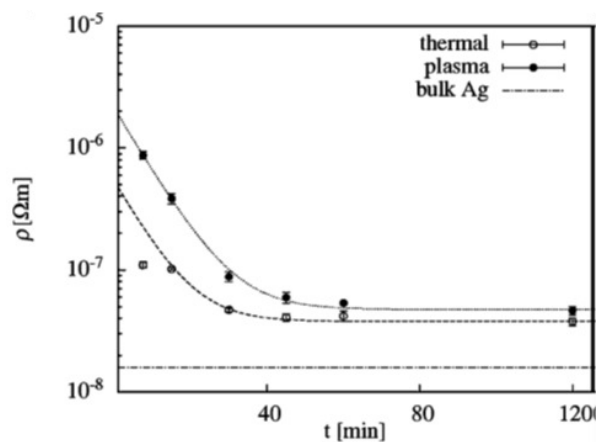


Figure 1.39. Effective resistivity of plasma (80 W) and thermal annealing of silver inks on glass substrates (Reinhold, 2009).

It should be mentioned that because of the high energy of the plasma ions, unwanted contamination by the plasma species in the annealed layers might occur.

IV.5. Summary

An annealing step is required to trigger sintering phenomenon after printing nanoparticles inks. There are several methods to achieve sintering and each one has its pros and cons: materials selectivity, time of processing, substrate compatibility. In the description of these methods we have focused on the sintering of conductive materials (in particular metals); however the presented techniques can also be used for other materials such as dielectrics and ceramics. As an example, Cappi *et al.* (2008) have realized silicon nitride gearwheels by inkjet printing and pressure less sintering at high temperatures.

In the particular case of silver nanoparticles inks, it is difficult to compare the resulting layers properties of each annealing method as they have not been tested yet on the same fabrication configuration: printing, ink, and substrate. Nonetheless, it must be noted that each presented annealing method aims to generate heat in the printed layers. Depending on the method the heat distribution in the layer might be:

- Isotropic: thermal, microwave, electrical and built-in annealing;
- Anisotropic: photonic and plasma sintering.

One can remember that the specifications of the annealing process are:

- Nature: irradiation, selective or global heating, electromagnetic, chemical, electrical, ...
- Duration: from μ s to hours;
- Scalability to industrial application;
- Interaction and compatibility with the substrate;
- Final properties of the printed layers: electrical conductivity, mechanical properties, structural properties (porosity, adhesion, skinning, cracking, ...).

In the framework of this thesis, thermal annealing in air was deeply studied. Results on the influence of the annealing conditions on the microstructure, electrical and mechanical properties will be presented in chapter 2.

V. Electronic transport in thin films

After annealing, inkjet printed silver layers result in thin films with a polycrystalline microstructure. Depending on the final microstructure, several properties of the material can be affected. In this paragraph, the fundamental models of electronic transport in thin films are reported.

The electrical conductivity σ is the macroscopic entity that describes the transport of electrons, namely the current density J , in a material submitted to an electrical field E (1. 7).

$$J = \sigma E \quad (1. 7)$$

V.1. Bulk metals

a) Drude model

The electrical conductivity value is confined by electron scattering. In 1900 Paul Drude proposed the free electron gas model for the transport of electric charges in metals. In this model, electrons are objects that do not interact with each other. The only interaction mechanism considered is the scattering of electrons with phonons due to thermal vibrations of the lattice. The resolution of the Boltzmann transport equation leads to the expression of the electrical conductivity in (1. 8), which only depends on τ , the average time between two scattering events.

$$\sigma = \frac{Ne^2\tau}{m_e} = \frac{Ne^2\lambda_0}{m_e v_F} \quad (1. 8)$$

where N is the charge carrier density, e the electron charge, m_e the electron mass, λ_0 the electron mean free path, and v_F the Fermi velocity. Here the mean free path of a conduction electron is defined by (1. 9) because phonon scattering only occurs on electrons near the Fermi surface. As a consequence, to calculate the mean free path of conduction electrons the Fermi velocity v_F is used, defined by (1. 10).

$$\lambda = \tau v_F \quad (1. 9)$$

$$v_F = \frac{\hbar k_F}{m_e}, \text{ with } k_F = \sqrt{2\pi m_e E_F} / \hbar \quad (1. 10)$$

where E_F is the Fermi energy, \hbar the reduced Planck constant and k_F the Fermi vector. Electron scattering induces a decrease of the electron mean free path and thus a decrease of the electrical conductivity.

b) Matthiessen's rule

The Drude model only takes into account electron scattering due to electron-phonon interaction. However, in bulk metals other sources of electron scattering occur such as impurities, lattice defects, and boundaries, which decrease the material electrical conductivity σ . The commonly used parameter when dealing with scattering losses is the electrical resistivity ρ defined as the inverse of σ .

If the scattering mechanisms can be considered independent, Matthiessen's rule (1864) (Kittel, 2007) states that the resistivity of a material is the sum of the contributions of each scattering phenomenon (1. 11).

$$\rho_e = \rho_{\text{phonons}} + \rho_{\text{defects}} + \rho_{\text{impurities}} + \rho_{\text{boundary}} \quad (1. 11)$$

V.2. Thin films metals

When one or more dimensions are in the same order of magnitude than the electron mean free path, scattering at boundaries of the material becomes significant in the total resistivity. In thin polycrystalline films, the thickness and the grain size might be in the order of the mean free path. Two fundamental scattering mechanisms that increase the electrical resistivity are:

- The scattering at the film surfaces and interfaces.
- The scattering at grain boundaries.

Two reference models describe the contribution of these scattering mechanisms, namely the Fuchs-Sondheimer model for surface scattering and the Mayadas-Schatzke model for grain boundary scattering.

a) Fuchs-Sondheimer (FS) model

The Fuchs-Sondheimer model describes the influence of the film thickness on the electrical resistivity of the thin film. It is developed on the resolution of the Boltzmann transport equation for free electrons in one dimension with boundary conditions at the external surfaces of the thin film. The resolution of the problem goes through the introduction of a specularity parameter p that describes the probability for an electron to be elastically scattered (no energy loss) at a surface (Figure 1.40). The problem and its resolution can be found in the articles of Fuchs (1938) and Sondheimer (1952/2001).

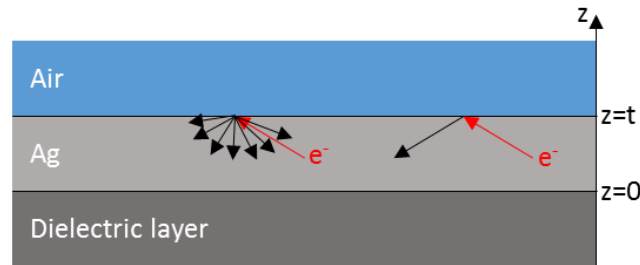


Figure 1.40. Electronic conduction in a thin film according to the FS model. If $p = 0$, electrons scatter inelastically at the surface (diffusion). If $p = 1$, electrons scatter elastically (reflection).

The hypotheses that were made to solve the problem are (Philipp, 2011):

- Disorder in the film does not depend on the thickness;
- Surfaces are clean and parallel;
- Electrons are on a spherical Fermi Surface;
- Scattering of electrons is isotropic and is characterized by an effective mean free path, meaning that Matthiessen's rule applies.

The general expression of the electrical conductivity σ_f of the thin film proposed by Sondheimer (1952/2001) is given by equation (1. 12).

$$\frac{\sigma_f}{\sigma_0} = 1 - \frac{3}{2\kappa_0} \int_1^\infty \left(\frac{1}{t^3} - \frac{1}{t^5} \right) * \frac{1 - e^{-\kappa_0 t}}{1 - p e^{-\kappa_0 t}} dt \quad (1. 12)$$

where σ_0 is the conductivity of the bulk material, t the film thickness, and $\kappa_0 = t/\lambda_0$ is the ratio of the film thickness to the mean free path in the bulk material. Equation (1. 12) does not have algebraic solutions, thus it is common to use the limiting expressions (1. 13) in (1. 14) depending on the ratio κ_0 .

$$\text{If } \kappa_0 \gg 1 \Rightarrow \frac{\sigma_f}{\sigma_0} = 1 + \frac{3\lambda_0}{8t}(1-p) \quad (1.13)$$

$$\text{If } \kappa_0 \ll 1 \Rightarrow \frac{\sigma_f}{\sigma_0} = -\frac{4}{3} \frac{1-p}{1+p} \frac{\lambda_0}{t \ln(\kappa_0)} \quad (1.14)$$

The FS model was modified to take account of experimental conditions. For example the relationship between the specularity parameter p and the surface roughness was studied by Ziman (1960) and Soffer (1967). Other works (Lucas, 1965; Juretschke, 1966) have included the influence of two different interfaces by the means of different scattering parameters p and q .

b) Mayadas-Shatzke (MS) model

The Mayadas-Shatzkes model describes the influence of electron scattering at grain boundaries on the electrical resistivity of both bulk material and thin films. Grain boundaries are commonly found in polycrystalline materials. As an example, in microelectronics manufacturing, thin film deposition by sputtering or vapor deposition result in polycrystalline microstructure. *Also, as it will be described in chapter 2.II, inkjet printed silver layers are polycrystalline.*

In the MS model, the material is modeled by a one-dimensional structure where grain boundaries are regarded as potential barriers for the charge carriers (Figure 1.41). The electrons have a probability, noted R , to either be reflected or transmitted to cross the potential barriers. The main experimental factor required to apply the MS model is the average grain size D that describes the density of grain boundaries.

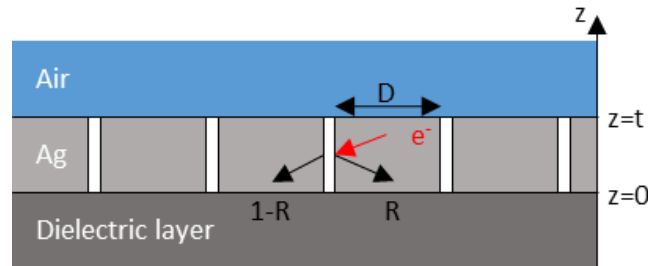


Figure 1.41. Electronic conduction in a thin film according to the MS model.

If $R = 0$, electrons are entirely transmitted through the potential barrier. If $R = 1$, the electrons are fully reflected and the resistivity is maximum.

Solving the Boltzmann transport equation in the MS model requires the following hypotheses (Philipp, 2011):

- Only the grain boundaries perpendicular to the electrical field cause charge carriers scattering while the influence of non-perpendicular grain boundaries is neglected (Pichard, 1980);
- The potential barriers created by the grain boundaries are represented by a Gaussian distribution with a mean distance D , corresponding to the average grain size;
- The potential of the barriers is described by a Dirac function.

The solution of the Boltzmann equation in a bulk polycrystalline material proposed by Mayadas and Schatzkes (1969) leads to the expression of the electrical conductivity σ_g in equations (1.15) and (1.16).

$$\frac{\sigma_g}{\sigma_0} = 1 - \frac{3}{2}\alpha + 3\alpha^2 - 3\alpha^3 \ln\left(1 + \frac{1}{\alpha}\right) \quad (1.15)$$

$$\alpha = \frac{\lambda_0}{D} \frac{R}{1-R} \quad (1.16)$$

In 1970, Mayadas and Schatzkes extended their model to the case of thin films by taking into account the surface scattering phenomena described by the FS model. The exact solution of the Boltzmann equation for thin films with grain boundary and surface scattering can be found in their article. In this situation, the scattering mechanisms, namely at surfaces and grain boundaries, cannot be considered independent from each other. As a consequence the Matthiessen's rule is no more valid and only numerical solutions are available.

However, in the case of thick films ($t \gg \lambda_0$), surface and grain boundary scattering can be considered independent and Matthiessen's rule is valid. This leads to the simplified expressions of the resistivity of thick films in (1.17) and (1.18).

$$\rho_f = \rho_0 + \rho_S + \rho_{GB} \quad (1.17)$$

$$\text{with } \rho_S = \frac{3}{8} \rho_0 (1-p) \frac{\lambda_0}{t} \text{ and } \rho_{GB} = \frac{3}{2} \rho_0 \frac{R}{1-R} \frac{\lambda_0}{D} \quad (1.18)$$

Where ρ_S and ρ_{GB} are the respective contribution of surface and grain boundary scattering. Fuchs-Sondheimer and Mayadas-Schatzkes models are broadly employed in the literature for the interpretation of the electrical resistivity in thin polycrystalline films, especially in their simplified expressions (equations (1.13)-(1.18)).

In this work, these equations are used to analyze our electrical measurements, knowing that deviations are to be expected because of the printed layers microstructure. The main parameters of bulk silver are summarized in Table 1.11 (cf. Conclusion of chapter 1).

VI. Mechanical characterization of thin films

When a solid is submitted to external forces, internal strains appear and induce deformations. The determination of its mechanical properties consists in establishing of the strain-deformation relationships.

In this thesis, the studied samples are thin films deposited on a bulk substrate. Nanoindentation is one of the most common techniques to characterize such systems. There are other methods such as bulge tests or vibration-based techniques, however they require the fabrication of specific test structures (membranes and oscillators).

Contact mechanics (Johnson, 1987) and *Nanoindentation* (Fischer-Cripps, 2004) are two major references for studying thin films mechanical properties. These books were used in the following paragraphs to introduce the fundamentals of nanoindentation.

Nanoindentation technique was employed for measuring the elastic and plastic mechanical properties of inkjet printed silver layers, namely the Young's modulus E and the hardness H .

VI.1. Nanoindentation

a) Instrumented nanoindentation

A nanoindentation test consists in establishing a mechanical contact between an indenter, whose geometry and properties are known, and the surface of the studied material. The test is said instrumented when the applied load P and the indentation depth h are continuously measured and recorded. The mechanical properties of the indented material are then extracted from the $P(h)$ data through an appropriate model.

The nanoindentation tests were realized on a MTS Systems Corporation nanoindenter (Figure 1.42) equipped with two indentation columns, namely the XP and the DCM (Dynamic Contact Module). The DCM column offers a better resolution both for load and displacement than the XP (Table 1.9).

The working principle of an indentation column is described in Figure 1.43. The load is applied by a column equipped with a coil surrounded by fixed a magnet. A current flow in the coil induces an electromagnetic force that moves the column in the vertical direction. A capacitive sensor measures the column displacement. At the bottom of the column is placed the indenter, whose properties will be discussed in paragraph VI.1.b.

The sample is mounted on a micrometric motorized chuck that can move between the two indentation columns and an optical column for positioning the indents locations. The columns and the samples are mounted on a very stiff frame (10^7 N.m^{-1}) supported by an anti-vibration table. The whole system is surrounded by a soundproof box that limits noise from vibrations and thermal variations.

Table 1.9. MTS XP Nanoindenter specifications (User manual MTS-XP, n.d.).

	XP Column	DCM Column
Maximum load	500 mN	20 mN
Displacement range	-750 – 750 μm	-17.5 – 17.5 μm
Force resolution	50nN	1nN
Displacement resolution	0.04nm	0.0002nm

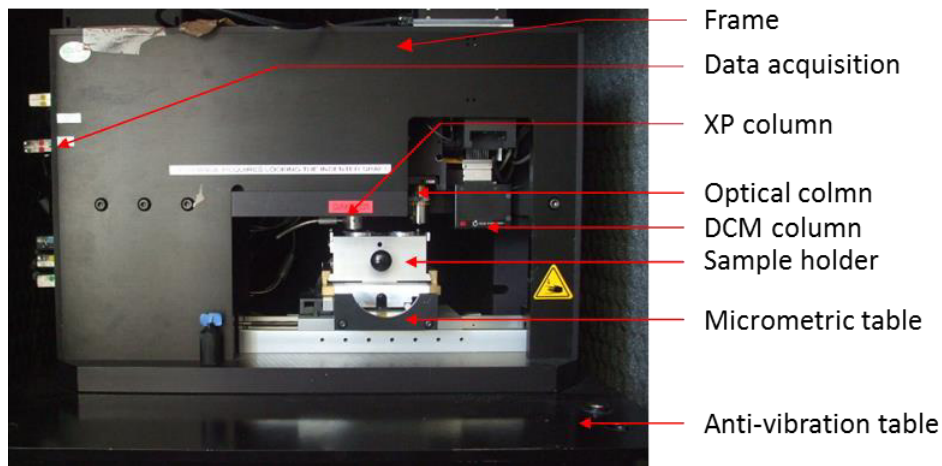


Figure 1.42. MTS Systems Corporation Nanoindenter.

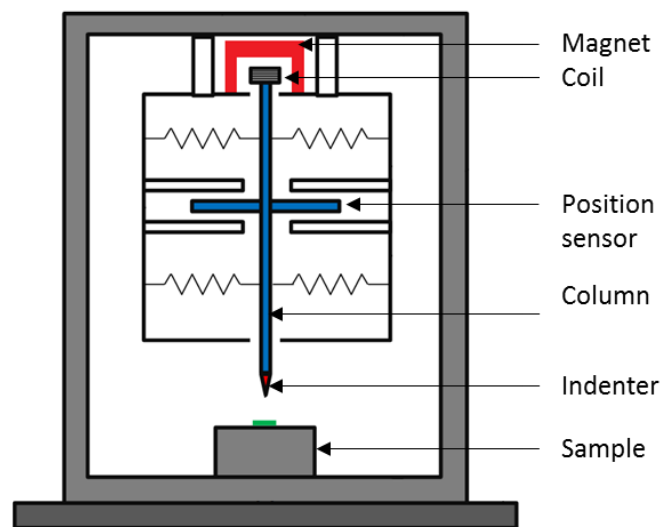


Figure 1.43. Working principle of a nanoindenter.

b) Indenter geometry

The indenter is usually made of a diamond or sapphire which are the hardest and stiffest available materials and thus less sensitive to deformation. During the indentation, the tip deformation must be as low as possible and it must remain in its elastic regime.

There are several indenter tip geometries, the most common being cones, spheres and pyramids. Each tip is characterized by its area function $A(h)$ that corresponds to the projected contact area at indentation depth h . An equivalent contact radius $r(h) = \sqrt{A(h)/\pi}$ is calculated for tips that do not have a revolution symmetry.

In the frame of the characterization of the mechanical properties of the printed silver layers, a Berkovich diamond indenter was employed. The Berkovich indenter is a three faces pyramid with an equivalent cone angle of 70.32°. A SEM view and the properties of the Berkovich indenter are given in Figure 1.44.

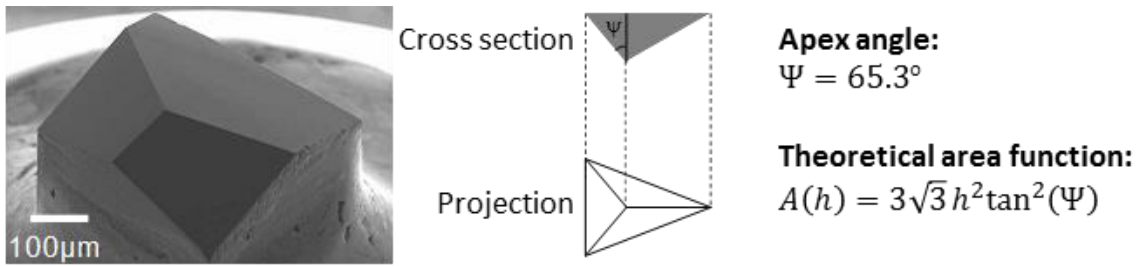


Figure 1.44. Berkovich diamond tip.

c) Load – displacement curve

A typical load-displacement curve $P(h)$ of an elasto-plastic material is presented in Figure 1.45. This type of data is obtained when an indenter is placed into contact with the flat surface of a sample with a steadily increasing load. The applied load and the indentation depth increase up to P_{max} and h_{max} . During unloading, the indenter goes back up until the contact between the sample and the indenter is lost. The loss of the mechanical contact happens at the residual indentation depth h_r . In the case of an ideal elastic material, load and unload curves are superimposed.

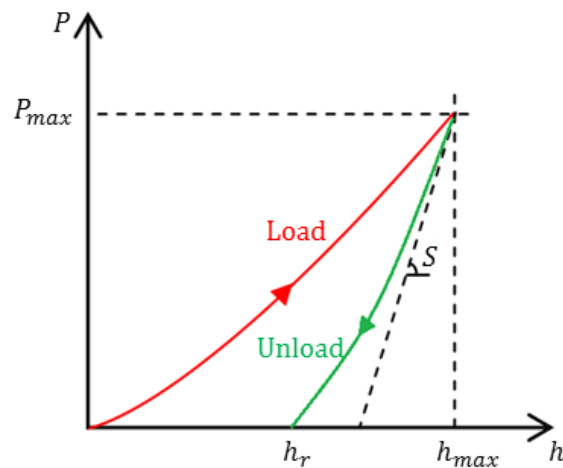


Figure 1.45. Typical load-indentation depth curve on an elasto-plastic material.

The measurement of the force and vertical displacement during unloading allows calculating the contact stiffness S defined by equation (1. 19). The contact stiffness is characteristic of the elastic properties of the materials in contact, namely the indenter and the sample under test.

$$S = \frac{dP}{dh} \quad (1. 19)$$

d) Continuous Stiffness Measurement (CSM)

The MTS nanoindenter is equipped with an optional module called “Continuous Stiffness Measurement” (CSM) that allows the measurement of the contact stiffness during the whole loading phase. The principle of CSM consists in superimposing a harmonic load to the nominal load, as illustrated in Figure 1.46. This harmonic component generates small oscillations of a few nanometers corresponding to loading-unloading cycles. It enables the dynamic measurement of the contact stiffness.

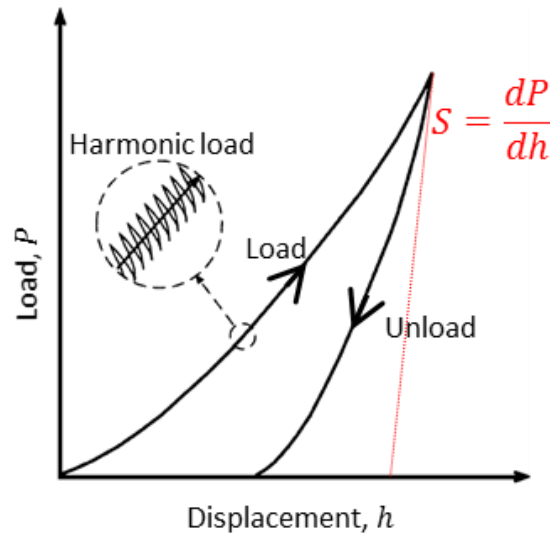


Figure 1.46. Principle of the Continuous Stiffness measurement. Adapted from Li (2002).

The harmonic load might influence the elastic and plastic properties of the studied sample. Pharr (2009) proposed a set of corrections for taking into account the CSM oscillations on the applied load, the indentation depth, and the contact stiffness in the case of a Berkovich indenter (Figure 1.44).

e) Contact topology

During the indentation of the sample, the effective indentation depth h_c is rarely equal to the measurement of the column displacement h . Two different behaviors can be observed (Figure 1.47):

- The surface of the indented material sinks under the indenter and $h_c < h$. This behavior is commonly called “sink-in”.
- The surface of the indented material piles-up around the indenter and $h_c > h$. This behavior is commonly called “pile-up”.

Cheng (2004) predicts a piling-up for materials with a strain hardening index n below 0.3 and a ratio of the elastic limit σ_e to the Young’s modulus E lower than 1%.

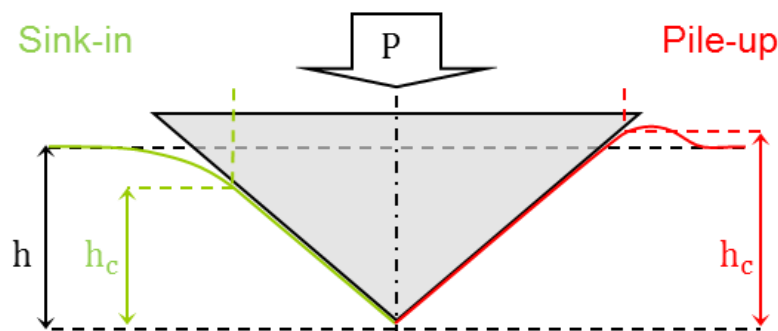


Figure 1.47. Illustration of sink-in and pile-up with a conic indenter.

The main models in the literature that take into account the influence of the contact topology are:

- Doerner and Nix (1986): they suppose that the contact area does not evolve at the beginning of the unload phase and the contact depth is given by (1. 20).

$$h_c = h - \frac{F}{S} \quad (1. 20)$$

- Oliver and Pharr (1992): the indentation depth is given by (1. 21). ϵ is a constant dependent on the geometry of the indenter ($\epsilon = 0.75$ for a Berkovich indenter).

$$h_c = h - \epsilon \frac{F}{S} \quad (1. 21)$$

- Loubet (1993): both models described by equations (1. 20) and (1. 21) do not consider the case of pile-up where $h_c > h$. Loubet proposed the expression (1. 22) for the contact depth, where α_L is a constant, depending on the indented material.

$$h_c = \alpha_L \left(h - \frac{F}{S} \right) \quad (1. 22)$$

The contact topology being usually unknown, a microscopic observation of the residual footprint has to be performed to select the appropriate indentation depth model. In Figure 1.48 is illustrated the AFM scan of the residual footprint of a Berkovich indenter on silver printed layer. On the footprint profile, pile-up can be observed. Hence, Loubet correction (1. 22) of the indentation depth should be applied in this case.

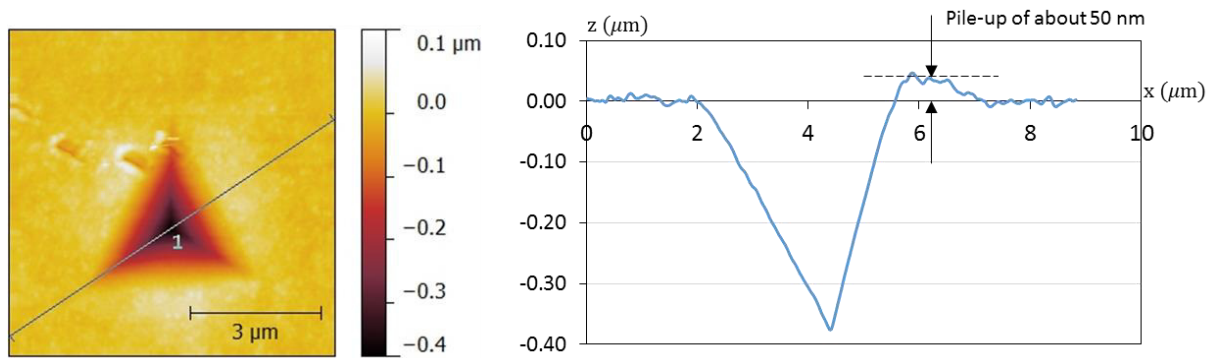


Figure 1.48. a) AFM scan of a residual footprint of a Berkovich indenter in a printed silver layer on SiO_2/Si substrate. b) Profile of the footprint showing pile-up of the indented material.

VI.2. Elastic Properties

a) Bulk material

The Young's modulus is calculated from the slope of the unloading curve at the maximum load (Fischer-Cripps, 2004). The CSM option allows the measurement of the modulus as a function of the indentation depth thanks to the harmonic load. Bulychev (1975) and Shorshorov (1982) found that the reduced elastic modulus can be expressed as a function of the contact stiffness S and the contact area A_c (1. 23).

$$E' = \frac{E}{1 - \nu^2} = \frac{S}{2\beta} \sqrt{\frac{\pi}{A_c}} \quad (1. 23)$$

where E and ν are the Young's modulus and the Poisson's ratio of the indented material. β is a correction coefficient depending on the indenter geometry ($\beta = 1.034$ for a Berkovich indenter) first introduced by King (1987). The main challenge in this method is the accurate determination of the contact area A_c .

The area function of the Berkovich indenter used in this thesis was calibrated following Oliver and Pharr method (1992). The area function is given by the polynomial expression in (1. 24), where the

coefficients C and C_i are adjusted on a fused silica reference sample. The Young's modulus should be constant over the indentation depth in the range 69-74 GPa and the hardness in the range 10-12 GPa (Fischer-Cripps, 2004).

$$A_c = Ch_c^2 + \sum_{i=0}^7 C_i h_c^{2^i} \quad (1. 24)$$

Finally, the expression of the reduced modulus in (1. 23) includes both the elastic response of the indented material and the indenter. Knowing the properties of the diamond indenter (Table 1.10), the reduced elastic modulus of the sample is determined by (1. 25).

$$E_s' = \left(\frac{1}{E'} - \frac{1 - \nu_{ind}^2}{E_{ind}} \right)^{-1} \quad (1. 25)$$

Table 1.10. Diamond indenter properties (Fischer-Cripps, 2004)

Material	Young's modulus (E_{ind})	Poisson's ratio (ν_{ind})
Diamond	1070 GPa	0.07

b) Thin film on substrate – Bec's model

The measured Young's modulus is an effective value which includes the combined mechanical response of the indented film and of the underlying films and/or substrate.

The first approach (Buckle, 1961), which is usually verified for films thicker than 1 μm , consists in considering that the indentation depth should be lower than 10% of the film thickness to neglect the influence substrate. However, this empirical method rapidly reaches its limits because of indenter imperfections and surface roughness that impose higher indentation depths.

In the literature, several models were proposed for the extraction of a thin film Young's modulus. These models are more or less complex, from empirical laws (Doerner, 1986) to finite element studies (Sakai, 2009).

In Bec's model, the system "film on substrate" is considered as serial springs. The contact stiffness K_z measured during the indentation test can be written as:

$$K_z = \frac{t}{(\pi a_c^2 + 2ta_c)E_f'} + \frac{1}{2E_s'(a_c + \frac{2t}{\pi})} = \frac{1}{2a_c E_{eq}'} \quad (1. 26)$$

where a_c is the contact radius, t the film thickness, E_f' , E_s' and E_{eq}' are respectively the Young's modulus of the film, the substrate and of the whole system. When applying Bec's model, the film thickness as well as the mechanical properties of the substrate must be known.

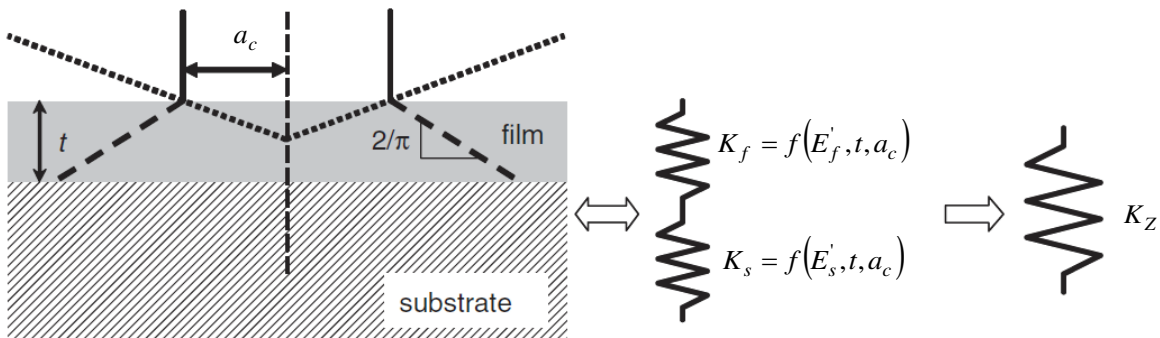


Figure 1.49. Bec's elastic model. Adapted from Bec (2006).

c) Multilayer stack on substrate – Mercier’s model

Mercier *et al.* (2010) proposed a generalization of Bec’s model to an elastic system composed by N-1 thin films on a substrate (Figure 1.50). The same hypotheses are applied and the system can be seen as a thin film on a substrate with an effective reduced modulus E'_{eff} that describes both the substrate and the underlying films. The equivalent stiffness of the multilayer stack is given by (1. 27). The use of Mercier’s model requires the iterative measurement of the elastic response of each thin film on its underlying layers.

$$K_z = \frac{1}{2a_{c,0}E'_{eq}} = \sum_{i=0}^N \frac{t_i}{(\pi a_{c,i}^2 + 2t_i a_{c,i})E'_{f,i}} + \frac{1}{2E'_s \left(a_N + \frac{2t_N}{\pi} \right)} \quad (1. 27)$$

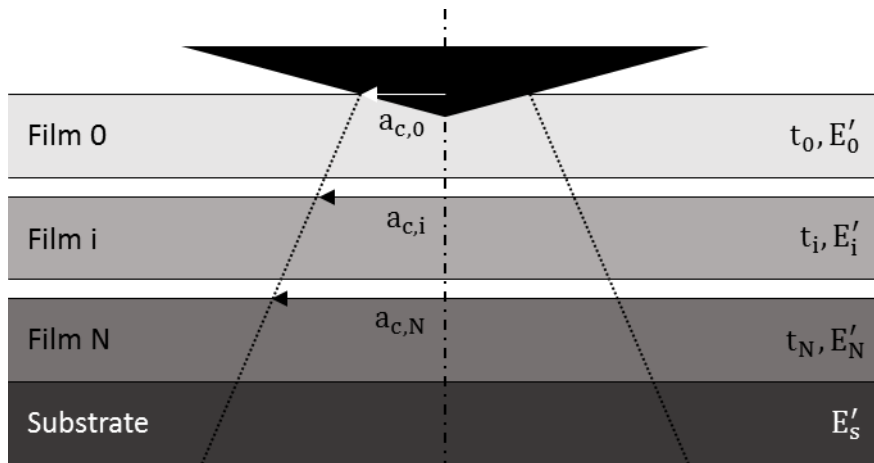


Figure 1.50. Mercier’s elastic model. Adapted from Mercier 2010.

The models of Bec (2006) and Mercier (2010) were employed to characterize the mechanical properties of the system “Ag/SiO₂/Si”.

VI.3. Plastic properties

The plastic properties of a material can be resumed to its elastic limit, hardness and strain hardening index. In this work, we have focused on the hardness of the printed silver layers defined as the pressure where the plastic deformation regime is reached. In practice, hardness H is calculated by (1. 28) (Fischer-Cripps, 2004).

$$H = \frac{P}{A_c} \quad (1. 28)$$

However, this formula is valid only for bulk materials. A semi-empiric rule allows the use of (1. 28) for thin films if the indentation depth does not exceed 20% of the film thickness. This rule can be defensible by calculating the radius r_p of the plastic deformation region under a conical indenter. If the value of r_p is lower than the film thickness, the plastic region is not confined nor influenced by the underlying layers or substrates.

Johnson (1987) described the expansion of the plastic region in the case of a conical indenter. In this model, commonly referred to as the expanding cavity model, the indented region is split in two regions (Figure 1.51):

- A hemi-spherical core of radius r_c (contact radius of the indenter) encased in the contacting surface of the indenter where there is a hydrostatic component of stress;
- Outside this core, there is a plastically deforming thick hemi-spherical shell wherein the radial stress decreases. The outer surface of this shell is at r_p , where stresses satisfy the yield condition. Hence, outside this surface deformations are fully elastic.

The elastic-plastic boundary defined at a radius r_p is given by:

$$\left(\frac{r_p}{r_c}\right)^3 = \left(\frac{E \tan \beta_{cone}}{\sigma_e} + 4(1 - 2\nu)\right) * \frac{1}{6(1 - \nu)} \quad (1. 29)$$

where E and ν are the Young's modulus and Poisson's ration of the indented material, β_{cone} the inclination of the face of the cone to the surface, and σ_e the elastic limit.

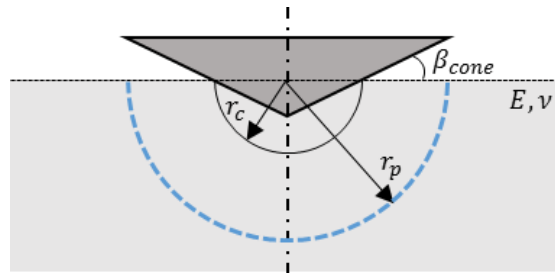


Figure 1.51. Elastic-plastic indentation by a cone. Adapted from Johnson (1987).

Finally, in polycrystalline materials, the Hall-Petch relationship (1. 30) (Hall, 1954) predicts that the hardness increases with decreasing grain size d .

$$H \propto \frac{1}{\sqrt{d}} \quad (1. 30)$$

Conclusion

Printing techniques for edition and packaging are being upgraded to fulfill the requirements of the expanding market of printed electronics. Simultaneously, chemical and material research has led to a wide spectrum of materials in the form of inks or paste than can be printed.

In this chapter, the main printing processes for printed electronics were presented. Among these, piezoelectric inkjet printing technique was selected for its many assets: versatility of the process, non-contact with the substrate, digital source pattern, fast setup for laboratory-scale studies and prototyping. Inkjet printing requires inks with low viscosity (1-30 mPa.s) and a surface tension of about 30 mJ.m⁻². The printing process goes through the ejection of droplets, their impact on the substrate and finally the drying of the ink. The interactions between the ink and the substrate have a strong influence on the morphology of the printed layers. Hence, a thorough analysis of these interactions is necessary to optimize printing.

Emphasis was put on the printing of colloidal suspensions of metallic nanoparticles. Commercial silver nanoparticles inks will be mainly employed in the following. Silver inks were chosen because of their shelf-life (>1 year), their commercial availability, and the high electrical conductivities (>10⁷ S.m⁻¹) that can be obtained. After printing, the layers must be provided with thermal energy to trigger sintering and coalescence phenomena. This energy can be supplied by different sources and in this thesis, thermal annealing in oven was mostly employed as it offers an isotropic and homogeneous annealing. The resulting layers have a polycrystalline microstructure that strongly influences their electrical and mechanical properties. The fundamental models for understanding electronic transport in polycrystalline films were addressed. Moreover, nanoindentation method for mechanical characterization “film on substrate” systems was presented.

In the next chapter, a thorough characterization of the printed silver layers is carried out and a particular attention will be given to the influence of the annealing conditions. Electrical and mechanical properties are investigated and analyzed through microstructural characterization.

The main properties of bulk silver that will serve as reference values in the study of the inkjet printed silver layers are summarized in Table 1.11.

Table 1.11. Properties of bulk silver.

Fermi's energy	5.48 eV	Kittel, 2007
Mean free path (25°C)	53 nm	Calculated (1. 9)
Melting temperature	961°C	Slade, 1999
Electrical resistivity (25°C)	1.61 * 10 ⁻⁸ Ω. m	Slade, 1999
Temp. Coeff. of Resistance	4100 ppm/°C	Slade, 1999
Coeff. of Thermal expansion	19.7 ppm/°C	Slade, 1999
Young's modulus	79 GPa	Slade, 1999
Poisson's ratio	0.37	Slade, 1999
Elastic limit	0.1 – 0.23 GPa	Slade, 1999
Hardness	0.3 – 0.7 GPa	Slade, 1999
Radius of plastic deformation	r _p = 1.68 r _c	Calculated (1. 29)

Chapter 2

Characterization of Inkjet Printed Silver Layers

Introduction

This chapter focuses on the study of the intrinsic properties of inkjet printed silver layers, namely the microstructure, the electrical properties and the mechanical properties. The annealing temperature, which has a strong influence on the printed material properties, is the driving parameter of the analysis.

In the literature, several authors have investigated the influence of the annealing conditions on the properties of silver nanoparticles printed layers (Moon, 2005; Park, 2006; Jung, 2008; Volkman, 2011). The most explored property is the electrical conductivity. The microstructure is also regularly analyzed as it governs the material properties. However, in most studies, an accurate porosity measurement is often missing. In particular, 3D measurements of the porosity have not been reported yet and only surface or cross-section 2D porosity values appear in the literature (Jung, 2008; Cauchois, 2012). Finally, only a few results concerning the mechanical properties such as hardness and Young's modulus have been reported (Cauchois, 2012).

The aim of this chapter is to propose an extensive study of the influence of the annealing temperature in the range 100°C to 300°C. This range is of particular interest because it is compatible with both plastic substrates and back-end processes in microelectronics. For most silver inks, a minimum value of about 100°C is required to obtain a conductive layer. Microstructural parameters, such as grain size, roughness and porosity must be carefully measured in order to understand how electrical and mechanical properties evolve. This study is carried out on silver layers printed with a commercial ink.

The first part of this chapter is focused on the ink rheology and the initial state of the silver nanoparticles, the substrate properties (Young's modulus and surface energy), and the fabrication process of the reference samples. Once the samples are prepared, the following parts of the chapter are focused on the evolution with the annealing temperature of the microstructure, the electrical and the mechanical properties.

I. Sample preparation

I.1. Silver ink

a) Ink composition

Inks for inkjet printing processes must fulfill several rheological conditions in order to be jetted. SunChemical EMD5714 (SunChemical, n.d.) is a silver ink with 40% in weight of silver nanoparticles whose characteristic size is announced by the supplier at 70 nm (Figure 2.1). This ink was chosen for several reasons:

- Affordable compared to other inks: 100 ml for 1000 euros.
- User friendly solvent: ethanol and ethylene glycol.
- Stable over time: 3 years usage under the same printing conditions.

The SunChemical EMD5603 (20 wt%) and 5714 (40 wt%) are out of production since summer 2013. However, the results and in particular the methods proposed in this chapter can be transposed to other silver inks with similar properties.

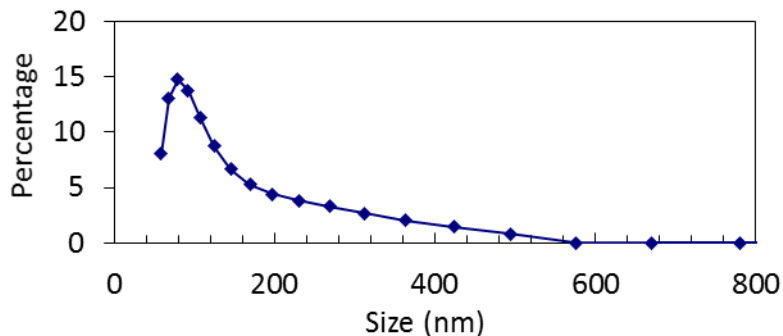


Figure 2.1. Size distribution of silver nanoparticles in EMD5714 SunChemical ink (SunChemical, n.d.).

It is necessary to precisely know the initial dimensions of the nanoparticles as they will define the microstructure of the printed metal structures (Shimada, 1994).

Atomic force microscopy (AFM) performed on the surface of the as dried printed layers on SiO₂/Si (60°C, 20 minutes) was not satisfying, probably because of the interaction between the tip and the organic contamination of the layer. Field-Effect Scanning Electron Microscopy (FE-SEM) with low acceleration voltage (2kV) allowed an adequate observation of the sample surface (Figure 2.2). Average grain size was measured through Feret's diameter (Feret, 1931). The Feret's diameter is defined by the average perpendicular distance between parallel tangents touching opposite sides of the grain perimeter (Walton, 1948).

The average grain size of the silver nanoparticles at the surface of the as dried sample follows a Gaussian distribution law with an average diameter μ of 32 nm and a standard deviation σ of 14 nm. The measured average grain diameter is about half the value announced by the ink supplier.

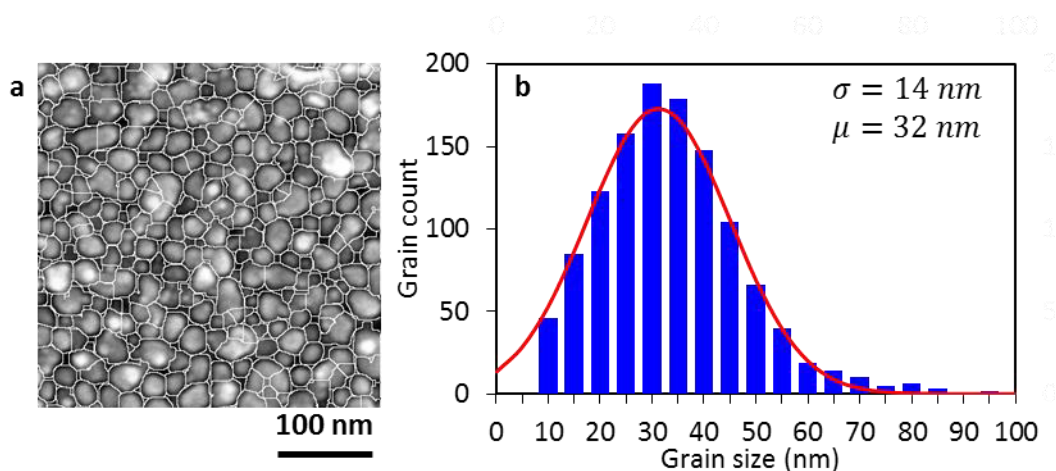


Figure 2.2. a) Surface of EMD5714 silver ink dried at 60°C during 20 min. b) Feret's diameter distribution.

According to the behavior of nanoparticles to temperature increase, the drying step at 60°C might have initiated the sintering process and thus modified their initial dimension. The observation of the cross-section of the same as dried sample with FE-SEM at 2 kV, in order to prevent charging phenomena and local sintering due to electrons high energy, shows that the polymeric coating of the nanoparticles is still in place (Figure 2.3). Such observation allows supposing that the silver nanoparticles does not evolve during the drying step at 60°C. Thus the FE-SEM measurement of the nanoparticles dimensions at the surface of the dried sample can be considered equivalent to their initial colloidal state.

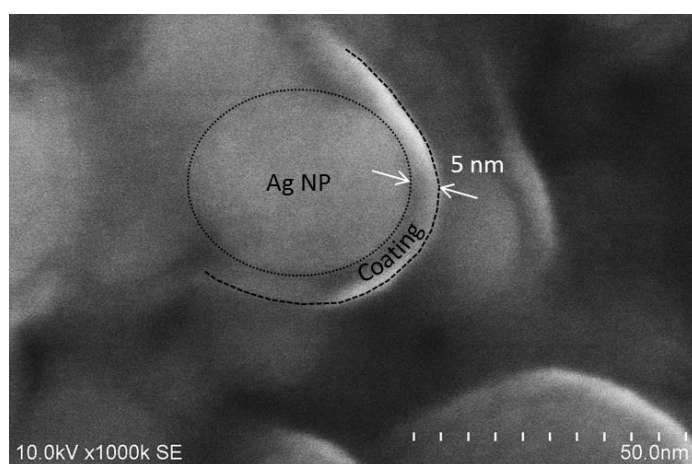


Figure 2.3. FE-SEM observation of a silver nanoparticle with its polymeric coating layer (cross-section).

The solvent of the EMD5174 ink is composed of ethanol and ethylene glycol. Other compounds such as surfactants and buffering agents are present in the ink to tune rheological properties. Usually they have organic and polymeric nature, but the exact composition is unknown. Moreover, as already stated, the silver nanoparticles are coated with polymer chains to prevent agglomeration and precipitation. These compounds are a source of chemical contamination in the printed layers. Increasing the annealing temperature purifies the layer as the C-C chains are broken and burned-out during the curing process.

b) Ink properties

As mentioned in chapter 1, inks for inkjet printing must satisfy several conditions to be jetted with accuracy and a reliable reproducibility:

- Surface tension: in the order of 10 mJ.m⁻².
- Viscosity: in the range 1 to 30 mPa.s.
- Dimensions of the nanoparticles lower than 200 nm.

Depending on the printer, viscosity and surface tension can be tuned by locally modifying the nozzles temperature. The Dimatix print head DMC11610 (10 pl droplets) can be heated up to 70°C.

➤ Surface tension

There are several methods to measure the surface tension of fluids. The most common and reliable methods are the du Noüy ring (1925) and Wilhelmy (Holmberg, 2002) plate methods. Unfortunately, both techniques require a volume of at least 10 ml of ink and high cleanliness of the plate or ring to avoid influencing the wettability. Taking into account the price of the ink and to prevent any contamination we used a less material consuming method, namely the pendant drop, described in Annex 1.

The measurement was performed on an OCA Dataphysics goniometer on 5 µl pending drops. Results are summarized in Table 2.1. They are in agreement with the supplier's value.

➤ Viscosity

The viscosity of the ink was measured on an Anton Paar Physica MCR 301 rheometer at 25°C and 1000 s⁻¹ resulting in a value of 13.5 mPa.s.

➤ Dimensions of the nanoparticles

In order to prevent nozzles clogging, nanoparticles dimensions must be at least 10 times lower than the nozzle characteristic size (square, $a = 21 \mu\text{m}$ side). The ink is filtered with a PTFE 200 nm filter before filling the cartridge.

c) Printability

According to the equations in chapter 1.II.1, the Z number of the SunChemical EMD5714 ink is 2.1 when used with the 10 pl cartridge of the Dimatix printer. Fromm (1984) and Reis (2000) predict that the ink can be properly jetted, while for Jang (2009), long filaments might occur hindering maximum jetting frequency. Hence, printing was realized at a jetting frequency of 5 kHz. The properties, measured and calculated, of SunChemical EMD5714 silver ink are reported in Table 2.1.

Table 2.1. Ink and ejection properties.

Viscosity η	13.5 ± 0.5	mPa.s	measured
Surface tension σ	24 ± 8	mJ. m ⁻²	measured
Density ρ	1560	kg. m ⁻³	supplier's data
Droplet velocity v	5	m. s ⁻¹	measured (Figure 2.6)
Square nozzle side a	21	µm	measured
Jetting frequency	5	kHz	set on printer
Reynolds Re	12.13	–	calculated (1. 1)
Weber We	34.13	–	calculated (1. 2)
Ohnesorge Oh	0.48	–	calculated (1. 3)
$Z = 1/Oh$	2.08	–	calculated

1.2. Substrate

a) Type

The samples studied in this chapter were printed on 200 mm silicon wafers with 500 nm thick thermal oxide. This substrate offers several advantages for studying the intrinsic properties of the printed silver layers. Indeed, it is stable in the annealing temperature range, has a smooth surface and no porosity that could absorb ink solvent or nanoparticles. The 500 nm thick thermal oxide is required to have an efficient electrical insulation between the semiconductive silicon substrate and the metallic printed silver layer.

b) Physical properties

The stability of the substrate to thermal variations is essential to minimize its influence on the printed silver layer properties. An example of such influence could be the release of mechanical stress in the substrate causing cracks and delamination of the printed layer.

In Table 2.2 are reported the values of the thermal coefficients of expansion of silicon and silicon oxide and the subsequent stress and strain for temperature variations of 300°C. The stress values clearly indicate that the substrate deformations are in the elastic domain.

Table 2.2. Coefficient of thermal expansion of the substrate

	Coeff. of thermal expansion (ppm/°C)	Young's Modulus	Yield strength	Stress $\Delta T = 300^\circ\text{C}$	Strain $\Delta T = 300^\circ\text{C}$
Bulk Si (Rebeiz, 2003)	2.6	162 GPa	2.6 – 6.8 GPa	130 MPa	0.08%
Bulk SiO_2 (Petersen, 1982)	0.55	73 GPa	8.4 GPa	12 MPa	0.02%
Thermal SiO_2 on Si	$\Delta\alpha = 2.05$	73 GPa	8.4 GPa	45 MPa	0.06%

The thermal silicon oxide layer growth on the silicon substrate is submitted to a tensile stress of 45 MPa for temperature variations of 300°C. This value is much lower than its yield strength, meaning that silicon oxide deformations remain in the elastic regime.

c) Surface properties

The surface roughness of the thermal silicon oxide measured by AFM was $R_a = 0.17$ nm.

The substrate surface energy measurement was carried out by the contact angle method using an OCA Dataphysics goniometer. The Owens-Wendt model (Owens, 1969) is used to calculate the surface energy using five different probe liquids (more details in Annex 1).

The total surface energy is $44.7 \text{ mJ} \cdot \text{m}^{-2}$. This value is higher than the surface tension of the ink, meaning that printing conditions are respected and that ink contact angle on the substrate will be lower than 90°.

1.3. Printing conditions

Van der Pauw patterns (Figure 2.4, cf. III.1.a) were printed with a 476 pixels/cm resolution. They were firstly used for electrical conductivity measurements (§III), and then either for microstructural analysis (§II) or nanoindentation tests (§IV).

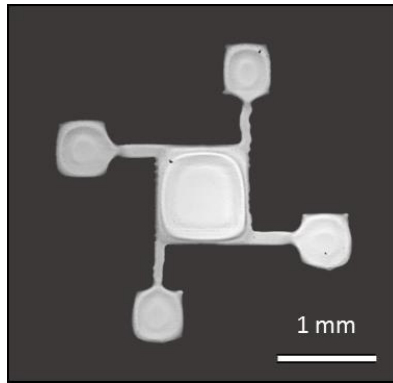


Figure 2.4. Van der Pauw printed patterns.

The ink solvents being ethanol and ethylene glycol, the nozzles temperature was set to ambient to prevent solvent evaporation which may cause nozzles clogging. The actuation voltage was set to approximately 23 V at a 5 kHz firing frequency, resulting in 28 μm diameter droplets, corresponding to a volume of about 11 pl. The jetting waveform is illustrated in Figure 2.5 and was advised by the ink supplier.

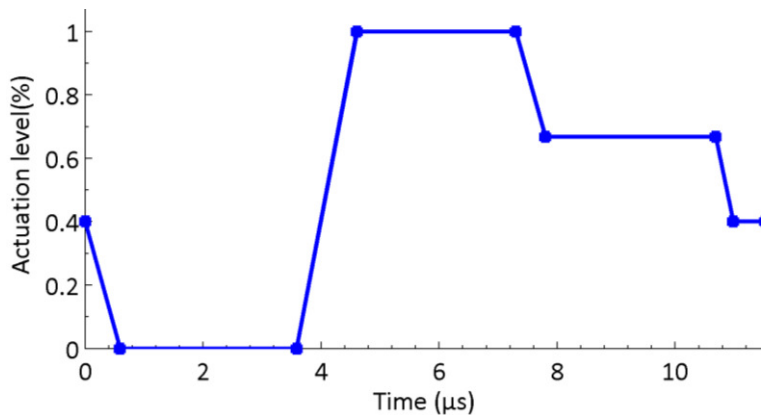


Figure 2.5. Jetting waveform.

As illustrated in Figure 2.6, during the droplet formation there are no visible satellite droplets and the filament is completely absorbed by the main droplet at 300 μm from the nozzle. Given this value, we set the distance between the substrate and the nozzle to 600 μm . The printer chuck was heated at 60°C to accelerate ink drying. After printing, the samples were dried in oven at 60°C during 20 minutes to complete solvent evaporation. Then the silicon substrate was cleaved to finally anneal the samples at different temperatures in oven. The thermal ramp applied was always the same:

- 15 minutes from ambient to temperature setpoint.
- 60 minutes soak at temperature setpoint.
- Instantaneous cooling of the samples at ambient temperature by placing them on a large aluminum plate.

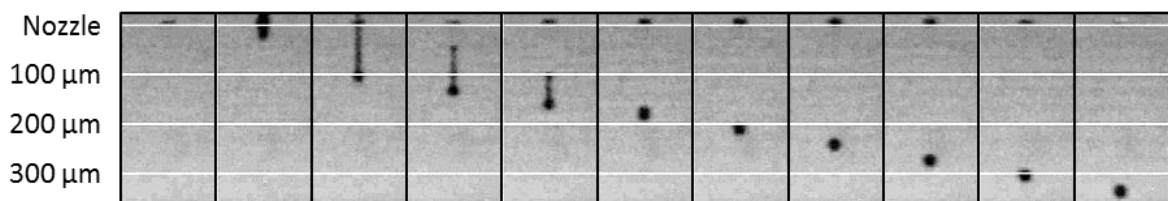


Figure 2.6. EMD5714 droplet generation. Interval: 8 μs .

II. Analysis of the microstructure

The mean grain diameter, the distribution of grain size as well as crystallographic orientation are primary parameters to understand electrical and mechanical properties of thin films. As a consequence, the knowledge of the grain size evolution offers the opportunity to optimize the performance and the reliability of the printed films. The aim of this paragraph is to describe the microstructural evolution of the nanoparticles of the inkjet printed silver layers with the increase of the annealing temperature.

II.1. Characterization methods

Because of the nanometric dimensions involved, high resolution instruments such as near field microscopy and field-effect scanning electron microscopy are employed.

a) Atomic force microscopy

Atomic force microscopy, or AFM, is a scanning probe technique which allows atomic resolution imaging. It consists in measuring the forces that interact between the surface of a sample and a very sharp tip with a radius of curvature of a few nanometers. This tip is located at the free end of a cantilever of about 150 μm long, as illustrated in Figure 2.7. The working principle of an AFM is further detailed in Annex 2.

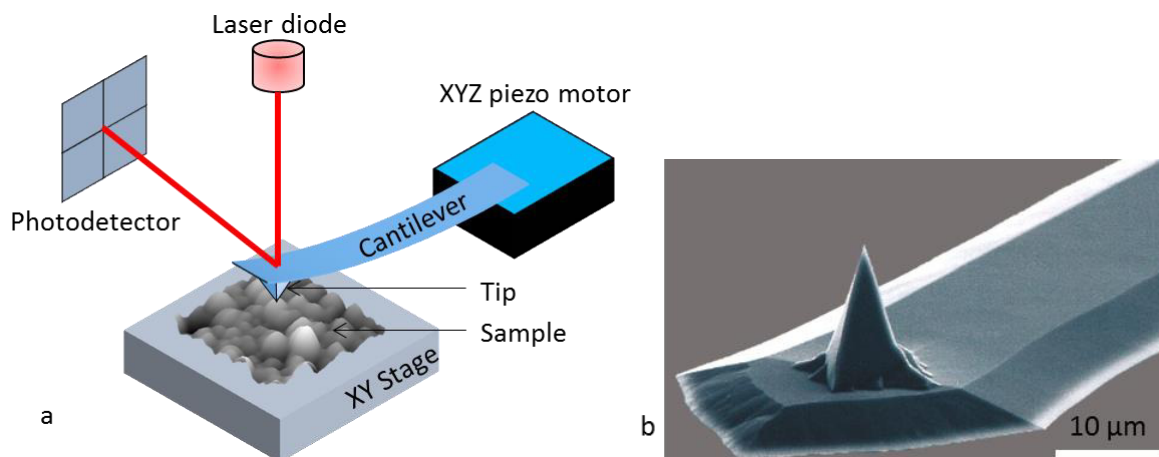


Figure 2.7. a) AFM working principle. b) AFM tip and cantilever (NanoWorld Arrow NCR tip).

b) Slice-and-view method

The slice-and-view method is a microscopy technique that has become very popular for 3D serial section imaging (Groeber, 2006). It can be realized on a dual-column system where a Focused Ion Beam (FIB) and a Scanning Electron Microscope (SEM) work together in order to build a 3D representation of the sample. Details on the working principle of SEM and FIB instruments are given in Annex 2.

The slice-and-view protocol consists in using the electron beam to realize a real-time imaging of the milling process by the ion beam. For an accurate 3D reconstruction of the region of interest (ROI), the ion beam has to be set to remove a thin slice (a few nm). Once the slice is removed, the electron beam scans the milled surface and records an image (Figure 2.8). These two steps are successively repeated until the volume to be analyzed has been completely removed.

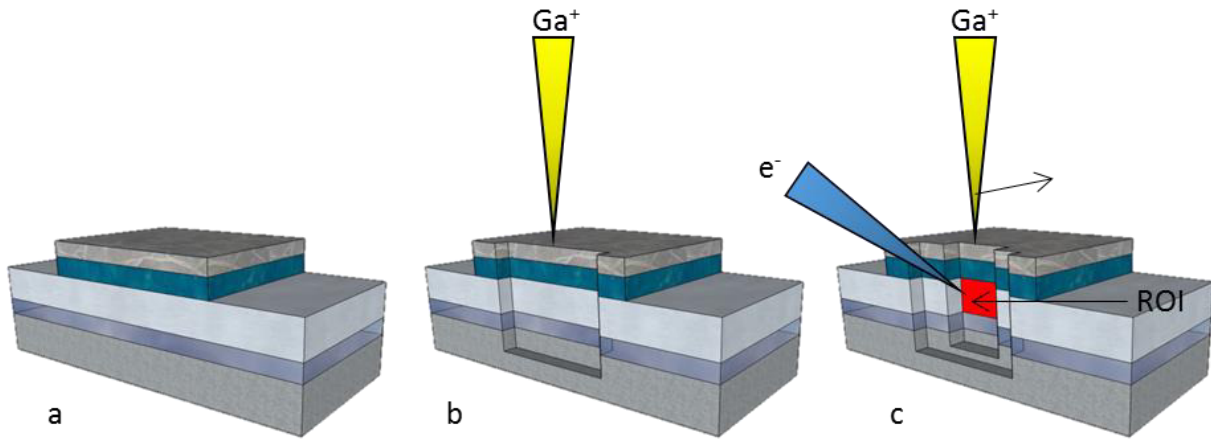


Figure 2.8. Slice-and-view process. a) Raw Sample. b) First Raw cut to step away from cleaved surface. c) Successive milling and observation steps.

The data acquisition can last several hours depending on the energy of the ion beam (milling speed) and the number of slices. Dual-beam instruments dedicated to slice-and-view are equipped with an automatic system that manages the two beams and image recording. The main challenge in the automation is the accurate focusing of the electron beam on the ROI.

As shown in Figure 2.8, the electron beam is not perpendicular to the scanned surface. Indeed, for high quality milling it is recommended to have an ion beam perpendicular to the sample surface and because of space limitations in the chamber, the two columns are usually mounted at a 52° angle. Such a positioning causes a systematic error on the SEM imaging that can be corrected afterwards. As a consequence, the autofocus must follow a surface that moves back from the focal plane because of the removed material. Moreover, the occurrence of drift phenomena, which may reach up to 250 nm/h (Cantoni, 2007), may cause difficulties in following ROI during several hours. Drift can be reduced by the metallization of the sample to ease the release of electrons and thus decrease charging effects.

Finally the drift of the sample in the chamber can also generate an error on the thickness of the milled slice. A calibration of the ion beam shift (Holzer, 2006) is required for an automated drift correction. Eventually, reference marks can be machined outside of the ROI to improve drift correction.

At the end of the slice-and-view protocol, data processing is necessary:

- Alignment of the stack of acquired the data.
- Correction of the SEM tilt.
- Image processing: filtering and segmentation.
- 3D reconstruction.

II.2. Image processing

Image processing is a powerful tool that consists in a set of mathematical operations applied to an image in order to highlight a property of the ROI and eventually to improve the quality of the measurement by correcting aberrations due to the recording equipment. Such processing usually employs complex algorithm and a large database is available through free softwares such as ImageJ (1997-2014) and Gwyddion (Nečas, 2012). Also, environments of numerical computing such as Matlab® and Scilab (2012) offer embedded tool boxes with ready-to-use functions for image processing.

We briefly describe here the mathematical operations that were applied so that the reader gets an exact idea on how data were processed:

- Filtering: removal of an exact range of the acquired data.
- Segmentation: process of separating the acquired data in different segments. *In our case, no more than two segments are employed (black and white).*

For the sake of clarity, these operations are illustrated on an AFM scan of a sample of inkjet printed silver on a SiO₂/Si substrate annealed at 150°C during one hour. Raw data of the height channel is shown in Figure 2.9.

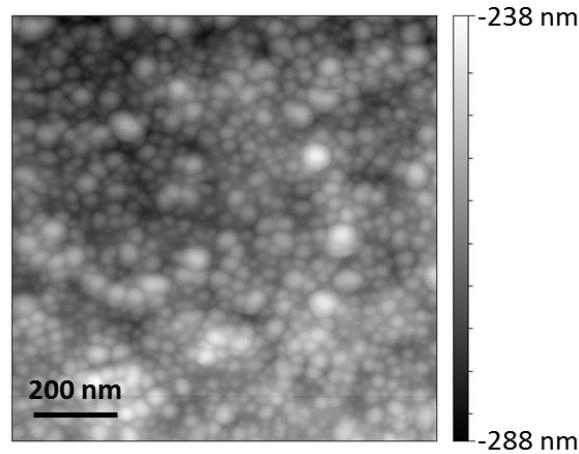


Figure 2.9. Raw AFM height data of a silver sample annealed at 150°C, 1h. Surface: 1 μm².

a) Plane fit: data leveling

The first applied operation is a first order plane fit along X and Y directions. This allows removing a plane which usually corresponds to the tilt of the sample. In this case, the silicon substrate is very flat thus a first order plane subtraction is satisfactory. When working on large or flexible substrates, it is possible to remove a 2nd order plane or a spherical plane. On samples with large height variations (a step for example) such background plane removal might cause aberrations. After leveling the data, minimum value is set to zero (Figure 2.10).

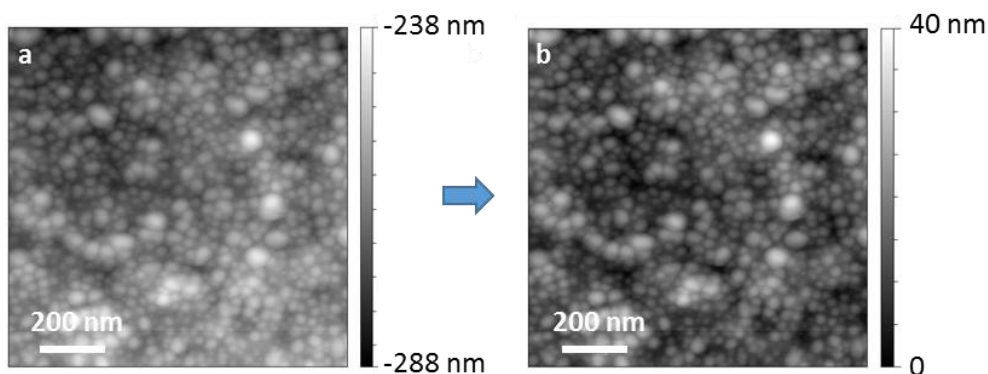


Figure 2.10. Plane fit. a) Raw data. b) Plane fit and minimum value set to 0.

b) 2D Fast Fourier Transform filtering

It is a common operation on AFM imaging because it allows removing specific noise coming from data acquisition. The two dimensional Fast Fourier Transform of a matrix $I(M, N)$ is calculated according to equation (2. 1). The graphical effect of a 2D FFT is illustrated in Figure 2.11. The frequency domain is

divided in four quadrants which all contain the same information. The suppression of a frequency range followed by the inverse FFT removes a set of data from the original image. High frequencies in the FFT correspond to fast changes in the spatial domain and can be interpreted as the details. Low frequencies correspond to slow modifications of the spatial domain: they can be both noise and periodic structures of the analyzed sample.

$$F(u, v) = \frac{1}{MN} \sum_{m=0}^{M-1} \sum_{n=0}^{N-1} I(m, n) * e^{-2i\pi(\frac{um}{M} + \frac{vn}{N})} \quad (2.1)$$

The most common suppressed regions in the frequency domain for AFM data are:

- Regions around the vertical and horizontal axis as they are characteristics of the AFM tip trace.
- The origin as it contains low frequency data. Such low frequencies are usually generated by building vibrations.

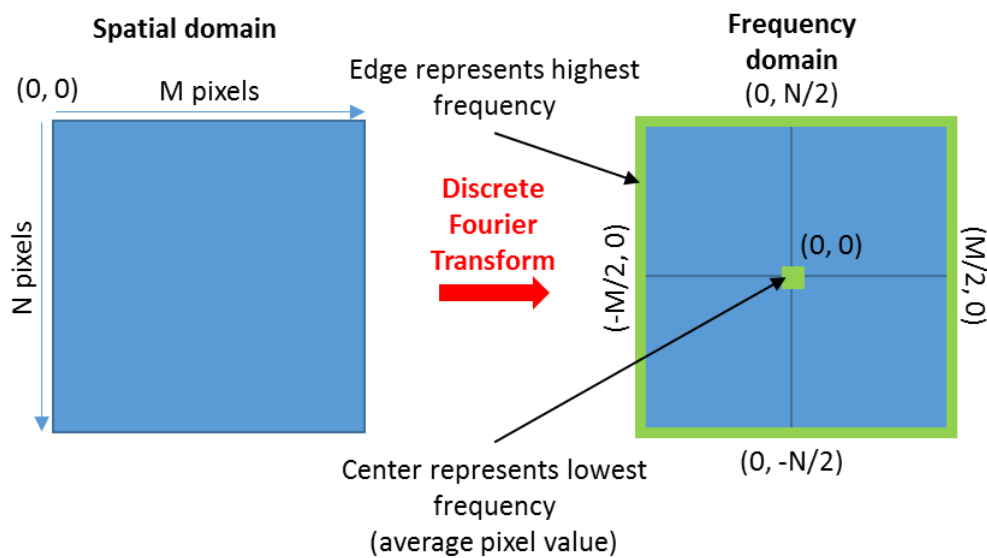


Figure 2.11. 2D Fast Fourier Transform.

Figure 2.12 shows the original data of the height signal and its 2D FFT. By masking some areas in the frequency domain and by returning to the spatial domain the quality of the image is improved.

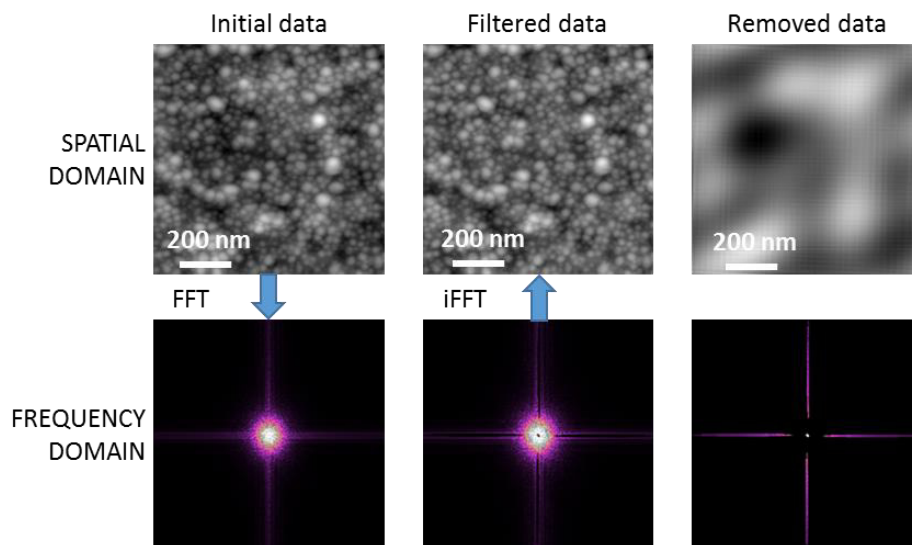


Figure 2.12. 2D Fast Fourier Transform on the height signal of the silver sample.

c) Gaussian blur

The Gaussian blur is a filter that smoothes data. It acts as a low pass filter that removes high frequencies data (details and noise).

In two dimensions, an isotropic Gaussian distribution is defined by equation (2. 2), where σ is the standard deviation of the distribution.

$$G(x, y) = \frac{1}{2\pi\sigma^2} e^{-\frac{x^2+y^2}{2\sigma^2}} \quad (2. 2)$$

Equation (2. 2) is defined for a continuous set of data. However, the acquired images are matrices representing the ROI in a discrete set of data. To apply the Gaussian filter, and in general to apply a mathematical operation to digital and discrete data, a convolution is employed. It consists in a “sliding multiplication” of the image matrix $I(M, N)$ by an operator matrix K of the same dimensionality, called the kernel, to produce a third matrix (Figure 2.13) in which each cell is calculated by equation (2. 3).

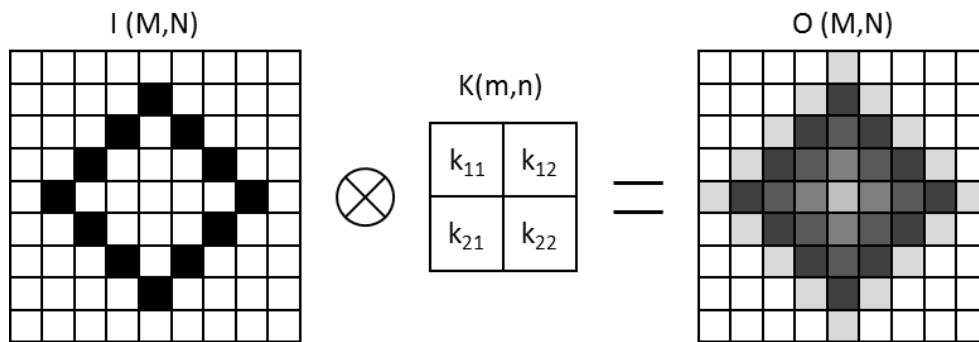


Figure 2.13. Convolution operation illustrated for a 2x2 Gaussian Kernel.

$$O(i, j) = \sum_{k=0}^m \sum_{l=0}^n I(i + k - 1, j + l - 1) * K(k, l) \quad (2. 3)$$

The kernel matrix is calculated by sampling the kernel function, namely equation (2. 2) for the Gaussian blur operation. Blurring was realized by the means of the embedded plugin “Gaussian blur” in ImageJ software. Its effects are illustrated in Figure 2.14 for different values of the standard deviation σ of the Gaussian kernel.

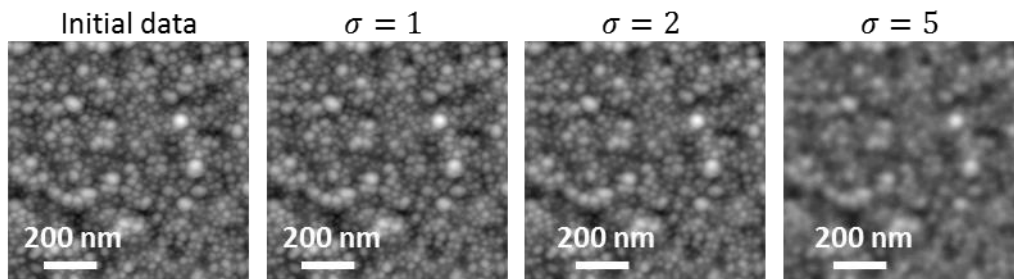


Figure 2.14. Gaussian blur for different values of the standard deviation.

d) Laplacian

The Laplacian operator calculates the 2nd derivative of an image. It highlights the regions where rapid intensity change occur. It is therefore of common use in edge detection. This filter is used after the Gaussian blur so it will be less sensitive to noise. The Laplacian operator is described by equation (2. 4) and illustrated in Figure 2.15.

$$L(x, y) = \frac{\partial^2 I}{\partial x^2} + \frac{\partial^2 I}{\partial y^2} \quad (2.4)$$

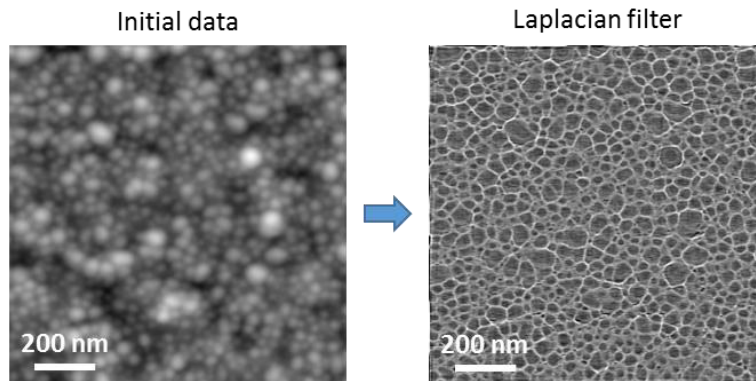


Figure 2.15. Laplacian filter.

e) Thresholding

Thresholding is one way to segment an image, meaning that the image is divided in a finite number of sets. Thresholding of gray scale images results in binary images, which is the simplest set of data to analyze for object counting and 2D measurements such as perimeter or Feret's diameter. Thresholding can be realized either manually or through one of the several existing algorithms. Otsu's thresholding method (Otsu, 1979) was applied on all of our data so that they can be compared (Figure 2.16). Otsu's method assumes that the image is composed of two classes of pixels: foreground and background pixels. The optimum threshold separating the two classes is calculated so that their combined spread is minimized.

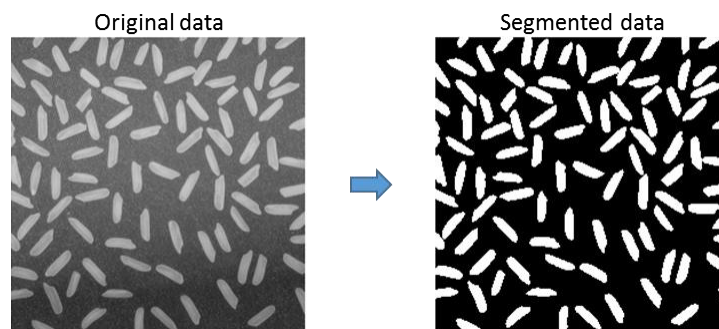


Figure 2.16. Otsu segmentation on rice grains.

f) Binary operations

Once the binary image is obtained, several operations can be applied in order to improve its matching with the initial data. The effects of the binary operators are illustrated in Figure 2.17. White pixels represent the foreground and black pixels the background.

- Dilation: enlarge the boundaries of object in the foreground. As a consequence, background holes become smaller.
- Erosion: remove pixels from the edges of the objects of the foreground.
- Opening: is defined as an erosion followed by a dilation. Less destructive than the erosion, it preserves the shape of the foreground regions.
- Fill holes: a hole can be defined as a background region surrounded by a connected object of foreground pixels. This operation allows filling these regions.
- Watershed: is an algorithm that automatically separates connected objects.

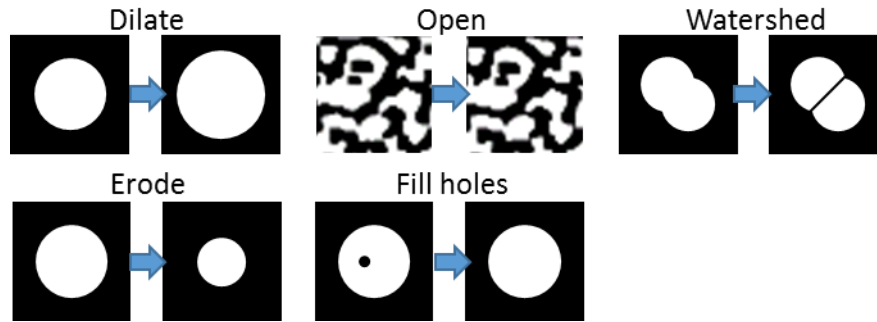


Figure 2.17. Binary operations. Adapted from Fisher (2000).

II.3. Grain morphology

The grain evolution with the annealing temperature of the inkjet printed silver layers was observed by atomic force microscopy on the layers surface. AFM is ideally suited to nanoparticles characterization in a wide range of dimensions: from a few nanometers up to several microns in the same scan. Moreover, compared to scanning electron microscopy, the calibration of the equipment is much more reliable when it comes to dimensions measurement.

a) AFM observation

The scans, realized on a Veeco 3100 AFM, offer the possibility of 3D visualization of the surface topology, qualitative and quantitative information on nanoparticles size, shape, surface texture and roughness. The samples were scanned with a NanoWorld Arrow NCR tip, designed for non-contact and tapping mode imaging. This probe, made of highly doped silicon, features a rectangular cantilever with triangular free end. The cantilever is 160 μm long, has a stiffness of 42 N/m and its resonant frequency is around 285 kHz. The tip is tetrahedral and has a radius of curvature of less than 10 nm.

The samples were scanned over a surface of 1 μm x 1 μm with a resolution 512 pixels along X and Y directions in tapping mode. The AFM allows measuring three signals, namely the height, the phase and the amplitude, which offers different information about the sample surface.

Height signal: it comes from the piezo-motor driving the cantilever. It represents the surface topography of the sample.

Amplitude signal: it comes from the cantilever oscillation. It shows how the cantilever is deflected when it encounters the surface topography. However, it cannot provide z-scale data. The best quality images are obtained when the amplitude signal is minimized.

Phase signal: it represents how the phase of the cantilever oscillations are affected by its interactions with the sample.

For the characterization of the surface of inkjet printed silver layers, we focus on height and phase signals. From these data, we are able to extract a large quantity of information concerning the analyzed sample:

- Grain morphology: shape, size distribution, number.
- Roughness: vertical deviations of the real surface from its ideal shape.

The height signal is used to evaluate the surface roughness while the phase signal is analyzed to extract grain dimensions.

b) Grain morphology

Phase signal is processed in order to extract grain dimensions and shape. Phase contrast imaging in AFM is a powerful technique which can reveal microstructure details obscured in topographic imaging (Pang, 2000). Such contrast can be attributed to an enhanced adhesion of the tip in a grain boundary region or a triple junction. The enhanced contrast of the grain boundaries in phase imaging makes image processing faster and lowers the errors.

The scans in Figure 2.18 show clearly an increase of the grain size with the annealing temperature. For annealing temperatures between 100°C and 350°C, scan dimensions were 500 nm x 500 nm while for the samples annealed at 450°C and 550°C, the scan size had to be increased to 5 μm x 5 μm in order to observe full grains and only the height signal was usable.

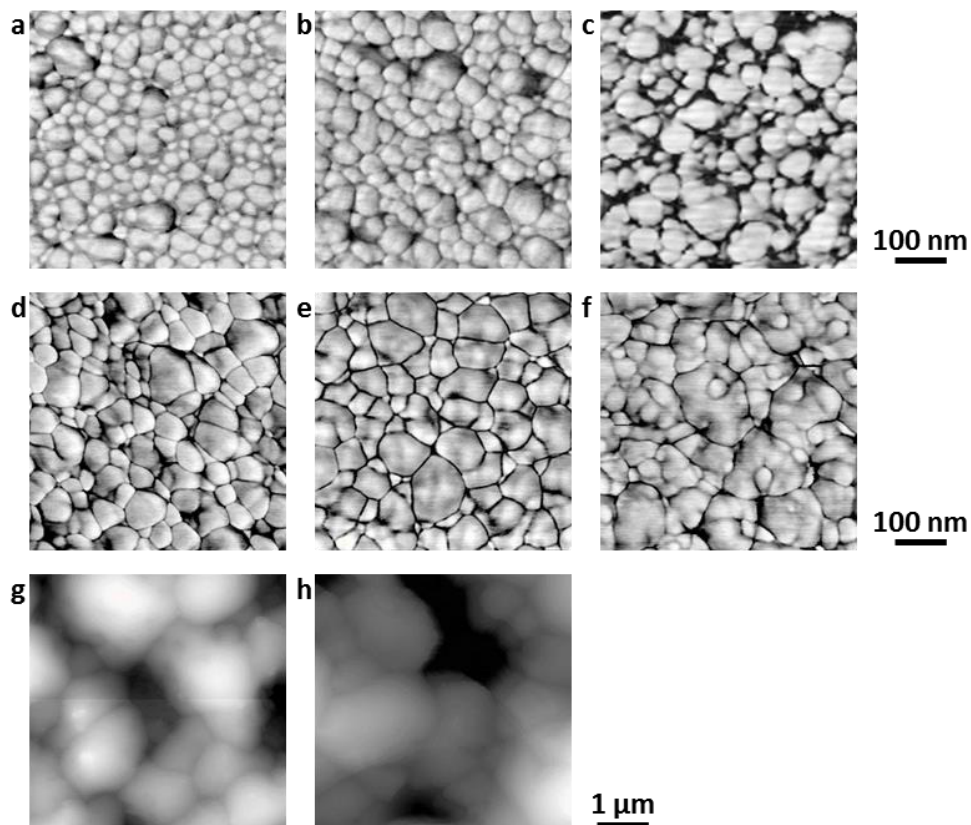


Figure 2.18. Grain growth of inkjet printed silver nanoparticles as a function of the annealing temperature. Annealing time is constant with a ramp of 15 min and a soak of one hour under air. Images a to f are phase signal and 500 nm x 500 nm. Images g and h are height signals and 5 μm x 5 μm . a) 100°C. b) 150°C. c) 200°C. d) 250°C. e) 300°C. f) 350°C. g) 450°C. h) 550°C.

Grain size and distribution measurements are realized through an automatic routine of image processing programmed on ImageJ software and illustrated in Figure 2.19 for the sample annealed at 100°C.

The source image has already been pre-processed according to the protocol described in Figure 2.23. The process consists in removing noise from the image (Gaussian blur), detecting grains edges (Laplacian) and converting the image into binary data (segmentation). Once the data are segmented, binary operations are applied to retrieve the most conformal shape of the grains (erosion, dilations, filling holes and watershed). The final step is the grain counting, realized with the “Analyze particles” plugin which works on binary images by detection of edges of closed objects. In this step, grains on the image borders are ignored. Errors in the detection can occur both at the segmentation step, which

may cancel particles because of low contrast grain boundaries, and at the watershed, which may create unreal particles. These aberrations during the image processing have opposite effects that can compensate each other. Moreover, a thorough ocular analysis of the sum of the particles outline with the source image demonstrate that the cited errors are usually lower than 1%.

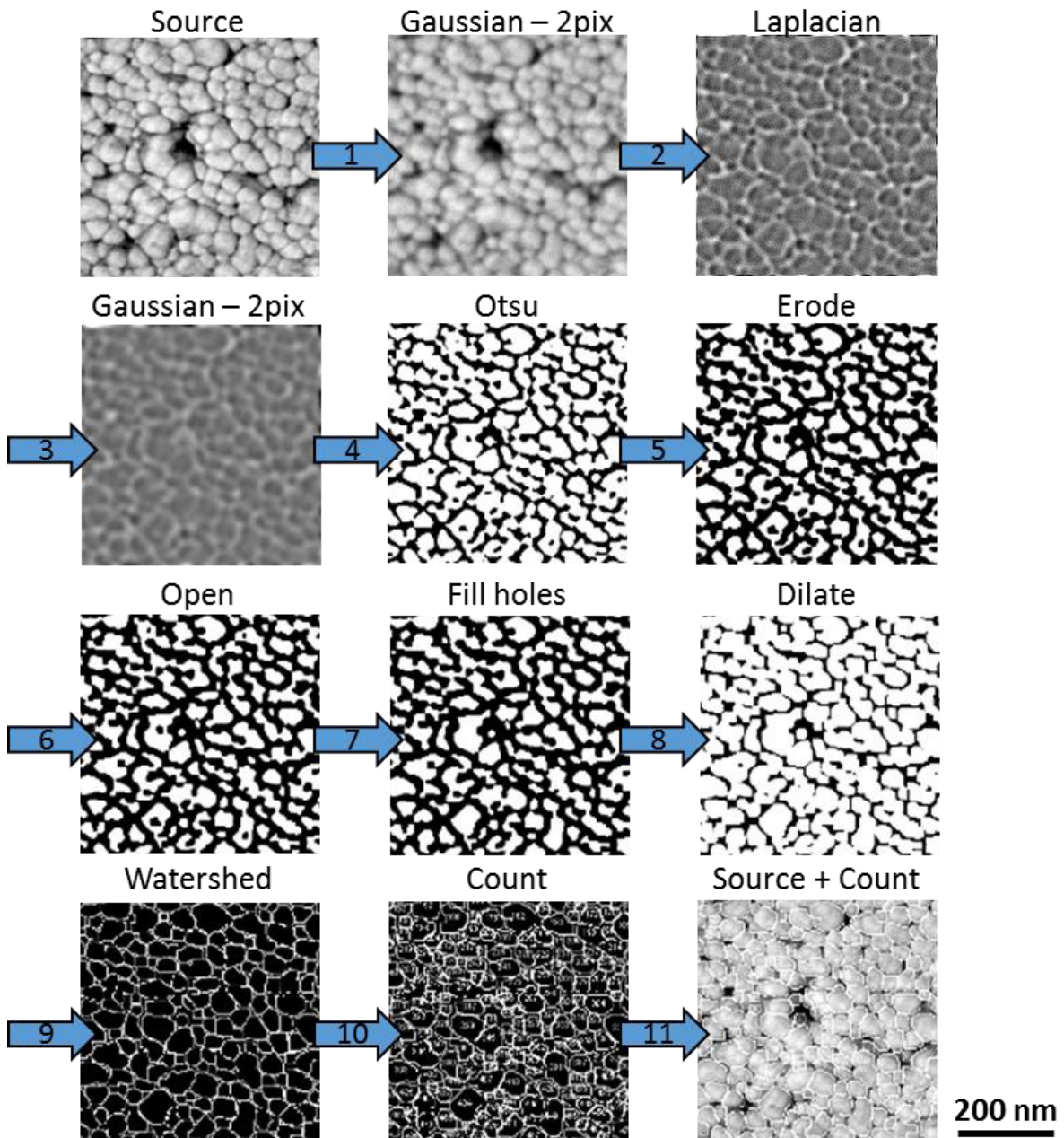


Figure 2.19. Image processing of AFM phase signal for grain size and distribution analysis for a sample annealed at 100°C during one hour. Scan dimensions: 500 nm x 500 nm.

Such processing is realized for samples annealed during one hour at temperatures between 100°C and 300°C and scanned over a 1 μm x 1 μm surface. Above 300°C, the grain population counted on 1 μm^2 is not large enough to establish a distribution law. Moreover, the segmentation routine reliability is decreased because of lower grain boundary contrast. Thus for samples annealed at more than 300°C, scan dimensions are increased and manual measurements are realized.

From the image processing several information concerning the grain geometry in the surface plane (two dimensions) can be extracted:

- Feret's diameter to describe the grain dimensions
- Circularity C of the grains defined by equation (2. 5).

$$C = 4\pi * \frac{Area}{Perimeter^2} \quad (2. 5)$$

The grain size distribution is plotted as a function of the annealing temperature in Figure 2.20. An increase of the average Feret's diameter can be observed from 40 nm at 100°C up to 100 nm at 300°C. Moreover, a drastic drop of the grain number appears at annealing temperatures between 150°C and 200°C, together with an increase of the standard deviation. The increase of the standard deviation of the average grain size is due to the abnormal grain growth phenomenon, which leads to a bimodal grain size distribution as illustrated in Figure 2.21.

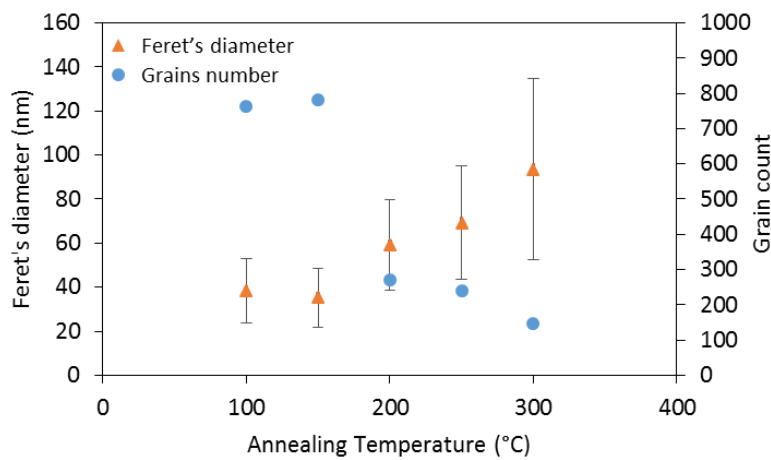


Figure 2.20. Evolution of Feret's diameter and grain number with the annealing temperature on 1 μm^2 AFM scans.

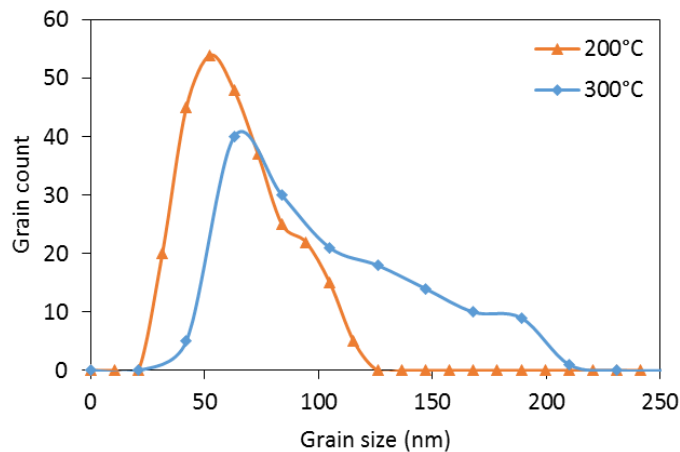


Figure 2.21. Grain size distribution on samples annealed at 200°C and 300°C during 1h.

The measured circularity of the grains, defined by (2. 5), is traced in Figure 2.22. The circularity estimator is between 0.7 and 0.9, meaning that the grain geometry can be likened to spherical objects. A slight decrease of the circularity appears for annealing temperatures higher than 250°C. This is consistent with AFM scans in Figure 2.18.d and e, where grains exhibit less circular shapes than in Figure 2.18.a, b and c.

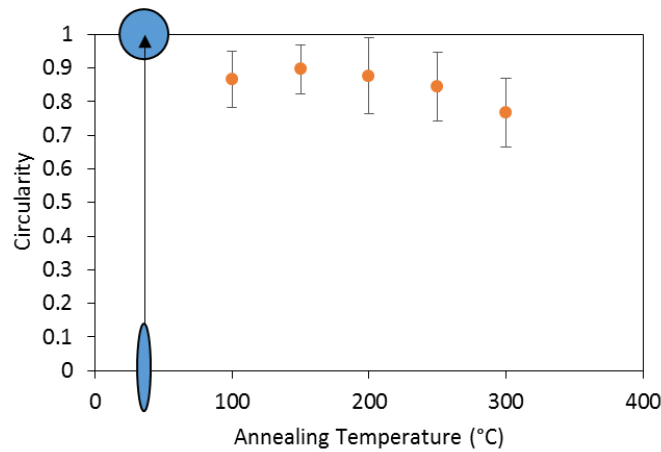


Figure 2.22. Evolution of the estimator “Circularity” as a function of the annealing temperature (Perfect circle = 1).

c) Roughness

Several parameters can be used to characterize surface roughness. The most commonly employed are R_a and R_{RMS} , namely the average and Root Mean Square roughness, that are calculated according to (2. 6) and (2. 7) (Whitehouse, 2011),

$$R_a = \frac{1}{N} \sum_{i=1}^n z_i \quad (2. 6)$$

$$R_{RMS} = \sqrt{\frac{1}{N} \sum_{i=1}^n z_i^2} \quad (2. 7)$$

where N is the number of pixels in the image and z_i the height value recorded for each pixel. For each AFM scan, the image processing protocol described in Figure 2.23 is applied. Roughness is related to the details (high frequencies) of the AFM scan, thus the Gaussian blurring is not applied. Moreover, only low frequency data and the high frequency noise coming from the scan are filtered with FFT (X and Y axis of the frequency domain).

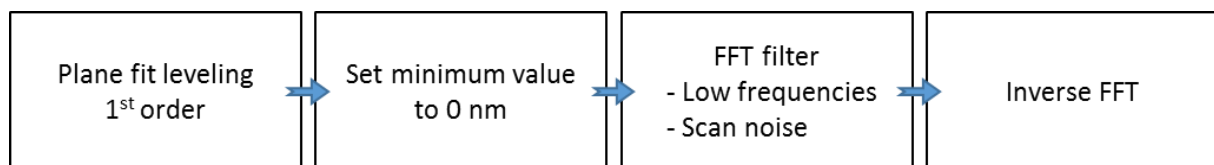


Figure 2.23. Image processing for roughness measurement.

The evolution of the roughness with the annealing temperature (Figure 2.24) is stable between 100°C and 200°C. A slight increase appears at temperatures up to 350°C. In this annealing temperature range, both estimators reveal low roughness of the printed silver layers surface, comprised between 5 and 11 nm. A severe increase of the roughness by at least one order of magnitude is measured for samples annealed at 450°C and 550°C.

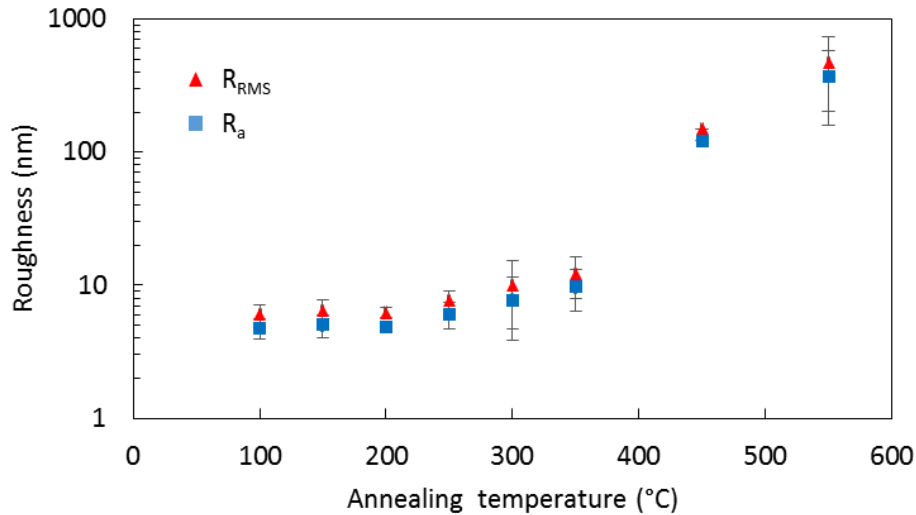


Figure 2.24. Roughness of the inkjet printed silver layers as a function of the annealing temperature.

d) Discussion

Grain morphology and surface roughness of the inkjet printed silver layers are strongly influenced by the annealing temperature. The investigation of the surface of the printed layers with AFM and image processing allowed a precise observation of the grain size and geometry, the roughness, and the occurrence of abnormal grain growth at temperatures higher than 200°C. For annealing temperatures in the range 100°C-300°C, AFM revealed well adapted for the analysis of the microstructure.

However, a major evolution of the microstructure occurs for annealing temperatures above 350°C, leading to grains diameter in the order of micrometers. As a consequence, further analysis of these samples is required. In Figure 2.25 is illustrated the height signal of an AFM scan over 5 μm x 5 μm of a sample annealed at 350°C during one hour. A single silver grain much larger and higher than the rest of the scanned area is observed, resulting from an abnormal grain growth.

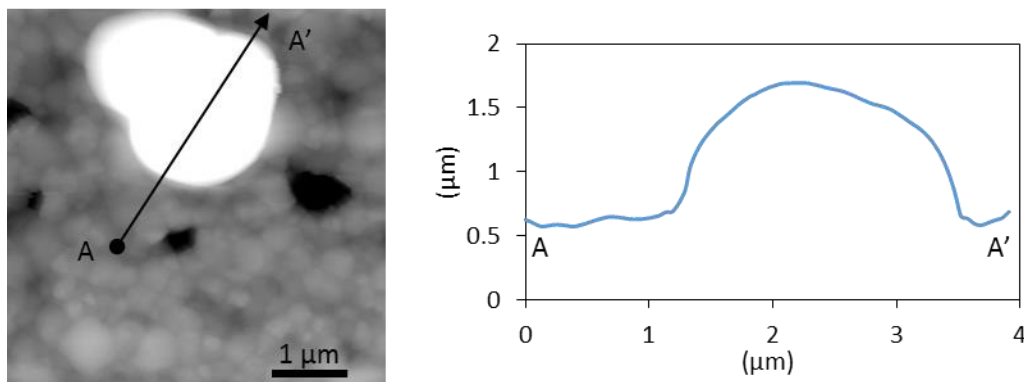


Figure 2.25. AFM scan of a silver sample annealed at 350°C during 1h.

AFM scans on samples annealed at 450°C and 550°C was not appropriate because of height variations up to 5 μm . As a consequence, the oscillating cantilever cannot follow the sample topography. However, SEM observation (Figure 2.26) of these samples is suitable.

On Figure 2.26, the layers have endured severe modifications. They become highly irregular with large holes where the substrate is deserted by the silver. Also, the grain size is in the order of microns, at least two orders of magnitude larger than the silver nanoparticles in the ink. FIB milling in these

samples shows that the silver grains have high density and that the thickness of the layer is made of single grains.

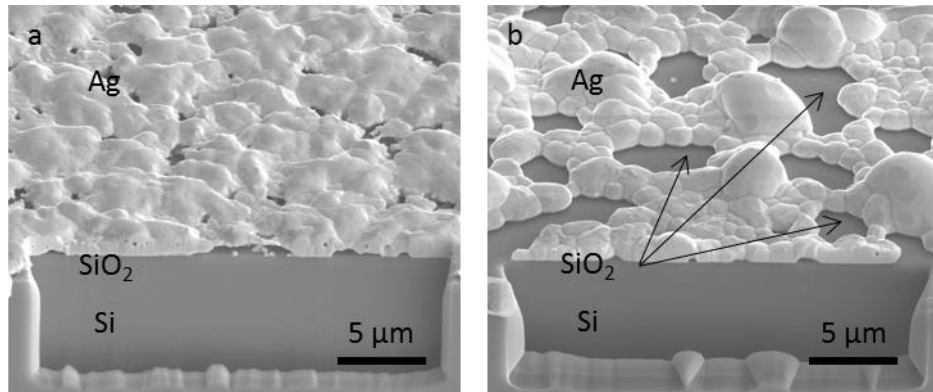


Figure 2.26. SEM observations of printed layers annealed at a) 450°C and b) 550°C with a 23 µm FIB milled window.

The observed desertion of silver material on the substrate is not only due to a lack of adhesion on the silicon oxide but also to the densifying transport mechanisms of the sintering process (chapter 1.IV.2). In spite of the observed desertion, electrical continuity of the pattern was verified at its center, while on the borders of the patterns grains are isolated (Figure 2.27). This is a consequence of the difference of neighboring droplets between the pattern borders and center: less material is deposited at the borders of the patterns.

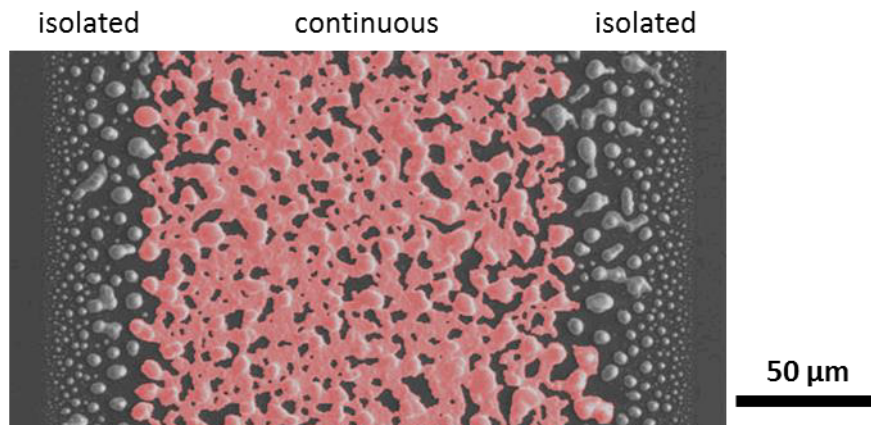


Figure 2.27. SEM observation of a silver line on SiO_2 substrate annealed at 550°C during one hour.

II.4. Porosity

Inkjet printed silver layers are the result of the assembly of nanoparticles whose mean diameter increases with annealing temperature. Their circularity was measured between 0.7 and 0.9. In a first approximation, if nanoparticles are considered spherical and with identical diameter, the best packing conditions would lead to a 26% porosity rate.

If morphological investigations of inkjet printed silver usually exhibit porous microstructures, to our best knowledge, few values of porosity or density are reported and considerable discrepancies can be noticed. As an example, on one hand, Jung *et al.* (2008) presented porosity rates between 0 and 5% for samples annealed between 100°C and 240°C during intervals from 0 up to 180 minutes. Their porosity measurements were realized in 2D on the samples surface. On the other hand, Cauchois *et al.* (2012) reported values of 54% and 34% for samples annealed respectively at 130°C and 300°C in

Rapid Thermal Annealing oven (RTA). These values were estimated with the Gibson and Ashby (1999) model from nanoindentation Young's modulus measurements.

The porosity of the printed silver layers was measured through FE-SEM observation of the layers cross-sections milled with FIB both in two and three dimensions. FIB milling revealed to be necessary because of the granular microstructure of the printed layers. In Figure 2.28 are illustrated the cross-sections of the same sample manually cleaved and FIB milled. The large roughness of the cleaved cross-section can be estimated in Figure 2.28.a, showing that this image is not appropriate for porosity measurements because pores disappear during the sample preparation. Whereas the FIB milled cross-section offers a very smooth surface where pores (dark) and silver grains (bright) areas can be discriminated.

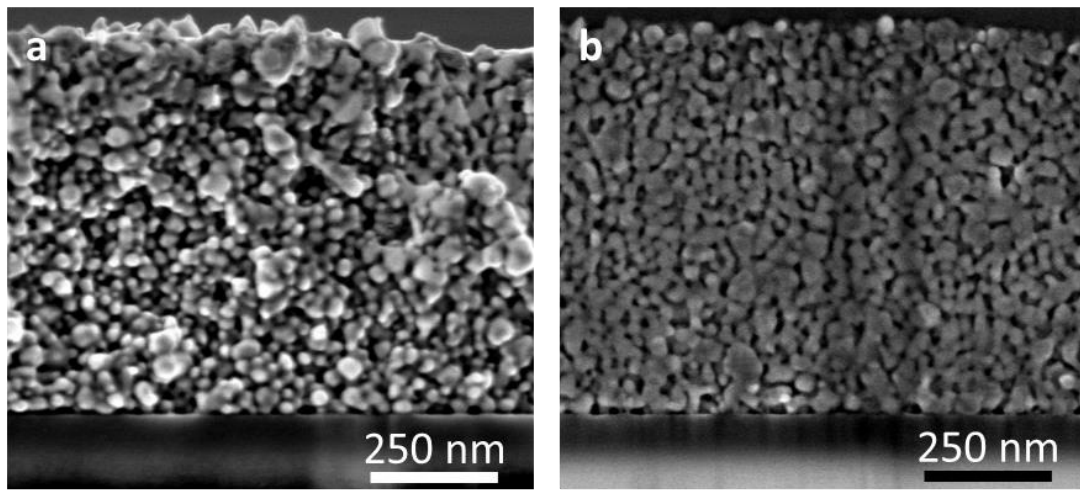


Figure 2.28. Cross-section of a silver layer annealed at 150°C during one hour. a) Manually cut. b) FIB milled.

a) 3D Porosity measurement

The technique employed for the 3D observation was FIB-SEM slice-and-view. Such a method, described in paragraph II.1.b), offers SEM resolution of 2 nm and the possibility to explore several μm^3 volume and thus provides a reliable statistical value.

The experiment was realized on a Zeiss Gemini N-Vision 40. Before milling, the deposition of a protective layer on the top of the sample is required. It was realized directly inside the FIB-SEM instrument and consisted in:

- A 200 nm thick silicon oxide layer from a tetraethyl orthosilicate gas precursor (TEOS);
- A 200 nm thick tungsten layer from tungsten hexacarbonyl gas precursor.

This protective layer has two major roles. Firstly, it prevents the surface of the ROI from being damaged by the ion beam as illustrated in Figure 2.29, where a local amorphization on the top of the printed silver layer might occur. Secondly, it lowers curtaining artifacts. Curtaining is a morphological imperfection on the milled cross-section caused by the irregularity of the FIB milling. This artifact is highlighted by lines parallel to the ion beam that appear in areas where there are large variations in material density or geometry (Bushby, 2011). Figure 2.30 shows examples of the curtaining phenomenon on two FIB milled samples without the protective layer.

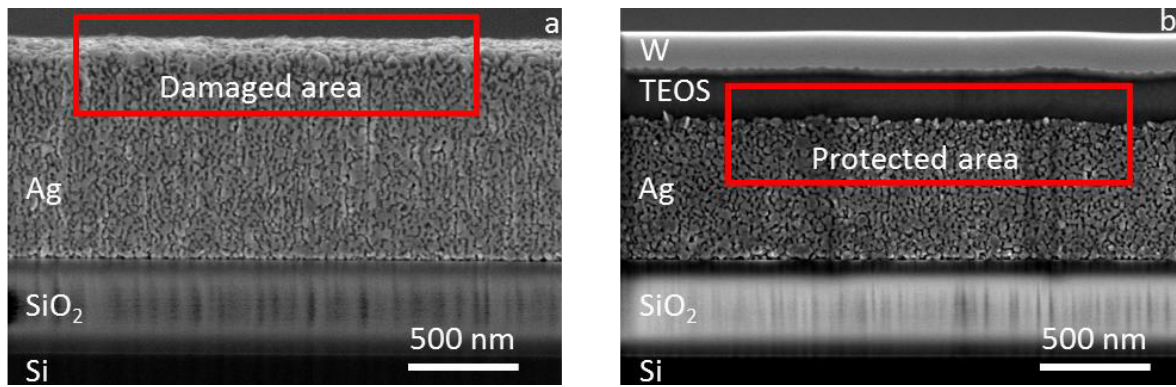


Figure 2.29. Effect of the protective layer on the FIB-cut cross-section (a. Without and b. with).

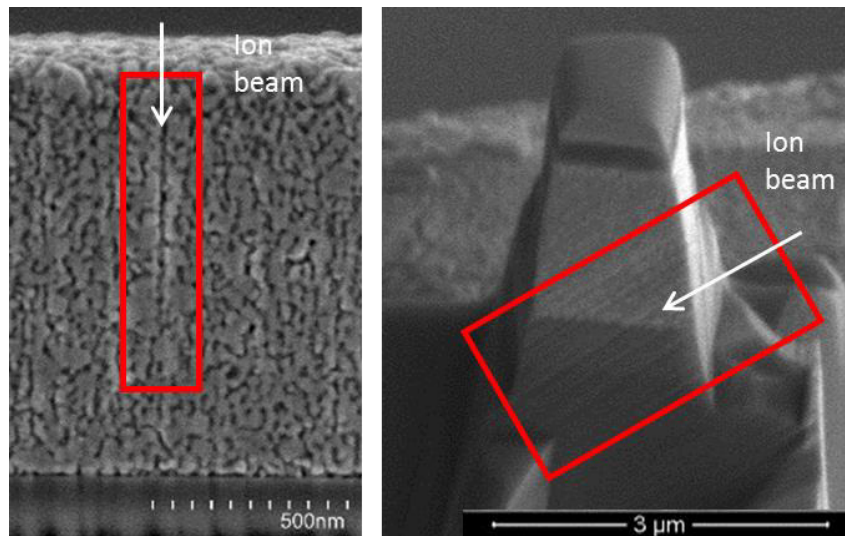


Figure 2.30. Curtaining phenomenon on inkjet printed samples.

Once the protective layer is achieved, the ion beam is set to a high current (>1 nA) to remove a slice of several microns on the cross-section of the sample in order to step away from the cleaved cross-section that may have been damaged or contaminated. The ion beam is then set to very low current (< 10 pA) to remove slices of 1 nm. Finally, milling (FIB) and observation (SEM) steps are switching to acquire the data.

Once data is acquired, each slice is aligned with a linear stack alignment SIFT algorithm (Lowe, 2004) embedded in ImageJ software. Finally, the image processing protocol described in Figure 2.31 is applied to discriminate silver from pores.

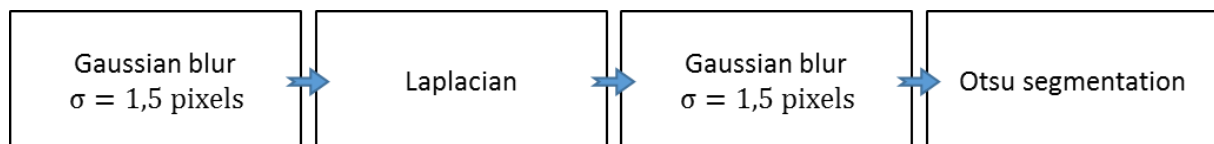


Figure 2.31. Image processing for 3D analysis of the slice-and-view data.

b) 2D porosity measurement

Samples were prepared in the same way as for the 3D measurement with a coating of TEOS and Tungsten. An approximately 20 μm long window was milled on a FEI Strata FIB. Then the milled areas of each sample were observed with a FE-SEM Hitachi 5500. The image processing described in

Figure 2.31 is applied and the 2D porosity can be estimated. The analyzed data is composed of a dozen of images acquired along the 20 μm window.

c) Results

The slice-and-view method is time consuming and requires a shift of 24 hours on the FIB-SEM. Only one sample was analyzed with this method: a silver layer annealed at 250°C during one hour. Three hundred 1 nm thick slices were milled and observed. One slice is illustrated in Figure 2.32.

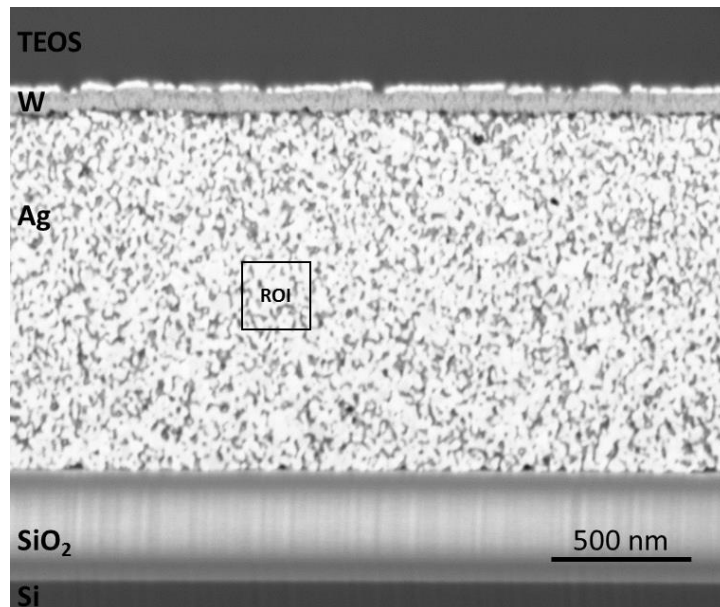


Figure 2.32. One slice of the slice-and-view 3D observation of a sample annealed at 250°C during 1 hour.

Slice alignment and image processing led to a 3D reconstruction of the milled volume of the silver sample. In Figure 2.33 are illustrated the orthogonal views of a segmented volume of 600x500x300 nm^3 . The fact that the images in the XY, XZ and YZ planes have similar structures means that the alignment, the image processing and the reconstruction of the volume are reliable.

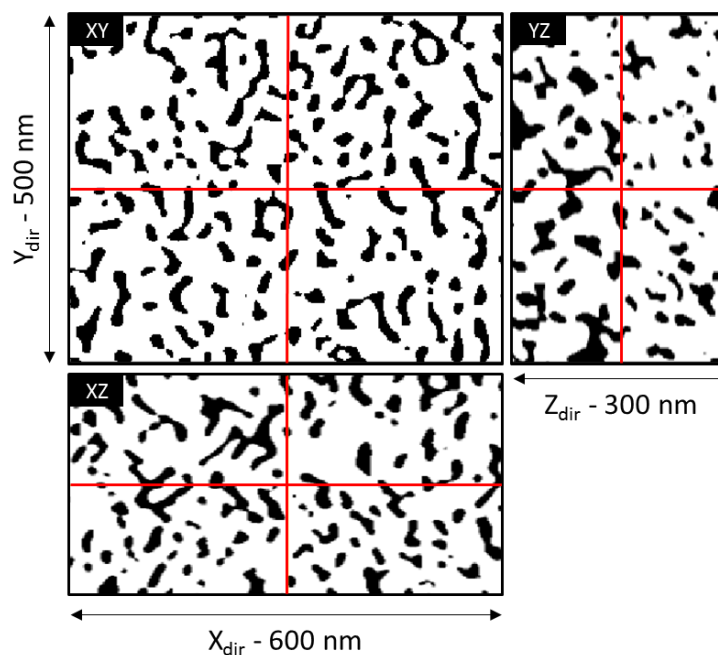


Figure 2.33. Orthogonal view of the segmented data. Volume of the sample: 600x500x300 nm^3 .

The 3D representation of the ROI is illustrated in Figure 2.34 with the silver and the pores. Several information can be extracted from this result:

- Porosity: 25%.
- Pores shape is random and does not have preferential orientation.
- Pores are communicating, meaning that the silver layer is permeable to fluids. This property is also confirmed by the 3D count of objects, which is limited to 7 objects in $0.5 \mu\text{m}^3$. Object counting was realized with the “3D Objects counter” plugin in ImageJ (Bolte, 2006), ignoring objects at the borders.

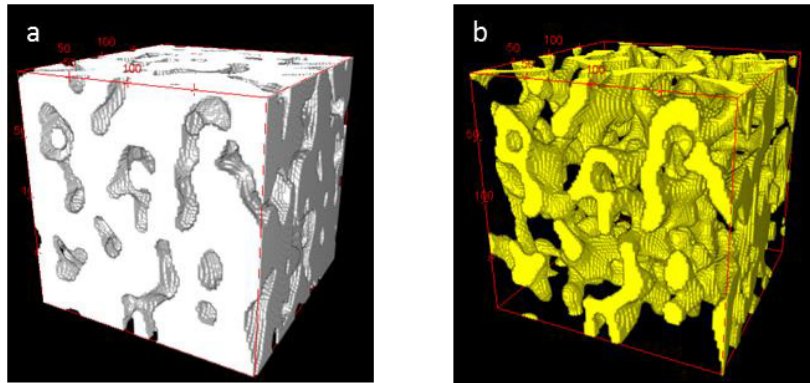


Figure 2.34. 3D representation of a 200 nm-side cube of a sample annealed at 250°C - 1 hour. a) Silver. b) Pores.

The porosity of the other silver printed samples, annealed in the range 100-300°C, was measured in two dimensions as described in paragraph II.4.b). The evolution of the porosity is traced as a function of the annealing temperature in Figure 2.35. In this graph, the values at 250°C measured both in 2D and 3D are almost the same. Thus the measurement of the porosity in 2D averaged on several images seems to be representative of the porosity of the analyzed medium.

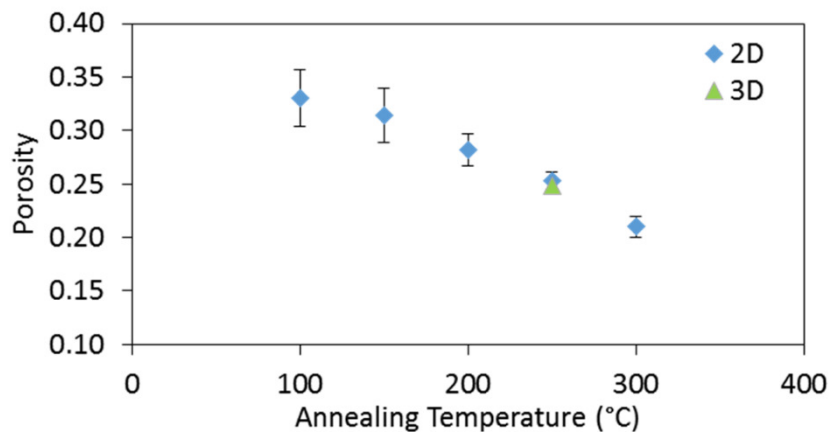


Figure 2.35. Evolution of the porosity in inkjet printed silver layers as a function of the annealing temperature.

The porosity decreases with the annealing temperature from 35% to 20%, meaning that the silver layers density increases. In the 2D measurements of the porosity, the pores dimensions increase while their number decreases. The pores distribution size evolves in the same way as the grains do. SEM imaging of FIB milled cross-sections allowed an accurate measurement of the porosity of printed silver layers. However, the employed protocol has two main drawbacks that must be considered. The first is that this technique is destructive and the second is that SEM imaging does not provide enough grain boundary contrast. Indeed, with an increased grain boundary contrast, the same measurements would

have resulted in the 3D reconstruction of the grains, offering more information on their dimensions and geometry. An alternative method to acquire more 3D information would be tomography. However, X-Ray tomography best resolution is of about 100 nm, which is not appropriate for nanoparticles. Electronic tomography realized on Transmission Electron Microscope (TEM) is a suitable candidate, however the analyzed samples must be smaller than 300 nm, hindering statistical results.

II.5. Thickness

The silver layer thickness was measured on the central square of a van der Pauw printed pattern (Figure 2.36) using an optical Wiko interferometer. This technique offers sub-nanometer resolution in the Z direction, and micrometer resolution in X and Y directions. The thickness of the printed layer is rather inhomogeneous because of the inkjet printing process: thin borders and thick center (Figure 2.36). Thus, an average thickness, defined by the ratio of the printed pattern volume to its surface, is calculated.

It has to be mentioned that the sample was covered with a 10 nm sputtered platinum layer. This is necessary for an accurate measurement because the silicon oxide substrate and the silver do not have the same refractive index.

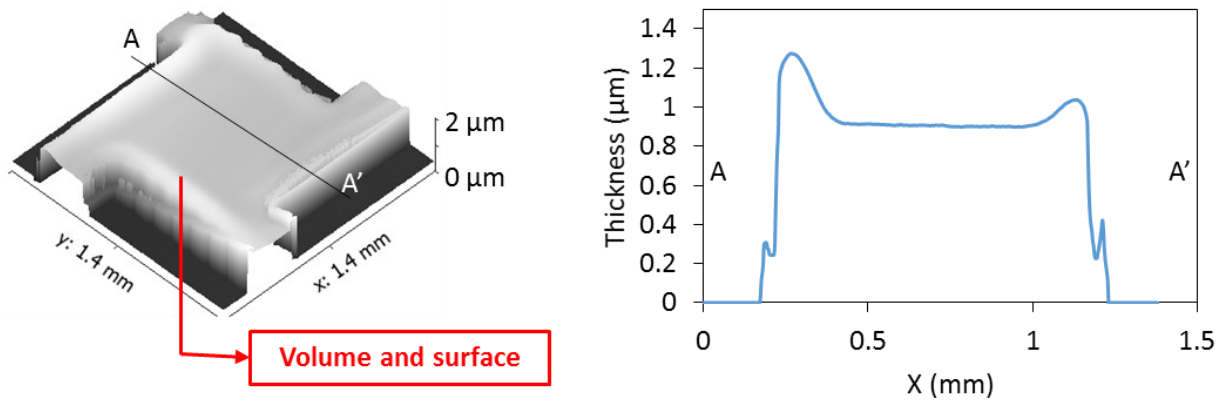


Figure 2.36. Thickness measurement of the van der Pauw pattern by optical interferometry.

In Figure 2.37 the measured thickness (round dots) is traced as a function of the annealing temperature. A decrease of the thickness can be observed, corresponding to a densification of the silver layers.

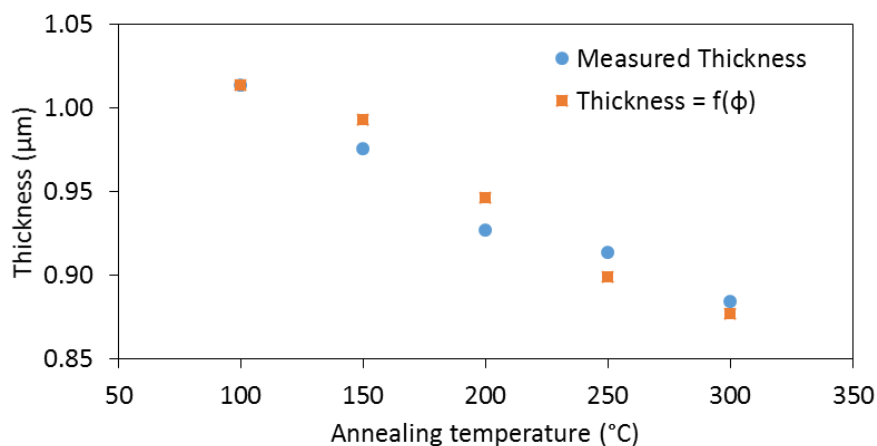


Figure 2.37. Average thickness of the silver printed layers.

In paragraph II.4.c, measurements of the porosity have also shown a densification of the silver layers with the increase of the annealing temperature. The porosity values can be correlated with the measured thickness with (2. 8) taking the measured thickness of the sample annealed at 100°C as a starting point.

$$t_i = t(100^\circ\text{C}) * (1 - (\phi_{i-1} - \phi_i)) \quad (2. 8)$$

where t_i is the calculated thickness and ϕ_i the measured porosity. The calculated thickness is plotted in Figure 2.37 (square dots). The measured and calculated thicknesses exhibit very similar values and behavior with the annealing temperature.

This comparison is of particular interest because it corroborates the porosity measurement which is strongly dependent on the image processing applied to the data, and particularly on the segmentation algorithm.

II.6. Summary

The microstructure of the inkjet printed silver layers was studied in depth as a function of the annealing temperature in the range 100°C - 300°C. Above 300°C, the microstructure of the layers endures drastic transformations, where grains diameter exceed micron size, the silicon oxide substrate is deserted because of poor affinity between the two materials and the areas with less deposited materials (less droplets) even become non-conductive because of grain segregation.

In the range of annealing temperature between 100°C-300°C, which is by the way compatible with most of flexible organic substrates and most of back-end processing in silicon technologies, the silver layers offer the following features:

- Average grain size increases from 40 nm to 100 nm.
- Grain circularity is between 0.7 and 0.9 and slightly decreases with the annealing temperature.
- Roughness (R_a and R_{RMS}) is lower than 10 nm.
- Porosity decreases from 35% to 20%.
- Thickness decreases from 1.05 μm to 0.88 μm .

The silver printed layers revealed a porous and polycrystalline microstructure with typical dimensions below 100 nm. The precise measurement of the macroscopic porosity was achieved both in 2D and 3D thanks to FIB-SEM imaging. This provided original information regarding the pores: geometry, size, communicating network.

In the following sections, a thorough characterization of the electrical conductivity, Young's modulus and Hardness of the silver layers is carried out. The microstructural results will be related to the electrical and mechanical properties of the silvers layers.

III. Electrical properties

III.1. Electrical resistivity

a) Measurement

The electrical resistivity of the printed silver layers was measured on van der Pauw (1958) printed patterns (Figure 2.38). The advantage of these cross-shaped patterns, commonly employed in microelectronics, is that the electrical resistivity of the layers can be determined with only two measurements, namely the layer thickness t_{exp} and the pattern resistance R_{exp} . From these experimental results, the electrical resistivity is calculated with equation (2.9).

$$\rho_{exp} = \frac{\pi t_{exp}}{\ln 2} R_{exp} \quad (2.9)$$

The resistance of the van der Pauw printed patterns was measured with a four point method by mean of rhodium spring probes with 20 μm radius of curvature on a PM8 manual prober. These probes are less aggressive than standard tungsten test probes. The spring probes were selected to prevent damaging of the patterns as they allow a better control of the applied contact force.

The electrical measurement setup is illustrated in Figure 2.38. The four point method is realized by applying a DC current of 0.1 mA by a Keithley 2400 source while the voltage is measured by a nanovoltmeter Keithley 2181a.

This electrical setup was chosen because the silver layers are expected to have a resistivity lower than $10^{-6} \Omega \cdot \text{m}$:

- The DC current supply at 0.1 mA prevents the layer from self-heating because of Joule effect power dissipation.
- The nanovoltmeter has a resolution of one nanovolt and a systematic error of 25 ppm for measurements lasting less than 24 hours. These characteristics allow accurate measurements of resistance values lower than 1Ω .

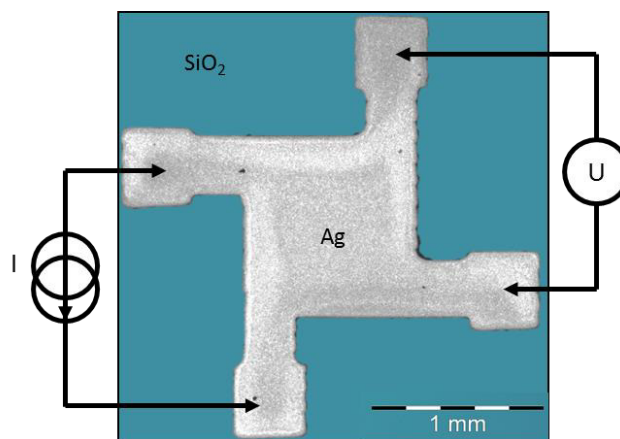


Figure 2.38. Electrical setup of the resistance measurement of the van der Pauw patterns.

b) Results

The resistance of the van der Pauw patterns, averaged on 25 measurements, is plotted as a function of the annealing temperature in Figure 2.39 (square dots). From the resistance and the thickness measurement (please refer to paragraph II.5), the electrical resistivity of the silver layers is calculated with (2.9) and traced in Figure 2.39 (round dots).

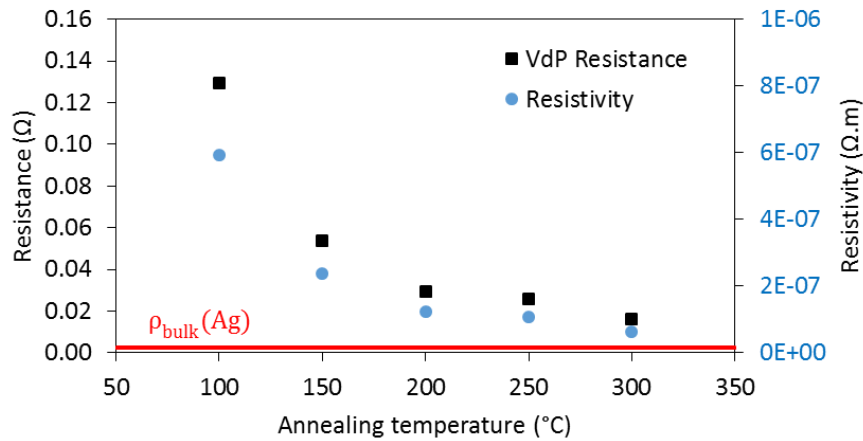


Figure 2.39. Resistance (a) and electrical resistivity (b) evolution of van der Pauw patterns as a function of the annealing temperature.

The electrical resistivity of the inkjet printed silver layers decreases with the annealing temperature in the range 100°C – 300°C. The standard deviation of the measurements is lower than 1%, thus error bars are not visible on the graph.

c) Discussion

The electrical resistivity drops with the annealing temperature and approaches the silver bulk value at annealing temperatures as low as 300°C. In this paragraph, the aim is to understand the physical phenomena leading to this resistivity decrease.

According to the conduction models introduced in chapter 1, our results cannot be fully described by Ohm's law. Indeed, the electrons mean free path in silver (53 nm) is in the same order of magnitude than the grain size.

Fuchs-Sondheimer (FS) and Mayadas-Shatzkes (MS) models describe the influence of electron scattering on the electrical resistivity of thin films, respectively at surfaces and grain boundaries. The FS model depends on the thickness, that can be measured, and a specular parameter p . The MS model depends on grain size, that can be measured, and the reflection coefficient R at grain boundaries. In Figure 2.40 are traced the electrical resistivity predicted by the FS model (equation (1. 13)) and by the MS model (equations (1. 15) and (1. 16)) as a function of their respective parameters. It must be noted that the curve for $p = 1$ in Figure 2.40.a is hidden by the bulk curve; indeed in equation (1. 13) $\rho(p = 1) = \rho_0$.

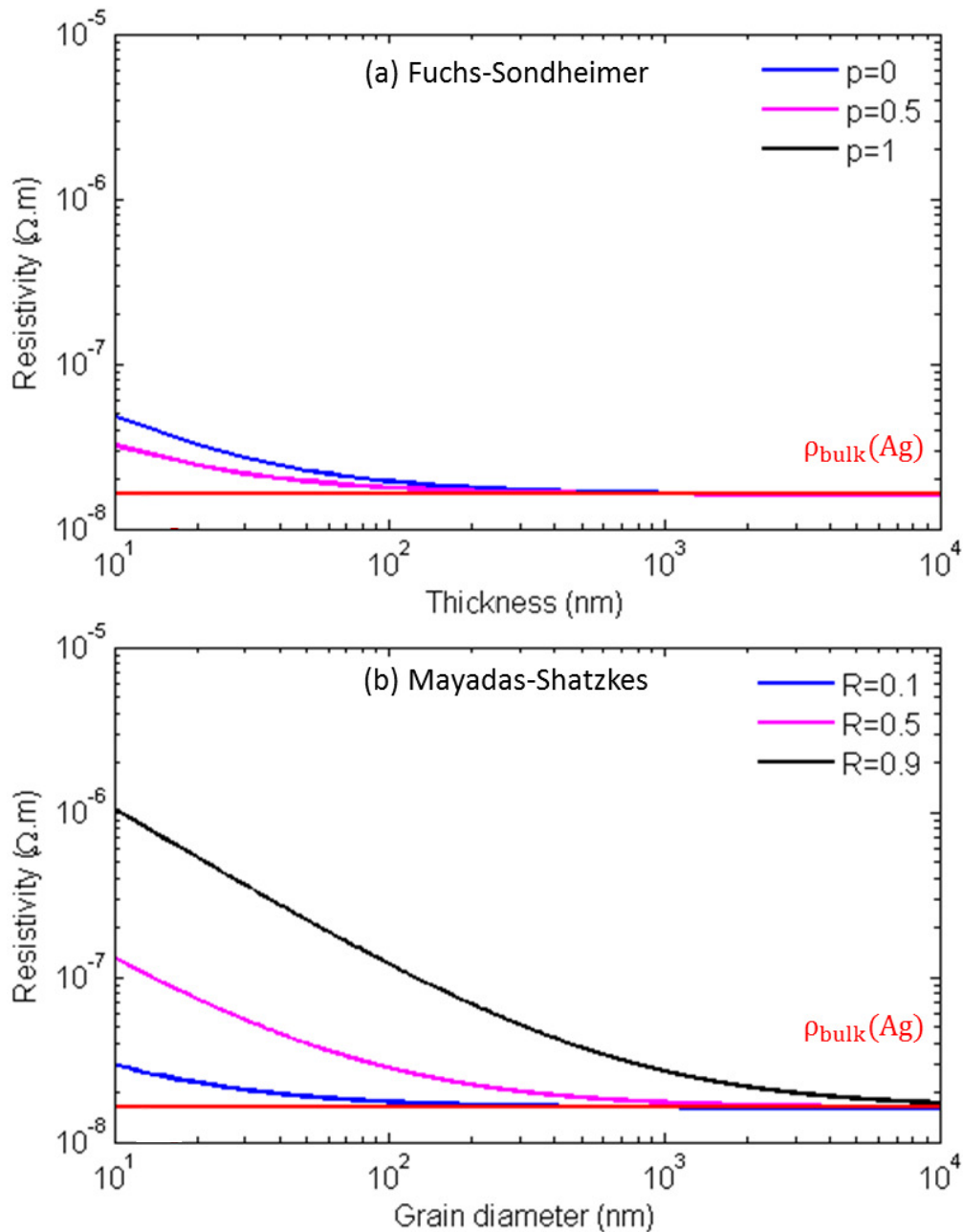


Figure 2.40. Theoretical electrical resistivity predicted by the FS and MS models.

Figure 2.40 shows that according to the FS model, the influence of the specular parameter p can be neglected for thicknesses around one micrometer, corresponding to the studied silver layers. However, the MS model curves illustrate that the influence of the reflection coefficient R has a strong impact on the resistivity value in the range 10-100 nm, which corresponds to the dimensions of the silver grains for annealing temperature lower than 300°C (cf. Figure 2.20).

The dimensions of the studied inkjet printed silver layers (thickness and grain diameter) are in agreement with the boundary conditions of the extended model of MS (1970), where surface scattering and grain boundary scattering are considered independent and Matthiessen's rule is valid. The measured resistivity is traced as a function of the annealing temperature in Figure 2.41 as well as the resistivity predicted by the extended model of MS (equations (1. 17) and (1. 18)).

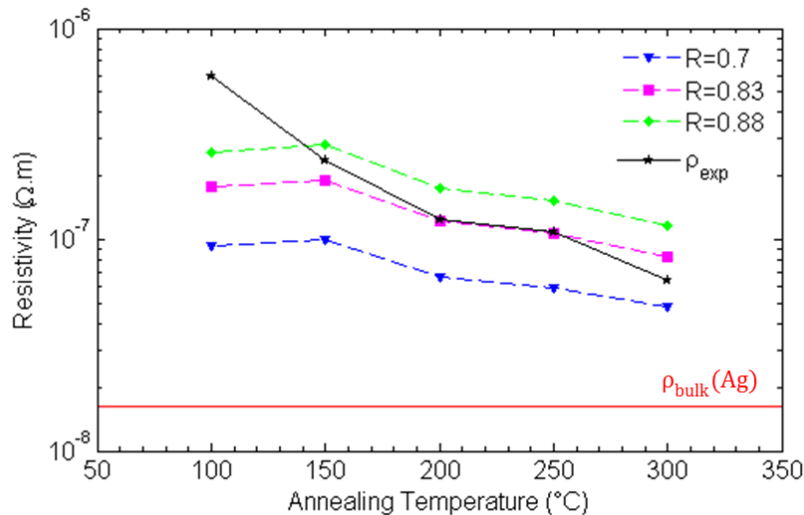


Figure 2.41. Experimental resistivity as a function of the annealing temperature compared to the extended MS model calculated with experimental thicknesses and grain diameters.

The specular parameter p was set to 0.3, even though its influence can be neglected for thicknesses above 200 nm. The experimental data for annealing temperatures higher than 150°C fit to the extended MS model for a reflection coefficient R between 0.7 and 0.88. The best fit is obtained for $R = 0.83$. This value is higher than those found in the literature.

To our best knowledge, few values of p and R for thin silver films are reported. De Vries (1987) gives a value $R = 0.24$ for high vacuum evaporated silver. Zhang (2004) also supposes a R value lower than 0.46 for evaporated silver. When looking at other metals such as copper and gold, more data are available in the literature. For example, Zhang (2004) reports R values between 0.38 (evaporated) and 0.8 (Chemical Vapor Deposition, CVD) for copper. According to Zhang, this large range seems to depend on the deposition technique, resulting in different types of grain boundaries and impurity rates.

The printed layers have a different microstructure and chemical composition from evaporated, sputtered or CVD thin films. The main differences reside in the porosity and the carbon contamination coming from ink additives. Indeed, in standard microelectronics processes the impurity rate is well-controlled and usually very low thanks to vacuum processing.

The large deviation between experimental and modeled values at annealing temperatures of 100°C can be attributed to the presence of impurities in the silver layer and especially at the grain boundaries, coming from the polymeric coating of the nanoparticles. Volkman (2011) has observed a strong endothermic response at 132°C of annealed silver nanoparticles coated with thiol chains. This response corresponds to the melting of the nanoparticles coating. In the same work, Thermal Gravimetric Analysis (TGA) shows that the mass of silver layers starts decreasing at around 200°C, corresponding to the burning-out of organic impurities from the layer.

For annealing temperatures above 150°C, experimental deviations with the extended MS model are less significant. However, it is genuine to suppose that the pores, whose dimensions are of the same order of magnitude as the grains and the electrons mean free path, have an influence on the resistivity. Assuming that the effective resistivity of a bulk porous silver is higher than a fully densified silver, equations (1. 17) and (1. 18) predict that the reflection coefficient R would be lower than the obtained values.

III.2. Temperature coefficient of resistance

The temperature coefficient of resistance (TCR) is an intrinsic property of a conductive element that relates its resistance R to its temperature T . It can be extracted from experimental data using equation (2. 10). For temperatures between -70°C and the melting temperature of the material, the TCR is usually constant.

$$R(T) = R_0(1 + \alpha(T - T_0)) \quad (2. 10)$$

where α is the TCR, expressed in $\text{ppm}/^{\circ}\text{C}$, and R_0 the resistance at room temperature T_0 . Equation (2. 10) shows that the electrical measurement of the resistance variation allows monitoring environmental variations for sensing applications (temperature, pressure, flux).

a) Samples

In order to achieve an accurate measurement of the TCR of inkjet printed silver layers, the pattern in Figure 2.42 was printed 24 times on a 200 mm silicon wafer with a $2\ \mu\text{m}$ thick thermal silicon oxide.

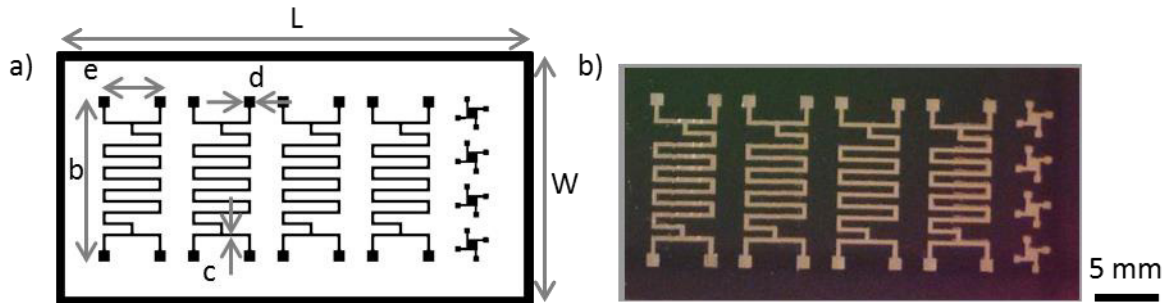


Figure 2.42. Test pattern for TCR measurement. a) Dimensions. b) Printed pattern annealed at 200°C during 1 hour.

Each pattern is made of four serpentine resistors whose dimensions are detailed in Table 2.3. There are also four $1\ \text{mm}^2$ van der Pauw patterns for resistivity measurements, however they are not used in this part of the study.

After printing, the whole wafer was dried in an oven at 60°C during one hour. Finally, the wafer was cut and the printed samples were annealed in an oven during one hour at different temperatures between 150°C and 350°C .

Table 2.3. Dimensions of the test pattern.

b	12.7 mm	e	5.3 mm
c	0.3 mm	L	42 mm
d	1 mm	W	22 mm

b) Thermal expansion

In a first order approximation, one can neglect the influence of thermal expansion of the silicon oxide layer on the silver printed layer and consider only the influence of the silicon substrate expansion. The strain ε in the printed film caused by thermal expansion of the substrate is given by (2. 11).

$$\varepsilon = (\alpha_{Ag} - \alpha_{Si}) \cdot \Delta T \quad (2. 11)$$

where α_{Ag} and α_{Si} are the respective coefficients of thermal expansion of bulk silver and silicon. In Table 2.4 are reported the values of stress and strain calculated from literature values of bulk silver material and silver films for temperature variations of 100°C , which corresponds to the length of the

explored range for TCR measurement. The yield strength σ_e was calculated from hardness H values given by Slade (1999) using Tabor' relationship $H = 3\sigma_e$.

Table 2.4. Thermal expansion of silver for $\Delta T = 100^\circ\text{C}$.

	Coeff. of thermal expansion	Young's Modulus	Yield strength	Stress $\Delta T = 100^\circ\text{C}$	Strain $\Delta T = 100^\circ\text{C}$
Bulk Si (Rebeiz, 2003)	2.6 ppm/ $^\circ\text{C}$	162 GPa	2.6 – 6.8 GPa	130 MPa	0.08%
Bulk Ag (Gibson, 1997)	19.7 ppm/ $^\circ\text{C}$	76 GPa	55 MPa	130 MPa	0.2%
Film Ag (Slade, 1999)	19.7 ppm/ $^\circ\text{C}$	79 GPa	100 – 230 MPa	130 MPa	0.2%

The values in Table 2.4 show that in the case of bulk silver, usually made of large grains with diameters in the range 1-100 μm , the elastic limit would be exceeded. However, in silver films the grains are much smaller (diameter lower than 1 μm) and the elastic limit increases. As a consequence, we can consider that in the explored temperature range, the silver printed films do not endure any plastic deformation.

c) Experimental setup and protocol

The measurement of the TCR requires an accurate measurement of both the resistance variation and the sample temperature, which has to be homogeneous and stable. The sample temperature was controlled with a programmable benchtop temperature forcing system (Flex TC from Mechanical Devices), allowing temperature variations up to 50 $^\circ\text{C}/\text{min}$ between -50 $^\circ\text{C}$ and 150 $^\circ\text{C}$. The sample under test was held on the thermal module with thermal grease on a contact area of about 3 cm^2 , which guarantees a fast thermal equilibrium compared to ovens (a few minutes).

The resistance of the sample was measured with Copper-Beryllium probes, which offer both a low electrical contact resistance and an elastic behavior. The resistance variation was measured by a four point electrical method with a Keithley 2182A nanovoltmeter and a DC current source set at 1 mA (Keithley 2400). The DC current supply at 1 mA prevents the material from self-heating by Joule effect. The temperature at the sample surface was measured by a PT100 temperature probe connected to a Keithley 2700. The experimental setup is illustrated in Figure 2.43.

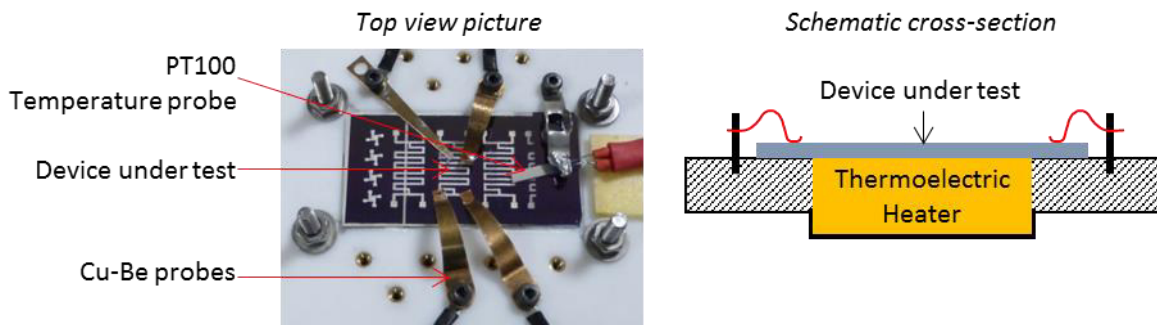


Figure 2.43. Experimental setup for the TCR measurements.

The first measurements were realized in air and condensation phenomena were avoided by applying temperatures higher than 25 $^\circ\text{C}$. Thermal steps of four minutes between 25 $^\circ\text{C}$ and 75 $^\circ\text{C}$ were applied while the resistance was measured. For temperatures higher than 75 $^\circ\text{C}$, a slow decrease of the resistance was observed, and attributed to the gradual sintering of the silver nanoparticles. The TCR was measured on decreasing temperature steps because slight variations of the resistance during

increasing temperature steps were observed. Figure 2.44 illustrates the simultaneous measurement of the resistance and the temperature for a sample annealed at 250°C during one hour. On this curve, it can be observed that the resistance variation follows the target temperature. The spikes at the beginning of the steps are due to temperature feedback regulation.

To extend the temperature measurement range, a hermetic chamber was developed. The chamber was mounted around the experimental setup allowing measurements under a nitrogen flux with an over pressure of 100mbar. A hygrometer placed inside the chamber shows that the relative humidity drops down to 1% in less than 5 minutes. Such configuration of the setup allowed measurements in a temperature range from -25°C up to 75°C without any condensation on the samples surface.

It was shown in paragraph II.4 that the inkjet printed silver layers exhibit a porous structure and thus a capacity to absorb water molecules. As a consequence, in the nitrogen flux configuration, the samples were heated at 75°C during 30 min in the chamber before the TCR measurement to degas the silver layers. Also, the soaks duration was extended from 4 min in air to 10 minutes in nitrogen because of a longer thermalization period.

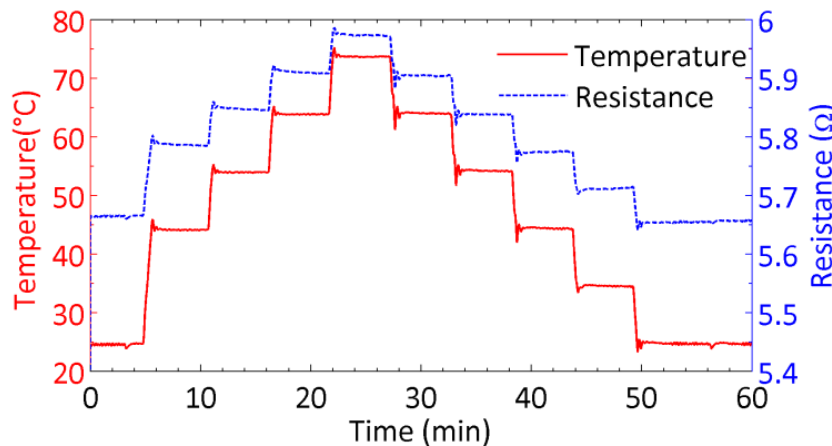


Figure 2.44. Temperature and resistance measurement in air of a sample annealed at 250°C during 1 hour.

d) Results

For each annealing temperature, three different resistors were measured. In Figure 2.45 are reported the extracted TCR values from the linear fit of the experimental data. Standard deviation is lower than 10% demonstrating the accuracy and repeatability of the measurements. After thermal cycling, microscopy investigation of the printed layers surface did not reveal any cracks or delamination.

The determination of the TCR is done through the linear fit of the relative resistance variation $\Delta R/R$ as a function of the sample temperature, traced in Figure 2.46. The TCR value is given by the slope of the curve. The curves in Figure 2.46 have the expected linear behavior predicted by (2. 10) both in air and nitrogen, and the coefficient of determination R^2 of the linear fit is higher than 0.99.

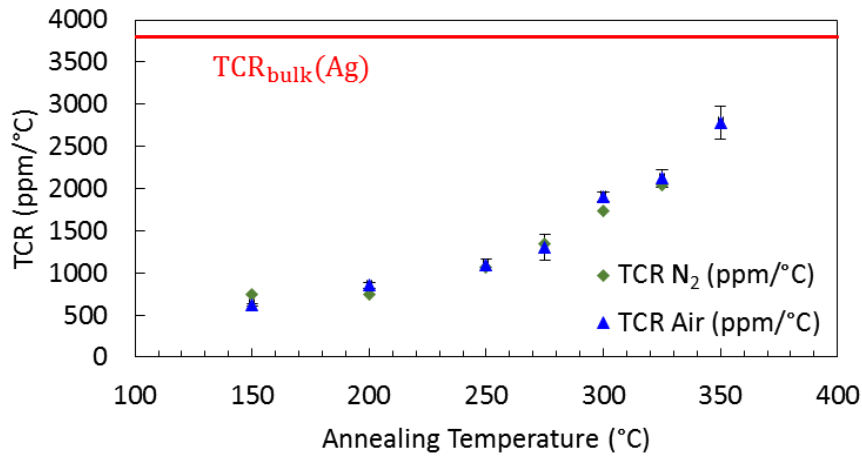


Figure 2.45. Evolution of the TCR with annealing temperature.

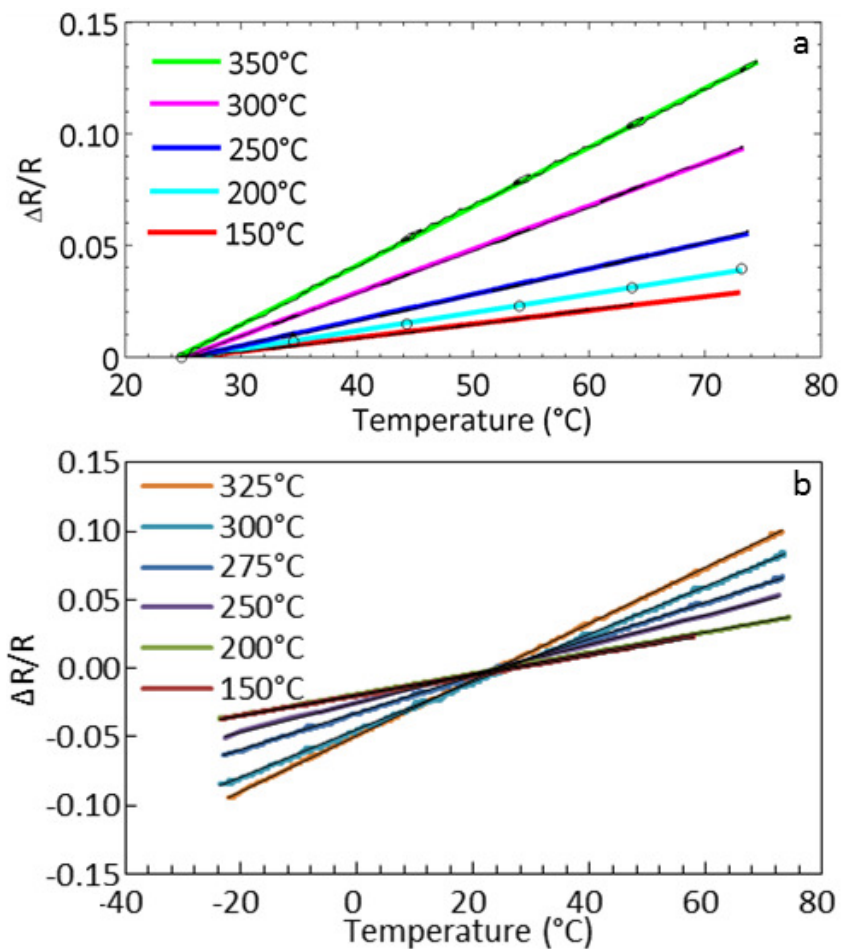


Figure 2.46. Relative resistance variation as a function of temperature for different annealing temperatures. Experimental (black lines and dots) and fitted data (color lines). Measurement in air (a) and under nitrogen (b).

Finally, the influence of the annealing time on the TCR was explored at 150°C (Figure 2.47). This temperature was chosen because it is compatible with most of plastic substrates. This curve shows that the TCR increases with the annealing time, although it seems to reach a limit value around 900 ppm/°C, which is about 4 times lower than the bulk value. This limit value is probably caused by the reach of a steady state of the silver microstructure after a several hours annealing at a given temperature (150°C).

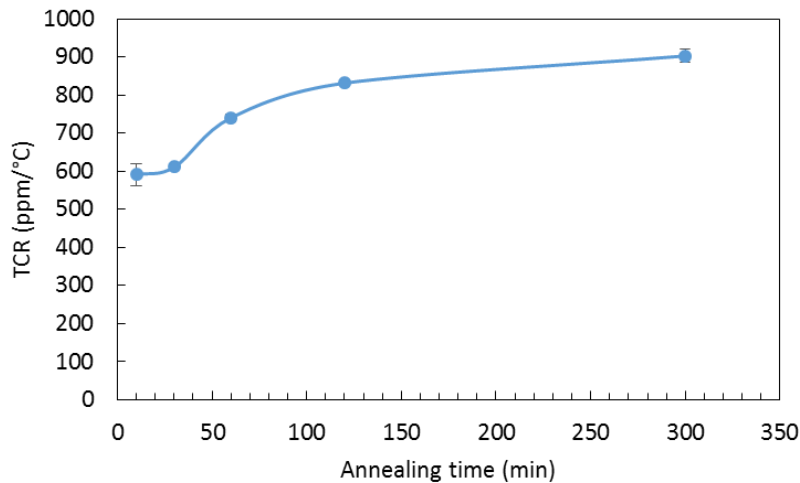


Figure 2.47. TCR of inkjet printed silver as a function of the annealing time at 150°C.

e) Discussion

The TCR increases with the annealing temperature and reaches 75% of the silver bulk value for the samples annealed at 350°C. Also, the measurements performed under the nitrogen flux show that the TCR value is stable in the range -25°C – 75°C, with values similar to those measured in air during the cooling process. Further investigations in controlled hygrometry atmospheres should bring major information on the effect of water absorbed by the silver layers.

The measured values are in agreement with measurements of other works, reported in Table 2.5. The comparison to the reported values of TCR shows that variations of the TCR can be attributed to several parameters: silver nanoparticles initial dimensions, annealing time and temperature, substrate, addition of tuning (Ni) or capping materials (parylene).

Several studies (Singh, 1974; Pichard, 1983; Zhang, 2006) demonstrated that the TCR depends on the same electron scattering mechanisms that govern the electrical resistivity. Moreover, Deschacht and Boyer (1985) have related the TCR of thin films to the mechanical constraints in the thin film generated by the difference of thermal expansion between the substrate and the film itself. Thus, when comparing the TCR values of the printed silver layers, the substrate nature has also to be considered.

Models based on the Mayadas-Schatzkes theory for electron scattering in thin films have been developed to study the TCR of thin films (Tellier, 1977). It would be interesting to apply these models to the experimental data presented so far.

Table 2.5. TCR of inkjet printed silver layers reported from literature (non-exhaustive list).

Reference	Sample	Substrate	TCR
Slade, 1999	Bulk silver	-	3800 ppm/°C
Sette <i>et al.</i>, 2013 (Transducers 2013)	Inkjet printed silver (SunChemical EMD5714) annealed at 150°C, 5h	Kapton HN 75 μm, Dupont	910 ppm/°C
Courbat <i>et al.</i> , 2011	Inkjet printed silver (DGP 40LT-15C , Anapro) with parylene coating annealed at 150°C, 1h	pe:smart paper type 2, Felix Schoeller	1100 ppm/°C
Molina-Lopez <i>et al.</i> , 2012	Inkjet printed silver (DGP 40LT-15C, Anapro) annealed at 150°C, 30 min Same sample with Ni electrodeposition	PET, Melinex ST506, Dupont	630 ppm/°C 4300 ppm/°C
Felba <i>et al.</i> , 2009	Inkjet printed silver (4-10 nm nanoparticles) annealed at 250°C, 1h	Microscope glass slides	2080ppm/°C
Tao <i>et al.</i> , 2013	Organic silver conductive ink (OSC ink) annealed at 120°C, 30s	PET	700 ppm/°C

III.3. Summary

The evolution of both the electrical resistivity and the temperature coefficient of resistance of inkjet printed silver layers on a SiO₂/Si substrate was investigated as a function of the annealing temperature in room atmosphere.

The electrical measurements on metallic layers require an appropriate method and protocol because of the low resistivity values. In particular, a dedicated test bench was developed and improved to measure the TCR of the printed silver both in air and nitrogen atmospheres.

Electrical resistivity and TCR increase and almost reach silver bulk values. Such behavior was related to the microstructural properties of the printed layers (thickness, grain size, and porosity). The analysis of the experimental results through models from the literature and the microstructural characterization offers an accurate understanding of the physical phenomena driving electron transport in the silver printed layers.

IV. Mechanical properties

The mechanical properties of the inkjet printed silver layers were measured by nanoindentation with a Berkovich diamond tip on the DCM column of a nanoindenter (MTS Systems Corporation, XP model).

Nanoindentation measurements are very sensitive to building noise and thermal variations. Moreover, surface contamination such as dusts and water can highly influence the mechanical response of the sample analyzed. The nanoindentation measurements were realized during the night in a closed room at ambient temperature. To decrease the influence of surface contamination, at least 20 indents with 50 μm spacing were realized for each sample. Eventually, discrepant load-indentation depth curves were eliminated for the results analysis. All the results presented in this part are averaged over the adopted measurement curves.

Finally all the measurements were realized following the standard method of the DCM column (high resolution). The main experimental parameters are:

- \dot{P}/P is constant, (where P = applied load).
- The CSM harmonic load is set at 1 nm amplitude oscillations.
- The maximum applied load is between 15-20 mN.

IV.1. Calibration

The first step of the mechanical characterization consists in calibrating the nanoindenter. Oliver and Pharr method (1992) was followed. The calibration can be divided in three main steps:

- i. Calibration of the column displacement and load sensors.
- ii. Calibration of the frame stiffness.
- iii. Calibration of the area function of the Berkovich indenter.

Steps (ii) and (iii) require the indentation of a reference material whose properties are known. Fused silica, which is amorphous and isotropic, was used. Frame stiffness was calculated in order to obtain a constant value of $P/S^2 = 1.5 \cdot 10^{-3}$ (where S = contact stiffness). The calibrated frame stiffness is $3.9 \cdot 10^5 \text{ N} \cdot \text{m}^{-1}$.

The calibration of the area function consists in fitting the C_i coefficients of (1. 24) by a least square method on the Young's modulus of fused silica (72 GPa). The Young's modulus and the hardness of fused silica after calibration of the frame stiffness and of the area function are plotted as a function of the indentation depth in Figure 2.48.

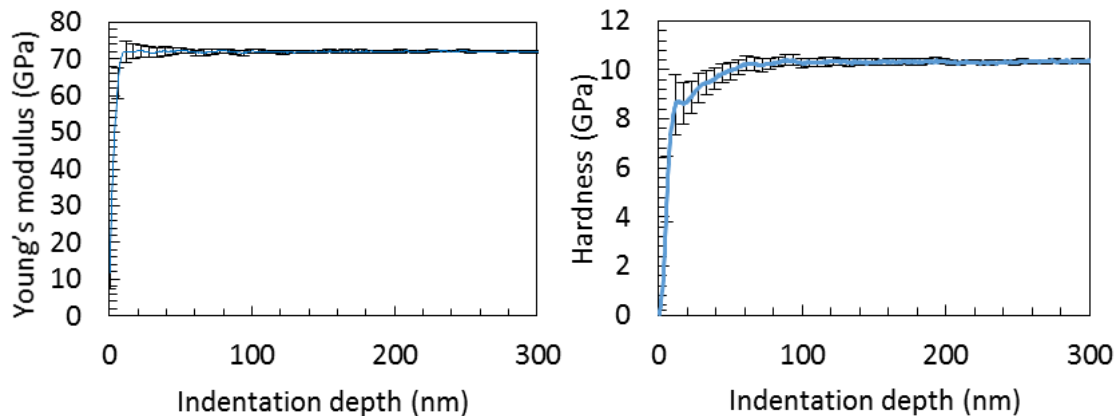


Figure 2.48. Young's modulus and hardness of fused silica after calibration of the nanoindenter.

The Young's modulus curve shows that the calibration of the indenter allows trusting the area function for indentation depth higher than 15 nm. Between 0 and 15 nm, the indenter defects prevent from a trustworthy measurement.

The hardness reaches a stable value of 10 GPa at 50 nm indentation depth, which is in agreement with the properties of fused silica.

IV.2. Elastic properties

a) Measurements

The measurements of the elastic properties of the inkjet printed silver layers as a function of the annealing temperature requires analyzing the nanoindentation data with the appropriate models. Indeed, the samples are a stack of two thin films (silver and silicon oxide) on a substrate (silicon). The measurement procedure is described in Figure 2.49.

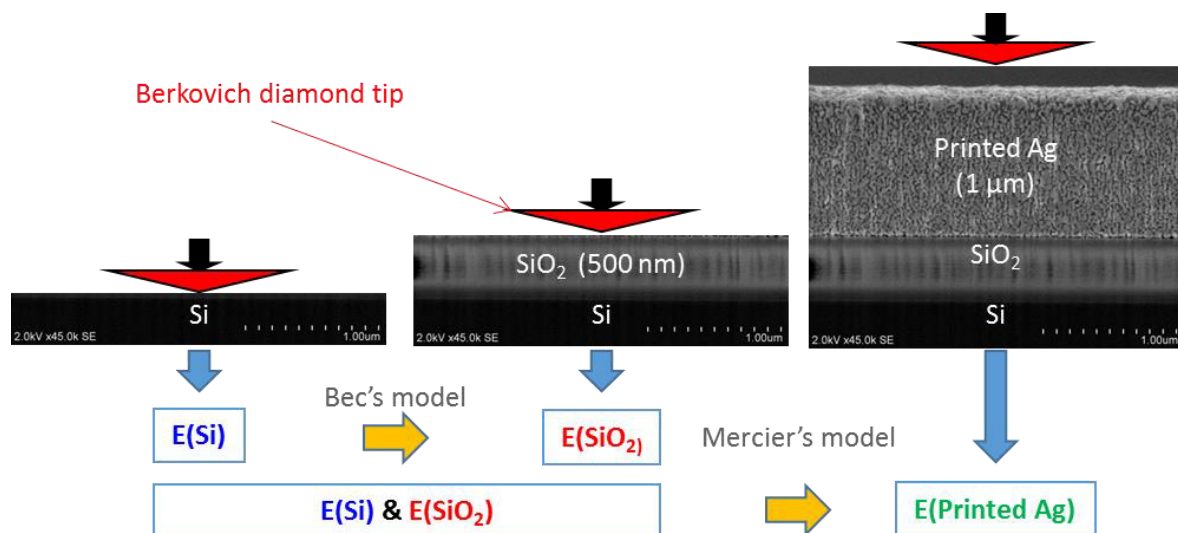


Figure 2.49. Experimental procedure for the measurement of the inkjet printed silver layers Young's modulus.

- The nanoindentation of the silicon substrate resulted in value of 162 GPa, which is in agreement with literature values. Depending on the orientation of the silicon crystal, values between 160-180 GPa are usually reported.
- The Young's modulus of the silicon oxide layer was extracted with Bec's model (2006). The measured Young's modulus is traced as a function of the indentation depth in Figure 2.50. This curve includes the contribution of the silicon oxide film and the silicon substrate. The increase of the apparent Young's modulus is due to the increasing influence of the silicon substrate, which is stiffer than the silicon oxide. The residual footprints exhibited sink-in of the indented area, thus indentation depth was corrected with Oliver (1992) equation (1. 21). The silicon oxide Young's modulus is extracted by a least square fit of the corresponding contact stiffness data with equation (1. 26). The extracted values are between 69 and 73 GPa, which are in agreement with literature data and the experimental value measured on fused silica (it is actually the same material in bulk state).

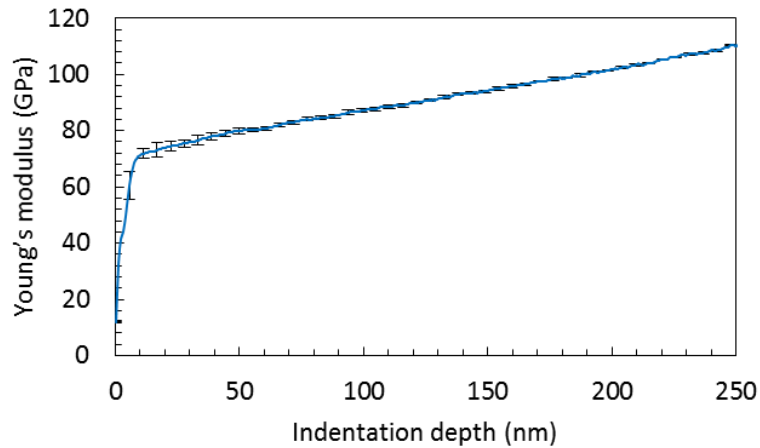


Figure 2.50. Apparent Young's modulus measured on 500 nm thick thermal silicon oxide on silicon.

- Finally, the Young's modulus of the printed silver layer was extracted with Mercier's model (2010). The measured Young's modulus is plotted as a function of the indentation depth in Figure 2.51. This curve includes the contribution of the silver layer, the silicon oxide film and the silicon substrate. The increase of the apparent Young's modulus is due to the increasing influence of the underlying film and substrate, which are stiffer than the printed silver. The residual footprints on silver exhibited pile-up of the indented area, thus indentation depth is corrected with Loubet (1993) equation (1. 22).

The silver printed layer Young's modulus is finally extracted by a least square fit of the corresponding contact stiffness data with equation (1. 27) and the measured properties of the underlying SiO_2 and Si.

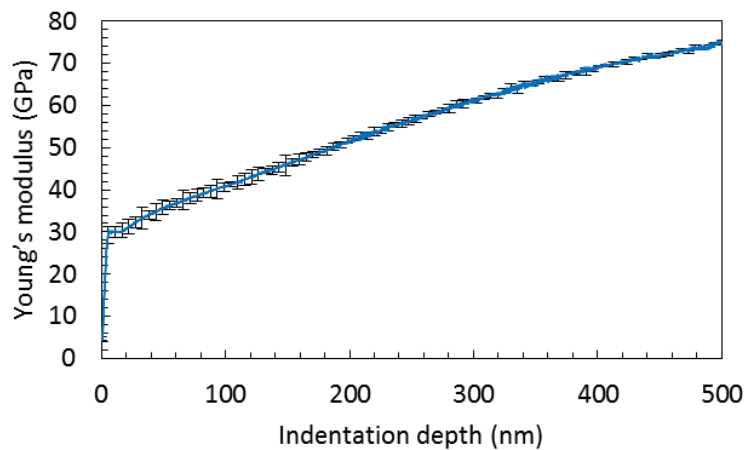


Figure 2.51. Apparent Young's modulus measured on a 1 μm thick inkjet printed silver layer annealed at 100°C during 1h.

b) Results

The Young's modulus of the silver layers is traced as a function of the annealing temperature in Figure 2.52. The first observation is that the Young's modulus is at least 50% lower than the silver bulk value. The second is the increase of the Young's modulus with annealing temperature.

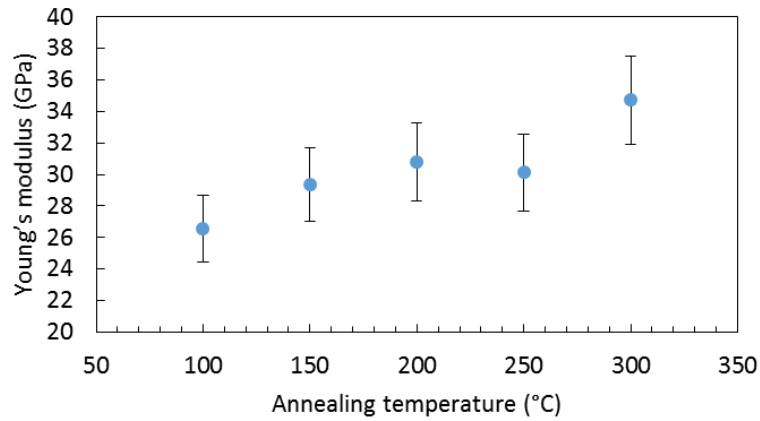


Figure 2.52. Young's modulus of the inkjet printed silver layers as a function of the annealing temperature.

c) Discussion

The Young's modulus of a material is highly dependent on its porosity rate (Gibson, 1999). There are several models in the literature offering empirical relationships between porosity and elastic modulus.

In this work, the empirical law (2. 12) was applied to correlate the measurements of the elastic properties to the porosity measurements. Equation (2. 12) was established by Roberts (2000) by finite element modeling of different structures in three dimensions (Figure 2.53) whose geometry is similar to the 3D reconstruction of the silver layers obtained in II.4.a.

$$\frac{E}{E_{Ag}} = \left(1 - \frac{\phi}{\phi_0}\right)^n \quad (2. 12)$$

where E and E_{Ag} are the respective Young's moduli of the silver printed layers and of bulk silver, ϕ is the porosity and ϕ_0 and n are given by Roberts for each simulated structure.

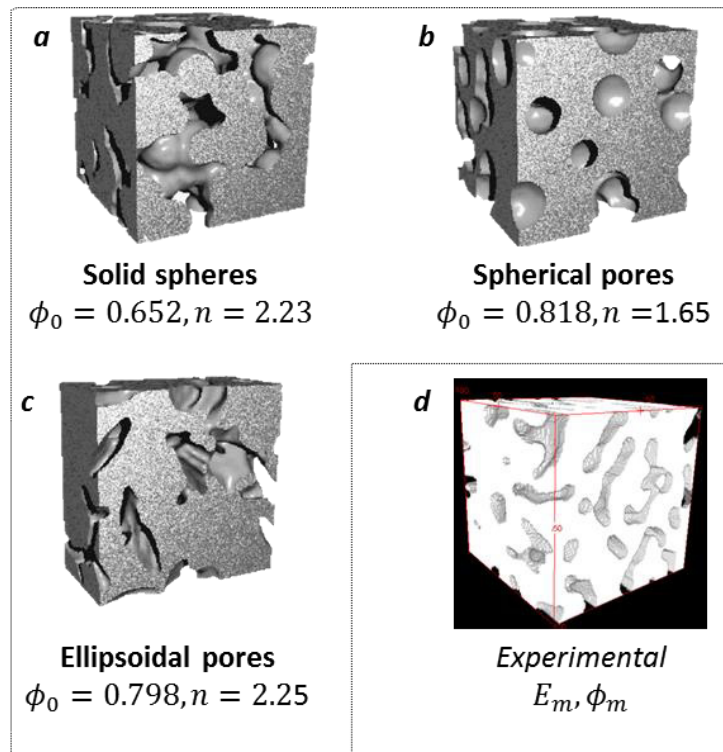


Figure 2.53. Structures simulated by Roberts (2000). a) Solid spheres. b) Spherical pores. c) Ellipsoidal pores. Adapted from Roberts (2000). d) 3D representation of a silver layer annealed at 250°C.

The experimental Young's modulus is plotted as a function of the measured porosity together with Roberts modelled laws in Figure 2.54. The experimental data fit between the curves corresponding to the solid spheres and the ellipsoidal pores laws. The porosity measurement and the extraction of the Young's modulus with Mercier's model correlate with Roberts' model.

The measurement of the porosity is challenging at the nanometric dimensions of the printed silver layers. Moreover, the porosity values were measured with image processing and are thus subjected to a subjective evaluation in the choice of the segmentation algorithm. As in the analysis of the thickness of the printed silver layers in II.5.c, these results corroborate the porosity rates measured by image processing of SEM imaging of the layers cross-sections. Moreover, the results offer an alternative method, namely the measurement of the Young's modulus, to estimate the porosity of the printed silver layers.

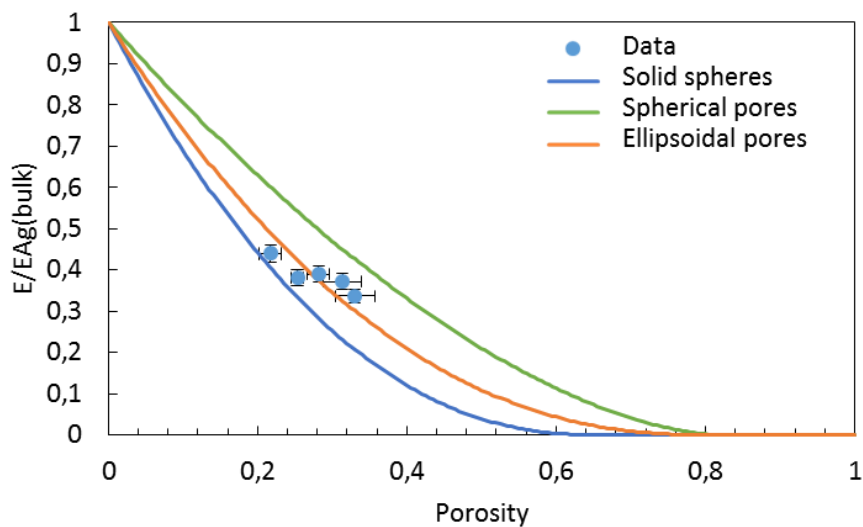


Figure 2.54. Normalized Young's modulus as a function of the material porosity. Experimental results and Roberts model.

IV.3. Plastic properties

a) Measurements

The hardness of the inkjet printed silver layers is calculated with (1. 28). However, for this relation to be valid, the radius r_p of the hemi-spherical region in elasto-plastic deformation regime must be lower than the silver layer thickness.

It was shown in chapter 1 that $r_p = 1.68r_c$ (r_c contact radius). In the case of a Berkovich indenter, in a first approximation, the indentation depth $h_c \approx 3 * r_c$. As a consequence, the hardness can be estimated for indentation depths lower than 20% of the film thickness.

In Figure 2.55, the hardness of a silver layer annealed at 150°C is traced a function of the indentation depth. A plateau where the hardness value is stable occurs between 50 and 150 nm indentation depth. This range is lower than 20% of the film thickness. Hence, the hardness value is calculated by averaging the values between 70 and 120 nm.

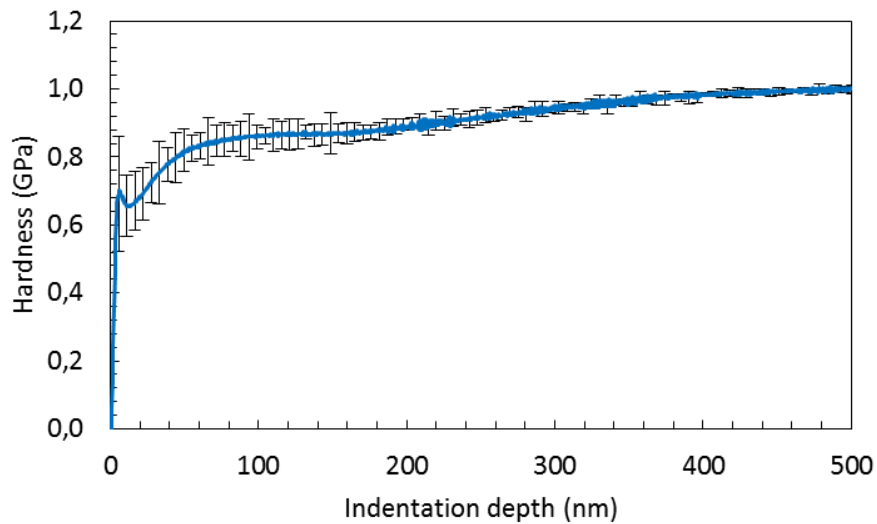


Figure 2.55. Hardness of 1 μm thick inkjet printed silver layer annealed at 100°C during one hour.

b) Results and discussion

The hardness is traced with the annealing temperature in Figure 2.56.a. A decrease of the hardness can be observed. In paragraph II.3.b, it was observed that the grain size increases with the annealing temperature. Tracing the hardness as a function of the grain size (Figure 2.56.b) shows that the hardness of the printed silver layers follows the behavior predicted by the Hall-Petch theory.

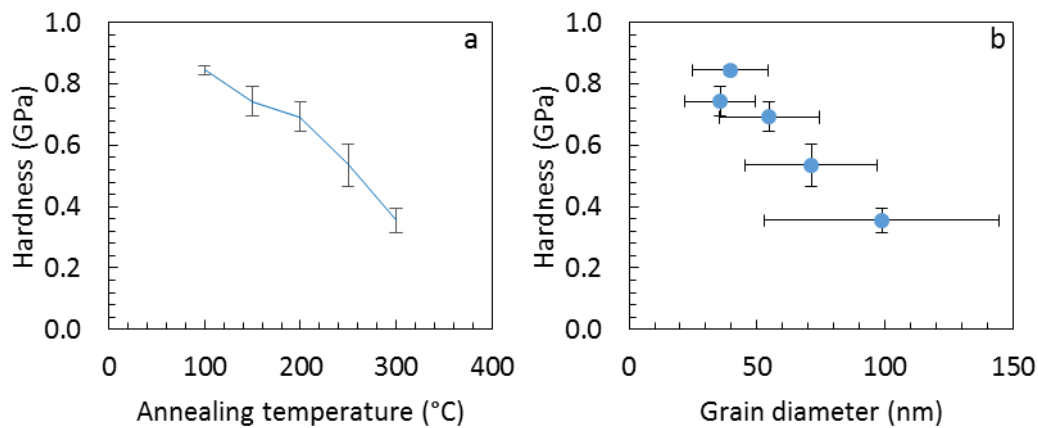


Figure 2.56. Hardness of the silver layers as a function of the annealing temperature (a) and the grain diameter (b).

IV.4. Summary

The evolution of the Young's Modulus and the hardness of inkjet printed layers with the annealing temperature was studied in the range 100°C-300°C. Concerning the elastic properties, the Young's modulus is less than half of the bulk value and it increases with the annealing temperature. Such a behavior is due to the densification of the printed layers with the annealing temperature. The hardness of the silver layers decreases with the annealing temperature, as predicted by the Hall-Petch theory. Its value is at least three times lower than the bulk value, mainly because of the grain size.

Conclusion

In the manufacturing of printed electronic devices, silver inks and pastes are the most employed when conductive materials are required. Indeed, the commercial offer for such inks covers lots of specifications:

- Silver nanoparticles or silver salt inks
- Silver content up to 60 wt%
- Nanoparticles size between 5 and 100 nm
- Different types of ink vehicles: water-based and solvent-based

Moreover, the knowledge of silver chemistry has reached a maturity that allows self-formulation in laboratories with special features. As a consequence, silver inks for functional printing have been extensively studied in the last decades: formulation, printing, and sintering.

In this chapter, a thorough study of the properties of inkjet printed silver layers was proposed. The evolution of the microstructure, the electrical conductivity, the TCR, the Young's modulus, and the hardness were monitored with the annealing temperature in the range 100°C-300°C. Microstructure evolution of silver layers annealed above 300°C was observed, showing that grain size exceeds the micron and that patterns might lose electrical continuity. A special attention was given to the morphological parameters of the silver layers, and in particular to their porosity. To our best knowledge, we have presented here the first 3D porosity measurements of inkjet printed silver layers. Moreover, this porosity characterization provided supplementary data for the analysis of electrical and mechanical properties. Crystallographic analysis was not performed in this work. A thorough study was realized by Cauchois (2012) using Backscattered Electron Diffraction (EBSD) and X-Ray Diffraction.

The knowledge of the mechanical properties of the inkjet printed silver layers is of major interest for flexible electronics applications. Further studies focused on the adhesion of silver layers printed on polyimide substrates are ongoing and will be pursued in a PhD thesis at our laboratory. Moreover, reliability issues to thermal and mechanical cycling will be investigated.

Besides the experimental results, several characterization methods were developed and adapted to the studied material. It must be noted that the presented results were obtained with a commercial silver ink from SunChemical. With other inks, if similar trends are to be expected, large deviations might occur, especially if the initial dimensions of the silver nanoparticles are very different. The proposed characterization approach revealed to be accurate thanks to the cross-correlation of microstructural, electrical and mechanical results.

Finally, in this chapter, several properties of inkjet printed silver layers were highlighted. Silver layers can be employed beyond their classical interconnection or electrode role. In the next chapter, the characterization results obtained in this chapter will serve the conception of flexible and printed electronic devices.

Chapter 3

Prototyping of Printed Flexible Devices

Introduction

Inkjet printing is being widely investigated for electronic components fabrication. Indeed, because low viscosity inks are required, a drastic reduction of binders in ink formulation is resulting in inks containing mainly active materials and solvent (Subramanian, 2008). This particular characteristic of inkjet inks led to major advances in ink formulation, which today offers a large spectrum of printable materials:

- Conductive materials: metallic nanoparticles (Ag, Au, Cu, Al), carbon nanotubes, graphene, etc.
- Ceramics: Al₂O₃, SiO₂, PZT, etc.
- Polymers: organic light emitting polymer, conductive polymers (PEDOT:PSS), organic semiconductors, UV-curing polymers, etc.

Thanks to the available inks either on the market or by self-formulation, inkjet printing of several types of electronic components is visible in the literature. One of the most advanced application fields is the Radio Frequency Identification (RFID) tags and antennas together with RF components (filters, couplers, etc.) (Yang, 2007; Sridhar, 2009; Arriola, 2011). The success of printing in RF applications relies on the dimensions of the components, usually in the millimeter range.

Printing of physical and chemical sensors is also being explored. Several examples of functional sensors were reported:

- Ammonia sensors were realized by inkjet printing of an aqueous solution of PANI-PSS¹ (Jang, 2007).
- Inkjet printed HgTe nanoparticles demonstrated highly sensitive photodetectors (Böberl, 2007).
- Temperature and humidity sensors were inkjet printed on paper with silver inks (Courbat, 2011).
- All-inkjet printed strain gauges were recently reported by Andò and Baglio (2013).

Besides, inkjet is also employed for printed organic electronics research and development. The first inkjet printed all-polymer transistor circuit was reported by Sirringhaus *et al.* in 2000. Since then, organic electronic components such as organic light emitting diodes (OLEDs) (Mauthner, 2008; Villani, 2009), and organic photovoltaics (Hoth, 2007; Aernouts, 2008) were demonstrated.

In this chapter, we took advantage of the physical properties of silver printed layers as well as the inkjet printing capabilities to propose original electronic components. Prototypes of RF filter, vacuum sensor and membrane switch were designed, fabricated and characterized. The last paragraph concerns the fabrication of a standard design Metal-Insulator-Metal (MIM) RF capacitor.

¹Polyaniline-Poly(4-styrenesulfonate)

These results were presented in different oral communications, posters and scientific journals. The following articles were adapted for this chapter.

➤ **17 GHz band-pass filter:**

D. Sette, D. Mercier, C. Poulain, A. Blayo, "Silver Nanoparticles Inkjet Printed 17 GHz Filter", International Microwave Symposium 2013 IEEE (Seattle, USA).

D. Sette, C. Poulain, A. Blayo, D. Mercier, "Design and Inkjet Printing of RF devices in the GHz Range", 40th International conference of IARIGAI, 2013 (Chemnitz, Germany).

D. Sette, C. Poulain, A. Blayo, D. Mercier, "Design and Inkjet Printing of a Bandpass Filter in the GHz Range", Journal of Print and Media Technology Research 2013.

➤ **Inkjet printed micro Pirani gauge (vacuum sensor):**

D. Sette, D. Mercier, P. Brunet-M., C. Poulain, A. Blayo, "Micro Pirani pressure sensor fabricated by inkjet printing", Transducers 2013 & Eurosensors XXVII (Barcelona, Spain).

➤ **Inkjet printed membrane switch:**

D. Sette, C. Poulain, A. Yakoub, M. Saadaoui, B. Dubois, A. Blayo, "Study of the electrical contact in a fully inkjet printed membrane switch", 59th IEEE HOLM Conference on Electrical Contacts 2013 (Newport RI, USA).

J. Ailuno, L. Rapp, D. Sette, A.P. Alloncle, C. Poulain, P. Delporte, "Laser-induced forward transfer of silver nanoparticles paste for membrane switch printing on flexible substrates", E-MRS 2013 Spring Meeting (Strasbourg, France).

➤ **Inkjet printed RF capacitor:**

D. Sette, V. Kovacova, E. Defay, "Printed Barium Strontium Titanate capacitors on silicon", to be submitted.

I. Optimization of printing conditions

The printing of a conformal pattern with respect to the design relies on the equilibrium of the printing process, the ink properties (physico-chemical and rheological), and the substrate properties.

This first paragraph focuses on the optimization of the printing parameters of the SunChemical EMD5714 silver ink on a polyimide substrate with the Dimatix DMP2831 printer for the fabrication of a RF band-pass filter and a Pirani gauge.

I.1. Flexible polyimide substrate

The polyimide substrate was Kapton HN, 75 μm thick from DuPont (DuPont, n.d.). It was chosen for its robustness and its compatibility with annealing temperatures up to 400°C.

The substrate surface energy measurement was carried out by the contact angle method (Annex 1) using an OCA Dataphysics goniometer. The contact angle measurements are reported in Table 3.1.

Table 3.1. Probe liquids for surface energy measurement and contact angle measured on Kapton HN.

	Surface tension at 25°C ($\text{mJ}\cdot\text{m}^{-2}$)			Contact angle (°)
	Total σ^T	Dispersive component σ^D	Polar component σ^P	
Water	72.8	21.8	51	73.9
Glycerol	63.4	37	26.4	70.4
Diiodomethane	50.8	50.8	0	38.7
Hexadecane	27.4	27.4	0	18.5
Bromonaphtalene	44.6	44.6	0	32.0

The extracted value of the Kapton HN surface energy using the Owens-Wendt model was $39 \pm 4 \text{ mJ}\cdot\text{m}^{-2}$ with a coefficient of determination of the linear fit $R^2 = 0.86$. This value is similar to the results of Huang (2003). Substrate properties are summarized in Table 3.2. It should be noted that no surface treatment was performed before printing. Moreover, the cleanroom environment prevented from dust contamination on the substrate surface.

Table 3.2. Properties of Kapton HN 75 μm , Dupont®.

Surface energy	39 ± 4	$\text{mJ}\cdot\text{m}^{-2}$	<i>measured</i>
Relative dielectric constant	3.5	-	<i>Datasheet</i>
Coeff. of thermal Conductivity	0.12	$\text{Wm}^{-1}\text{K}^{-1}$	<i>Datasheet</i>
Thermal Coeff. of Expansion	20	$\text{ppm}/^\circ\text{C}$	<i>Datasheet</i>

I.2. Optimization of the printed pattern

The most compelling pattern requirements arise from the micro-strip lines at the input and output of the RF filter. The pattern of the microstrip is illustrated in Figure 3.1. Consequently, this pattern is employed to illustrate the optimization steps and the encountered issues.

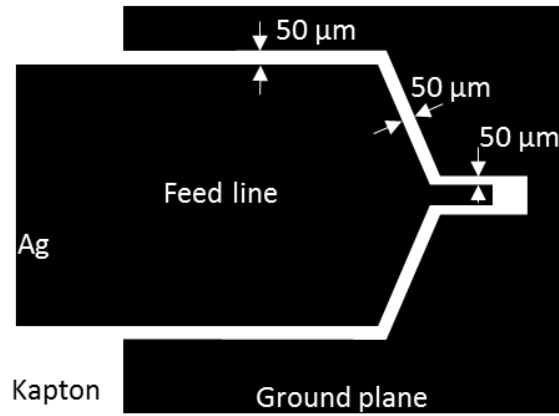


Figure 3.1. Micro-strip line pattern (black area corresponds to ink).

a) Pattern resolution

The volume V per unit area of ink deposited when printing a pattern is defined by the number of ejected droplets per unit area. This volume can be calculated with equation (3.1), showing the square dependence of the printed volume to the pattern resolution R_p ,

$$V = V_{droplet} * R_X * R_Y = V_{droplet} * R_p^2 \quad (3.1)$$

where $V_{droplet}$ is the volume of a droplet, R_X and R_Y the resolution along X and Y directions. The optimal printing resolution on the Dimatix printer with the EMD5714 silver ink, the 10 pl cartridge and the Kapton substrate was experimentally determined.

For pattern resolutions higher than 555 pix/cm, corresponding to an 18 μm pitch between droplets, borders were well defined during printing, although a few minutes afterwards the ink spreads under the influence of gravity and the pattern loses its shape (Figure 3.2.a). Decreasing the resolution down to 400 pix/cm led to a dewetting phenomenon during drying at 60°C as shown in Figure 3.2.b.

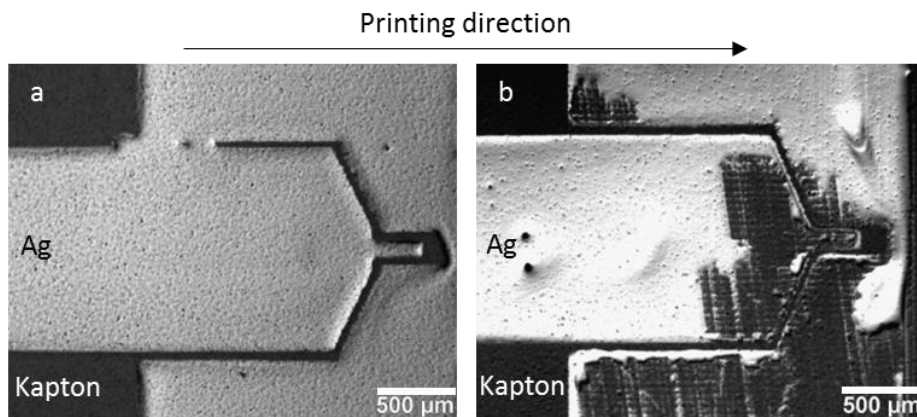


Figure 3.2. Ink spreading (a) and dewetting (b) on a micro-strip line pattern.

These unwanted phenomena were eliminated by accelerating the drying step by heating the printer chuck at 60°C during ink deposition, and the best printing definition on the Kapton HN substrate was obtained at 476 pixels/cm (21 μm pitch). A conformal printed micro-strip line is illustrated in Figure 3.3.

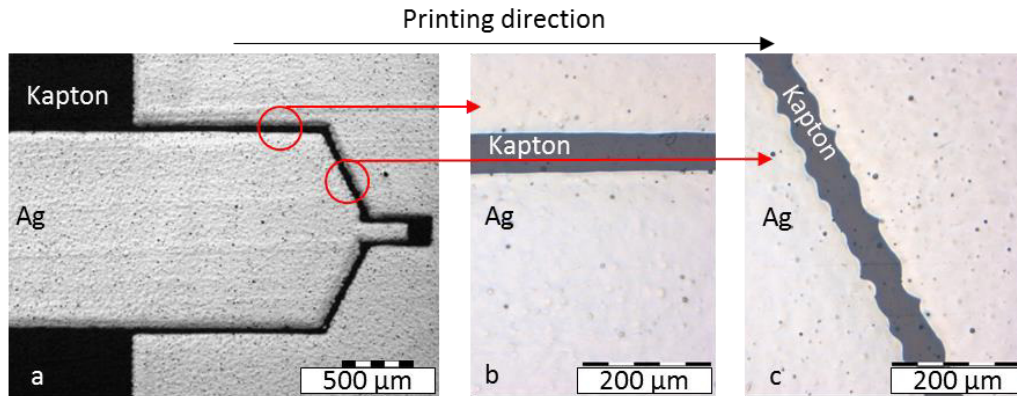


Figure 3.3. a) Conformal printed pattern at 476 pixels/cm. b) Pattern edges parallel to printing direction. c) Pattern edges not parallel to printing direction.

In this optimized configuration of the printing, the chuck at 60°C has an influence on the nozzles temperature because of the 600 μm stand-off distance. The nozzles temperature increases from ambient to 32-33°C after a few minutes of printing. To take account of this temperature increase, the setting of the actuation voltage is realized by heating the nozzles at 33°C. As a consequence, the viscosity of the ink is reduced and so is the actuation voltage.

b) Pattern design

The gap between the feed line and the ground plane is designed at 50 μm and a single pixel connecting these two elements will cause a critical short-circuit (Figure 3.4). The scratches visible on the silver surface occurred after printing and annealing as the sample was left unprotected during several months.

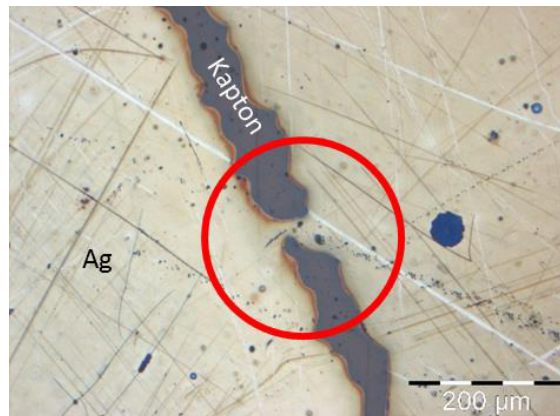


Figure 3.4. Critical short-circuit between feeding strip and ground plane.

Figure 3.3.b illustrates that edges parallel to the printing direction are well defined while droplets shape (pixels) is visible when the pattern edges are not parallel to the printing direction (Figure 3.3.c).

The input binary bitmap pattern was created using the layout software CleWin4. The automatic conversion from the desired design (vectorial data) to a discrete pixelated pattern generates random and irregular spacing on the Input/Output (I/O) feed lines patterns. The random arrangement of the pixels has been identified as a cause of failure during the printing. To overcome this critical issue, the pixels of the border were manually set in a regular arrangement, e.g. in Figure 3.5, and different configurations of spacing were printed in order to approximate the desired design while obtaining a reliable and repeatable printing.

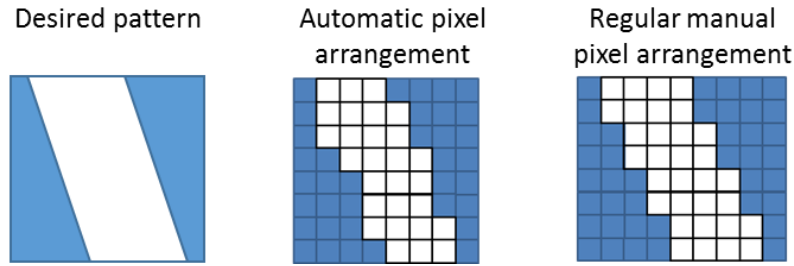


Figure 3.5. Examples of pixel arrangement.

I.3. Drying and annealing

The printed patterns were firstly dried at 60°C during 20 to 60 minutes depending on their dimensions. Then, the annealing step was performed in an oven. The conditions will be specified for each prototype.

I.4. Summary

The optimization of the printing conditions goes through the settings of the printer which mainly depends on the interaction between the ink and the substrate. Moreover, the arrangement of pixels has to be optimized where gaps of 50 µm are required in order to get a reliable and repeatable printing. The optimized printing parameters that were used to print both the band-pass filter and the Pirani gauge are summarized in Table 3.3.

Table 3.3. Optimized printing parameters.

Settings	Value	Comments
Nozzles temperature	33°C	Match heating from the chuck
Actuation voltage	17-19V	21-23 V at room temperature
Waveform	Figure 2.5, chapter 2.I.3	-
Firing frequency	5kHz	-
Meniscus	5 inches of H ₂ O	Prevents from clogging
Droplet diameter	28 µm	-
Droplet volume	11 pl	-
Droplet velocity	≈ 5 m.s ⁻¹	-
Filament disappearing	300 µm from the nozzle	Spherical droplet, no satellites
Stand-off distance	600 µm	-
Chuck temperature	60°C	Fix pattern borders
Resolution	476 pixels.cm ⁻¹	Optimal resolution

II. 17 GHz band-pass filter

II.1. State-of-the-art

The most advanced potential RF application of printing technologies on flexible substrate is the RFID tag in the UHF range (Ultra High Frequency – 0.3-3 GHz). Although other inkjet printed devices at higher frequencies have been developed, they are usually printed on specific substrates in order to decrease the transmission losses. For example, antennas on LCP (Liquid Crystal Polymer) substrate at 60 GHz (Shaker, 2010), couplers on Chuko substrate at 6 GHz (Arriola, 2011), coplanar waveguides on LCP substrate up to 110 GHz and bandpass filters on alumina substrate at 2.4 GHz (Sridhar, 2009) have been reported.

The purpose of this work is to demonstrate that it is possible to use inkjet printing on low-cost substrates for filtering applications at frequencies much higher than what has been made up to now. The reported filters fabricated by inkjet printing technology have shown relatively good performance up to 2.4 GHz, but their center frequency and their minimum bandwidth is mainly limited by the substrate dielectric losses that increase at high frequencies. To overcome this issue, Blondy (1998) proposed to use micromachined suspended silicon substrates for designing high performances RF filters. The major drawback of this solution is the micromachining that requires deep silicon etching and photolithography steps, which increase the fabrication cost and complexity. Moreover, the cost of silicon substrate rapidly increase for large area components.

In this work, we show that it is possible to fabricate low-cost RF filters by using inkjet printed technology on polyimide films. The fabricated filter has been designed at 17 GHz and it combines both inkjet printing and suspended technologies.

II.2. Filter design

The designed filter is a two pole device centered at 17 GHz and has a 4% bandwidth with transmission zeros to improve the rejection. The filter is based on suspended microstrip lines as shown in Figure 3.6 with coplanar feed lines for the measurements. The filter was designed following the procedures detailed by Blondy (1998) and Hong (2001). The feed lines are capacitively coupled while the resonators are magnetically coupled. The filter response was computed and optimized with the software Agilent Momentum based on the method of moments. The filter layout is presented Figure 3.6 and the optimized dimensions are given in Table 3.4.

The filter and the feed lines including the transition from coplanar to microstrip lines have been simulated at the same time as they are both suspended on the polyimide film. The width of the coplanar line center conductor and gaps are respectively 120 μm and 50 μm . With such dimensions only one mode of propagation is possible at the input of the filter as the cutoff frequency of the first higher mode is well above the frequency of interest. The relative permittivity ϵ_r of the polyimide is 3.5 and the loss tangent extrapolated from Kapton HN datasheet is about 0.05 at 17 GHz. The conductivity of the brass cavity is 1.5×10^7 S/m. With such dimensions and material properties, the unloaded quality factor Q_0 , the external quality factor Q_{ext} and the inter-resonator coupling coefficient k_{12} extracted from computations are $Q_0 \approx 100$, $Q_{\text{ext}} = 29$ and $k_{12} = 0.034$.

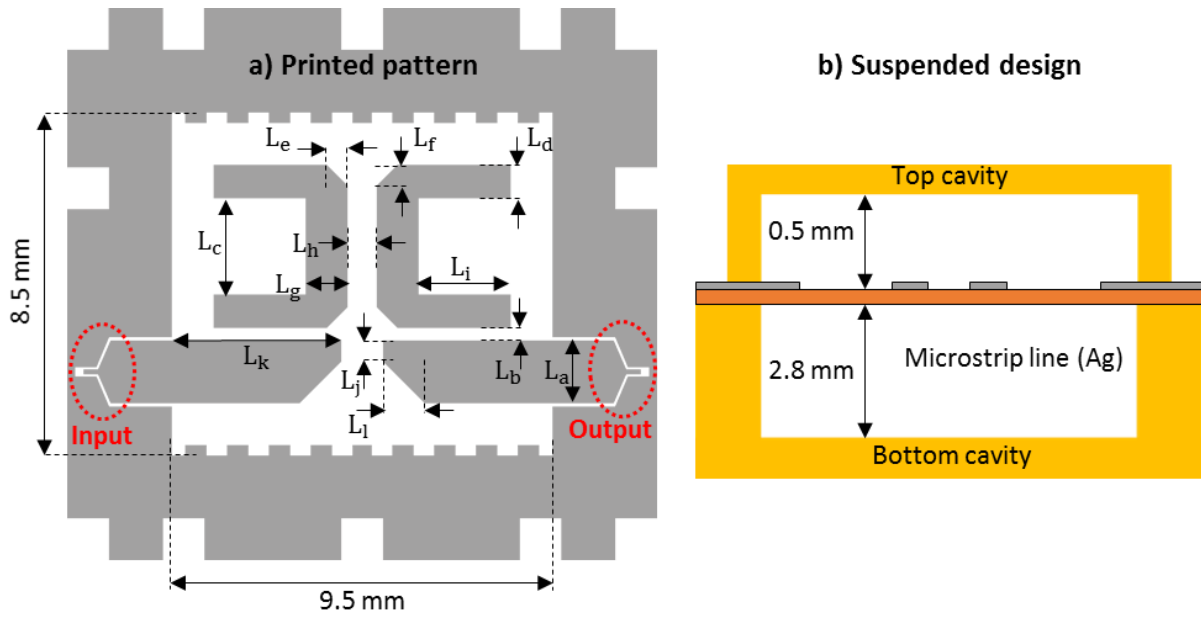


Figure 3.6. a) Top view of the printed pattern. b) Schematic design of the suspended structure (cross-section view).

Table 3.4. Dimensions of the filter.

	Length (μm)		Length (μm)
L_a	1500	L_g	1000
L_b	300	L_h	700
L_c	2300	L_i	2200
L_d	800	L_j	500
L_e	500	L_k	4250
L_f	500	L_l	1000

II.3. Fabrication details

a) Printing and annealing steps

Silver nanoparticle ink was chosen since electrical conductivity higher than 10^7 S.m^{-1} can be obtained. The polyimide substrate was selected because of its low dielectric constant for a plastic substrate and its tolerance to temperatures up to 400°C . Moreover, it has a smooth surface and low porosity, which prevents major defects on the printed layer and nanoparticle permeation into the substrate.

The filter pattern was printed with one and two silver layers according to the procedure detailed in paragraph I. Ten minutes lasted between the printing of the two layers by keeping the substrate at 60°C on the printer chuck. After printing the pattern, which is approximately 1 cm^2 , it was dried in an oven during 1 hour at 60°C . This was necessary to fully evaporate the ink solvent.

The characterization of the silver layers in chapter 2 and the properties of the substrates led to the following annealing conditions: 220°C during one hour. The requirements were:

- Uniform microstructure
- Electrical conductivity above 10^7 S.m^{-1} .
- Prevent substrate damaging.

To precisely measure the electrical conductivity of the filter silver layer, two van der Pauw patterns were printed at the same time (Figure 3.7). The measured thickness and electrical conductivity are given in Table 3.5.

Table 3.5. Measured conductivity of the silver layers.

Number of layers	Thickness (μm)	Conductivity ($\text{S}\cdot\text{m}^{-1}$)
1	0.9	$1.4 \cdot 10^7$
2	1.30	$1.5 \cdot 10^7 \text{ S}$

b) Filter assembly

The final step in fabricating the filter is the assembly of the printed layer with top and bottom cavities. The top cavity is glued with silver paste on the ground plane while the substrate is glued with Araldite on the bottom cavity. Both cavities are electrically connected with silver paste. After assembly, the filter was cured at 150°C during 15 minutes on a hot-plate to evaporate the silver paste solvent. Figure 3.7 illustrates the final device with the opened top cavity.

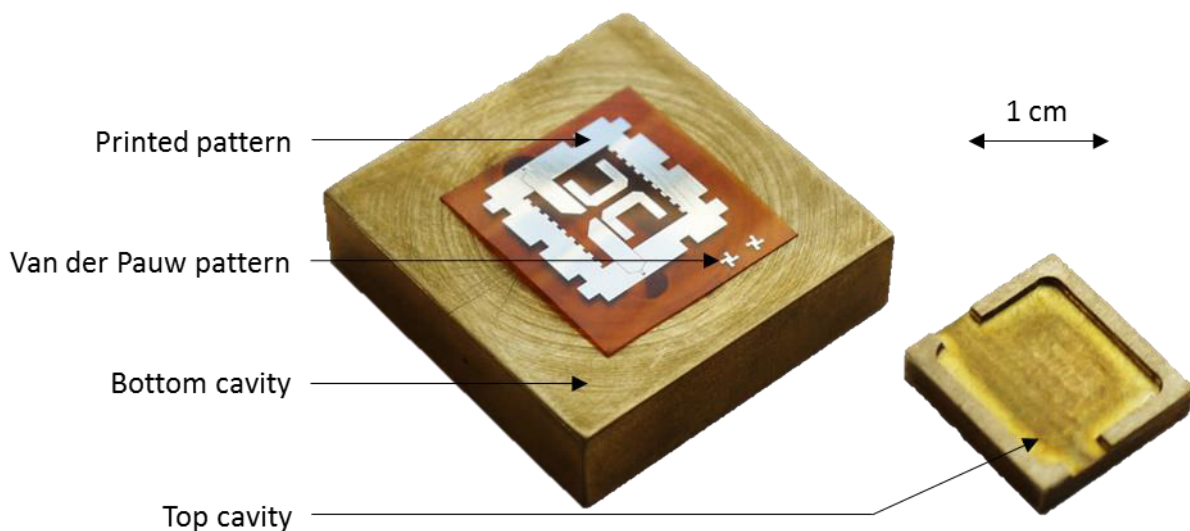


Figure 3.7. Printed band-pass filter.

II.4. Frequency response of the filter

The filter response was measured using an Agilent N5230A vectorial network analyzer and a SOLT calibration (Short, Open, Load, Thru). The results in Figure 3.8 show the response of the one and the two printed layers filters. In both cases, the filters are centered at 17 GHz and have a 4% bandwidth. Insertion losses (S_{21}), corresponding to the attenuation of the transmitted signal in the pass-band filter, are 5.7 dB for the one layer filter and decrease to 3.6 dB for the two layers filter. Such a difference is equivalent to an increase of the signal amplitude by a factor 1.6. The reduction of the conduction losses is due to a higher electrical conductivity and a more homogeneous silver layer: better covering of the substrate defects and more homogeneous thickness of the silver layer. For both filters, the return losses (S_{11}) are lower than -20 dB on the whole bandwidth and the rejection up to 20 GHz is better than -20 dB.

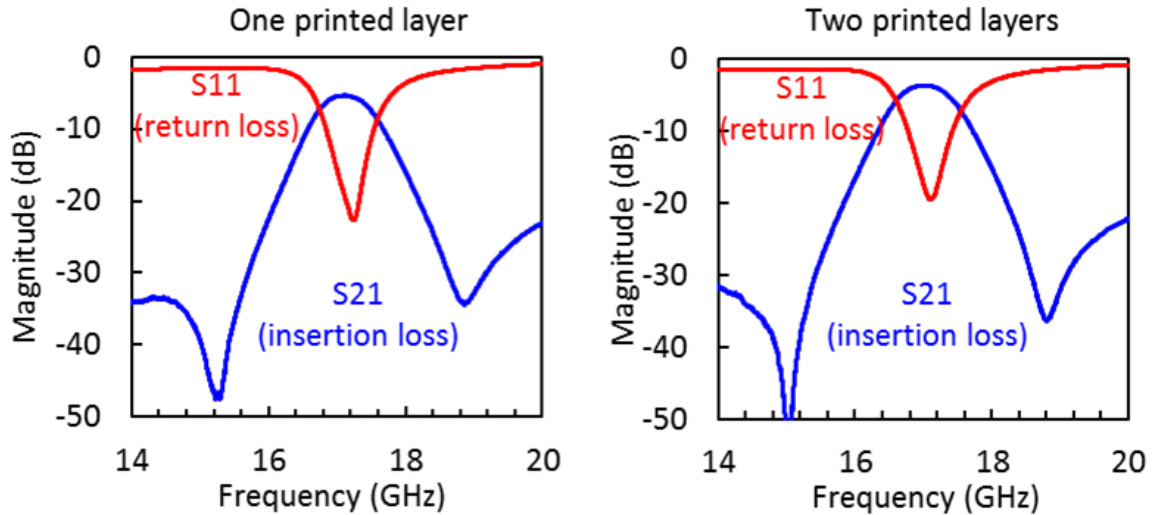


Figure 3.8. Measured response of filters printed with one and two layers.

The simulated response of the filter with two layers presented in Figure 3.9 is in good agreement with the measurements even if the simulated insertion losses are slightly underestimated. Also, a small frequency shift can be observed. It may arise from the misalignment of the top cavity with the silver pattern, its irregular thickness and edges, and the polycrystalline and porous microstructure. Indeed, the simulation considers the conductive printed layer as a bulk material with straight borders (no scalloping) and steps (pattern edges are thinner than at the center).

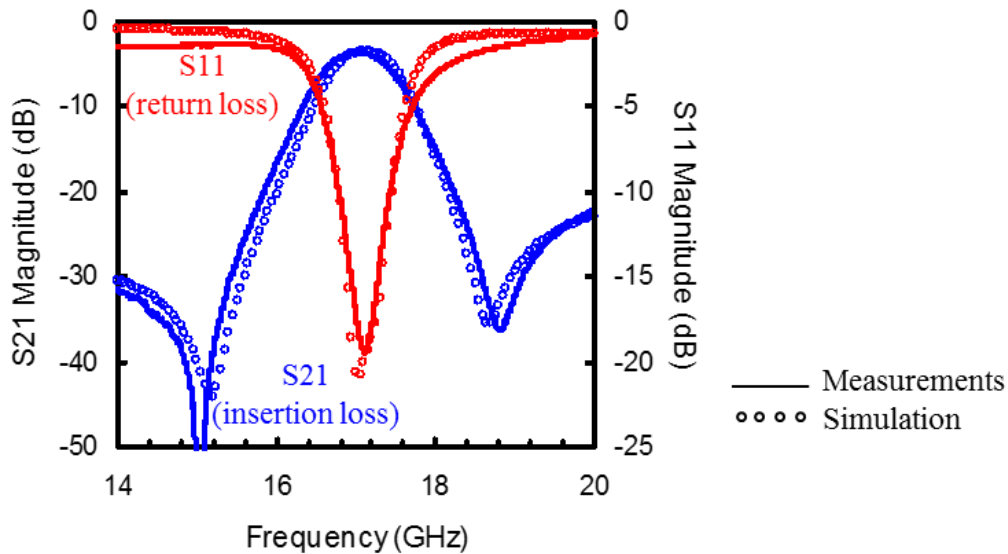


Figure 3.9. Measured and simulated response of the filter (two layers) including metallic and dielectric losses.

Further simulations have shown that the 3.6 dB insertion losses arise both from metallic and dielectric losses. Metallic losses in the brass cavities and printed silver layer, which have the same electrical conductivity at $1.5 \cdot 10^7 \text{ S} \cdot \text{m}^{-1}$, account for 0.9 dB. The dielectric losses in the Kapton HN substrate, which was simulated with 0.05 loss tangent at 17 GHz, account for 2.7 dB.

II.5. Conclusion

This first application demonstrates that inkjet printing on low-cost substrates can be employed for the fabrication of RF devices working beyond 10 GHz frequencies. Insertion losses as low as 3.6 dB were obtained on several prototypes and there is a possibility of improving the filter performances.

Indeed, conduction losses can be reduced by increasing the electrical conductivity of the silver layer (annealing temperature and time) and of the metallic cavity (silver or gold metallization). However, simulations have shown that doubling the electrical conductivity would decrease conduction losses of only 0.3 dB (ie 8%). Transmission losses mainly arise from the dielectric losses in the Kapton flexible substrate. Reducing the substrate thickness and/or loss tangent would drastically decrease the insertion loss.

We have tried to print a pattern on a Kapton HN substrate 25 μm thick. However, thermo-mechanical strains during the annealing step led to the failure of the silver layers: cracking and loss of planarity.

III. Micro Pirani gauge

III.1. State-of-the-art

Micro Pirani gauges are pressure sensors typically used in medium to high vacuum systems (10^{-5} - 100 mbar). The Pirani principle consists in measuring the resistance of a heated conductor placed in the vacuum environment to be monitored. When gas molecules collide with the heated conductor, thermal energy is transferred away. As the electrical resistance of the heated conductor is related to its temperature and as the frequency of molecular collisions increase with the gas residual pressure, the resistance variation of the conductor is pressure-dependent.

The most common micro Pirani sensors are either micro hotplates (Herwaarden, 1988, Weng, 1994) or micro bridges (Mastrangelo, 1991; Baar, 2001) fabricated by silicon micromachining techniques which are complex and time consuming. Here an alternative fabrication technique using inkjet printing of silver nanoparticles is implemented for the first time. Electrical properties of the printed layer and response of the pressure sensor are investigated and correlated with thermal conduction models.

III.2. Printed micro Pirani design

The layout of the printed Pirani gauge is illustrated in Figure 3.10. The sensitive element is a serpentine planar resistor with four connection lines. Its dimensions are detailed in Table 3.6. The overall occupied active surface of the sensor is less than 1 mm^2 .

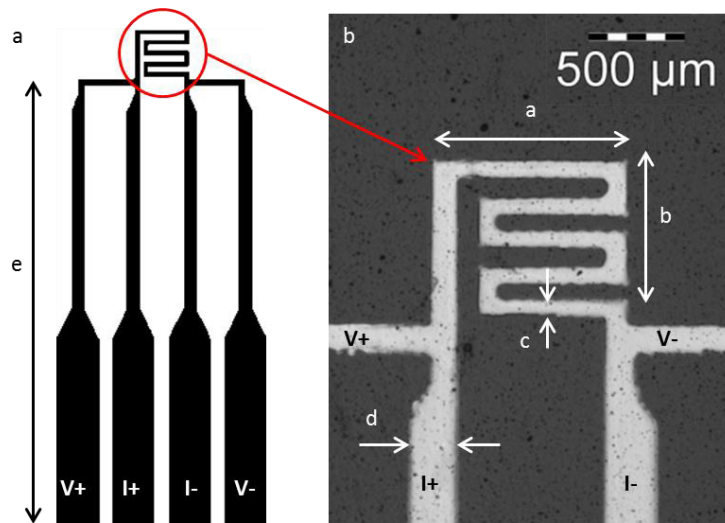


Figure 3.10. a) Design of the micro Pirani gauge with connection pads b) Microphotograph of the active part of the sensor.

Table 3.6. Dimensions of the printed micro Pirani gauge.

a (μm)	b (μm)	c (μm)	d (μm)	e (mm)
990	830	90	250	12.2

III.3. Fabrication details

a) Printing and annealing steps

The micro Pirani gauge was printed following the procedure described in paragraph I. The Kapton HN substrate was chosen for its low cost and its thermal properties. Indeed, it has a thermal conductivity of $0.12 \text{ W.m}^{-1}.\text{K}^{-1}$, more than 100 times smaller than the one of silicon. This property favors thermal

exchanges of the printed resistor with the surrounding gas rather than with the substrate. The pattern has been printed with two passes in order to improve thickness homogeneity and to better cover substrate defects.

The gauge temperature is expected to reach a maximum around 100°C at the lower working pressure. Thus, the annealing temperature was set to a higher temperature, namely 150°C, for two reasons: firstly to prevent further annealing due to working temperature, and secondly to reach a nominal resistance value of a few ohms in order to be able to accurately measure the resistance variations. Finally, the annealing time was set to 5 hours in order to stabilize the layer microstructure because of the temperature elevation of the sensor.

These annealing conditions resulted in a 1.3 μm thick layer. The electrical conductivity is of about $10^6 \text{ S} \cdot \text{m}^{-1}$ at room temperature and pressure.

b) Gauge mounting

The printed micro Pirani gauge is mounted on a circuit board using a vertical four point electrical connector which holds the sensor suspended to optimize thermal exchanges with the gas. A copper pipe surrounding the sensor at a 6 mm distance is used as heat-sink. The connector allows four point electrical measurements of the resistance, giving an accurate measurement of the resistance variations by removing the resistance of the electrical printed lines, the pads and the cables. The four point measurement is realized with two coaxial cables which are connected to the circuit board through SMA connectors. The gauge mounted on the circuit board is illustrated in Figure 3.11.

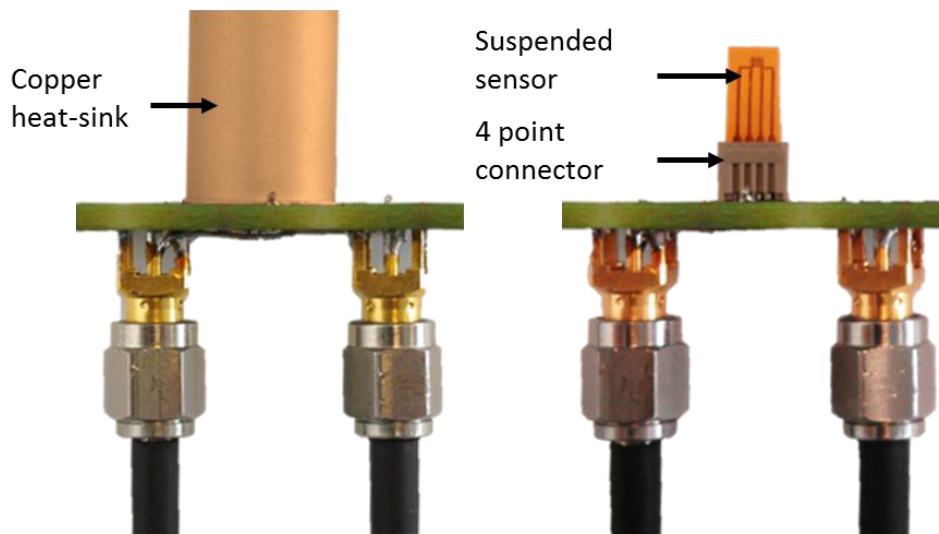


Figure 3.11. Mounting of the micro Pirani printed gauge.

III.4. Test bench

The circuit board with the gauge is placed in a vacuum-controlled chamber (Figure 3.12) in order to characterize its response to pressure variations. A reference micro Pirani pressure gauge MKS 925 is used to monitor the pressure in the chamber while a variable leak valve allows controlling the pressure. The resistance variation is measured with a four point method under a DC current supplied by a Keithley 2400 while the voltage is monitored by a Keithley 2700. Data are recorded with a Labview program.

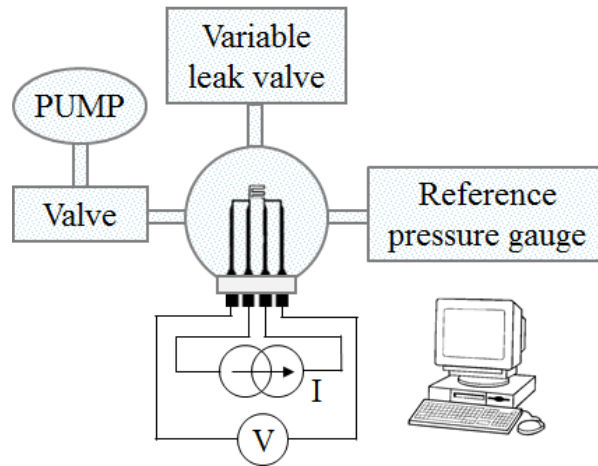


Figure 3.12. Test bench with controlled pressure.

III.5. Experimental results

a) Temperature coefficient of resistance

From the results in chapter 2.III.2, the TCR of inkjet printed silver annealed at 150°C during 5 hours should be around 900 ppm. °C⁻¹. The TCR of the printed Pirani gauge was measured in an oven in the range 25-100°C (Figure 3.13). The measured value is 910 ppm. °C⁻¹, in agreement with the previous results.

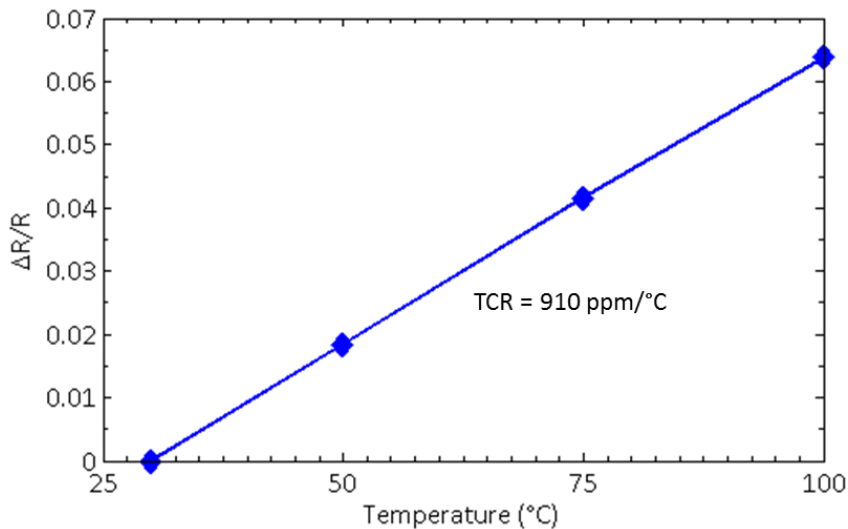


Figure 3.13. Experimental determination of the TCR of the printed Pirani gauge.

b) Set point determination

The nominal resistance R_0 of the sensor is 3.83 Ω measured at atmospheric pressure with 1 mA DC current. To determine the optimal current set point, the micro Pirani gauge is tested in the vacuum chamber both at atmospheric pressure and at 10⁻³ Pa. The relative resistance variation versus current at constant pressure is plotted in Figure 3.14. The TCR value combined with resistance measurements as a function of the applied current allows extracting the transducer temperature elevation according to equation (3. 2).

$$\Delta T = \frac{\Delta R}{R_0} \frac{1}{TCR} \quad (3. 2)$$

In Figure 3.14, relative resistance variation and temperature elevation curves are overlapped and follow the quadratic behavior dictated by Joule effect power dissipation. It must be noticed that above 40 mA the quadratic behavior is no longer respected at 10^{-3} Pa, probably because the sensor reaches a temperature higher than 100°C and the microstructure evolves. As a consequence, a safe value of 40 mA is chosen to perform the characterization of the gauge versus pressure as it offers the highest temperature elevation, and thus the highest sensitivity.

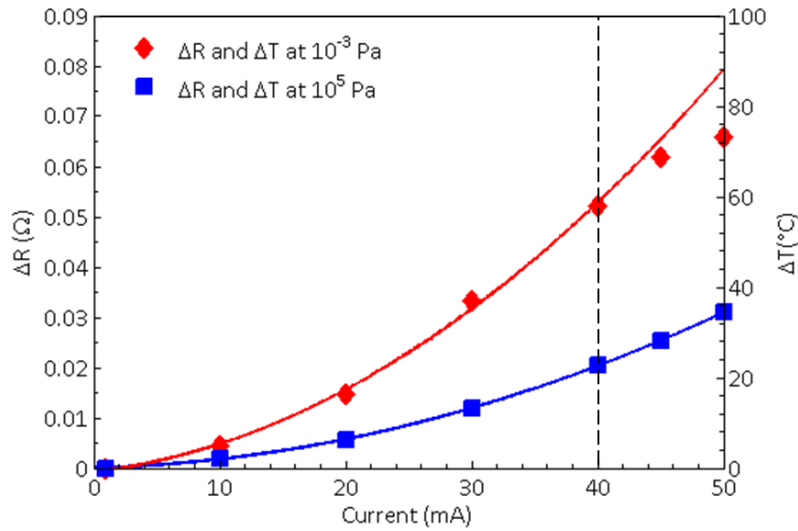


Figure 3.14. Resistance and temperature variation as a function of the applied current.

c) Gauge characterization

The resistance variation of the gauge with pressure was measured in the vacuum chamber under a DC current $I_{sp} = 40$ mA. The normalized resistance variation with respect to the resistance value of the device at 10^{-3} Pa under 40 mA is plotted versus the residual pressure measured by the reference MKS 925 Pirani gauge in Figure 3.15.

The measured sensitivity range goes from 10^{-2} to 10^4 Pa. It corresponds to a 4% variation of the resistance. Also, hysteresis of the response to increasing and decreasing pressure is lower than 0.2%.

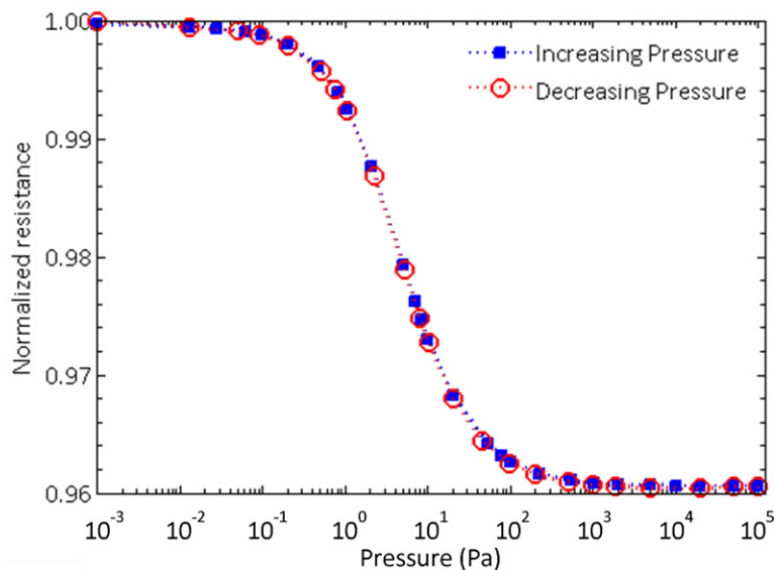


Figure 3.15. Variation of the normalized resistance versus chamber pressure for $I_{sp} = 40$ mA applied current.

III.6. Discussion

a) Thermal conductance of the system

The total thermal conductance G_{tot} of the micro Pirani gauge can be modeled with equation (3. 3) (Stark, 2003). Radiation losses are neglected because of the low temperatures involved.

$$G_{tot} = G_{solid} + G_{gas}(P) \quad (3. 3)$$

where G_{solid} corresponds to thermal conduction through the solid, which is constant with pressure, while G_{gas} is the thermal conduction of the gas, expressed by equation (3. 4) (Zhang, 2009).

$$G_{gas}(P) = G_0 \frac{P/P_{tr}}{1 + P/P_{tr}} \quad (3. 4)$$

where G_0 is the thermal conductance of air in the continuum regime and P_{tr} the empirical transition pressure. Knowing that the electrical dissipated power is related to the total thermal conductance by equation (3. 5), experimental data are fitted with a least square method in order to extract the values of G_{solid} , G_0 and P_{tr} . The fitted values are reported in Table 3.7.

$$G_{tot} = \frac{P_{elec}}{\Delta T} \quad (3. 5)$$

Table 3.7. Thermal conductance and transition pressure.

G_{solid} (W/K)	G_0 (W/K)	P_{tr} (Pa)
$1.23 * 10^{-4}$	$1.22 * 10^{-3}$	51.1

The experimental thermal conductance of the system and of the gas are plotted with pressure in Figure 3.16. On this graph, it can be noticed that the total thermal conductance sweeps across one decade. Its value in free molecular regime approaches solid thermal conductance G_{solid} while in continuum regime it tends to air thermal conductance G_0 .

The gas conductance, in the free molecular regime, decreases linearly with pressure. The lower limit of the sensitive range is imposed by the ratio G_{gas}/G_{solid} , which tends to zero in this regime. When the pressure is higher than P_{tr} , G_{gas} is approximately five times G_{solid} , meaning that gaseous thermal conduction is the main factor for power dissipation. The upper limit of the sensitivity range may be increased by narrowing the gap with the heat sink (Puers, 2002; Brun, 2012).

b) Power consumption

The maximum power consumption is 6.2 mW and it is reached in free molecular regime. Despite the high functioning current, this value is in the same order than those of micromachined Pirani gauge, mainly because of the low value of the sensor nominal resistance.

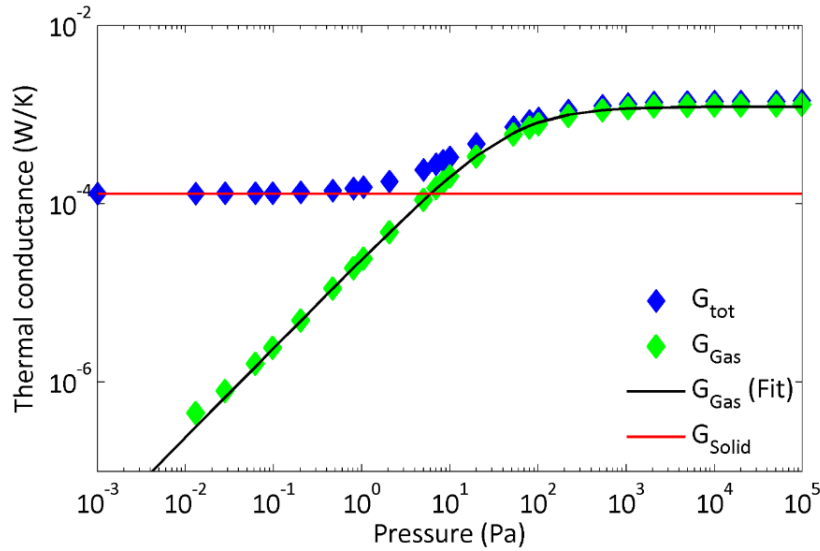


Figure 3.16. Total and gas conductance versus pressure.

III.7. Conclusion

Inkjet printing of silver nanoparticles on Kapton HN flexible substrate allowed the fabrication of the first printed micro Pirani gauge. The sensitive element of the gauge is a printed silver resistor with a measured TCR of $910 \text{ ppm. } ^\circ\text{C}^{-1}$. The characterization of the sensor showed a sensitivity range from 10^{-2} to 10^4 Pa in DC current functioning mode. Also, the response to increasing and decreasing pressure did not revealed any significant hysteresis.

In chapter 2, it was demonstrated that TCR values as high as $3000 \text{ ppm. } ^\circ\text{C}^{-1}$ can be reached with inkjet printed silver layers. However, the layer resistivity also drops with the annealing temperature. As a consequence, the required DC current to heat the resistor by Joule effect would be much higher. As an example, the same micro Pirani gauge annealed at 250°C during one hour required a DC current of 80 mA to obtain the same normalize resistance variation of 4% in the same pressure range. Hence, a trade-off has to be done between the sensitivity of the printed silver to temperature variations, the nominal resistance value and the power consumption. Finally, other measurements configuration such as Wheatstone bridge or working at constant sensor temperature with a current feedback should improve accuracy.

This work offers a novel application to inkjet printing of silver nanoparticles inks and demonstrates that printed sensors with performances similar to silicon micromachining can be achieved.

IV. Membrane switch

This work describes a membrane switch fully printed with silver nanoparticles on PI and PET substrates. It is focused on the electrical measurements of the contact resistance between two printed silver layers. The membrane switch was developed in the frame of the I2Flex project to qualify printing technologies for electrical contact applications. Inkjet printing is the technique of main interest, but LIFT technology was also tested. The final scope of this study was to design a flat-type switch for finger actuation that can be integrated in smart-cards. The specifications of the membrane switch are:

- An electrical contact resistance of 1Ω for an actuation force of 5N.
- Endurance up to 10^4 actuation cycles under cold and hot switching at 5V and 10 mA.

IV.1. State-of-the-art

The idea of inkjet printed membrane switches has been previously mentioned in the literature and in market forecasts for printed electronics. However, to our best knowledge, the demonstration of switching devices with an inkjet printed contact material has not been reported up to now. In this paragraph, an electrical contact manufactured by inkjet printing of silver nanoparticles is investigated.

A membrane switch is a temporary electrical switch for turning a circuit on and off. The typical structure of such a device consists in a stack of several layers, one at least being flexible (Figure 3.17). The top layer is bent under finger pressure to connect a pattern on the bottom layer. Membrane switches are typically used as an interface in remote controls, keyboards and other electronic devices. The main fabrication technique of the conductive patterns in commercial membrane switches is screen printing. The most employed materials are copper, silver and graphite. Screen printing requires a hard mask, inks with high viscosity and the typical final thickness of the patterns is around ten microns.

In this work, the design, fabrication and characterization of a fully inkjet printed membrane switch are presented. The aim is to demonstrate the potential of inkjet printing technology for electrical contact applications. The electrical and mechanical properties of the printed layer as well as its microstructure are investigated. Endurance tests under hot and cold switching are performed while actuation force and contact resistance are monitored.

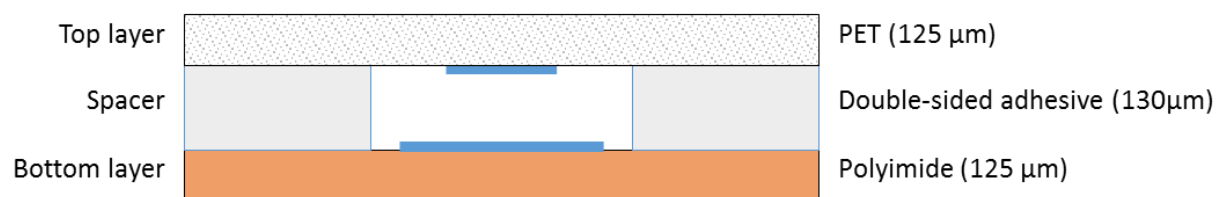


Figure 3.17. Cross-section of a flat type membrane switch.

IV.2. Membrane switch fabrication

a) Design

A simplified non-tactile membrane switch, i.e. without snap action, is designed. The studied device is a flat-type membrane switch composed of three layers (Figure 3.17). Commercial membrane switches usually incorporate a front graphic overlay and a rear adhesive layer.

The fixed contact part is printed on the bottom layer, a $125 \mu\text{m}$ thick Kapton HN sheet. The middle layer acts as a spacer, it has a circular opening of 8 mm diameter which allows mechanical contact between the top and bottom layers. The spacer is a $130 \mu\text{m}$ thick double-sided adhesive that defines

the contact gap. The mobile contact consists of a pill printed on the top layer which is a 125 μm thick PET sheet. The top layer is considered as the mobile element of the device, meaning that only the PET membrane is subjected to deformations under finger pressure. Thus, its mechanical properties, the spacer thickness and opening diameter define the restoring force of the contact.

The pattern of the fixed contact is illustrated in Figure 3.18. The four connection pads were employed to measure the contact resistance by a four point method. The contact zone is composed of four regularly spaced lines that can be connected through the 5 mm diameter circular contact pill.

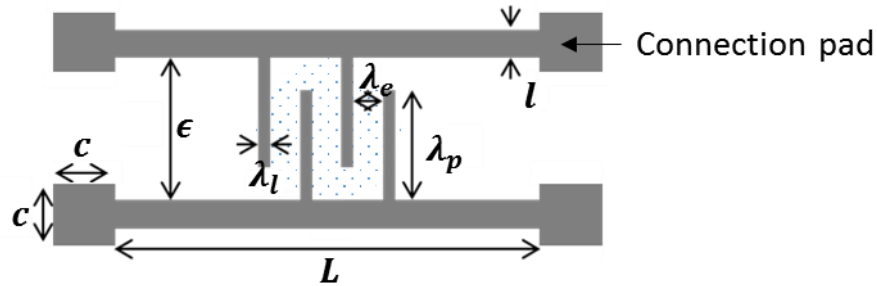


Figure 3.18. Top view of the pattern of the fixed contact. The dotted area corresponds to the potential contact zone.

Table 3.8. Dimensions of the fixed contact part.

c	3 mm	λ_p	3 mm
ϵ	4 mm	l	1 mm
λ_l	0.4 mm	L	26 mm
λ_e	0.4 mm		

b) Fabrication details

The membrane switch printed layers have been deposited with a semi-industrial prototype printer *JetPac* (cf. chapter 1). The *JetPac* printer (Figure 3.19) includes all the modules required to perform the fabrication steps for printed electronics. The first module consists in surface cleaning and, if necessary, surface energy enhancement using atmospheric plasma treatment. The second module includes two drop-on-demand inkjet printing heads and an alignment camera. The final module is dedicated to post-printing treatment and allows both UV curing for dielectric inks photopolymerization and microwave annealing for nanoparticles sintering.

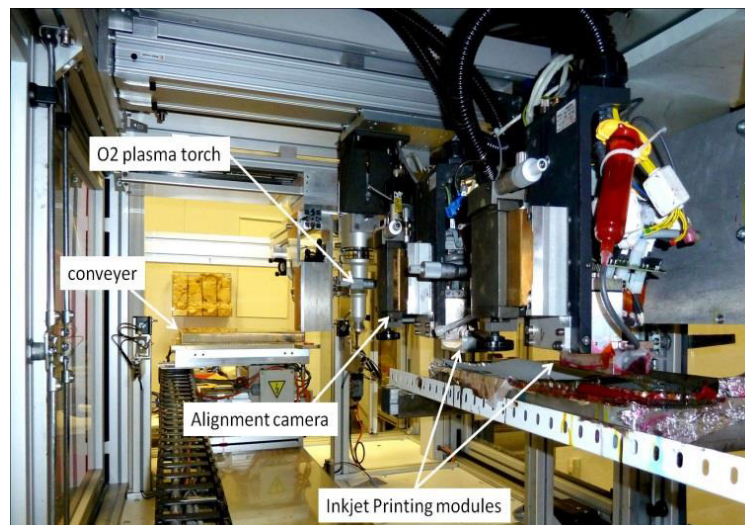


Figure 3.19. Inkjet printer *JetPac* prototype at the Center of Microelectronics in Provence (CMP).

Both bottom and top layers patterns were printed with an EMD5603 SunChemical silver nanoparticles ink. This ink has the same formulation as the EMD5714 except the weight percentage of silver, which is 20%. The ink rheological properties are reported in Table 3.9. The piezoelectric printer nozzles are actuated at 90V and their temperature is set to 35°C resulting in 30 pL droplets. The control of the nozzles temperature allows tuning ink viscosity in order to perform fine ink jetting and droplet generation. The patterns are printed with a resolution of 608 dpi, corresponding to a pitch of 42µm. Photographs of the printed layers are shown in Figure 3.20.

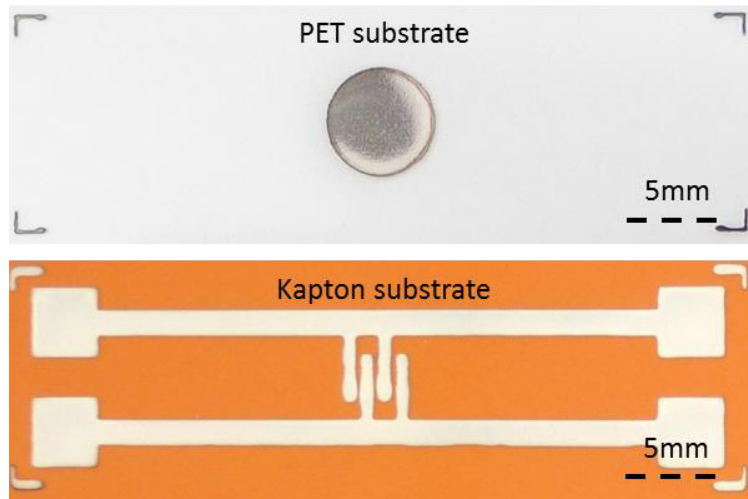


Figure 3.20. Top view of the top (a) and bottom (b) inkjet printed layers.

The properties of the top and bottom substrates are reported in Table 3.9. PI and PET substrate have similar surface energy values which allow proper wettability of the silver ink without changing printing conditions.

Table 3.9. Ink rheology and substrates surface energy.

Ink EMD5603 – SunChemical		
Viscosity at 25°C	10 – 13	mPa. s
Surface tension at 25°C	27 – 31	mJ. m ⁻²
Density at 25°C	1.24	
Bottom substrate - Kapton HN 125 µm - DuPont		
Surface energy	39 ± 4	mJ. m ⁻²
Top substrate - PET 125 µm - Toray		
Surface energy	46	mJ. m ⁻²

PET substrate can withstand temperatures up to 180°C, thus annealing was realized at 150°C during 1 hour on both patterns to get the same properties. The final device is presented in Figure 3.21.

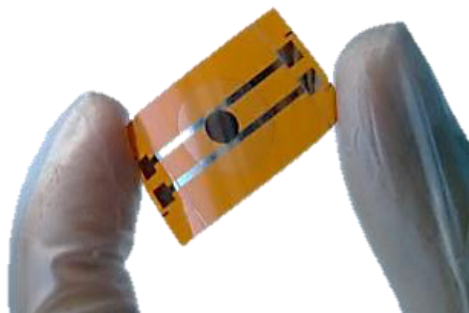


Figure 3.21. Prototype of the fully inkjet printed membrane switch.

IV.3. Experimental procedure

The device under test (DUT) is characterized on a test bench developed at our laboratory that allows both the measurement of the contact resistance and of the actuation force. The device reliability may also be assessed through mechanical cycling which is performed with simultaneous monitoring of the contact resistance and of the applied force on the membrane switch. The DUT is glued on a rigid substrate and aligned with a rubber knob actuator (5 mm diameter) thanks to a manual micrometric XY stage. A schematic view of the test bench is illustrated in Figure 3.22.

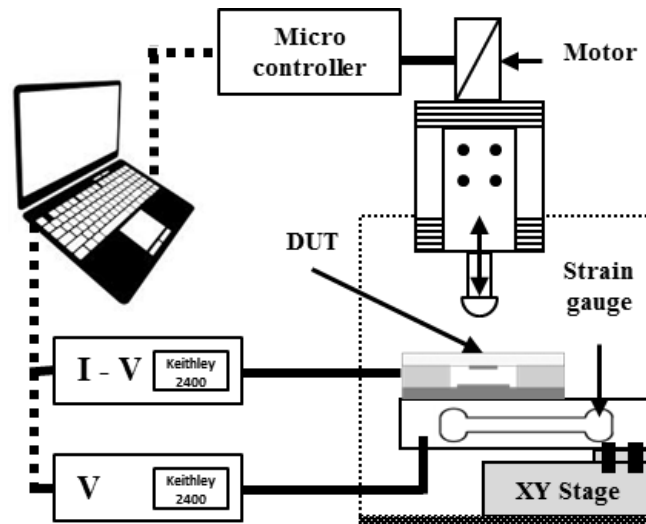


Figure 3.22. Cycling test bench.

The contact resistance is measured with a four point method by a Keithley 2400. The force applied on the strain gauge (Tedeia-Huntleigh 1042-30N) is measured by monitoring the unbalance voltage with a Keithley 2400 on a Wheatstone bridge powered by a constant DC voltage. The mechanical actuation is driven by a high-load motor Newport LTA-HL with $\pm 4 \mu\text{m}$ accuracy. Its maximum speed being 1mm/s, cycling frequency is around 0.5 Hz.

Reliability investigations have been realized under hot and cold switching cycling conditions. In the cold switching configuration, a DC voltage source is applied to the DUT whereas the current is measured. The source output is turned on only when the contact is closed.

In the hot switching configuration, a DC current source is applied to the DUT whereas the voltage is measured. The source output is always on during the approach of the contact pill, thus the open circuit voltage across the fixed contact lines corresponds to the voltage compliance of the current source. The cycling conditions are indicated in Table 3.10.

Table 3.10. Cycling conditions.

Cold Switching – 10^4 cycles	
V source	1 mV
I compliance	10 mA
Hot Switching – 10^4 cycles	
I source	10 mA
V compliance	5 V

IV.4. Experimental results

a) Inkjet printed lines microstructure

The printed silver layers are expected to have the same microstructure that was observed with EMD5714 (chapter 2). The microstructure of the EMD5603 silver layers was analyzed on 1 cm² pattern printed on silicon and annealed at 150°C.

Surface roughness R_a extracted from the AFM scans is 5.6 nm. Cross-section SEM observation allowed precise measurement of the thickness of the printed silver layers, whose value is of about 560 nm. This is about half the thickness obtained with EMD5714 silver ink, corresponding to the factor 2 on the silver weight percentage. Moreover, the microstructure in Figure 3.23 is very similar to the observations realized in chapter 2.

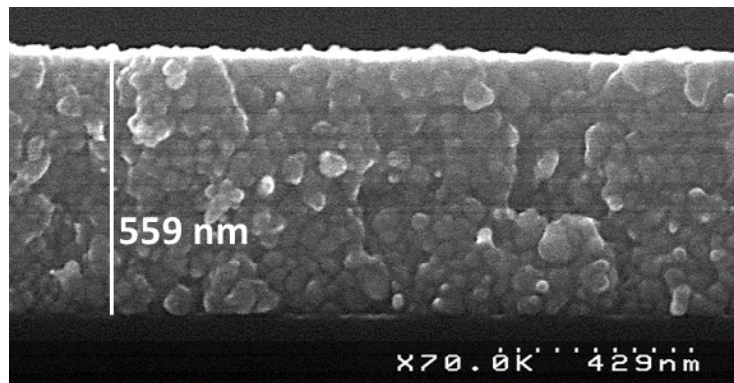


Figure 3.23. SEM observation of the printed silver layers (cross-section) of a sample annealed at 150°C.

b) Mechanical properties

To characterize the mechanical properties of the printed silver nanoparticles, nanoindentation tests were performed on a MTS-XP nanoindenter with a Berkovich diamond tip. The silicon substrate was preferred to Kapton because of its higher hardness and Young's modulus with respect to silver. Indeed, the extraction of elastic and hardness is much more reliable when studying a soft material on a hard substrate. The measured Silver Young's modulus is 31 ± 5 GPa and the hardness is 0.93 ± 0.1 GPa.

Finally, the lack of adhesion of the printed layer on the substrate was identified as a potential failure mode of the membrane switch. Because of the small surface of the printed samples, all the recommendations of the tape test - ASTM method D3359 – could not be applied. Results of the tape tests on the printed contact patterns on Kapton showed traces of peeling and removal, while on PET the printed layer remained firmly stuck.

c) Electrical properties

Resistivity was evaluated from 1 cm² printed patterns on Kapton substrate with a four point in-line spreading resistance measurement method. The resistivity measured on the printed patterns which compose the membrane switch is $6 \cdot 10^{-8}$ Ω.m, achieved with 150°C annealing during one hour. The value is about half the value measured for the EMD5714 silver ink in the same conditions.

IV.5. Membrane switch characterization

In order to evaluate the reliability of the electrical contact between inkjet printed silver lines, cycling tests were achieved on the test bench described in paragraph IV.3. The measurements of the actuation force and contact resistance are traced with the number of cycles in Figure 3.24 for hot and cold

switching conditions. Actuation force was set around 8N, although other tests have been performed between 4N and 13N.

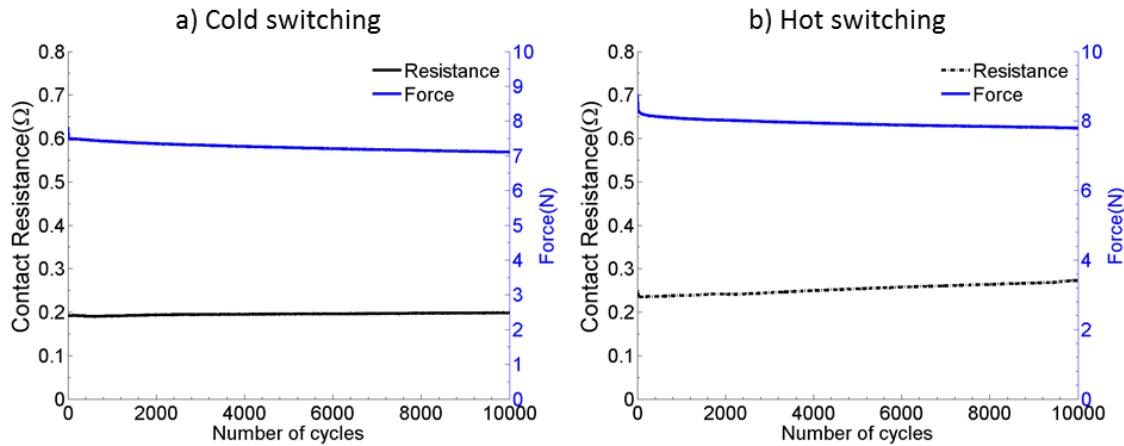


Figure 3.24. Actuation force and contact resistance of the membrane switch over 10^4 cycles. a) Cold switching. b) Hot switching.

The actuation force slowly decreases during the 10^4 cycles due to creep of the testing equipment and in particular of the rubber knob. As a consequence, a slight contact resistance increase can be observed. However, the cycling tests reveal that the membrane switch electrical contact remains stable despite the high actuation force involved. In cold switching cycling conditions, the evolution of the contact resistance is lower than in hot switching, demonstrating that hot switching corresponds to more drastic endurance conditions. Observations of the contact surfaces after cycling with AFM and optical microscopy did not reveal any major degradation such as delamination and cracking of the printed silver layers. Finally, cycling tests were performed up to 10^5 cycles (non-stop during one week), revealing the stability and reliability of the membrane switch.

In Figure 3.25, the contact resistance versus the actuation force is traced before and after the cycling test. The first contact is established around 2N, corresponding to the necessary force to bend the membrane over the contact gap. The contact resistance strongly decreases for actuation forces up to 10 N while for higher force its value tends toward a lower limit. According to Figure 3.25, the electrical contact resistance exhibits three steps, corresponding to the sequential addition of a contact line.

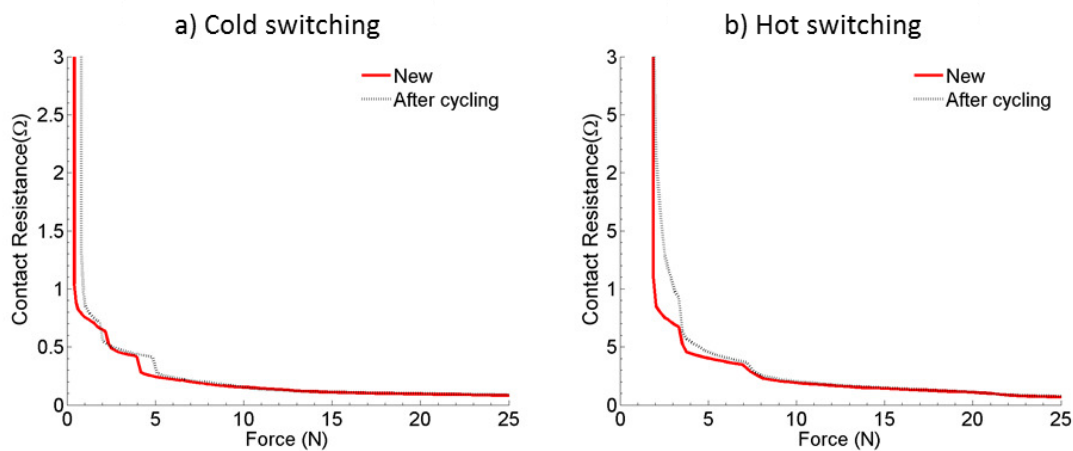


Figure 3.25. Evolution of the contact resistance before and after 10^4 cycles. a) Cold switching. b) Hot switching

IV.6. Electrical contact

When closing the membrane switch, a resistance network appears and evolves with the applied force on the top layer. As the contact pill spreads on the contact zone, a resistance decrease due to the contact area expansion is measured as illustrated in Figure 3.26.

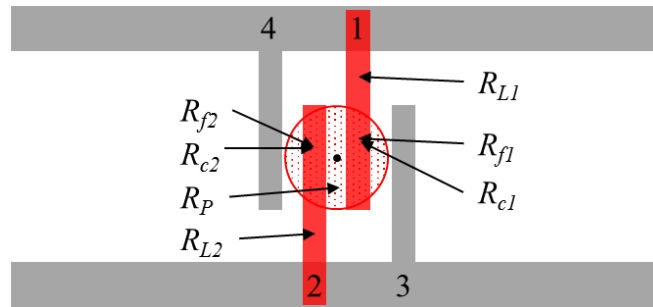


Figure 3.26. Increase of the contact area.

The total resistance resulting from the contact between the pill and the two central lines can be modeled with the equivalent electrical circuit in Figure 3.27. It is the sum of the series resistances of the contact lines R_{L1} and R_{L2} , the contact pill resistance R_{P12} , the film resistance R_{f1} and R_{f2} and the constriction resistance R_{c1} and R_{c2} . Both film and constriction resistances are located at the intersection of the contact pill and contact lines.

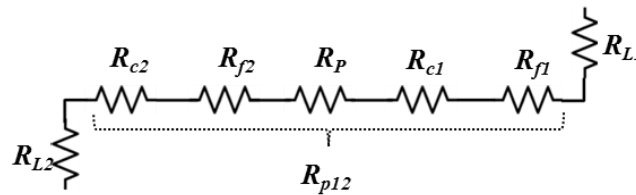


Figure 3.27. Model of the electrical contact between two lines and the contact pill.

Several arguments allow neglecting both the constriction and the film resistances compared to line resistance. Indeed, because of the membrane switch geometry and dimensions, high loads and large contact areas are involved. I-V plot at constant load reveal a linear behavior confirming that the electrical contact behavior corresponds to an ohmic regime. Low surface roughness $R_a = 5.6 \text{ nm}$ indicates a multi-spot contact configuration with large contact radii. Finally, the printed silver films have an average thickness of 570 nm and a resistivity of $6 \cdot 10^{-8} \Omega \cdot \text{m}$, owing to a full contact line a theoretical resistance of 0.79Ω , much higher of the eventual constriction and film resistances. As a consequence, the electrical contact can be simulated by considering only the line resistance with geometric approximation of the intersection of the contact lines and the contact pill. When the contact zone extends to the other contact lines, the electrical contact can be modeled as in Figure 3.28.

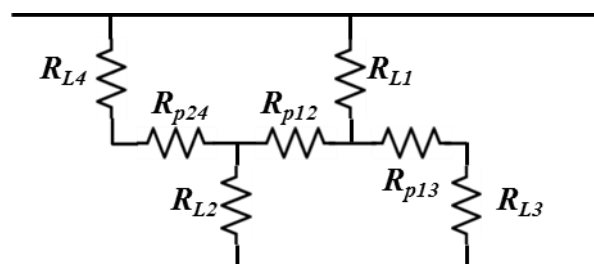


Figure 3.28. Equivalent electrical model.

The expansion of the contact pill on the contact lines was simulated on Matlab®. The contact pill and lines cannot be perfectly aligned, meaning that lines 3 and 4 are not connected at the same actuation force. In order to replicate this misalignment, the contact geometry is simulated by shifting the contact pill center by 100 μm from the contact lines center towards line 3. In the model, the contact radius is increased, and geometrical intersections of the contact lines with the pill are used to approximate the resistances R_{Li} and R_{Pij} using equation (3. 6).

$$R = \rho * \frac{L}{S} \quad (3. 6)$$

The resistance values calculated from the geometry are then introduced in the equivalent electrical circuit of the contact (Figure 3.28) and lead to the curve traced in Figure 3.29. The insets describe the different possible configurations of the contact between the silver pill and the lines. The curve shape is very similar to the experimental one. Also, the simulated and experimental contact resistance values are very similar, despite the large geometrical approximations and the neglecting of the constriction resistance.

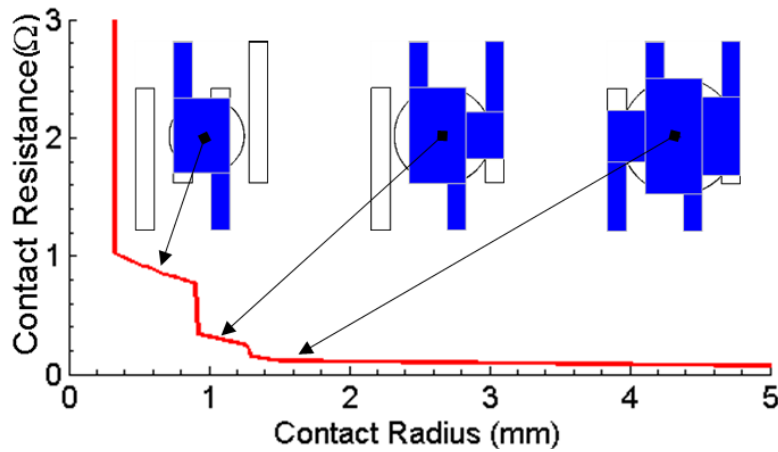


Figure 3.29. Simulated contact resistance of the membrane switch.

IV.7. LIFT membrane switch

In the framework of the I2Flex project, a membrane switch with similar design was fabricated by LIFT technique at LP3 laboratory in Luminy (France). These results were presented at E-MRS Spring Meeting 2013 (Ailuno, 2013).

The LIFT printed material was Harima silver nanoparticles paste whose properties are reported in Table 3.11. The donor substrate (quartz suprasil) was prepared with a doctor blade resulting in 10-20 μm thick silver paste layer. LIFT Printing was realized with a laser Nd:YAG at 355 nm wavelength and pulses were 50 ps long. Well-defined pixels were transferred at 100 mJ.cm⁻². After LIFT printing, the patterns were annealed at 220°C during one hour. The resulting thickness, measured with confocal microscope, is of about 15 μm. The measured resistivity on van der Pauw patterns was 6 μΩ. cm.

Table 3.11. Harima NPS paste properties.

Viscosity (mPa.s)	Particle size (nm)	Silver NPs wt%
70 – 120 · 10 ³	8 – 15	80 – 85

The contact pattern (Figure 3.30.a) was printed on a polyimide substrate. The contact electrodes were 350 μm large and 400 μm spaced. The circular contact pill (Figure 3.30.b) was also printed on polyimide and had a 5 mm diameter. The same 130 μm double-sided adhesive was employed for the spacer.

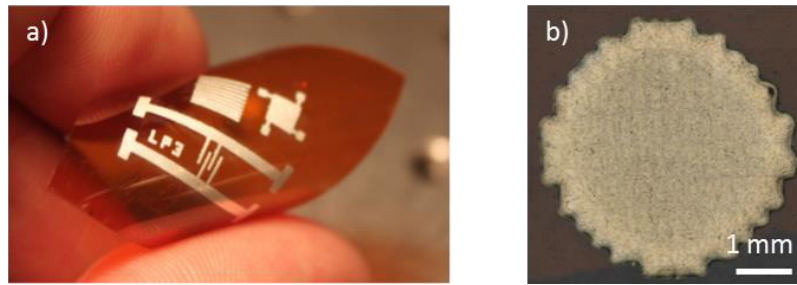


Figure 3.30. LIFT printed a) contact pattern and b) contact pill.

The LIFT membrane switch was cycled in the same conditions (cold and hot switching) as the inkjet printed device. Endurance tests revealed the stability of the contact resistance on 10000 actuation cycles at 8-9 N (Figure 3.31). The contact resistance is about twenty times lower than the values measured on the inkjet printed device. This large difference is due to the thicker silver layers and the higher annealing temperature.

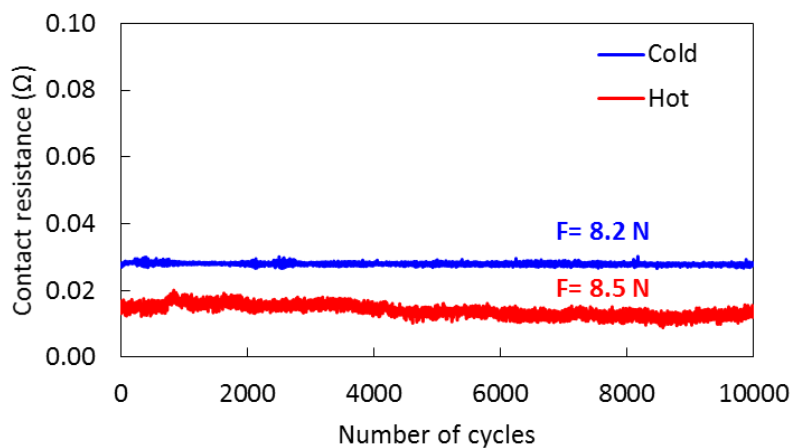


Figure 3.31. Contact resistance of the LIFT membrane switch over 10^4 cycles in cold and hot switching conditions.

IV.8. Conclusion

A fully inkjet printed membrane switch was designed, fabricated and characterized. The electrical contact between silver printed layers, despite their thickness of 560 nm, exhibits an electrical resistance lower than 1 Ω and can reach values as low as 100 m Ω under high actuation forces. The actuation force might be decreased by reducing the contact gap (spacer thickness). Even though resistivity could be lowered with higher annealing temperatures, a 150°C curing step remains compatible with most of plastic substrates. Also, printing with several passes could be considered to improve the printed layer electrical properties.

The realization of the membrane switch with LIFT technique resulted in lower contact resistance values than the inkjet device because of the thicker silver layers. The LIFT devices also fulfilled the initial specifications for the final application.

A simplified electrical contact model based on geometrical considerations qualitatively describes the behavior of the contact resistance with the applied load with an acceptable accuracy.

The printed material withstood actuation loads up to 10 N and up to 10^5 actuation cycles without any critical damage. This study demonstrates the potential of both inkjet printed and LIFT printed silver nanoparticles for electrical contact applications.

V. Printed Barium Strontium Titanate Capacitors

This paragraph is focused on the fabrication of Metal-Insulator-Metal (MIM) capacitors on silicon substrate. The aim of this work is to prove that printing technology can be used to efficiently process Barium Strontium Titanate (BST) varactors² on silicon with no need of complex clean room operations.

Here, the approach is substantially different than the previous prototypes. The silicon substrate is not flexible and has already been processed to realize a full-sheet platinum bottom electrode. Then, a dielectric layer is inkjet printed with a BST sol-gel. This allows the direct-patterning of the dielectric layer and avoids lithography and etching usual steps. Finally, a top electrode is printed with silver ink.

V.1. State-of-the-art

Barium Strontium Titanate (BST) films have been studied for more than 20 years especially for their tunable properties (Padmini, 1999; Cole, 2002; Tagantsev, 2003; Noren, 2004; Zhu, 2009). Indeed, BST exhibits a large variation of dielectric constant when an external DC electric field is applied. Moreover, BST can handle large radio frequency (RF) power as high as 30 dBm (Entesari, 2008). Besides, BST composition can be chosen in order to avoid any hysteretic behavior, which in turn reduces dielectric losses and simplify the associated electronics (Tagantsev, 2003; Setter, 2006). Consequently, BST-based materials are nowadays the best tunable dielectric candidates to fulfill the tough requirements of tunable RF varactors for impedance matching. Industrial solutions have even been very recently proposed.

Technologically speaking, BST can be deposited by several means, namely Pulsed Laser Deposition (PLD) (Craciun, 2000), sputtering (Zhu, 2009), sol-gel (Wang, 2008) or MOCVD (Sbrockey, 2011). Each of these techniques is mostly compatible with microelectronic standards and requires photolithography and etching steps.

A promising alternative deposition technique could be inkjet printing, enabling to quickly process small series of devices. In the case of BST, this technique has been already investigated in the literature. In 2007, Kaydanova *et al.* printed 420 nm thick - Ba_{0.6}Sr_{0.4}TiO₃. BST was deposited on MgO substrate and interdigitated (IDT) structures were used to demonstrate the tunability of printed BST at 1 MHz. In 2013, Nikfalazar *et al.* showed that IDT structures of copper-fluorine-co-doped Ba_{0.6}Sr_{0.4}TiO₃ printed on alumina were able to work until 12 GHz. Recently, the same team proved that BST MIM varactors can be printed on a bottom electrode made of Cr/Ni/Au that was deposited and patterned by lithography on alumina substrate (Nikfalazar, 2014). The top electrode was made by gold electroplating and photolithography.

V.2. Experimental procedure

a) MIM capacitor design

MIM capacitors are planar passive components whose basic structure consists in stacking three layers, namely a bottom electrode, a dielectric and a top electrode. The capacitance C is defined by the surface of the smallest electrode and can be calculated with the well-known formula:

$$C = \epsilon_0 \epsilon_r \cdot \frac{S}{t} \quad (3.7)$$

² Varactors are capacitors whose capacitance can be tuned by mean of a DC electrical field.

where ϵ_0 and ϵ_r are respectively the vacuum and relative dielectric permittivity, t the thickness of the dielectric layer, and S the area of the smallest electrode.

In this work, the objective is to show that BST capacitors can be fully printed on a bottom sputtered platinum electrode. For this proof of concept, two capacitors design were realized:

- The first was designed for capacitance values in the order of nanofarads for low frequency (LF) measurements in the kHz range;
- The second was designed for capacitance values in the order of picofarads for RF measurements in the GHz range.

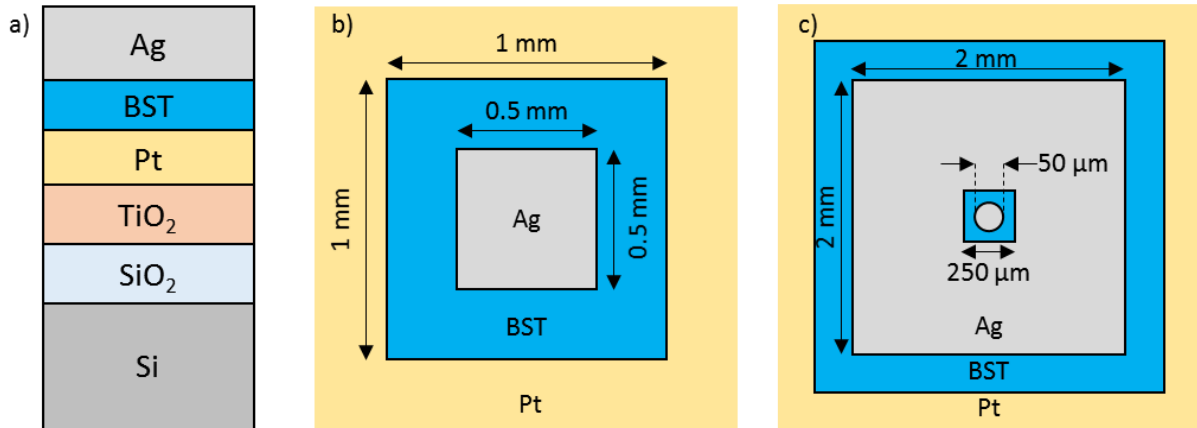


Figure 3.32. BST MIM capacitors design. a) Stack. b) Low frequency capacitor. c) RF capacitor.

b) Fabrication details

The MIM capacitors were fabricated on a 200 mm-diameter silicon wafer. After 0.5 μm -thick thermal oxidation, 10 nm thick TiO_2 and then 100 nm thick Pt were sputtered on the wafer, acting as bottom electrode. Printing of the dielectric layer and top electrode was realized on the Dimatix DMP2831.

The first printed layer is made of commercial BST sol-gel with 7% weight percentage. The exact composition of the sol-gel, designed for spin-coating deposition, is reported in Table 3.12. Its main component is the isoamyle acetate solvent, which defines both its viscosity and surface tension. Two BST patterns were printed, namely rectangles of 3x2 cm^2 and squares of 1 mm^2 . Printing resolution was set to 476 pixels per cm, corresponding to a pitch of 21 μm between adjacent droplets.

Table 3.12. Composition and properties of BST sol-gel.

	Viscosity (mPa.s)	Surface tension (mJ/m ²)	wt%
BaO	-	-	3
SrO	-	-	1
TiO ₂	-	-	3
Isoamyl acetate	0.741	24.7	88
Isoamyl alcohol	4.37	23.73	5

BST sol-gel viscosity is around 1 mPa.s, defined by the solvent viscosity, which is one order of magnitude lower than the range recommended for the Dimatix printer. In order to obtain a correct ink ejection, the actuation voltage was set to 13 V and the nozzles were kept at ambient temperature. The actuation waveform used was the same as in chapter 2.1.3, Figure 2.5. BST droplet ejection versus time is illustrated in Figure 3.33. The droplet diameter is 24 μm , corresponding to a volume of 7.2 pl. In the

second photograph of Figure 3.33, a satellite droplet appears because of the filament break. This satellite droplet is then absorbed by the main droplet and remains stable at a distance of 120 μm from the nozzle. Here, the nozzle-substrate distance was set to 350 μm (600 μm for silver ink) to reduce the time of flight of BST droplets. Increasing the actuation voltage caused a longer filament and a higher velocity of the main droplet. Hence, filament break induced satellite droplets that could not catch up with the main droplet. Satellite droplets lower the quality of the printing and might induce killer defects such as holes in the dielectric layer inducing short-circuits between bottom and top electrodes.

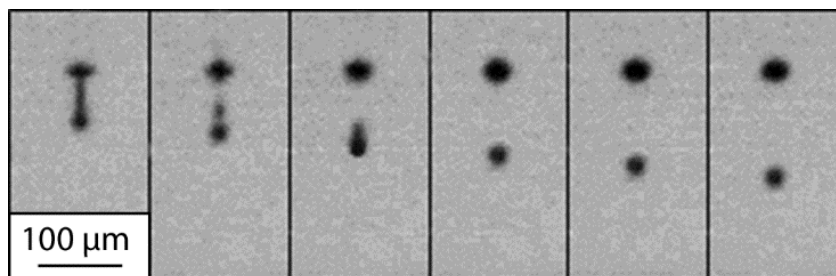


Figure 3.33. Sequence of photographs of the ejection of BST sol-gel droplets. Interval: 8 μs .

After BST printing, the wafer was dried on a hot-plate for 5 minutes at 130°C followed by 5 minutes at 360°C for calcination of organic compounds. Finally, crystallization was performed by Rapid Thermal Annealing (RTA) at 700°C under O₂ for 1 minute.

The final step of the MIM capacitors fabrication consists in printing the top electrode. The ink EMD5714 from SunChemical at 40 wt% of silver nanoparticles was employed. Printing conditions were the same as in paragraph I. A second annealing was then realized at 250°C for one hour to anneal the silver ink.

c) Characterization

➤ X-Ray diffraction and Microstructure

The printed BST layer crystalline orientation was measured by X-Ray Diffraction (XRD) on a four circle X-Pert PANalytical diffractometer using a fixed divergence $\frac{1}{2}^\circ$ slit, a Cu W/Si mirror, a Soller slit and a 10 mm mask as incident optics and a parallel plate collimator, a Soller slit, a graphite monochromator and a proportional detector as diffracted beam optics. The $\theta/2\theta$ symmetrical measurement was performed from 20° to 50° in 2θ , with scan step size of 0.05° and an acquisition time of 5s per step. XRD was realized on the large BST 6 cm² rectangles.

The surface roughness was measured on a Veeco 3100 AFM. The microstructure of the MIM capacitors was analyzed by Field-Effect Scanning Electron Microscopy (FE-SEM) (Hitachi 5500) on cleaved and FIB-milled cross-sections.

➤ Electrical characterization

The low frequency capacitors were measured on a manual prober with an Agilent HP-LCR meter with a 10 kHz AC signal with 50 mV amplitude.

The RF measurements were performed on a semi-automatic prober with a RF ground-signal-ground probe. Spectral response of the capacitor was recorded with a Vectorial Network Analyzer (VNA) Agilent N5230A from 100 MHz up to 2 GHz after a Short-Open-Load calibration. DC bias was applied by an Agilent E3631 DC source. Capacitance and dielectric loss of the measured capacitors were deduced from S11 parameters.

V.3. Results

a) Printed capacitors

The low frequency and RF capacitors are respectively illustrated in Figure 3.34.a and b. Image analysis allowed measuring the surface of the top printed silver electrode, which defines the capacitance value.

- Area of the low frequency capacitor top electrode: 0.32 mm^2 .
- Area of the RF capacitor top electrode: $3 \cdot 10^{-3} \mu\text{m}^2$.

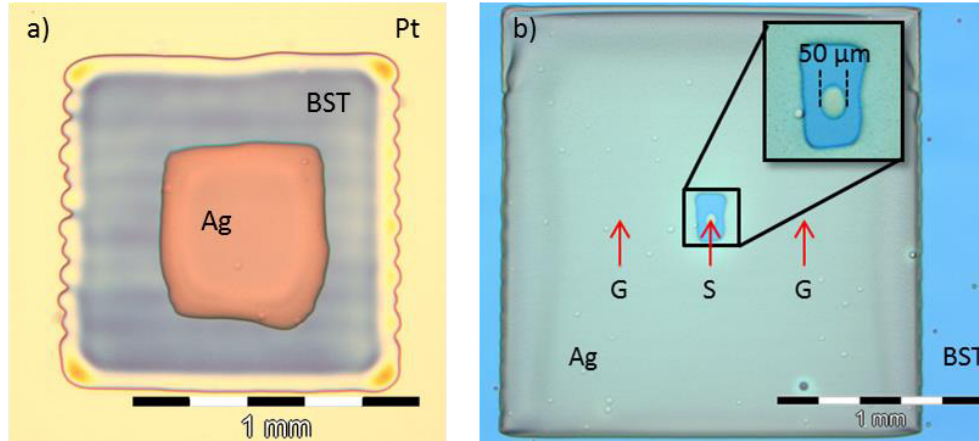


Figure 3.34. Printed BST MIM design. a) Low frequency capacitor. b) RF capacitor.

The surface roughness of the inkjet printed BST on the platinum electrode after crystallization is $R_a = 1.46 \text{ nm}$. This value is similar to the surface roughness of crystallized BST sol-gel deposited by spin-coating in our laboratory. As depicted in Figure 3.35, the $\theta/2\theta$ X-ray diagram shows that the deposited BST film is crystallized in perovskite phase only. The diffraction pattern is very similar to BST powder, meaning that there is no preferential orientation.

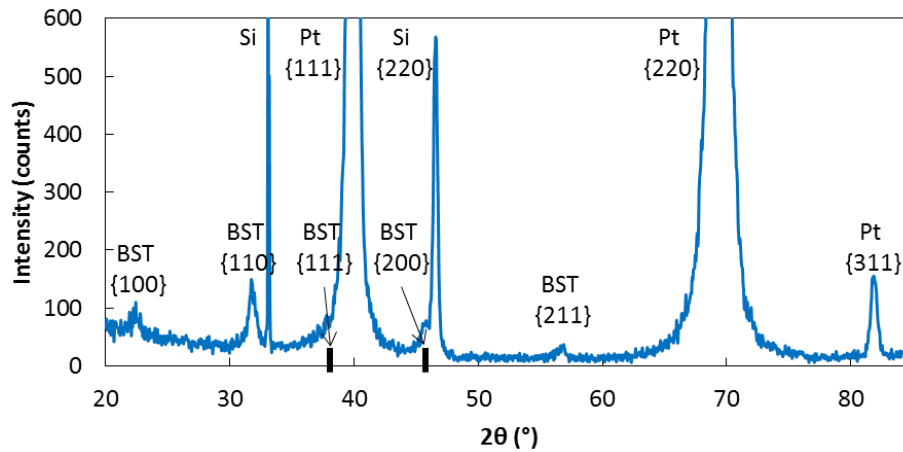


Figure 3.35. $\theta/2\theta$ X-Ray diffraction spectrum of a 6 cm^2 BST printed rectangle.

The MIM capacitor was cleaved manually and FIB-milled for FE-SEM observation (Figure 3.36). The respective thickness of each layer is reported in Table 3.13.

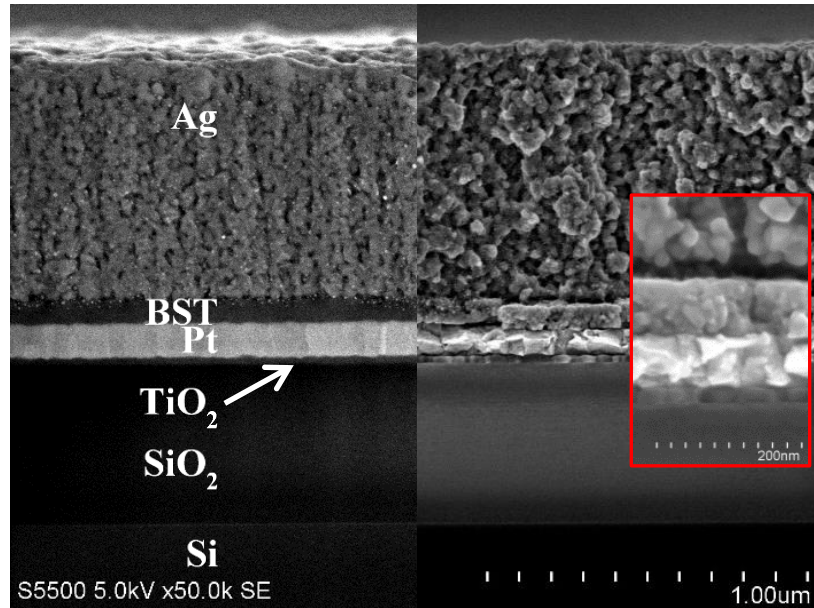


Figure 3.36. FE-SEM observation of the cross-section FIB-cut (left) and cleaved (right).

The silver top electrode is much thicker than the other layers. The microstructure is polycrystalline and porous. Both grains and pores dimensions are around 70 nm, in agreement with the results in chapter 2.II.3. According to the electrical characterization in chapter 2.III.1, after annealing at 250°C for one hour, the expected electrical conductivity is $2.10^7 \text{S} \cdot \text{m}^{-1}$. Crystallized BST thickness is 65 nm, its microstructure is polycrystalline with low porosity and there are no large cracks.

Table 3.13. Measured thickness of the MIM capacitor layers.

Silver	750 nm
BST	65 nm
Pt	100 nm
TiO ₂	18 nm
SiO ₂	500 nm
Si	Substrate

b) Capacitance measurements

The LF capacitor exhibited a capacitance value of 3.4 nF at 10 kHz. From the top electrode area of 0.32 mm² and the BST thickness of 65 nm, one can infer a relative dielectric constant of the BST dielectric layer of about 100. On this capacitor, the application of an electrical field caused a voltage breakdown of the BST dielectric layer. This was probably caused by thickness irregularities of the dielectric causing a localized high electrical field.

RF measurements performed on the BST MIM capacitor show that BST behaves like an actual capacitor of 18.2 pF at 2GHz. Observing the silver electrode after electrical measurement showed that a third of its surface was damaged by the RF probe. Thus considering an electrode area of $2.10^{-3} \mu\text{m}^2$ and the thickness of BST layer 65nm, one can calculate the relative dielectric constant ϵ_r and the dielectric losses $\tan\delta$, plotted versus the applied electrical field in Figure 3.37. ϵ_r decreases from 67 to 61 as long as electric field increases whereas $\tan\delta$ remains nearly constant at 0.18.

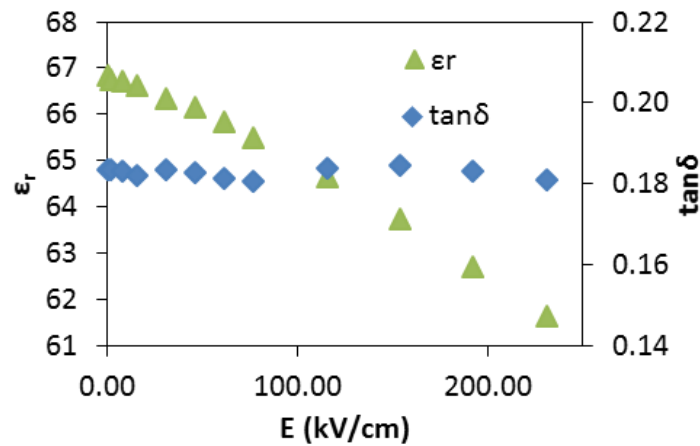


Figure 3.37. Relative dielectric constant and dielectric losses at 2 GHz.

V.4. Discussion

In the case of dense and smooth substrates, the interaction between the ink and the substrate is driven by their respective surface energies. The average surface energy of Pt is $2.7 \text{ J} \cdot \text{m}^{-2}$ (Mezey, 1982), which is much higher than the surface tension of BST solvent. Hence, BST droplets are expected to greatly spread on the Pt surface. This is inferred by the 30% larger surface of BST compared to the 1 mm^2 initial design. Besides, the edges of the BST printed patterns exhibit a yellowish outside ring due to lower BST thickness (Figure 3.34.a). This phenomenon is caused by the lower covering of the droplets at the pattern edges. Indeed, the color of the BST layer becomes homogeneous at a $80 \mu\text{m}$ distance from the borders, where each droplet has the same number of neighboring droplets.

Thickness homogeneity and sharp edges of printed layers are among the main challenges of inkjet printing. There are ways of improvement by optimizing droplets positioning and solvent evaporation that might induce coffee-ring effects (Soltman, 2007).

Besides, Figure 3.36 reveals that BST/Pt and Ag/BST interfaces are well defined, all interfaces being very neat whatever the sample prepared, either cleavage or FIB. In particular, the silver does not diffuse through BST, even after annealing at 250°C . However, the lower dielectric constant than usual suggests that silver is not optimal as top electrode, though very practical to be inkjet deposited. This result proves that Ag is compatible with BST.

It is also worth reporting that inkjet BST has the same XRD pattern as BST processed in different ways in our lab, either by sol gel or sputtering (Zhu, 2009). No secondary phase is observed and no strong crystalline orientation has been spotted.

The decrease of ϵ_r versus applied electrical field reported is in line with what one would expect from a perovskite thin film. Note that ϵ_r is basically a third of the value published by Basceri *et al.* (1997) in their reference paper on BST thin films deposited on Si substrate for such thickness range. Note that their results were collected at 1 kHz and ours at 2 GHz. It is also very likely that the silver top electrode has a negative influence on the dielectric results, as the standard metal is Pt rather than any other metal. The losses could be considered as large but they are mostly dominated by the resistive contribution of the bottom electrode and not the film dielectric losses themselves. A rough estimation of the series resistance imposed by the bottom electrode made of Pt is 1Ω (Pt film resistivity = $18 \mu\Omega \cdot \text{cm}$) while BST impedance module is around 5Ω at 2 GHz. Therefore, as no de-embedding of the series resistance has been performed, losses in the 20% range are logical ($= 1/5$). The quite constant

value of $\tan\delta$ versus field is also a clue that resistive losses are involved rather than dielectric losses that normally follow the behavior of ϵ_r with field. The slight increase of $\tan\delta$ versus field in the 100-200 kV/cm window is therefore well explained by the constant value of resistance associated with the decrease of the dielectric constant.

The tuning ratio C_{max}/C_{min} is 10%, which could sound rather weak compared with the literature (Basceri, 1997). However, the main reason is related to the small maximum field withstood by this inkjet BST around 200 kV/cm. However, the intrinsic tunability of this film is very similar to 0.5 μm thick sputtered BST reported by Tagantsev (2003) for the same electrical field. It shows therefore that tunability is equivalent to well crystallized BST films. The reason for the weak breakdown field is most probably related to:

- 1) Ag/BST interface as Ag is normally used only for BST ceramics and not for thin films;
- 2) and non-optimized process that could induce slight cracks in BST films inferring a local thinner thickness resulting in a stronger local field.

Finally, we assessed how much BST precursors can be saved by using this inkjet technique instead of standard sol gel spin coating. From our estimation, the consumption ratio is basically 40 in favor of inkjet. To do so, we considered that 100% of the final substrate has been covered with BST, which is normally far from being true. It means that this ratio of 40 is a lower bound for raw material consumption and practically speaking it is even larger than this. Therefore using this inkjet technique could end up with substantial savings not only on processing but also with respect to precursors as well.

V.5. Conclusion

In this paragraph, we show that it is possible to process BST thin films by inkjet deposition on silicon substrate without using lithography and etching. A BST sol-gel that was not designed for inkjet printing has been used to realize both LF and RF capacitors.

The LF capacitor was functional with a capacitance of 3.4 nF. However, the tunability of dielectric with an electrical field layer could not be measured because of voltage breakdown. This result shows the limits of inkjet printing for patterning layers with high thickness homogeneity. The RF capacitor remained functional up to 2GHz, with most of characteristics similar to what is obtained with standard BST films processed in clean rooms. Moreover, thanks to the smaller top electrode area, tunability of the dielectric constant of 10% was demonstrated.

The developed technology infers using 40 times less BST precursor amount than standard sol-gel deposition mean. Consequently, this inkjet technology enables to prepare functional BST films on silicon substrate inducing many perspectives for electronics applications, in particular for impedance matching in the GHz range.

Conclusion

The results presented in this chapter demonstrate that silver printed layers can be used to achieve much more than electrical interconnections. The technological background for the design of sensors and RF components, as well as the knowledge in device characterization of our laboratory made the design, fabrication and characterization of several fully printed prototypes:

- A 17 GHz band-pass filter with 3.6 dB insertion losses
- A micro Pirani vacuum sensor working between 10^{-4} and 100 mbar.
- A 250 μm thick membrane switch working after 10^5 actuation cycles at 5 N.
- A low frequency and a RF MIM tunable capacitor working at 2 GHz.

The extended analysis of the printed silver layers achieved in chapter 2 allowed the optimization of the printing and annealing conditions to fulfill the requirements of the designed components. In particular, the small gaps (50 μm) of the feed lines of the RF filter required an optimization of the printing conditions on all fronts: ejection parameters, pattern resolution, pixels arrangements, substrate temperature, and drying conditions. However, the time spent on the improvement of the printing led to reliable and repeatable printing conditions that revealed more than useful for the preparation of all the other samples.

Finally, the versatility of the inkjet printing process allowed adapting the patterns to the existing test benches in our laboratory, minimizing the efforts for the devices characterizations. The only exception was for the endurance bench entirely developed for the mechanical cycling with contact resistance and actuation force measurement to assess the reliability of the membrane switch.

General Conclusion & Perspectives

The main objective of this work was to contribute to the development of functional printing by enhancing the connections between inkjet printing and material science. In the framework of the research activities of Leti and LGP2, we have mobilized our knowledge and know-how in electronics design, materials and components characterization to develop a new expertise in printing technology.

In the first chapter, the state-of-the-art of printing technologies for functional printing was presented and our attention was drawn towards inkjet because of its several assets. Indeed, inkjet printing, as a non-contact direct-writing technique, offers innovative opportunities in the fabrication of electronic devices. It can be adapted to rigid, flexible and even 3D shaped substrates, a large spectrum of printable materials can be found on the market, and the available inkjet printing equipment allows patterning features with minimum dimensions in the order of 10 μm . Last but not least, the digital source-patterns of inkjet offers design flexibility that is of much interest for prototyping and small series fabrication.

Among the spectrum of printable materials, silver nanoparticles inks are undoubtedly the most widespread with many commercial references, and they were thus selected for this study. Silver inks exhibit the lowest achievable electrical resistivity and a long shelf-life (more than one year). The well-controlled fabrication of silver nanoparticles allows the formulation of inks with high silver load (up to 60 wt%), and low dispersion of the NPs size.

Metallic nanoparticles inks require a post-printing thermal annealing to achieve conductive patterns. This step induces an evolution of the printed layers microstructure affecting their intrinsic properties. We have inferred this evolution by microscopic analysis in the range 100-300°C. AFM and SEM images of our samples are illustrated in Figure C.1.

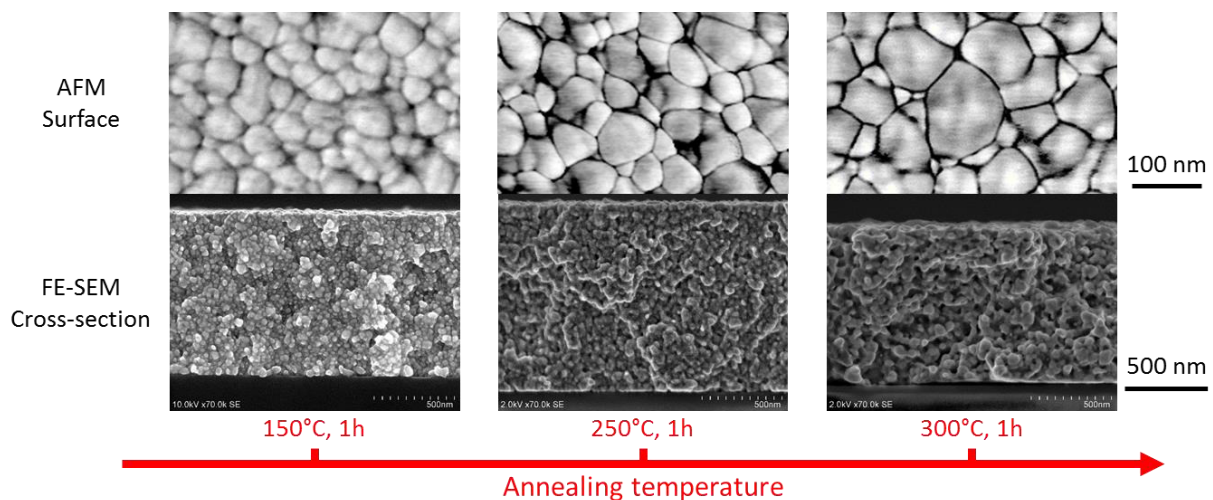


Figure C.1. Evolution of the microstructure of inkjet printed silver nanoparticles layers.

In the second Chapter, we have focused on the evolution of the intrinsic properties of the printed silver layers. Our characterization tools were hence adapted to their features. The investigation of the microstructure resulted in typical measurements of roughness and grain size, highlighting normal and secondary growth mechanisms. Moreover, SEM observation revealed a porous microstructure with dimensions below 100 nm. The quantification of porosity rates at such dimensions was a real challenge. FE-SEM observation of FIB-milled cross-sections gave accurate results in 2D that were corroborated by the 3D reconstruction of a silver layer by FIB-SEM slice-and-view. We have recently investigated the silver layers with electronic tomography on a 300 nm diameter cylinder. This

technique offers a much higher resolution than FIB-SEM slice-and-view, especially for the 3D characterization of the grain boundaries (Figure C.2).

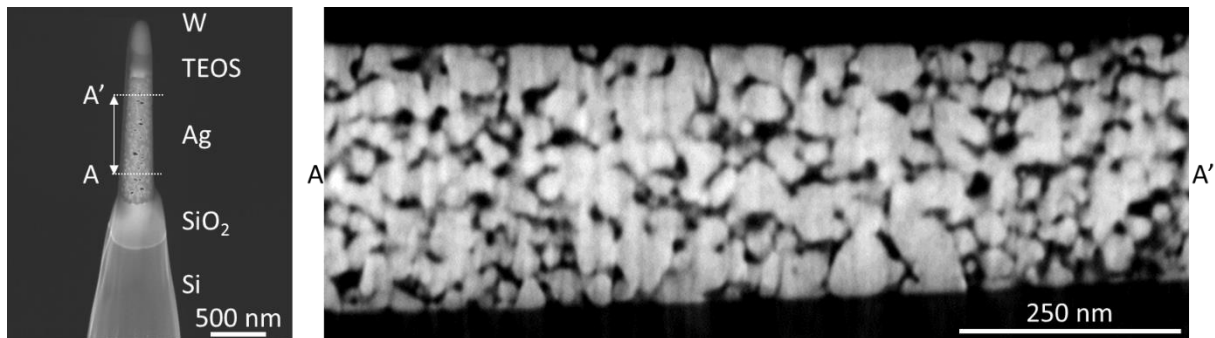


Figure C.2. Electronic tomography of a printed silver layer annealed at 150°C during 1 hour.

Afterwards, electrical and mechanical properties of the printed layers were studied as a function of the annealing temperature focusing on the following parameters: electrical resistivity, temperature coefficient of resistance, Young's modulus, and hardness. Because of the porous and polycrystalline microstructure, the measurement of these properties required adjusting our equipment as well as the analysis methods. In this characterization study, the accuracy of the measurements was always questioned. Hence, to ensure the reliability of our results, they were either correlated one-to-another or to theoretical models. In this chapter, the results were obtained on a single commercial silver ink. It would be of much interest to employ these experimental protocols to qualify and characterize other metallic nanoparticles inks. Moreover, our study focused mainly on thermal annealing in oven under standard atmospheres conditions. When using other annealing methods are available, a different evolution of the silver nanoparticles is to be expected. Attempts were realized with laser annealing in the UV range (192 nm). This method revealed poorly effective because of the low absorption rate of silver. Also, we had the opportunity to test a Xenon flash from Polytec PI on silver layers printed on polyimide and silicon oxide on silicon substrate. These trials emphasized the influence of the substrate thermal properties when exposing samples to light flashes: with two flashes on polyimide, silver patterns exploded while at least twenty flashes were necessary to remove the bluish color of the undried ink.

The detailed characterization of the silver layers features led to the final part of this study, namely the prototyping of inkjet printed electronic devices. We have first focused on the design and fabrication of a 17 GHz band-pass filter on a flexible and low-cost substrate compared to standard RF substrates (quartz and sapphire). The filter pattern had compelling dimensions near the resolution limits of the Dimatix printer. A methodical improvement of the printing conditions on a polyimide substrate eventually resulted in stable and reliable printing conditions that were used along the whole thesis.

The optimization of the printing conditions led to the reliable and repeatable printing of silver patterns for the realization of:

- i. **A 17 GHz band-pass filter printed with one and two layers.** The characterization of the two layers filter demonstrated transmission losses as low as 3.6 dB. Simulations of the device showed that these losses mainly occur because of the polymer substrate. They could be improved by reducing its thickness, however thermal constraints during annealing in oven led to cracks and delamination. The use of a selective annealing techniques such as photonic or microwave might prevent the experienced failure mechanisms.

- ii. **A micro-Pirani gauge sensitive between 10^{-4} and 100 mbar.** The sensitivity of this gauge can be increased with the annealing temperature. Indeed, a higher TCR would offer higher resistance variations to temperature and thus pressure. Nevertheless, this would also decrease the resistivity of the sensor making the measurement more difficult. A Wheatstone bridge measurement configuration seems a suitable solution to free oneself from very low voltage measurements (in the order of microvolts).
- iii. **Low frequency and radio-frequency tunable capacitors printed on platinum substrate.** The MIM structure of the capacitors was achieved by inkjet printing a BST sol-gel for spin-coating processes. Printing conditions were found to print this solution that was not designed to fulfill inkjet ejection requirements. The successful realization printing of the BST sol-gel highlights the versatility of the printing process. Moreover, the direct-writing of ceramic materials such as BST offers promising fabrication assets: it decreases consumption of precursors by at least a factor 40 and it removes the difficult etching steps of crystallized ceramics.

Finally, a **250 μm thick membrane switch** was fully inkjet printed in the frame of the I2Flex project on the *JetPac* industrial inkjet printer prototype. Endurance tests demonstrated that inkjet printed silver layers are compatible with electrical contact applications. The demonstrator that was realized offers new opportunities to inkjet patterning in smart cards and keyboards systems.

In this thesis, which mainly took place in the silicon environment of Leti, studies were conducted to evaluate the potential of inkjet printing to solve some issues in standard microelectronics.

➤ Through Polymer Vias (TPV) filling

TPV are vertical electrical connections between two levels of electronic devices. This type of structures allows increasing the density per unit area thanks to the 3D stacking of silicon chips. Large vias with 80-100 μm were filled with silver ink on the Dimatix printer resulting in a conductive liner deposited on the walls of the vertical holes. Larger ink quantities would have been necessary to completely fill the vias. However, the Dimatix printer is not well-adapted for ink dispensing because the cartridge carrier cannot be stopped in one position and deliver a pre-defined quantity of ink. Filling of through silicon vias (TSV) with inkjet droplets has recently been the object of several works demonstrating the potential of this method (Quack, 2013; Khorramdel, 2014).

➤ Fabrication of standards for contamination measurements

The ability of inkjet printing to deliver a known quantity of material attracted the contamination laboratory of Leti. The idea here is to deliver single droplets of silver ink at a precise location on a silicon wafer in order to fabricate standards samples for the calibration of metrology equipment. Silver ink droplets were deposited on silicon wafers, then the silver was quantified with Vapor Phase Decomposition (VPD) Inductively Coupled Plasma-Mass Spectrometry (ICP-MS) technique and also with Total Reflection X-ray Fluorescence.

➤ Fabrication of silver electrodes on polyimide substrates for microfluidics circuits

In a recent work at Leti (Renaudot, 2014) reconfigurable and programmable microfluidics circuits fabricated on silicon substrates were designed and fabricated with standard lithographic processes. The typical dimensions of such circuits being in the order of centimeters, the cost of the silicon substrate might become prohibitive for industrial production. Successful printing of silver electrodes

networks were realized on polyimide substrates to replace the silicon patterning (Figure C.3). Printing these electrodes saved a dozen of processing steps in clean room environment. Moreover, this application clearly demonstrates the assets of printing techniques for large area patterning.

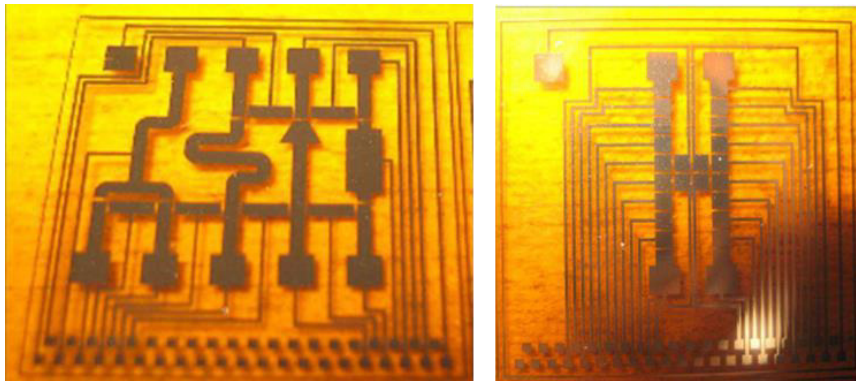


Figure C.3. Inkjet printed electrodes for microfluidics applications on polyimide substrate.

As a conclusion, this thesis provides original results on the intrinsic properties of inkjet printed silver layers as well as experimental methods for their measurement. Moreover, optimization of the printing and annealing conditions led to the fabrication of near state-of-the-art flexible electronic devices whose performances still have a margin of improvement. Besides, regarding resolution, the Japanese company SIJTechnology (www.sijtechnology.com) has recently pushed droplet ejection to its limit and managed to deliver one femtoliter droplets. This allows printing micrometer scale patterns comparable to the photolithographic methods to be drawn directly under normal temperature and normal atmospheric pressure.

In this thesis, reliability issues of flexible components have not been addressed. However, a preliminary study to identify the failure mechanisms of printed silver layers under mechanical strain was conducted and showed cracking, delamination, and buckling. This work is being pursued in a PhD thesis.

With this work, we have assessed the potential of inkjet printing for the patterning of conductive materials and showed that their functionality can go beyond electrical conduction. This multidisciplinary approach was made possible by bringing together industrial actors and research institutes with expertise in electronics design, material science and printing technologies.

References

- Adrian, F.J., Bohandy, J., Kim, B.F., Jette, A.N., Thompson, P., 1987. A study of the mechanism of metal deposition by the laser-induced forward transfer process. *Journal of Vacuum Science & Technology B* 5, 1490–1494. doi:10.1116/1.583661.
- Aernouts, T., Aleksandrov, T., Giroto, C., Genoe, J., Poortmans, J., 2008. Polymer based organic solar cells using ink-jet printed active layers. *Applied Physics Letters* 92, 033306. doi:10.1063/1.2833185.
- Akhavan, V., 2014. Roll-to-Roll Manufacturing Using PulseForge Systems, 41st International conference of IARIGAI, Swansea, UK.
- Allen, M., Alastalo, A., Suhonen, M., Mattila, T., Leppaniemi, J., Seppä, H., 2011. Contactless Electrical Sintering of Silver Nanoparticles on Flexible Substrates. *IEEE Transactions on Microwave Theory and Techniques* 59, 1419–1429. doi:10.1109/TMTT.2011.2123910.
- Allen, M.L., Aronniemi, M., Mattila, T., Alastalo, A., Ojanperä, K., Suhonen, M., Seppä, H., 2008. Electrical sintering of nanoparticle structures. *Nanotechnology* 19, 175201. doi:10.1088/0957-4484/19/17/175201.
- Ando, B., Baglio, S., 2013. All-Inkjet Printed Strain Sensors. *IEEE Sensors Journal* 13, 4874–4879. doi:10.1109/JSEN.2013.2276271.
- Arriola, W., Lee, M., Kim, Y., Ryu, E., Kim, I.S., 2011. New inkjet printed wideband 3 dB branch line coupler, in: *Microwave Symposium Digest (MTT), 2011 IEEE MTT-S International*. IEEE, pp. 1–4.
- Atkinson, H.V., 1988. Overview no. 65: Theories of normal grain growth in pure single phase systems. *Acta Metallurgica* 36, 469–491. doi:10.1016/0001-6160(88)90079-X.
- Basaran, O.A., 2002. Small-scale free surface flows with breakup: Drop formation and emerging applications. *AIChE Journal* 48, 1842–1848.
- Basceri, C., Streiffer, S.K., Kingon, A.I., Waser, R., 1997. The dielectric response as a function of temperature and film thickness of fiber-textured (Ba,Sr)TiO₃ thin films grown by chemical vapor deposition. *Journal of Applied Physics* 82, 2497. doi:10.1063/1.366062.
- Bec, S., Tonck, A., Loubet, J.L., 2006. A simple guide to determine elastic properties of films on substrate from nanoindentation experiments. *Philosophical Magazine* 86, 5347–5358. doi:10.1080/14786430600660856.
- Bhardwaj, R., Fang, X., Attinger, D., 2009. Pattern formation during the evaporation of a colloidal nanoliter drop: a numerical and experimental study. *New Journal of Physics* 11, 075020. doi:10.1088/1367-2630/11/7/075020.
- Bhatti, A.R., Mott, M., Evans, J.R.G., Edirisinghe, M.J., 2001. PZT pillars for 1-3 composites prepared by ink-jet printing. *Journal of materials science letters* 20, 1245–1248.
- Bieri, N.R., Chung, J., Haferl, S.E., Poulidakos, D., Grigoropoulos, C.P., 2003. Microstructuring by printing and laser curing of nanoparticle solutions. *Applied Physics Letters* 82, 3529. doi:10.1063/1.1575502.
- Blaudeck, T., Ersman, P.A., Sandberg, M., Heinz, S., Laiho, A., Liu, J., Engquist, I., Berggren, M., Baumann, R.R., 2012. Simplified Large-Area Manufacturing of Organic Electrochemical Transistors

- Combining Printing and a Self-Aligning Laser Ablation Step. *Advanced Functional Materials* 22, 2939–2948. doi:10.1002/adfm.201102827.
- Blayo, A., 2007. Formulation des encres pour l'impression. *Techniques de l'ingénieur, Élaboration des formulations*. Base documentaire : TIB335DUO.
- Blayo, A., Pineaux, B., 2005. Printing processes and their potential for RFID printing. *ACM*, pp. 27–30.
- Blondy, P., Brown, A.R., Cros, D., Rebeiz, G.M., 1998. Low-loss micromachined filters for millimeter-wave communication systems. *Microwave Theory and Techniques, IEEE Transactions on* 46, 2283–2288.
- Böberl, M., Kovalenko, M.V., Gamerith, S., List, E.J.W., Heiss, W., 2007. Inkjet-Printed Nanocrystal Photodetectors Operating up to 3 μm Wavelengths. *Advanced Materials* 19, 3574–3578. doi:10.1002/adma.200700111.
- Bogy, D.B., Talke, F.E., 1984. Experimental and Theoretical Study of Wave Propagation Phenomena in Drop-on-Demand Ink Jet Devices. *IBM Journal of Research and Development* 28, 314–321. doi:10.1147/rd.283.0314.
- Bohandy, J., Kim, B.F., Adrian, F.J., 1986. Metal deposition from a supported metal film using an excimer laser. *Journal of Applied Physics* 60, 1538. doi:10.1063/1.337287.
- Bolte, S., Cordelières, F.P., 2006. A guided tour into subcellular colocalization analysis in light microscopy. *J Microsc* 224, 213–232. doi:10.1111/j.1365-2818.2006.01706.x.
- Brun, T., Mercier, D., Koumela, A., Marcoux, C., Duraffourg, L., 2012. Silicon nanowire based Pirani sensor for vacuum measurements. *Applied Physics Letters* 101, 183506. doi:10.1063/1.4765665.
- Buckle H., VDI Berichte, 1961, 41, p. 14.
- Bulychev, S. I., Alekhin, V. P., Shorshorov, M. Kh., Ternovskii, A. P., Shnyrev, G.D., 1975. Determining Young's modulus from the indenter penetration diagram, *Zavod Lab.* 41, 1137.
- Buffat, P., Borel, J.P., 1976. Size effect on the melting temperature of gold particles. *Physical Review A* 13, 2287.
- Burgelman, M., 1998. Thin film solar cells by screen printing technology. Citeseer.
- Bushby, A.J., P'ng, K.M.Y., Young, R.D., Pinali, C., Knupp, C., Quantock, A.J., 2011. Imaging three-dimensional tissue architectures by focused ion beam scanning electron microscopy. *Nature Protocols* 6, 845–858. doi:10.1038/nprot.2011.332.
- Cabot CCI-300 datasheet, n.d.
- Cantoni, M., 2007. Focused Ion Beam: Present situation and vision, <http://cime.epfl.ch/webdav/site/cime2/shared/Files/Executice%20Commity/General/2007/FIB%20at%20CIME%20by%20Marco%20Cantoni>, last access 27/09/2014.
- Cappi, B., Özkol, E., Ebert, J., Telle, R., 2008. Direct inkjet printing of Si₃N₄: Characterization of ink, green bodies and microstructure. *Journal of the European Ceramic Society* 28, 2625–2628. doi:10.1016/j.jeurceramsoc.2008.03.004.
- Carel, R., 1995. Grain growth and texture evolution in thin films (Thesis). Massachusetts Institute of Technology.

- Carter, C.B., Norton, M.G., 2013. *Ceramic Materials: Science and Engineering*. Springer Science & Business Media.
- Cauchois, R., 2012. Microstructuring inkjet-printed deposits from silver nanoparticles coalescence to the fabrication of interconnections for electronic devices. Ecole Nationale Supérieure des Mines de Saint-Etienne.
- Cauchois, R., Saadaoui, M., Inal, K., 2014. Impression et recuit de nanoparticules métalliques pour l'électronique imprimée. *Techniques de l'ingénieur Nanotechnologies pour l'électronique, l'optique et la photonique base documentaire : TIB198DUO*.
- Cauchois, R., Saadaoui, M., Yakoub, A., Inal, K., Dubois-Bonvalot, B., Fidalgo, J.-C., 2012. Impact of variable frequency microwave and rapid thermal sintering on microstructure of inkjet-printed silver nanoparticles. *Journal of Materials Science* 47, 7110–7116. doi:10.1007/s10853-012-6366-6.
- Chang, H.-K., Chou, D.-Y., LaBonte, B., Team, T.O.N., others, 1997. Ambient acoustic imaging in helioseismology. *Nature* 389, 825–827.
- Chen, A.U., Basaran, O.A., 2002. A new method for significantly reducing drop radius without reducing nozzle radius in drop-on-demand drop production. *Physics of Fluids* 14, L1. doi:10.1063/1.1427441.
- Cheng, Y.-T., Cheng, C.-M., 2004. Scaling, dimensional analysis, and indentation measurements. *Materials Science and Engineering: R: Reports* 44, 91–149. doi:10.1016/j.mser.2004.05.001.
- Cheon, J., Lee, J., Kim, J., 2012. Inkjet printing using copper nanoparticles synthesized by electrolysis. *Thin Solid Films* 520, 2639–2643. doi:10.1016/j.tsf.2011.11.021.
- Cherrington, M., Claypole, T.C., Deganello, D., Mabbett, I., Watson, T., Worsley, D., 2011. Ultrafast near-infrared sintering of a slot-die coated nano-silver conducting ink. *Journal of Materials Chemistry* 21, 7562. doi:10.1039/c1jm10630a.
- Cho, J.H., Lee, J., Xia, Y., Kim, B., He, Y., Renn, M.J., Lodge, T.P., Daniel Frisbie, C., 2008. Printable ion-gel gate dielectrics for low-voltage polymer thin-film transistors on plastic. *Nature Materials* 7, 900–906. doi:10.1038/nmat2291.
- Chung, J., Ko, S., Bieri, N.R., Grigoropoulos, C.P., Poulikakos, D., 2004. Conductor microstructures by laser curing of printed gold nanoparticle ink. *Applied Physics Letters* 84, 801. doi:10.1063/1.1644907
- Cole, M.W., Hubbard, C., Ngo, E., Ervin, M., Wood, M., Geyer, R.G., 2002. Structure–property relationships in pure and acceptor-doped $Ba_{1-x}Sr_xTiO_3$ thin films for tunable microwave device applications. *Journal of Applied Physics* 92, 475. doi:10.1063/1.1484231.
- Colina, M., Duocastella, M., Fernandez-Pradas, J.M., Serra, P., Morenza, J.L., 2006. Laser-induced forward transfer of liquids: Study of the droplet ejection process. *Journal of Applied Physics* 99, 084909–084909–7. doi:10.1063/1.2191569.
- Colina, M., Serra, P., Fernández-Pradas, J.M., Sevilla, L., Morenza, J.L., 2005. DNA deposition through laser induced forward transfer. *Biosensors and Bioelectronics* 20, 1638–1642. doi:10.1016/j.bios.2004.08.047.
- Constantinescu, C., Diallo, A.K., Rapp, L., Cremillieu, P., Mazurczyk, R., Serein-Spirau, F., Lère-Porte, J.P., Delaporte, P., Alloncle, A.P., Videlot-Ackermann, C., 2014. Laser-induced forward transfer of multi-layered structures for OTFT applications. *Applied Surface Science*. doi:10.1016/j.apsusc.2014.06.155.

- Cook, B.S., Cooper, J.R., Tentzeris, M.M., 2013. Multi-Layer RF Capacitors on Flexible Substrates Utilizing Inkjet Printed Dielectric Polymers. *IEEE Microwave and Wireless Components Letters* 23, 353–355. doi:10.1109/LMWC.2013.2264658.
- Courbat, J., Kim, Y.B., Briand, D., de Rooij, N.F., 2011. Inkjet printing on paper for the realization of humidity and temperature sensors, in: *Solid-State Sensors, Actuators and Microsystems Conference (TRANSDUCERS)*, 2011 16th International. IEEE, pp. 1356–1359.
- Craciun, V., Singh, R.K., 2000. Characteristics of the surface layer of barium strontium titanate thin films deposited by laser ablation. *Applied Physics Letters* 76, 1932. doi:10.1063/1.126216.
- Crowley, K., Morrin, A., Hernandez, A., Omalley, E., Whitten, P., Wallace, G., Smyth, M., Killard, A., 2008. Fabrication of an ammonia gas sensor using inkjet-printed polyaniline nanoparticles. *Talanta* 77, 710–717. doi:10.1016/j.talanta.2008.07.022.
- Dearden, A.L., Smith, P.J., Shin, D.-Y., Reis, N., Derby, B., O'Brien, P., 2005. A Low Curing Temperature Silver Ink for Use in Ink-Jet Printing and Subsequent Production of Conductive Tracks. *Macromolecular Rapid Communications* 26, 315–318. doi:10.1002/marc.200400445.
- Deegan, R.D., Bakajin, O., Dupont, T.F., Huber, G., Nagel, S.R., Witten, T.A., 1997. Capillary flow as the cause of ring stains from dried liquid drops. *Nature* 389, 827–829. doi:10.1038/39827.
- Deegan, R.D., 2000. Pattern formation in drying drops. *Physical Review E* 61, 475.
- Denneulin, A., Blayo, A., Neuman, C., Bras, J., 2011. Infra-red assisted sintering of inkjet printed silver tracks on paper substrates. *Journal of Nanoparticle Research* 13, 3815–3823. doi:10.1007/s11051-011-0306-2.
- Denneulin, A., Bras, J., Blayo, A., Khelifi, B., Roussel-Dherbey, F., Neuman, C., 2009. The influence of carbon nanotubes in inkjet printing of conductive polymer suspensions. *Nanotechnology* 20, 385701. doi:10.1088/0957-4484/20/38/385701.
- Deschacht, D., Boyer, A., 1985. General expression for the temperature coefficient of resistivity of polycrystalline semi-metal films. *J Mater Sci* 20, 807–811. doi:10.1007/BF00585718.
- De Vries, J.W.C., 1988. Temperature and thickness dependence of the resistivity of thin polycrystalline aluminium, cobalt, nickel, palladium, silver and gold films. *Thin Solid Films* 167, 25–32. doi:10.1016/0040-6090(88)90478-6.
- Dimatix DMP2831 User Manual, n.d.
- Dinca, V., Ranella, A., Farsari, M., Kafetzopoulos, D., Dinescu, M., Popescu, A., Fotakis, C., 2008. Quantification of the activity of biomolecules in microarrays obtained by direct laser transfer. *Biomedical Microdevices* 10, 719–725. doi:10.1007/s10544-008-9183-6.
- Doerner, M. f., Nix, W. d., 1986. A method for interpreting the data from depth-sensing indentation instruments. *Journal of Materials Research* 1, 601–609. doi:10.1557/JMR.1986.0601.
- Du Noüy, P.L., 1925. An interfacial tensiometer for universal use. *The Journal of general physiology* 7, 625–631.
- Dupont, Kapton HN datasheet, n.d.

- Ebert, J., Ozkol, E., Zeichner, A., Uibel, K., Weiss, O., Koops, U., Telle, R., Fischer, H., 2009. Direct inkjet printing of dental prostheses made of zirconia. *J. Dent. Res.* 88, 673–676. doi:10.1177/0022034509339988.
- Entesari, K., Rebeiz, G.M., 2008. RF MEMS, BST, and GaAs varactor system-level response in complex modulation systems. *International Journal of RF and Microwave Computer-Aided Engineering* 18, 86–98. doi:10.1002/mmce.20275.
- Felba, J., Nitsch, K., Piasecki, T., Paluch, P., Moscicki, A., Kinart, A., 2009. The influence of thermal process on electrical conductivity of microstructures: Made by ink-jet painting with the use of ink containing nano sized silver particles, in: *Nanotechnology, 2009. IEEE-NANO 2009. 9th IEEE Conference on. IEEE*, pp. 408–411.
- Fenoll, M., 2007. Optimisation des paramètres d'impression pour l'électronique imprimée sur supports souples. Institut National Polytechnique de Grenoble-INPG.
- Feret, L. R., 1931. *Assoc. Internat. pour l'Essai des Mat.*, Zurich, 2, Group D.
- Fischer-Cripps, A.C., 2011. *Nanoindentation*. Springer Science & Business Media.
- R. Fisher, S. Perkins, A. Walker, and E. Wolfart, http://homepages.inf.ed.ac.uk/rbf/HIPR2/hipr_top.htm, last accessed 25/09/2014, (2000).
- Fromm, J.E., 1984. Numerical Calculation of the Fluid Dynamics of Drop-on-Demand Jets. *IBM Journal of Research and Development* 28, 322–333. doi:10.1147/rd.283.0322.
- Frost, H.J., Thompson, C.V., 1988. Computer simulation of microstructural evolution in thin films. *Journal of Electronic Materials* 17, 447–458.
- Fuchs, K., 1938. *The conductivity of thin metallic films according to the electron theory of metals*. Cambridge Univ Press, pp. 100–108.
- Gan, H.Y., Shan, X., Eriksson, T., Lok, B.K., Lam, Y.C., 2009. Reduction of droplet volume by controlling actuating waveforms in inkjet printing for micro-pattern formation. *Journal of Micromechanics and Microengineering* 19, 055010. doi:10.1088/0960-1317/19/5/055010.
- Gibson, L.J., Ashby, M.F., 1999. *Cellular Solids: Structure and Properties*. Cambridge University Press.
- Gohier, A., Dhar, A., Gorintin, L., Bondavalli, P., Bonnassieux, Y., Cojocar, C.S., 2011. All-printed infrared sensor based on multiwalled carbon nanotubes. *Applied Physics Letters* 98, 063103. doi:10.1063/1.3552686.
- Groeber, M.A., Haley, B.K., Uchic, M.D., Dimiduk, D.M., Ghosh, S., 2006. 3D reconstruction and characterization of polycrystalline microstructures using a FIB–SEM system. *Materials Characterization* 57, 259–273. doi:10.1016/j.matchar.2006.01.019.
- Grouchko, M., Kamyshny, A., Mihailescu, C.F., Anghel, D.F., Magdassi, S., 2011. Conductive Inks with a “Built-In” Mechanism That Enables Sintering at Room Temperature. *ACS Nano* 5, 3354–3359. doi:10.1021/nn2005848.
- Gunde, M.K., 2012. Material Science meets graphic communication for a joint venture beyond the conventional, 39th International conference of IARIGAI, Ljubljana, Slovenia.
- Hall, E.O., 1954. Variation of Hardness of Metals with Grain Size. *Nature* 173, 948–949. doi:10.1038/173948b0.

- Halperin, W.P., 1986. Quantum size effects in metal particles. *Reviews of Modern Physics* 58, 533.
- Harrey, P.M., Ramsey, B.J., Evans, P.S.A., Harrison, D.J., 2002. Capacitive-type humidity sensors fabricated using the offset lithographic printing process. *Sensors and Actuators B: Chemical* 87, 226–232. doi:10.1016/S0925-4005(02)00240-X.
- Hebner, T.R., Wu, C.C., Marcy, D., Lu, M.H., Sturm, J.C., 1998. Ink-jet printing of doped polymers for organic light emitting devices. *Applied Physics Letters* 72, 519. doi:10.1063/1.120807.
- Henglein, A., 1993. Physicochemical properties of small metal particles in solution: “microelectrode” reactions, chemisorption, composite metal particles, and the atom-to-metal transition. *The Journal of Physical Chemistry* 97, 5457–5471.
- Holmberg, K., 2002. *Handbook of Applied Surface and Colloid Chemistry*, New York, Wiley and Sons.
- Holzer, L., Muench, B., Wegmann, M., Gasser, P., Flatt, R.J., 2006. FIB-Nanotomography of Particulate Systems—Part I: Particle Shape and Topology of Interfaces. *Journal of the American Ceramic Society* 89, 2577–2585. doi:10.1111/j.1551-2916.2006.00974.x.
- Hong, J.-S.G., Lancaster, M.J., 2004. *Microstrip Filters for RF/Microwave Applications*. John Wiley & Sons.
- Hon, K.K.B., Li, L., Hutchings, I.M., 2008. Direct writing technology—Advances and developments. *CIRP Annals - Manufacturing Technology* 57, 601–620. doi:10.1016/j.cirp.2008.09.006.
- Hopp, B., Smausz, T., Kresz, N., Barna, N., Bor, Z., Kolozsvári, L., Chrisey, D.B., Szabó, A., Nógrádi, A., 2005. Survival and Proliferative Ability of Various Living Cell Types after Laser-Induced Forward Transfer. *Tissue Engineering* 11, 1817–1823. doi:10.1089/ten.2005.11.1817.
- Hörteis, M., Mette, A., Richter, P.L., Fidorra, F., Glunz, S.W., 2007. Further progress in metal aerosol jet printing for front side metallization of silicon solar cells. *Proceedings of the 22nd EU-PVSEC*.
- Hösel, M., Krebs, F.C., 2012. Large-scale roll-to-roll photonic sintering of flexo printed silver nanoparticle electrodes. *Journal of Materials Chemistry* 22, 15683. doi:10.1039/c2jm32977h.
- Hoth, C.N., Choulis, S.A., Schilinsky, P., Brabec, C.J., 2007. High Photovoltaic Performance of Inkjet Printed Polymer:Fullerene Blends. *Advanced Materials* 19, 3973–3978. doi:10.1002/adma.200700911.
- Hrehorova, E., Rebros, M., Pekarovicova, A., Bazuin, B., Ranganathan, A., Garner, S., Merz, G., Tosch, J., Boudreau, R., 2011. Gravure Printing of Conductive Inks on Glass Substrates for Applications in Printed Electronics. *Journal of Display Technology* 7, 318–324. doi:10.1109/JDT.2010.2065214.
- Huang, X.D., Bhangale, S.M., Moran, P.M., Yakovlev, N.L., Pan, J., 2003. Surface modification studies of Kapton HN polyimide films. *Polymer International* 52, 1064–1069. doi:10.1002/pi.1143.
- Hu, H., Larson, R.G., 2006. Marangoni Effect Reverses Coffee-Ring Depositions. *The Journal of Physical Chemistry B* 110, 7090–7094. doi:10.1021/jp0609232.
- Hutchings, I.M., Martin, G.D., 2012. *Inkjet Technology for Digital Fabrication*. John Wiley & Sons.
- ImageJ, Rasband, W.S., 1997-2014. U. S. National Institutes of Health, Bethesda, Maryland, USA, <http://imagej.nih.gov/ij/>.
- Jang, D., Kim, D., Moon, J., 2009. Influence of Fluid Physical Properties on Ink-Jet Printability. *Langmuir* 25, 2629–2635. doi:10.1021/la900059m.

- Jang, J., Ha, J., Cho, J., 2007. Fabrication of Water-Dispersible Polyaniline-Poly(4-styrenesulfonate) Nanoparticles For Inkjet-Printed Chemical-Sensor Applications. *Advanced Materials* 19, 1772–1775. doi:10.1002/adma.200602127.
- Jiang, Q., Zhang, S., Zhao, M., 2003. Size-dependent melting point of noble metals. *Materials Chemistry and Physics* 82, 225–227. doi:10.1016/S0254-0584(03)00201-3.
- Johnson, K.L., Johnson, K.L., 1987. *Contact Mechanics*. Cambridge University Press.
- Joo, S., Baldwin, D.F., 2010. Adhesion mechanisms of nanoparticle silver to substrate materials: identification. *Nanotechnology* 21, 055204. doi:10.1088/0957-4484/21/5/055204.
- Jung, J.-K., Choi, S.-H., Kim, I., Jung, H.C., Joung, J., Joo, Y.-C., 2008. Characteristics of microstructure and electrical resistivity of inkjet-printed nanoparticle silver films annealed under ambient air. *Philosophical Magazine* 88, 339–359. doi:10.1080/14786430701846198.
- Jung, S., 2011. Fluid characterization and drop impact in inkjet printing for organic semiconductor devices (Thesis). University of Cambridge.
- Juretschke, H.J., 1966. Influence of the surface scattering of electrons on the metallic field effect in thin layers. *Surface Science* 5, 111–119.
- Kamyshny, A., Magdassi, S., 2014. Conductive Nanomaterials for Printed Electronics. *Small* 10, 3515–3535. doi:10.1002/smll.201303000.
- Kamyshny, A., Steinke, J., Magdassi, S., 2011. Metal-based inkjet inks for printed electronics. *Open Applied Physics Journal* 4, 19–36.
- Kang, J.S., Ryu, J., Kim, H.S., Hahn, H.T., 2011. Sintering of Inkjet-Printed Silver Nanoparticles at Room Temperature Using Intense Pulsed Light. *Journal of Electronic Materials* 40, 2268–2277. doi:10.1007/s11664-011-1711-0.
- Kapoor, S., 1998. Preparation, characterization, and surface modification of silver particles. *Langmuir* 14, 1021–1025.
- Kaydanova, T., Miedaner, A., Perkins, J.D., Curtis, C., Alleman, J.L., Ginley, D.S., 2007. Direct-write inkjet printing for fabrication of barium strontium titanate-based tunable circuits. *Thin Solid Films* 515, 3820–3824. doi:10.1016/j.tsf.2006.10.009.
- Kettle, J., Lamminmäki, T., Gane, P., 2010. A review of modified surfaces for high speed inkjet coating. *Surface and Coatings Technology* 204, 2103–2109. doi:10.1016/j.surfcoat.2009.10.035.
- Khorramdel B. and Mäntysalo M., 2014. Inkjet filling of TSVs with silver nanoparticle ink, *Electronics System-Integration Technology (ESTC) Conference*, (Helsinki, Finland).
- Kim, D., Moon, J., 2005. Highly Conductive Ink Jet Printed Films of Nanosilver Particles for Printable Electronics. *Electrochemical and Solid-State Letters* 8, J30. doi:10.1149/1.2073670.
- Kim, H.-S., Dhage, S.R., Shim, D.-E., Hahn, H.T., 2009. Intense pulsed light sintering of copper nanoink for printed electronics. *Applied Physics A* 97, 791–798. doi:10.1007/s00339-009-5360-6.
- Kimura K., 2000. Formation in gas phases. In: Schick MJ, Hybbard AT, Eds. *Fine particles. Synthesis, characterization, and mechanisms of growth*, Surf. Sci. Ser. 92. New York-Basel: Marcel Dekker 2000.
- King, R.B., 1987. Elastic analysis of some punch problems for a layered medium. *International Journal of Solids and Structures* 23, 1657–1664. doi:10.1016/0020-7683(87)90116-8.

- Kipphan, H., 2001. Handbook of Print Media: Technologies and Production Methods. Springer Science & Business Media.
- Kittel, 2007. Introduction to solid state physics. Wiley India Pvt. Limited.
- Ko, S.H., Chung, J., Choi, Y., Hwang, D.J., Grigoropoulos, C.P., Poulikakos, D., 2005. Subtractive laser processing of low temperature inkjet printed micro electric components of functional nano-ink for flexible electronics. American Society of Mechanical Engineers, pp. 1935–1941.
- Ko, S.H., Pan, H., Grigoropoulos, C.P., Luscombe, C.K., Fréchet, J.M.J., Poulikakos, D., 2007. All-inkjet-printed flexible electronics fabrication on a polymer substrate by low-temperature high-resolution selective laser sintering of metal nanoparticles. *Nanotechnology* 18, 345202. doi:10.1088/0957-4484/18/34/345202.
- Krebs, F.C., Jørgensen, M., Norrman, K., Hagemann, O., Alstrup, J., Nielsen, T.D., Fyenbo, J., Larsen, K., Kristensen, J., 2009. A complete process for production of flexible large area polymer solar cells entirely using screen printing—First public demonstration. *Solar Energy Materials and Solar Cells* 93, 422–441. doi:10.1016/j.solmat.2008.12.001.
- Kumpulainen, T., Pekkanen, J., Valkama, J., Laakso, J., Tuokko, R., Mäntysalo, M., 2011. Low temperature nanoparticle sintering with continuous wave and pulse lasers. *Optics & Laser Technology* 43, 570–576. doi:10.1016/j.optlastec.2010.08.002.
- Lame, O., Bellet, D., Michiel, M.D., Bouvard, D., 2003. In situ microtomography investigation of metal powder compacts during sintering. *Nuclear Instruments and Methods in Physics Research Section B: Beam Interactions with Materials and Atoms* 200, 287–294.
- Lee, C.-L., Chang, K.-C., Syu, C.-M., 2011. Silver nanoplates as inkjet ink particles for metallization at a low baking temperature of 100°C. *Colloids and Surfaces A: Physicochemical and Engineering Aspects* 381, 85–91. doi:10.1016/j.colsurfa.2011.03.034.
- Lee, H.-H., Chou, K.-S., Huang, K.-C., 2005. Inkjet printing of nanosized silver colloids. *Nanotechnology* 16, 2436–2441. doi:10.1088/0957-4484/16/10/074.
- Le, H.P., 1998. Progress and Trends in Ink-jet Printing Technology. *Journal of Imaging Science and Technology* 42, 49–62.
- Li, D., Sutton, D., Burgess, A., Graham, D., Calvert, P.D., 2009. Conductive copper and nickel lines via reactive inkjet printing. *Journal of Materials Chemistry* 19, 3719. doi:10.1039/b820459d.
- Lim, J.A., Lee, W.H., Lee, H.S., Lee, J.H., Park, Y.D., Cho, K., 2008. Self-Organization of Ink-jet-Printed Triisopropylsilylethynyl Pentacene via Evaporation-Induced Flows in a Drying Droplet. *Advanced Functional Materials* 18, 229–234. doi:10.1002/adfm.200700859.
- Liu, Y., Varahramyan, K., Cui, T., 2005. Low-Voltage All-Polymer Field-Effect Transistor Fabricated Using an Inkjet Printing Technique. *Macromolecular Rapid Communications* 26, 1955–1959. doi:10.1002/marc.200500493.
- Li, X., Bhushan, B., 2002. A review of nanoindentation continuous stiffness measurement technique and its applications. *Materials characterization* 48, 11–36.
- Loffredo, F., Mauro, A.D.G.D., Burrasca, G., La Ferrara, V., Quercia, L., Massera, E., Di Francia, G., Sala, D.D., 2009. Ink-jet printing technique in polymer/carbon black sensing device fabrication. *Sensors and Actuators B: Chemical* 143, 421–429. doi:10.1016/j.snb.2009.09.024.

- Loubet, J. L., Bauer, M., Tonck, A., Bec, S., and Gauthier-Manuel, B., 1993. Nanoindentation with a surface force apparatus. In *Mechanical Properties and Deformation Behavior of Materials Having Ultra-Fine Microstructures*, Springer Netherlands, pp. 429-447.
- Lowe, D.G., 2004. Distinctive Image Features from Scale-Invariant Keypoints. *International Journal of Computer Vision* 60, 91–110. doi:10.1023/B:VISI.0000029664.99615.94.
- Lucas, M.S.P., 1965. Electrical Conductivity of Thin Metallic Films with Unlike Surfaces. *Journal of Applied Physics* 36, 1632. doi:10.1063/1.1703100.
- Madej, E., Espig, M., Baumann, R.R., Schuhmann, W., La Mantia, F., 2014. Optimization of primary printed batteries based on Zn/MnO₂. *Journal of Power Sources* 261, 356–362. doi:10.1016/j.jpowsour.2014.03.103.
- Mafuné, F., Kohno, J., Takeda, Y., Kondow, T., Sawabe, H., 2000. Formation and Size Control of Silver Nanoparticles by Laser Ablation in Aqueous Solution. *The Journal of Physical Chemistry B* 104, 9111–9117. doi:10.1021/jp001336y.
- Mastrangelo, C.H., Muller, R.S., 1991. Microfabricated thermal absolute-pressure sensor with on-chip digital front-end processor. *Solid-State Circuits, IEEE Journal of* 26, 1998–2007.
- Mauthner, G., Landfester, K., Köck, A., Brückl, H., Kast, M., Stepper, C., List, E.J.W., 2008. Inkjet printed surface cell light-emitting devices from a water-based polymer dispersion. *Organic Electronics* 9, 164–170. doi:10.1016/j.orgel.2007.10.007.
- Mayadas, A.F., 1969. Electrical resistivity model for polycrystalline films: the case of specular reflection at external surfaces. *App. Physics Letters* 14, 345. doi:10.1063/1.1652680.
- Mayadas, A.F., Shatzkes, M., 1970. Electrical-resistivity model for polycrystalline films: the case of arbitrary reflection at external surfaces. *Physical Review B* 1, 1382.
- Mercier, D., Mandrillon, V., Verdier, M., Brechet, Y., 2011. Mesure de module d'Young d'un film mince à partir de mesures expérimentales de nanoindentation réalisées sur des systèmes multicouches. *Matériaux & Techniques* 99, 169–178. doi:10.1051/mattech/2011029.
- Mezey, L.Z., Giber, J., 1982. The Surface Free Energies of Solid Chemical Elements: Calculation from Internal Free Enthalpies of Atomization. *Jpn. J. Appl. Phys.* 21, 1569. doi:10.1143/JJAP.21.1569.
- Molina-Lopez, F., Quintero, A.V., Mattana, G., Briand, D., de Rooij, N.F., 2012. P1. 8.6 All-additive Inkjet Printed Humidity and Temperature Sensors Fabricated and Encapsulated at Foil Level. *Tagungsband* 1122–1125.
- Moon, K.-S., Dong, H., Maric, R., Pothukuchi, S., Hunt, A., Li, Y., Wong, C.P., 2005. Thermal behavior of silver nanoparticles for low-temperature interconnect applications. *Journal of Electronic Materials* 34, 168–175.
- MTS-XP Nanoindenter User Manual, n.d.
- Nastasi, M.A., Parkin, D.M., Gleiter, H., 1993. *Mechanical Properties and Deformation Behavior of Materials Having Ultra-Fine Microstructures*. Springer Science & Business Media.
- Nečas, D., Klapetek, P., 2012. Gwyddion: an open-source software for SPM data analysis. *centr.eur.j.phys.* 10, 181–188. doi:10.2478/s11534-011-0096-2.

- Nikfalazar, M., Sazegar, M., Zheng, Y., Wiens, A., Jakoby, R., Friederich, A., Kohler, C., Binder, J.R., 2013. Compact tunable phase shifter based on inkjet printed BST thick-films for phased-array application, in: Microwave Conference (EuMC), 2013 European. IEEE, pp. 432–435.
- Mohammad Nikfalazar, M., Friederich, A., Kohler, C., Sazegar, M., Zheng, Y., Wiens, A., Binder, J. R., and Jakoby, R., 2014. Metal-Isolator-Metal Varactor Based on Inkjet-Printed Tunable Ceramics, GeMiC, Aachen, Germany.
- Noren, B., 2004. Thin film barium strontium titanate (BST) for a new class of tunable RF components. *Microwave Journal*, 47(5), 210–221.
- Oliver, W. c., Pharr, G. m., 1992. An improved technique for determining hardness and elastic modulus using load and displacement sensing indentation experiments. *Journal of Materials Research* 7, 1564–1583. doi:10.1557/JMR.1992.1564.
- Otsu, N., 1975. A threshold selection method from gray-level histograms. *Automatica* 11, 23–27.
- Owens, D.K., Wendt, R.C., 1969. Estimation of the surface free energy of polymers. *J. Appl. Polym. Sci.* 13, 1741–1747. doi:10.1002/app.1969.070130815.
- Padmini, P., Taylor, T.R., Lefevre, M.J., Nagra, A.S., York, R.A., Speck, J.S., 1999. Realization of high tunability barium strontium titanate thin films by RF magnetron sputtering. *Applied Physics Letters* 75, 3186. doi:10.1063/1.125272.
- Palmer, J.E., Thompson, C.V., Smith, H.I., 1987. Grain growth and grain size distributions in thin germanium films. *Journal of Applied Physics* 62, 2492. doi:10.1063/1.339460.
- Pang, G.K., Baba-Kishi, K.Z., Patel, A., 2000. Topographic and phase-contrast imaging in atomic force microscopy. *Ultramicroscopy* 81, 35–40.
- Park, B.K., Kim, D., Jeong, S., Moon, J., Kim, J.S., 2007. Direct writing of copper conductive patterns by ink-jet printing. *Thin Solid Films* 515, 7706–7711. doi:10.1016/j.tsf.2006.11.142.
- Park, H., Carr, W.W., Zhu, J., Morris, J.F., 2003. Single drop impaction on a solid surface. *AIChE journal* 49, 2461–2471.
- Park, J.-W., Baek, S.-G., 2006. Thermal behavior of direct-printed lines of silver nanoparticles. *Scripta Materialia* 55, 1139–1142. doi:10.1016/j.scriptamat.2006.08.032.
- Pasquarelli, R.M., Ginley, D.S., O’Hayre, R., 2011. Solution processing of transparent conductors: from flask to film. *Chemical Society Reviews* 40, 5406. doi:10.1039/c1cs15065k.
- Perelaer, J., de Gans, B.-J., Schubert, U.S., 2006. Ink-jet Printing and Microwave Sintering of Conductive Silver Tracks. *Advanced Materials* 18, 2101–2104. doi:10.1002/adma.200502422.
- Petersen, K.E., 1982. Silicon as a mechanical material. *Proceedings of the IEEE* 70, 420–457. doi:10.1109/PROC.1982.12331.
- Pharr, G. m., Strader, J. h., Oliver, W. c., 2009. Critical issues in making small-depth mechanical property measurements by nanoindentation with continuous stiffness measurement. *Journal of Materials Research* 24, 653–666. doi:10.1557/jmr.2009.0096.
- Philipp, M., 2011. Electrical Transport and Scattering Mechanisms in Thin Silver Films for Thermally Insulating Glazing.

- Pichard, C.R., Komnik, Y.F., Belevtsev, B.I., Tosser, A.J., 1983. Effect of grain boundary scattering on the TCR of thin tin films. *Journal of materials science letters* 2, 360–362.
- Pichard, C.R., Tellier, C.R., Tosser, A.J., 1980. Superimposed Effects of Three Arrays of Scattering Planes on Electrical Conductivity. *phys. stat. sol. (b)* 99, 353–358. doi:10.1002/pssb.2220990138.
- Pimenov, S.M., Shafeev, G.A., Smolin, A.A., Konov, V.I., Vodolaga, B.K., 1995. Laser-induced forward transfer of ultra-fine diamond particles for selective deposition of diamond films. *Applied surface science* 86, 208–212.
- Piner, R.D., 1999. “Dip-Pen” Nanolithography. *Science* 283, 661–663. doi:10.1126/science.283.5402.661.
- Puers, R., Reyntjens, S., De Bruyker, D., 2002. The NanoPirani—an extremely miniaturized pressure sensor fabricated by focused ion beam rapid prototyping. *Sensors and Actuators A: Physical* 97, 208–214.
- Qi, W.H., 2005. Size effect on melting temperature of nanosolids. *Physica B: Condensed Matter* 368, 46–50. doi:10.1016/j.physb.2005.06.035.
- Quack, N., Sadie, J., Subramanian, V., Wu, M. C., (2013). Through Silicon Vias and thermocompression bonding using inkjet-printed gold nanoparticles for heterogeneous MEMS integration. In *Solid-State Sensors, Actuators and Microsystems (TRANSDUCERS & EUROSENSORS XXVII), 2013 Transducers & Eurosensors XXVII: The 17th International Conference on*.
- Rebeiz, G.M., Tan, G.-L., 2003. Introduction: RF MEMS for Microwave Applications, in: *RF MEMS*. John Wiley & Sons, Inc., pp. 1–20.
- Reinhold, I., Hendriks, C.E., Eckardt, R., Kranenburg, J.M., Perelaer, J., Baumann, R.R., Schubert, U.S., 2009. Argon plasma sintering of inkjet printed silver tracks on polymer substrates. *Journal of Materials Chemistry* 19, 3384. doi:10.1039/b823329b.
- Reis, N., Ainsley, C., Derby, B., 2005. Ink-jet delivery of particle suspensions by piezoelectric droplet ejectors. *Journal of Applied Physics* 97, 094903. doi:10.1063/1.1888026.
- Reis, N., Derby, B., 2000. Ink Jet Deposition of Ceramic Suspensions: Modeling and Experiments of Droplet Formation, in: *MRS Online Proceedings Library*. doi:10.1557/PROC-625-117.
- Renaudot, R., 2014. Conception, fabrication de puces microfluidiques à géométrie programmable reposant sur les principes d'électromouillagesur diélectrique et de diélectrophorèse liquide.
- Reuter, K., Kempa, H., Brandt, N., Bartzsch, M., Huebler, A.C., 2007. Influence of process parameters on the electrical properties of offset printed conductive polymer layers. *Progress in Organic Coatings* 58, 312–315. doi:10.1016/j.porgcoat.2007.01.004.
- Roberts, A.P., Garboczi, E.J., 2000. Elastic Properties of Model Porous Ceramics. *Journal of the American Ceramic Society* 83, 3041–3048. doi:10.1111/j.1151-2916.2000.tb01680.x.
- Roy, R., Agrawal, D., Cheng, J., Gedevanishvili, S., 1999. Full sintering of powdered-metal bodies in a microwave field. *Nature* 399, 668–670. doi:10.1038/21390.
- Sakai, M., 2009. Substrate-affected indentation contact parameters of elastoplastic coating/substrate composites. *Journal of Materials Research* 24, 831–843. doi:10.1557/jmr.2009.0102.

- Sakata, H., Chakraborty, S., Yokoyama, E., Wakaki, M., Chakravorty, D., 2005. Laser-induced forward transfer of TiO₂-Au nanocomposite films for maskless patterning. *Applied Physics Letters* 86, 114104. doi:10.1063/1.1879092.
- Sbrockey, N.M., Cole, M.W., Kalkur, T.S., Luong, M., Spanier, J.E., Tompa, G.S., 2011. MOCVD Growth of Compositionally Graded Ba_xSr_{1-x}TiO₃ Thin Films. *Integrated Ferroelectrics* 126, 21–27. doi:10.1080/10584587.2011.574975.
- Schmidt, M., Kusche, R., von Issendorff, B., Haberland, H., 1998. Irregular variations in the melting point of size-selected atomic clusters. *Nature* 393, 238–240.
- Scilab Enterprises, 2012. Scilab : Open source free software for numerical computing, (OS, Version 5.4.1), available at <http://www.scilab.org>.
- Seerden, K.A., Reis, N., Evans, J.R., Grant, P.S., Halloran, J.W., Derby, B., 2001. Ink-Jet Printing of Wax-Based Alumina Suspensions. *Journal of the American Ceramic Society* 84, 2514–2520.
- Setter, N., Damjanovic, D., Eng, L., Fox, G., Gevorgian, S., Hong, S., Kingon, A., Kohlstedt, H., Park, N.Y., Stephenson, G.B., Stolitchnov, I., TagansteV, A.K., Taylor, D.V., Yamada, T., Streiffer, S., 2006. Ferroelectric thin films: Review of materials, properties, and applications. *Journal of Applied Physics* 100, 051606. doi:10.1063/1.2336999.
- Shaker, G., Tentzeris, M., Safavi-Naeini, S., 2010. Low-cost antennas for mm-Wave sensing applications using inkjet printing of silver nano-particles on liquid crystal polymers, in: *Antennas and Propagation Society International Symposium (APSURSI), 2010 IEEE*. IEEE, pp. 1–4.
- Shi, J., 2002. MSE.
- Shorshorov, M. Kh., Bulychev, S. I., Alekhin, V. P., 1982. *Sov. Phys. Doklady* 26, 769.
- SIJTEchnology, <http://www.sijtechnology.com/en/about/index.html>.
- Singh, A., 1973. Grain-size dependence of temperature coefficient of resistance of polycrystalline metal films. *Proceedings of the IEEE* 61, 1653–1654.
- Sirringhaus, H., Kawase, T., Friend, R.H., Shimoda, T., Inbasekaran, M., Wu, W., Woo, E.P., 2000. High-Resolution Inkjet Printing of All-Polymer Transistor Circuits. *Science* 290, 2123–2126. doi:10.1126/science.290.5499.2123.
- Slade, P.G., 1999. *Electrical Contacts: Principles and Applications*. CRC Press.
- Soffer, S.B., 1967. Statistical Model for the Size Effect in Electrical Conduction. *Journal of Applied Physics* 38, 1710. doi:10.1063/1.1709746.
- Soltman, D., Subramanian, V., 2008. Inkjet-Printed Line Morphologies and Temperature Control of the Coffee Ring Effect. *Langmuir* 24, 2224–2231. doi:10.1021/la7026847.
- Sommer, A.P., 2004. Suffocation of Nerve Fibers by Living Nanovesicles: A Model Simulation–Part II. *Journal of Proteome Research* 3, 1086–1088. doi:10.1021/pr049935v.
- Sondheimer, E.H., 2001. The mean free path of electrons in metals. *Advances in Physics* 50, 499–537.
- Sridhar, A., Reiding, J., Adelaar, H., Achterhoek, F., van Dijk, D.J., Akkerman, R., 2009. Inkjet-printing- and electroless-plating- based fabrication of RF circuit structures on high-frequency substrates. *Journal of Micromechanics and Microengineering* 19, 085020. doi:10.1088/0960-1317/19/8/085020.

- Stark, B.H., Mei, Y., Zhang, C., Najafi, K., 2003. A doubly anchored surface micromachined Pirani gauge for vacuum package characterization, in: *Micro Electro Mechanical Systems, 2003. MEMS-03 Kyoto. IEEE The Sixteenth Annual International Conference on. IEEE*, pp. 506–509.
- Subramanian, V., Chang, J.B., de la Fuente Vornbrock, A., Huang, D.C., Jagannathan, L., Liao, F., Mattis, B., Molesa, S., Redinger, D.R., Soltman, D., others, 2008. Printed electronics for low-cost electronic systems: Technology status and application development, in: *Solid-State Circuits Conference, 2008. ESSCIRC 2008. 34th European. IEEE*, pp. 17–24.
- SunChemical Silver ink EMD5603 datasheet, n.d.
- SunChemical Silver ink EMD5714 datasheet, n.d.
- Sung, D., de la Fuente Vornbrock, A., Subramanian, V., 2010. Scaling and Optimization of Gravure-Printed Silver Nanoparticle Lines for Printed Electronics. *IEEE Transactions on Components and Packaging Technologies* 33, 105–114. doi:10.1109/TCAPT.2009.2021464.
- Tagantsev, A.K., Sherman, V.O., Astafiev, K.F., Venkatesh, J., Setter, N., 2003. Ferroelectric materials for microwave tunable applications. *Journal of electroceramics* 11, 5–66.
- Tao, Y., Tao, Y., Wang, B., Wang, L., Tai, Y., 2013. A facile approach to a silver conductive ink with high performance for macroelectronics. *Nanoscale research letters* 8, 1–6.
- Tekin, E., Smith, P.J., Schubert, U.S., 2008. Inkjet printing as a deposition and patterning tool for polymers and inorganic particles. *Soft Matter* 4, 703. doi:10.1039/b711984d.
- Tellier, C.R., Tossier, A.J., 1977. Exact and approximate expressions for the temperature coefficient of resistivity of polycrystalline films using the Mayadas-Shatzkes model. *Thin Solid Films* 44, 141–147. doi:10.1016/0040-6090(77)90448-5.
- Thompson, C.V., Carel, R., 1996. Stress and grain growth in thin films. *Journal of the Mechanics and Physics of Solids, Mechanics and Physics of Layered and Graded Materials* 44, 657–673. doi:10.1016/0022-5096(96)00022-1.
- Thompson, C.V., Frost, H.J., Spaepen, F., 1987. The relative rates of secondary and normal grain growth. *Acta Metallurgica* 35, 887–890. doi:10.1016/0001-6160(87)90166-0.
- Torrisi, F., Hasan, T., Wu, W., Sun, Z., Lombardo, A., Kulmala, T.S., Hsieh, G.-W., Jung, S., Bonaccorso, F., Paul, P.J., Chu, D., Ferrari, A.C., 2012. Inkjet-Printed Graphene Electronics. *ACS Nano* 6, 2992–3006. doi:10.1021/nn2044609.
- Van Baar, J.J.J., Wiegerink, R.J., Lammerink, T.S.J., Krijnen, G.J.M., Elwenspoek, M.C., 2001. Pirani pressure sensor with distributed temperature sensing.
- Van der Pauw, L. J., 1958. A Method of Measuring Specific Resistivity and Hall Effect of Discs of Arbitrary Shape, *Philips Research Reports*, 13, 1.
- Van Herwaarden, A.W., Sarro, P.M., 1988. Floating-membrane thermal vacuum sensor. *Sensors and Actuators* 14, 259–268. doi:10.1016/0250-6874(88)80073-8.
- Villani, F., Vacca, P., Nenna, G., Valentino, O., Burrasca, G., Fasolino, T., Minarini, C., della Sala, D., 2009. Inkjet Printed Polymer Layer on Flexible Substrate for OLED Applications. *The Journal of Physical Chemistry C* 113, 13398–13402. doi:10.1021/jp8095538.

- Volkman, S.K., Yin, S., Bakhishev, T., Puntambekar, K., Subramanian, V., Toney, M.F., 2011. Mechanistic Studies on Sintering of Silver Nanoparticles. *Chemistry of Materials* 23, 4634–4640. doi:10.1021/cm202561u.
- Walton, W. H., 1948. Feret's Statistical Diameter as a Measure of Particle Size, *Nature* 162, 329. doi:10.1038/162329b0.
- Wang, J., Zhang, T., Xiang, J., Zhang, B., 2008. High-tunability and low-leakage current of the polycrystalline compositionally graded (Ba,Sr)TiO₃ thin films derived by a sol-gel process. *Materials Chemistry and Physics* 108, 445–448. doi:10.1016/j.matchemphys.2007.10.023.
- Weng, P.K., Shie, J.-S., 1994. Micro-Pirani vacuum gauge. *Review of Scientific Instruments* 65, 492. doi:10.1063/1.1145163.
- Whitehouse, D.J., 2010. *Handbook of Surface and Nanometrology*, Second Edition. CRC Press.
- Wijshoff, H., 2010. The dynamics of the piezo inkjet printhead operation☆. *Physics Reports* 491, 77–177. doi:10.1016/j.physrep.2010.03.003.
- Wu, H.-C., Shan, T.-R., Hwang, W.-S., Lin, H.-J., others, 2004. Study of micro-droplet behavior for a piezoelectric inkjet printing device using a single pulse voltage pattern. *MATERIALS TRANSACTIONS*. 45, 1794–1801.
- Yang, A.-S., Yang, J.-C., Hong, M.-C., 2006. Droplet ejection study of a Picojet printhead. *Journal of Micromechanics and Microengineering* 16, 180–188. doi:10.1088/0960-1317/16/1/024.
- Yang, L., Tentzeris, M.M., 2007. Design and characterization of novel paper-based inkjet-printed RFID and microwave structures for telecommunication and sensing applications, in: *Microwave Symposium, 2007. IEEE/MTT-S International*. IEEE, pp. 1633–1636.
- Yole Développement, July 2013. Status of the MEMS Industry report.
- Yu, J.-S., Kim, I., Kim, J.-S., Jo, J., Larsen-Olsen, T.T., Søndergaard, R.R., Hösel, M., Angmo, D., Jørgensen, M., Krebs, F.C., 2012. Silver front electrode grids for ITO-free all printed polymer solar cells with embedded and raised topographies, prepared by thermal imprint, flexographic and inkjet roll-to-roll processes. *Nanoscale* 4, 6032. doi:10.1039/c2nr31508d.
- Yung, K.C., Gu, X., Lee, C.P., Choy, H.S., 2010. Ink-jet printing and camera flash sintering of silver tracks on different substrates. *Journal of Materials Processing Technology* 210, 2268–2272. doi:10.1016/j.jmatprotec.2010.08.014.
- Zhang, J., Jiang, W., Zhou, J., Wang, X., 2009. A simple micro pirani vacuum gauge fabricated by bulk micromachining technology, in: *Solid-State Sensors, Actuators and Microsystems Conference, 2009. TRANSDUCERS 2009. International*. IEEE, pp. 280–283.
- Zhang, Q.G., Zhang, X., Cao, B.Y., Fujii, M., Takahashi, K., Ikuta, T., 2006. Influence of grain boundary scattering on the electrical properties of platinum nanofilms. *Applied Physics Letters* 89, 114102. doi:10.1063/1.2338885.
- Zhang, W., Brongersma, S.H., Richard, O., Brijs, B., Palmans, R., Froyen, L., Maex, K., 2004. Influence of the electron mean free path on the resistivity of thin metal films. *Microelectronic Engineering* 76, 146–152. doi:10.1016/j.mee.2004.07.041.

Zhang, Z., Zhang, X., Xin, Z., Deng, M., Wen, Y., Song, Y., 2011. Synthesis of monodisperse silver nanoparticles for ink-jet printed flexible electronics. *Nanotechnology* 22, 425601. doi:10.1088/0957-4484/22/42/425601.

Zhu, X.H., Guigues, B., Defaÿ, E., Dubarry, C., Aïd, M., 2009. Low temperature perovskite crystallization of highly tunable dielectric Ba_{0.7}Sr_{0.3}TiO₃ thick films deposited by ion beam sputtering on platinized silicon substrates. *Journal of Applied Physics* 105, 044108. doi:10.1063/1.3080247.

Ziman, M., 1960. *Electrons and Phonons*. Oxford University Press, London.

Annex I: surface energy measurement

I.1. Pendant drop

The pendant drop method consist in determining the surface tension of the analyzed fluid from the measurement of the pendant drop equilibrium shape and size as illustrated in Figure A.1. Shape and size depends on two basic equations:

- The Young-Laplace equation (A.1), which relates interfacial tension to drop-shape

$$\Delta P = \gamma \left(\frac{1}{R_1} + \frac{1}{R_2} \right) \quad (\text{A.1})$$

where R_1 and R_2 are the principal radii of curvature, γ the surface tension and ΔP the difference pressure between the fluids, namely inside and outside the drop.

- The expression of the fluid equilibrium through the balance of the vertical forces acting across any horizontal plane, equation (A.2).

$$2\pi x \gamma \sin(\theta) = V\rho g + \pi x^2 \Delta P \quad (\text{A.2})$$

where V is the drop volume, ρ the effective density and g the acceleration of gravity.

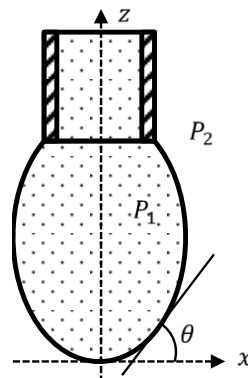


Figure A.1. Pendant drop of EMD5714 ink.

1.2. Owens-Wendt Method

The Owens-Wendt model relates the surface energy of a solid surface to the measured contact angle of a probe liquid with

$$\sigma_{Liquid}^{Tot}(1 + \cos \theta) = 2\sqrt{\sigma_{Solid}^D \sigma_{Liquid}^D} + \sqrt{\sigma_{Solid}^P \sigma_{Liquid}^P} \quad (A.3)$$

To determine the polar σ^P and dispersive σ^D components of the solid surface energy σ^{Tot} , the method consists in measuring the contact angle of several probe liquids which must be either polar or fully dispersive.

The method is illustrated with the measurement of the surface energy of a thermal silicon oxide on a wafer of silicon. For each used liquid, the total surface energy σ^T , the dispersive component σ^D , the polar component σ^P and the measured contact angle are reported in Table A.1.

Table A.1. Probe liquids for surface energy measurement, contact angle measured thermal silicon oxide

Surface tension at 25°C (mJ.m ⁻²)	Total σ^T	Dispersive component σ^D	Polar component σ^P	Contact angle (°)
Water	72.8	21.8	51	60.9 ± 1.1
Glycerol	63.4	37	26.4	55.8 ± 1.5
Diiodomethane	50.8	50.8	0	53.7 ± 0.2
Hexadecane	27.4	27.4	0	9.1 ± 2.9
Bromonaphtalene	44.6	44.6	0	37.7 ± 0.5

From the contact angle measurement, the graph in Figure A.2 is traced and the polar and dispersive components of the surface energy of silicon oxide are calculated by the linear fit of data by equation (A.4).

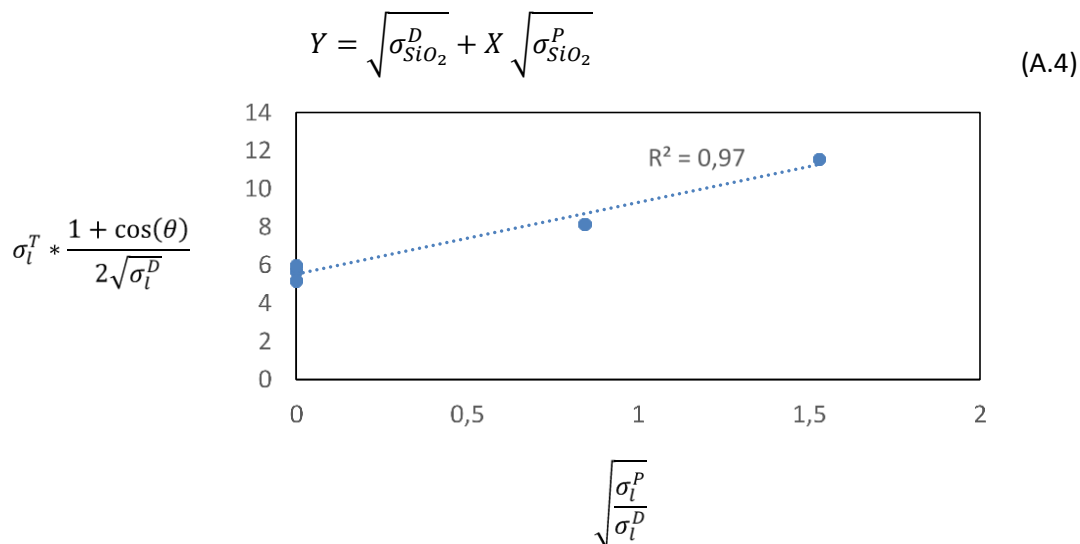


Figure A.2. Owens-Wendt plot for surface energy calculation of silicon oxide.

The total, polar and dispersive components of the silicon oxide substrate are detailed in Table A.2.

Table A.2. Surface energy of thermal silicon oxide.

Total (mJ.m ⁻²)	Polar (mJ.m ⁻²)	Dispersive (mJ.m ⁻²)
44.7	14.1	30.6

Annex II: microscopy instruments

II.1. Atomic force Microscopy

Atomic force microscopy, or AFM, is a scanning probe technique which allows atomic resolution imaging. It consists in measuring the forces that interact between the surface of a sample and a very sharp tip with a radius of curvature of a few nanometers. This tip is located at the free end of a cantilever that is between 100 and 200 μm long, as illustrated in Figure A.3.

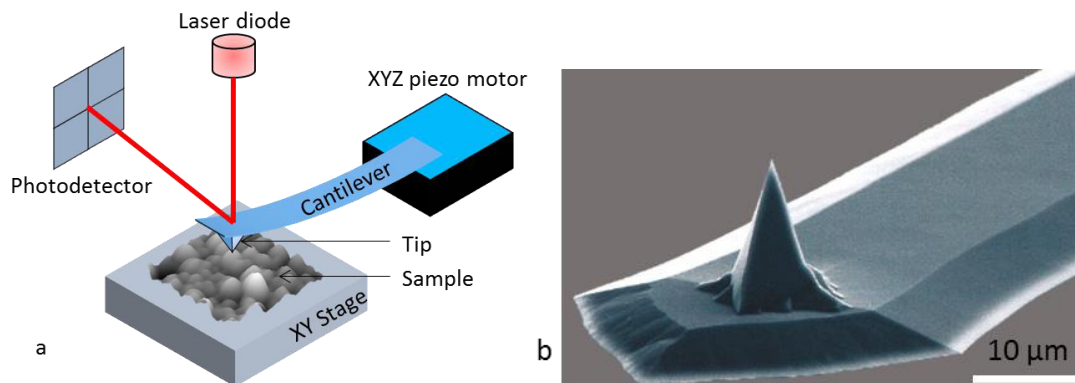


Figure A.3. a) AFM working principle. b) AFM tip and cantilever.

When the tip is scanned over a surface, forces of different nature (contact, Van der Waals, capillary, etc.) cause a deflection of the cantilever. A laser beam is focused on the backside of the cantilever, which is usually metalized to improve light reflection, and reflected onto a matrix of photodiodes able to measure laser shift position due to the cantilever deflection. The tip is usually mounted on a tri-axial piezoelectric motor controlled by a feedback loop that maintains the tip at either a constant force (to obtain height information), or a constant height (to obtain force information) above the sample surface.

The interaction between the tip and the sample surface is described by the Lennard-Jones potential. The tip – sample interaction in equation (A.5) results from the derivation the Lennard-Jones potential function.

$$F(r) = 24\epsilon \left(\frac{2\sigma^{12}}{r^{13}} - \frac{\sigma^6}{r^7} \right) \quad (\text{A.5})$$

Where r is the tip – sample distance, σ and ϵ are constants depending on the sample properties. In Figure A.4 is plotted the Lennard-Jones potential. In the region above the r -axis the repulsive force dominates while below the attractive forces are stronger. According to the potential curve, the AFM can be operated in three different modes:

- **The contact mode:** The tip scans the sample in close contact with the surface. The force on the tip is repulsive with a mean value of 10^{-6} N. This force is set by pushing the cantilever against the sample surface with the piezoelectric positioning elements. In contact mode, electrostatic and/or surface tension forces pull the scanning tip toward the surface. It can damage samples and distort image data. Therefore, contact mode imaging is heavily influenced by frictional and adhesive forces compared to non-contact or tapping mode.
- **The non-contact mode:** This mode is used when tip contact might alter the sample. The tip floats 50 – 150 \AA above the sample surface. Attractive Van der Waals forces acting

between the tip and the sample are detected, and topographic images are constructed by scanning the tip above the surface. The attractive forces from the sample are substantially weaker than the forces used by contact mode. Therefore the tip must be given a small oscillation so that AC detection methods with high sensitivity can be used to detect the small forces. Non-contact mode generally provides low resolution imaging and can also be hampered by contaminant layer (water vapor and nitrogen) which can interfere with oscillations.

- **The tapping mode:** Tapping mode overcomes problems associated with friction, adhesion, electrostatic forces, and other difficulties of conventional AFM scanning methods by alternately placing the tip in contact with the surface to provide high resolution and then lifting the tip off the surface to avoid dragging the tip across the surface. Tapping mode imaging is implemented in ambient air by oscillating the cantilever assembly at or near the cantilever's resonant frequency using a piezoelectric crystal. The oscillation amplitude is in the order of 20 nm, and when the cantilever contacts the surface, its oscillation is reduced due to energy loss caused. The reduction in oscillation amplitude is used to identify and measure surface features. Tapping mode allows achieving high resolution imaging without inducing destructive frictional forces both in air and fluid. With the Tapping mode technique, the soft and fragile samples can be imaged successfully.

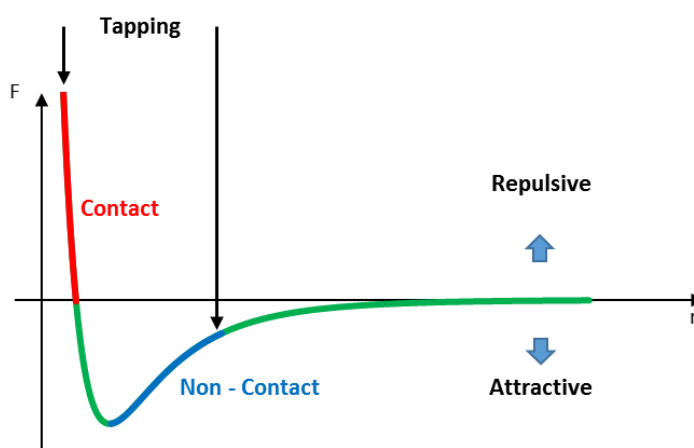


Figure A.4. Lennard-Jones Potential.

II.2. Scanning electron microscopy¹

Imaging with a scanning electron microscope is realized in high vacuum through the analysis of the signals that derive from the interaction between the region of interest (ROI) and an impinging beam of electrons. Electrons are generated by an electron gun and are then focused by a series of electron lenses. These lenses allow improving the coherence of the electron beam and correcting stigmatic aberrations. When the electrons collide with the sample surface, several signals are generated. Depending on the detectors that are mounted on the microscope, several information can be obtained.

¹ <http://www-g.eng.cam.ac.uk/125/achievements/mcmullan/mcm.htm>

- Secondary electrons are the product of the inelastic scattering of the sample electrons with the beam electrons. They usually have low energy, below 50 eV. Secondary electrons detection offers valuable information on both the topology and morphology of the surface.
- X-ray generation is produced by inelastic collisions of the incident electrons with electrons in the atomic orbitals of the sample. As the excited electrons return to lower energy states, they yield X-rays that are of a fixed wavelength, producing characteristic X-rays each chemical element.
- Backscattered electrons are the product of elastic scattering of the beam electrons with the samples atoms (reflection). They have high energy, almost the same as the beam. Backscattered electrons produce a chemical contrast between the chemical elements contained in the sample: brighter areas usually correspond to greater atomic number Z.

Other types of signals (Figure A.5) that can be analyzed in a SEM are generated by the interaction between the high energy beam electrons and the sample such as Auger's electrons and cathodoluminescence.

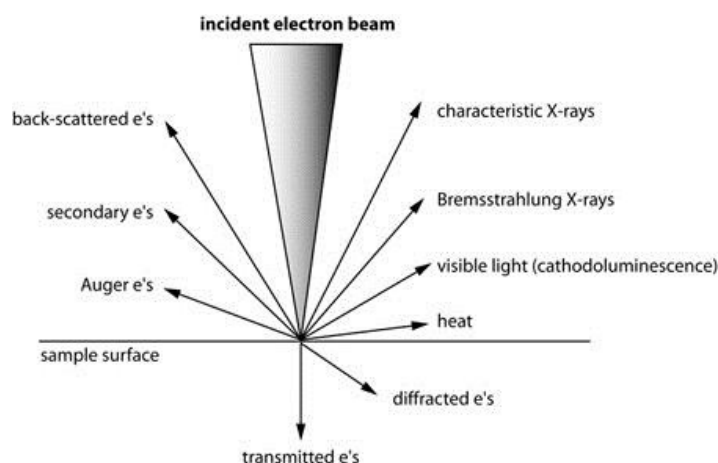


Figure A.5. Types of interaction between electrons and a sample².

If several signals can be acquired by electron microscopy without damaging the samples, it provides only two dimensional information and cannot image buried defects.

II.3. Focused Ion Beam

Focused ion beam instruments allow both imaging and micromachining at micro and nanoscale. The instrument is similar to SEM, except that the raster beam is composed of ions rather than electrons. The most common ions employed in FIB are Ga⁺. They allow precise micromachining as well as ion beam activated deposition when used in conjunction with gas injection.

The most common and employed ion source for micromachining applications is the liquid-metal ion source (LMIS) as it provides the brightest and highly focused ion beam. The column is always composed of at least two lenses, a condenser to define the beam and an objective lens to focus it on the sample. Moreover, there are beam-defining apertures to define the beam diameter, stigmation poles to ensure a spherical beam profile and a high-speed beam blanker to quickly deflect the beam.

FIB techniques have demonstrated their potential in the semiconductor industry for both fabrication and characterization. However, several limitations of a single-beam are to be addressed:

² http://serc.carleton.edu/research_education/geochemsheets/electroninteractions.html

- As in electron microscopy, ions interact with the samples and generate signals that can be analyzed for imaging. Although, the ion beam removes material from the sample which alters the ROIs.
- When imaging crystalline structures, the highly energetic ions might cause local amorphization of the ROIs.
- Another issue that goes together with the amorphization is ion implantation which modifies the chemical composition of the ROIs.

The association of the two beams, namely electrons and ions, in the same equipment offers a wide range of operations for high resolution imaging and 3D inspection.

Résumé

Impression fonctionnelle :
de l'étude de couches imprimées
au prototypage de composants flexibles

Introduction

Le développement industriel du XX^e siècle est sans aucun doute fortement marqué par le développement de l'électronique. Depuis la réalisation du premier transistor dans les laboratoires Bell en 1947, les techniques de fabrication pour les composants électroniques n'ont cessé d'évoluer. Les défis majeurs à relever encore aujourd'hui sont la miniaturisation, l'intégration et la consommation énergétique.

Pour fabriquer des composants électroniques, différents types de matériaux (conducteurs, semi-conducteurs et isolants) sont usinés. Dans la communauté de l'électronique, le terme "patterning" (création d'un motif) est communément employé. Au cours des vingt dernières années, l'essor de l'électronique flexible et grande surface a mis en évidence certaines limites des procédés du silicium. En effet, le prix des composants sur silicium augmente exponentiellement à cause du fort coût par unité de surface des substrats (Hutchings, 2012).

Pour répondre à cette problématique du coût par unité de surface, les techniques d'impression, naturellement compatibles avec des substrats grande surface et bas-coût, ont été adaptées à des matériaux fonctionnels. C'est dans ce contexte que les mondes de l'impression, de la science des matériaux et de l'électronique collaborent, dans le but de réaliser des fonctions imprimées (Gunde, 2012).

Cependant, l'impression fonctionnelle ne cherche pas à remplacer ni entrer en compétition avec les techniques standard du silicium. Elle offre plutôt des solutions technologiques complémentaires, en particulier pour des applications qui ne sont pas contraintes en surface.

Contexte de la thèse

Cette thèse s'est déroulée au CEA, Leti à Grenoble en collaboration avec le *Laboratoire Génie des Procédés Papetiers* (LGP2) de l'école d'ingénieur *Grenoble INP-Pagora*. Le Leti est un centre de recherche appliquée pour l'innovation et le transfert industriel. Ses domaines d'excellence sont les micros et nanotechnologies et leurs applications (télécommunications, photonique, biomédical). Au sein du Laboratoire de Caractérisation et Fiabilité des Composants (LCFC) du Leti, un savoir et un savoir-faire en science des matériaux et caractérisation de composants MEMS (radio-fréquence, capteurs, et actionneurs) ont été développés pour répondre aux enjeux de cette nouvelle famille de composants. Le LGP2 est un laboratoire universitaire historiquement dédié à la recherche dans le domaine du papier et des procédés d'impression et son activité s'est récemment élargie vers les bio-matériaux. De plus, son expérience en traitement de surface et formulation des encres a permis de créer de nouvelles thématiques de recherche pour la fonctionnalisation de surface et la formulation d'encres fonctionnelles pour la fabrication d'objets intelligents avec une forte valeur ajoutée.

En parallèle, cette thèse s'est inscrite dans le cadre du **projet I2Flex** – Intégration Imprimée sur support FLEXible – en partenariat avec des acteurs industriels majeurs comme *Gemalto* et *STMicroelectronics* ainsi que des petites et moyennes entreprises (*ASK*, *SANSystems*, *STID*, *Smart Packaging Solution*) et des laboratoires académiques : le *Centre de Microélectronique de Provence (Mines de Saint-Etienne)* et le laboratoire de *Lasers, Plasmas et Procédés Photoniques (CNRS, LP3, Luminy)*. L'objectif de ce projet était de qualifier et développer des procédés de fabrication par impression pour l'intégration hybride de puces silicium et d'interconnexions imprimées sur des substrats plastiques et papiers. Les aspects innovants du projet I2Flex reposent sur l'estimation du potentiel de l'impression par jet d'encre pour de la production industrielle, au travers de l'étude approfondie du procédé et des matériaux imprimés et de la conception, la fabrication et la caractérisation de prototypes fonctionnels

Les opportunités de l'impression fonctionnelle

Les procédés d'impression ont atteint un niveau de maturité qui offre une alternative à la lithographie pour la fabrication de composants électroniques grande surface dont les dimensions minimales sont supérieures à 10 μm . L'intérêt croissant pour les procédés d'impression est généralement motivé par l'idée d'une technologie à faible coût. Subramanian *et al.* (2008) ont proposé une analyse précise de cette attente industrielle :

i. L'impression n'est pas synonyme de bas-coût

En effet, des équipements de lithographie fortement dépréciés sont disponibles et leur maturité industrielle est loin devant le jeune âge des technologies d'impression fonctionnelles. Cependant, l'expérience existante dans l'impression conventionnelle peut accélérer leur développement industriel.

ii. L'impression réduit la complexité du procédé

L'impression est une technique de formation de motifs entièrement additive qui permet le dépôt d'un matériau uniquement lorsque cela est nécessaire. Par rapport à la photolithographie, le nombre d'étapes de fabrication est au moins divisé par deux. De plus, les procédés d'impression utilisent principalement des matériaux sous la forme d'encre ou de pâte, par conséquent les environnements sous vide et de salle blanche ne sont plus obligatoires.

L'électronique flexible fabriquée avec des procédés d'impression est un domaine avec de fortes attentes économiques. Une étude du cabinet *Yole Développement* (Février 2014) indique que le

marché de l'électronique flexible imprimée est susceptible d'atteindre près d'un milliard de dollars d'ici 2020, avec un taux de croissance annuel moyen de 27% (TCAM). En particulier, comme le montre la Figure I.1, l'impression fonctionnelle représentera 89 % de ce marché.

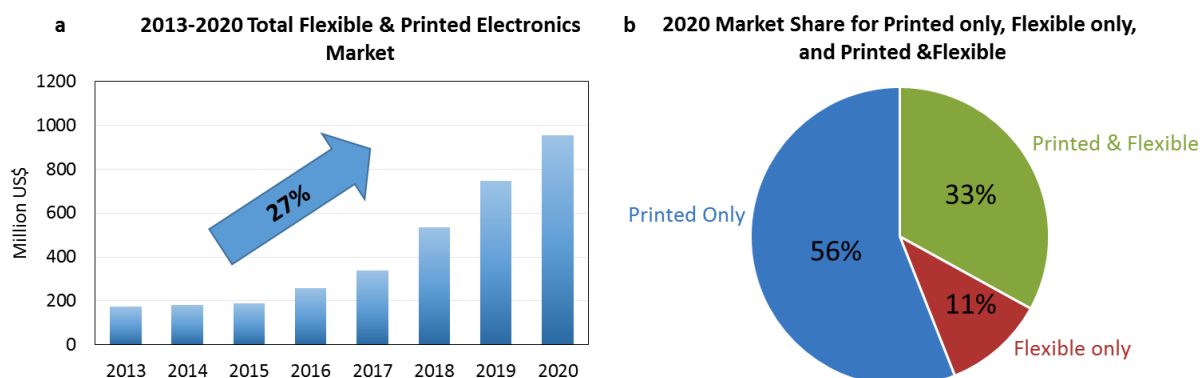


Figure I.1. a) Marché de l'électronique flexible imprimée entre 2013-2020. b) Parts de marché l'électronique Imprimée, Flexible et Imprimée et Flexible en 2020.

Adapté de *Materials & Equipment for Printed and Flexible Electronics*, Yole Développement, 2014.

Il semble y avoir de réelles opportunités industrielles à saisir dans plusieurs domaines d'applications. Si le marché de l'électronique flexible est fortement soutenu par les matériaux organiques pour le photovoltaïque, les écrans et l'éclairage, il existe d'autres domaines à croissance rapide tels que les capteurs, les papiers et les textiles intelligents. Les instituts de recherche appliquée tels que Leti ont donc un grand intérêt à explorer le potentiel de ce marché émergent.

Les objectifs de la thèse

Parmi les technologies existantes pour l'électronique imprimée, notre étude s'est concentrée sur les procédés de goutte à la demande (Drop-On-Demand). L'impression jet d'encre est une technique numérique sans contact qui permet de réaliser des motifs dont les dimensions varient entre 10 μm et plusieurs centimètres. Ce procédé numérique est particulièrement bien adapté au prototypage et à la fabrication en petites séries.

Aux cours des dix dernières années, de nombreux efforts ont été fournis pour la formulation d'encres conductrices. La littérature montre qu'une large gamme de résistivité est aujourd'hui couverte par ces encres ($10^{-7} - 10^{12} \Omega \cdot \text{m}$). En particulier, grâce au potentiel avéré de la technologie jet d'encre pour la réalisation d'interconnexions électriques, d'électrodes et d'antennes, les encres à base de nanoparticules métalliques (Au, Ag, Cu et Al) ont fait l'objet de nombreuses études. La formulation de ces suspensions colloïdales permet d'atteindre jusqu'à 60 % en taux massique du matériau actif sans modifier les performances du procédé de fabrication. Enfin, les effets de tailles connues nanoparticules, qui réduisent leur température de fusion et leur énergie d'activation, rendent les traitements thermiques post-impression compatibles avec les substrats polymères utilisés dans les applications flexibles. Ces traitements thermiques sont en effet indispensables pour éliminer le véhicule de l'encre et ainsi assurer la continuité électrique de la couche imprimée.

Les encres à base de nanoparticules d'argent sont sans aucun doute les plus répandues sur le marché des matériaux conducteurs imprimables. La formulation avec des fonctionnalités spécifiques est couramment réalisée à l'échelle du laboratoire et de nombreuses références commerciales sont aujourd'hui disponibles. Ces encres ont donc été sélectionnées et sont étudiées de manière approfondie dans cette thèse.

Le premier chapitre de cette thèse est dédié à une revue bibliographique des techniques d'impression pour des applications fonctionnelles. En particulier, nous décrivons l'impression par jet d'encre par actionnement piézoélectrique. Les étapes de ce procédé d'impression sont détaillées, à partir de l'éjection jusqu'à l'impact des gouttes sur le substrat. Les conditions d'impression qui permettent d'obtenir des motifs conformes sont mises en évidence. Après le dépôt de l'encre, un traitement thermique est indispensable. Différentes techniques sont disponibles pour fournir l'énergie thermique nécessaire au frittage des nanoparticules : transfert par convection, conduction et irradiation. Les spécificités de chacune de ces méthodes sont résumées dans ce chapitre. Enfin, nous apportons les bases théoriques pour l'analyse et la caractérisation des propriétés électriques et mécaniques des couches minces imprimées.

Le deuxième chapitre est entièrement dédié à la caractérisation et à l'évolution des propriétés de couches d'argent imprimées par jet d'encre à partir d'une encre commerciale, en fonction des conditions de traitement thermique. Les motifs de tests sont imprimés sur un substrat SiO₂/Si sélectionné pour sa stabilité aux variations de température entre l'ambiante et 300°C. La méthode retenue dans cette étude est le traitement en étuve. Ce chapitre s'articule autour de trois catégories de propriétés des couches d'argent imprimées :

- iii. La microstructure et les paramètres morphologiques comme la taille de grain, la rugosité et la porosité.
- iv. Les propriétés de conduction électronique comme la conductivité et le coefficient de température.
- v. Les propriétés mécaniques comme le module d'Young et la dureté.

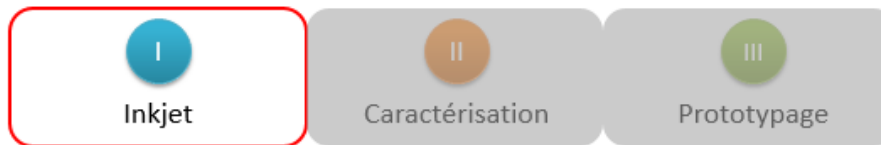
Les protocoles expérimentaux mis au point pour la caractérisation de ces paramètres sont détaillés et les propriétés fonctionnelles des couches d'argent sont corrélées avec la microstructure au travers de modèles existants.

Le troisième et dernier chapitre s'appuie sur la maîtrise des conditions de dépôts et les propriétés des couches d'argent mises en évidence précédemment pour le prototypage de composants électroniques entièrement imprimés : un filtre passe-bande centré à 17 GHz et un micro-capteur de vide imprimé sur des substrats flexibles en polyimide, un interrupteur de type « membrane switch » de 250 µm d'épaisseur et des capacités de type Métal-Isolant-Métal pour des applications radio-fréquence. La fabrication et la caractérisation de ces prototypes dont les caractéristiques sont proches de l'état de l'art ont fait l'objet de plusieurs publications et suggèrent de nouvelles opportunités pour les technologies d'impression.

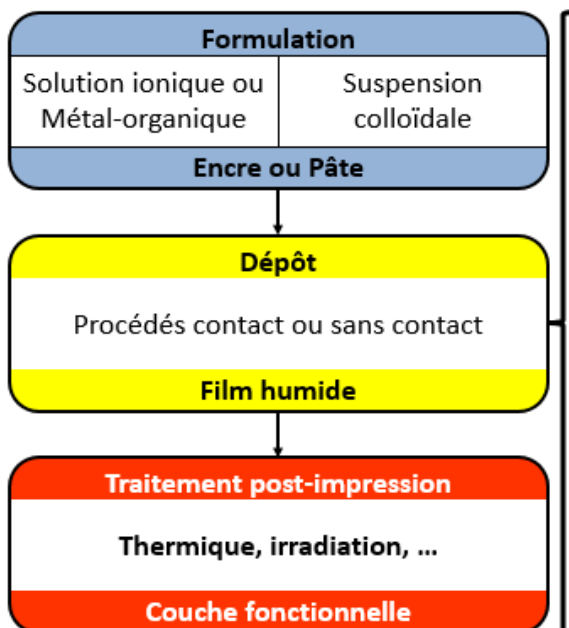
L'expérience acquise au cours de cette thèse sur le dépôt la fabrication de motifs imprimés par jet d'encre dans l'environnement silicium du CEA, Leti ouvre des perspectives prometteuses qui seront discutées dans un chapitre de conclusion.

Dans le cadre de ce résumé, nous présentons les principaux résultats de cette thèse sous forme de diapositives commentées et adaptées, provenant de la soutenance de thèse.

Technologie d'impression jet d'encre



Les procédés pour l'impression fonctionnelle



Procédés contact

- Contact mécanique entre le système de dépôt de l'encre et le substrat
- Nécessite un masque rigide

Lithographie offset, Flexographie, Héliogravure, Sérigraphie

Procédés sans contact

- Pas de contact mécanique entre le système de dépôt et le substrat
- Source numérique du motif à imprimer

*Rayonnement à haute énergie, Système d'impression continu ou **goutte-à-goutte***

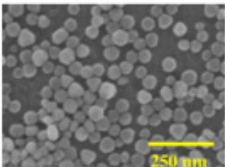
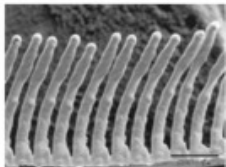
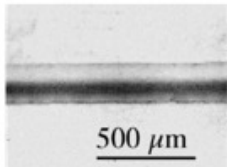
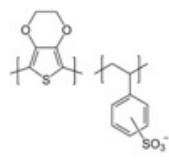
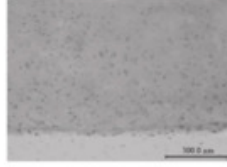
Pourquoi le jet d'encre ?

Les avantages

- Direct writing → Pas de déchets, pas de lithographie ni de gravure
- Motif numérique → Pas de masques, flexibilité
- Méthode sans contact → Compatibilité avec les substrats
- Résolutions d'impression très élevées → Gap minimum d'environ 10 μm

➔ Technique largement utilisée à l'échelle du laboratoire pour le prototypage et l'étude de nouvelles encres

- Grande variété de matériaux imprimables et divers types de véhicules d'encres

Métaux	Céramiques	Diélectriques	Polymères	Carbone
Au, Ag, Cu, ...	PZT, Al ₂ O ₃ , ...	BST, resin, ...	SU-8, PEDOT	CNTs, Graphène
				
Cu NPs ink Park, 2007	PZT μ-pillars Bhatti, 2001	Inkjet BST Kaydanova, 2007	PEDOT:PSS mol.	Inkjet MWCNTs, Denneulin, 2009

leti Inkjet Functional printing – 11/12/2014 | Daniele Sette | 3/34

Préparation des échantillons

Traitement thermique: étuve

- Séchage: évaporation du solvant
- Frittage des nanoparticules



Substrat flexible:
polyimide

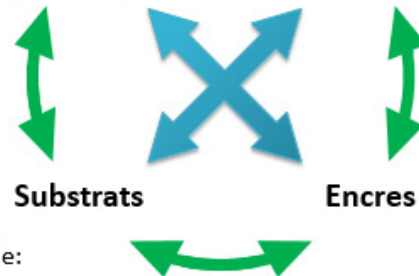


Substrat rigide:
SiO₂/Si



$$\sigma_{substrat} = 40 - 50 \text{ mJ} \cdot \text{m}^{-2}$$

Traitement post-impr. Imprimante



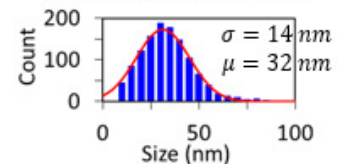
$$\sigma_{substrat} > \sigma_{encre}$$

Dimatix DMP 2831



- Imprimante de laboratoire
- 1 tête avec 16 buses
- Gouttes de 1 ou 10 pL
- Actionnement piézoélectrique

SunChemical EMD5714



- 40 wt% de NPs d'argent
- Solvant: éthanol/éthylène glycol
- Diamètre moyen < 50 nm
- $\eta_{encre} = 13.5 \text{ mPa} \cdot \text{s}$
- $\sigma_{encre} = 24 \pm 8 \text{ mJ} \cdot \text{m}^{-2}$

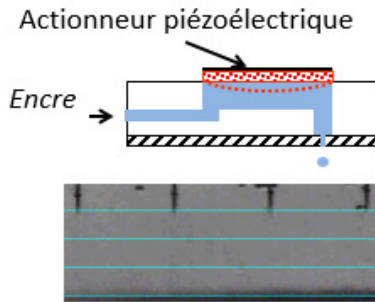
leti Inkjet

Functional printing – 11/12/2014 | Daniele Sette | 4/34

Impression jet d'encre



Ejection



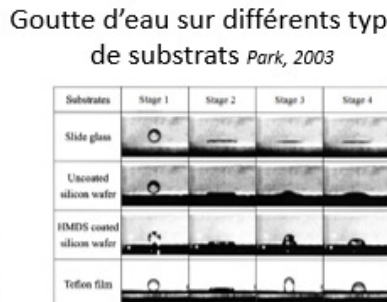
Paramètres

- Tension d'actionnement et forme du pulse
- Viscosité et tension de surface

$$Z = \frac{1}{Oh} = \frac{\sqrt{ap\sigma}}{\eta}$$

Fromm, 1984

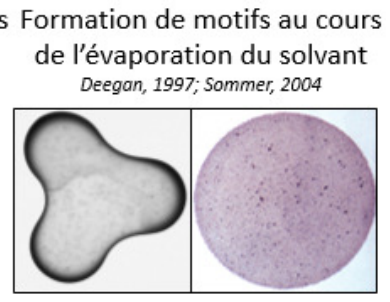
Impact



Paramètres

- Encre: densité, viscosité, tension de surface
- Goutte: vitesse et dimensions
- Substrat: rugosité, porosité, énergie de surface, planéité, homogénéité chimique

Séchage



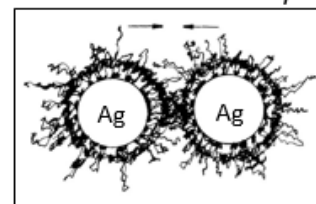
Paramètres

- Solvant et additifs de l'encre
- Propriétés du substrats
- Température

Encres argent: suspension colloïdale de NPs

- Encres conductrices les plus utilisées: produits du commerce et formulation en laboratoire
- Longue durée de vie > 6 mois
- Solvant peu dangereux : à base d'eau et alcool, ...
- Conductivité électrique > $10^7 S.m^{-1}$
- Spécifications
 - Stabilité colloïdale → stabilisation par des polymères
 - Traitement thermique post-impression

Stabilisation stérique

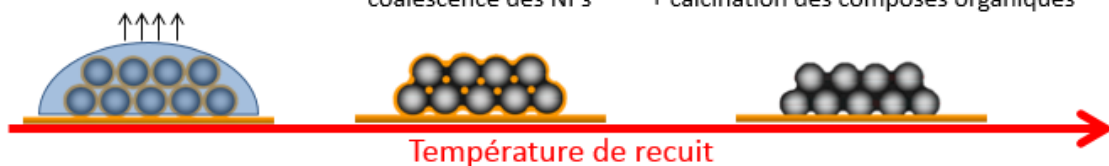


Le traitement thermique

Evaporation du solvant

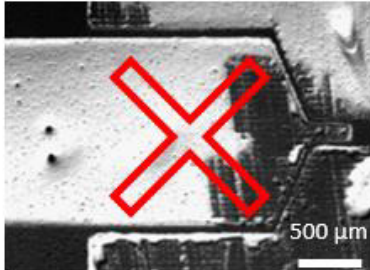
Début de la coalescence des NPs

Coalescence des NPs + calcination des composés organiques

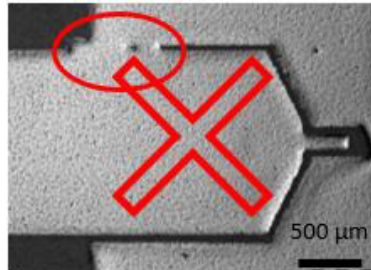


Motifs imprimés – Encre NPs Ag 40 wt%

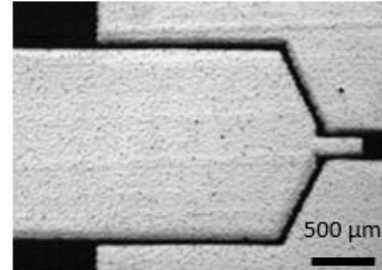
Démouillage de l'encre



Étalement de l'encre



Motif conforme

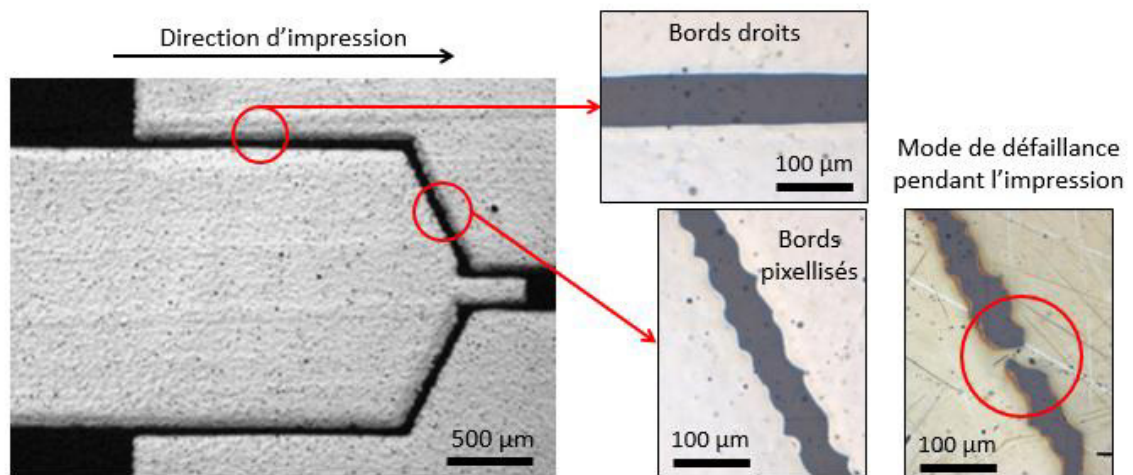


Substrat: Kapton HN, 75 µm d'épaisseur – Séchage @ 60°C, 60 min

■ Optimisation des paramètres:

- Température du substrat
- Conditions des séchage du motif
- Source numérique du motif: résolution et pixellisation

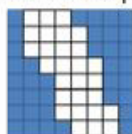
Motifs imprimés – Encre NPs Ag 40 wt%



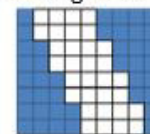
Motif désiré



Disposition automatique des pixels

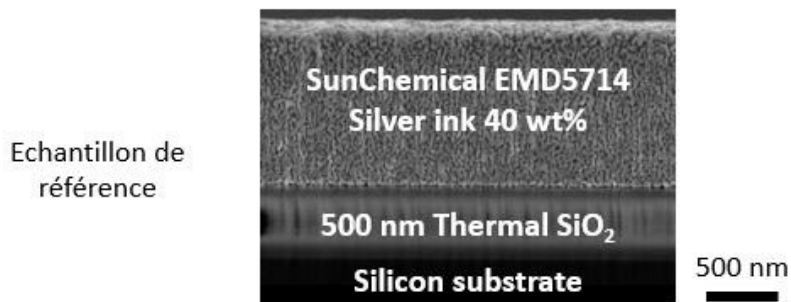


Disposition régulière des pixels



Augmente la fiabilité de l'impression

Propriétés des couches d'argent imprimées par jet d'encre



Traitement thermique de couches de NPs d'argent imprimées

→ Frittage: coalescence des NPs et croissance de grains

- Effets de taille des NPs
 - Ratio volume/surface très grand
 - Diminution de la température de fusion

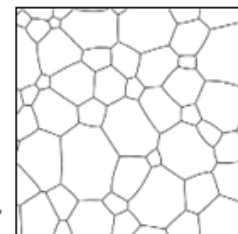
Température de frittage compatible avec des substrats polymères

- Le frittage modifie fortement les propriétés des couches imprimées

- Microstructure
- Propriétés électriques : conductivité, TCR, ...
- Propriétés mécaniques: module d'Young, dureté

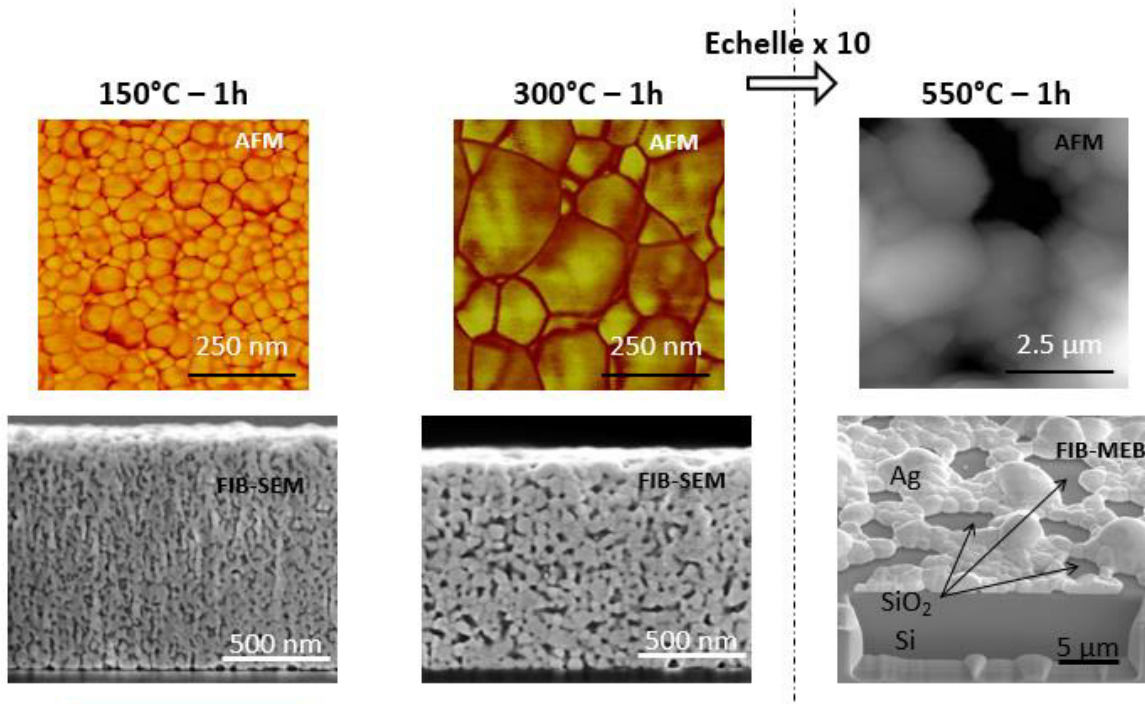
- Méthode: étuve, laser, microonde, plasma, ...

Simulation de la croissance des grains
[CORE-Materials](#) – Open Educational Resources

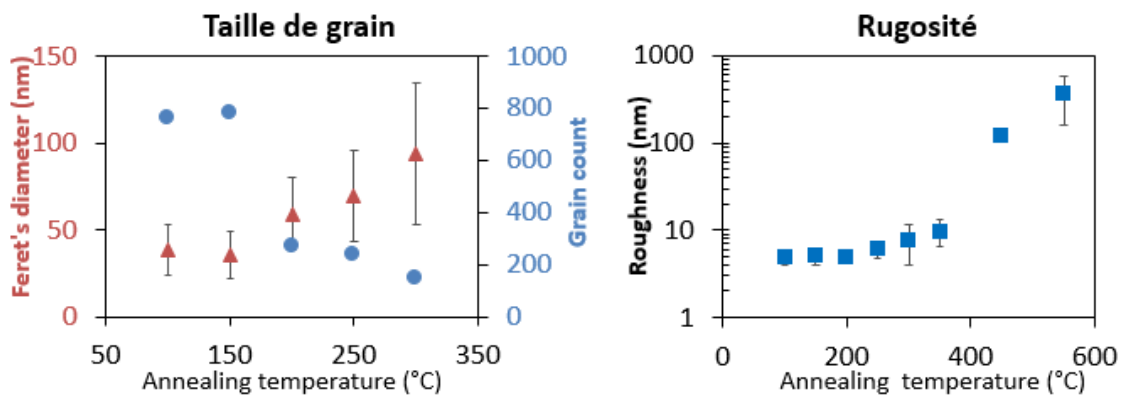


→ Etude de l'influence des conditions de traitement thermique

Evolution de la microstructure

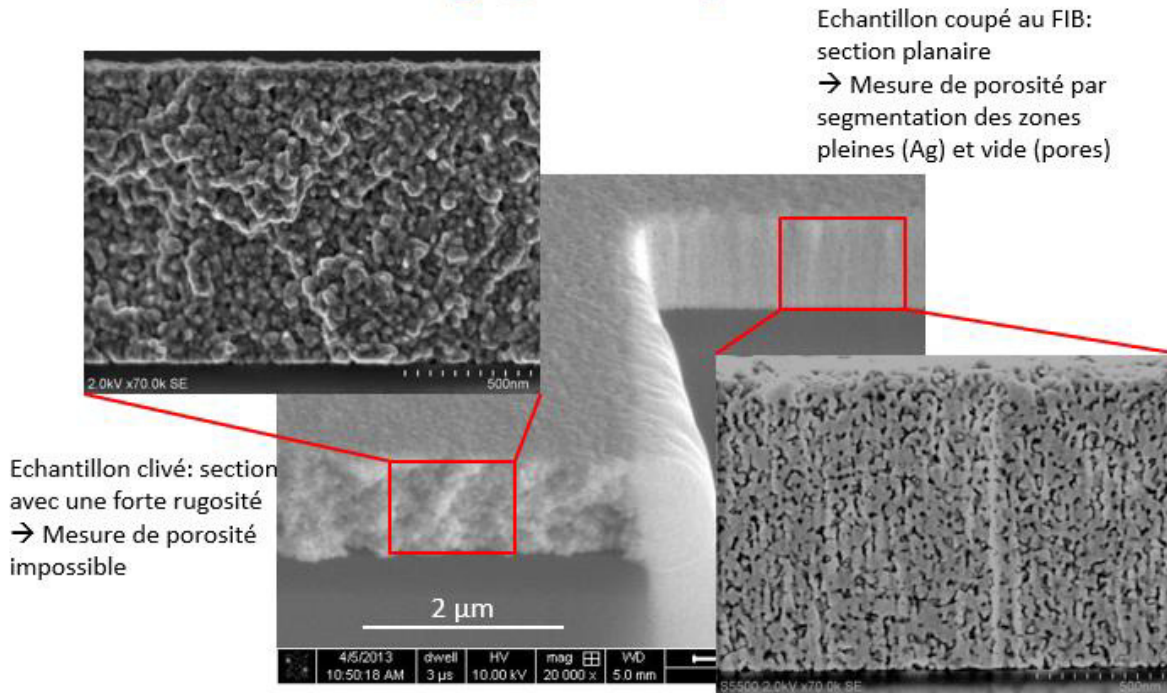


Caractérisation de la surface



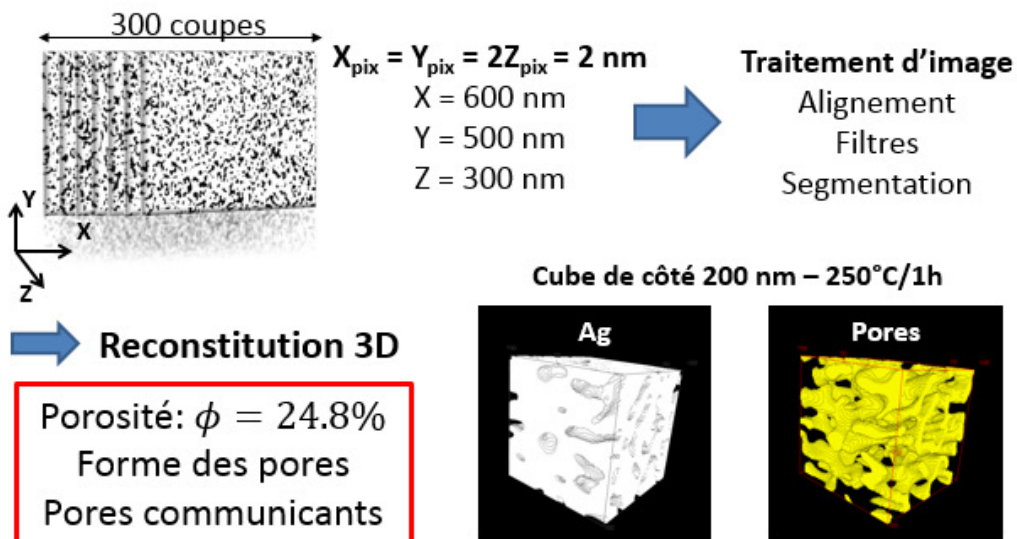
Taille de grain ↗
Rugosité ↗
Porosité ?

Porosité 2D – Ag @ 250°C, 1h

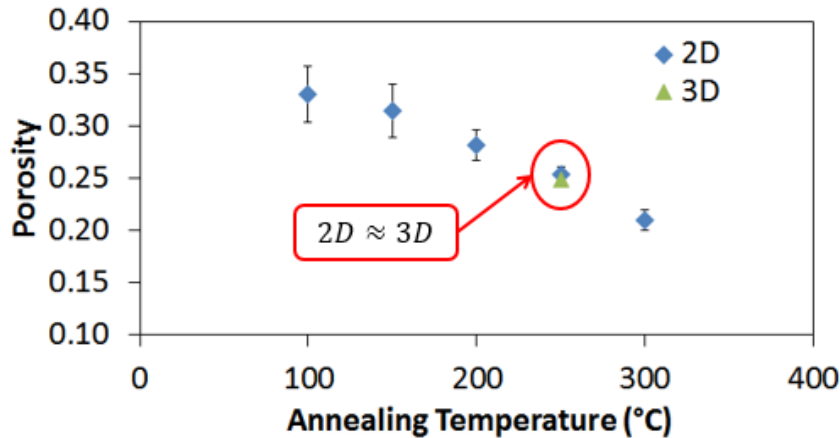


Porosité 3D – Ag @ 250°C, 1h

- Méthode slice & view au FIB-MEB



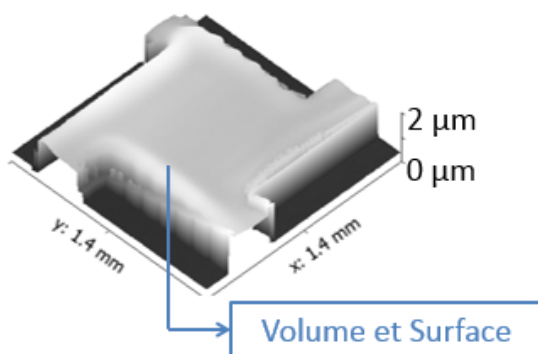
Mesure de la porosité



- Les valeurs dépendent de l'algorithme de traitement
→ Etude comparative en appliquant toujours le même
- Comment vérifier les valeurs expérimentales?

Mesure de l'épaisseur

Interférométrie optique



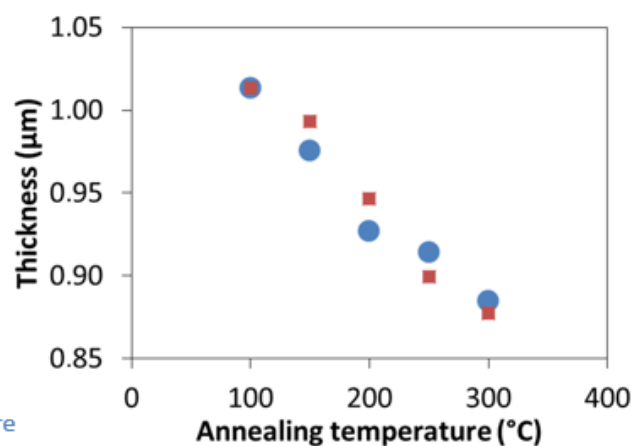
L'épaisseur des couches imprimées est irrégulière
→ Valeur moyenne en mesurant la surface et le volume d'un motif

Calcul itératif de l'épaisseur en prenant en compte les valeurs de porosité extraites précédemment

● Mesure moyenne $t = V/A$

■ Calculée $t_i = t_{100}(1 - (\phi_{i-1} - \phi_i))$

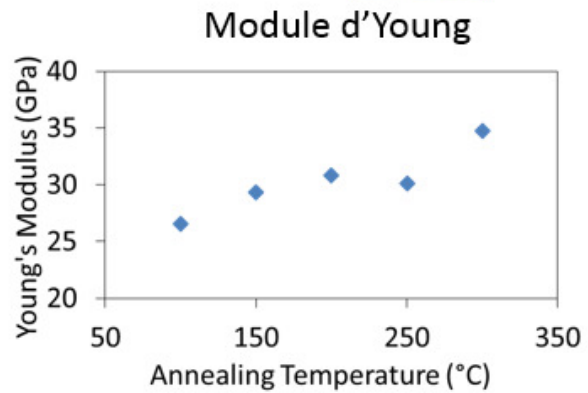
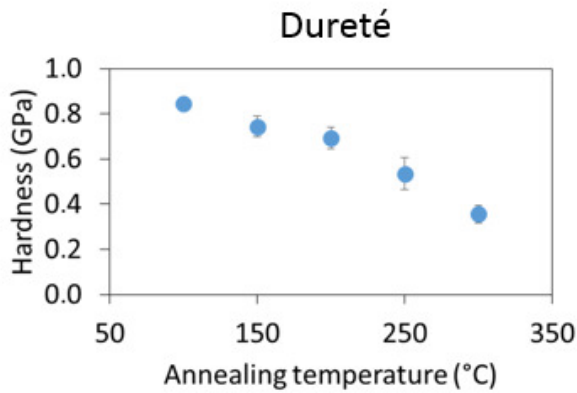
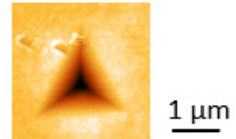
Epaisseur t



Très bon accord entre les valeurs mesurées et calculées de l'épaisseur

→ 1^{ère} méthode de validation de la mesure de la porosité

Dureté et module d'Young



- $H \searrow$ avec la température de traitement thermique
- Théorie de Hall-Petch :

$$H \propto \frac{1}{\sqrt{\text{grain size}}}$$

- $E \nearrow$ avec la température de traitement thermique
- $E(\text{Ag massif}) = 83 \text{ GPa}$

$$E_{\text{Ag imprimé}} < E_{\text{Ag massif}}$$

→ Porosité des couches imprimées

Module d'Young de matériaux poreux

Modélisation par éléments finis, Roberts, 2000

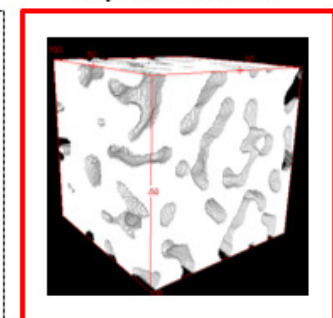
Résultat expérimental

(a) **Solide sphérique**
 $\phi_0 = 0.652, n = 2.23$

(b) **Pore sphérique**
 $\phi_0 = 0.818, n = 1.65$

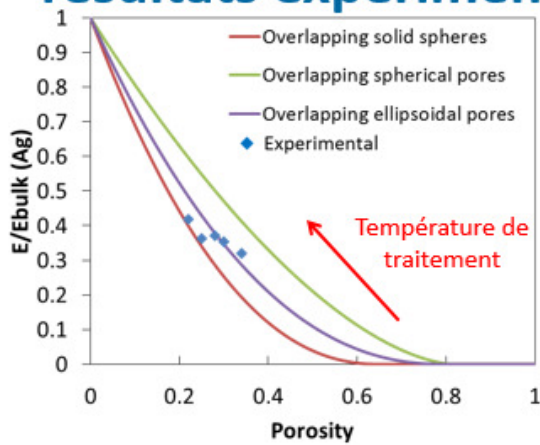
(c) **Pore ellipsoïdal**
 $\phi_0 = 0.798, n = 2.25$

→ Loi empirique: $\frac{E}{E_{\text{massif}}} = \left(1 - \frac{\phi}{\phi_0}\right)^n$



↓ E_m, ϕ_m
→ Comparaison ?

Comparaison du modèle FEM et des résultats expérimentaux

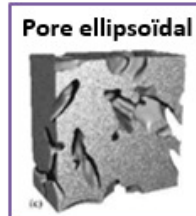
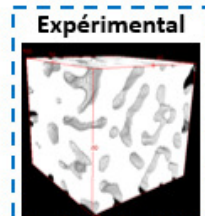


Mesure du module d'Young
+
Modèle FEM



Estimation de
la porosité

→ 2^{ème} méthode de validation de la mesure de la porosité



Porosité \propto algo. Traitement d'image

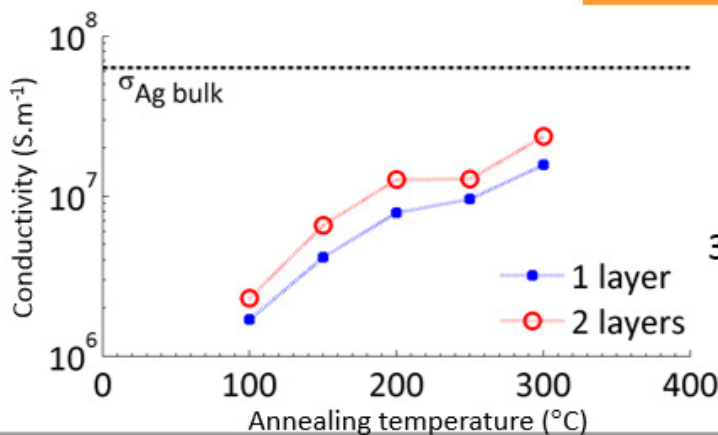
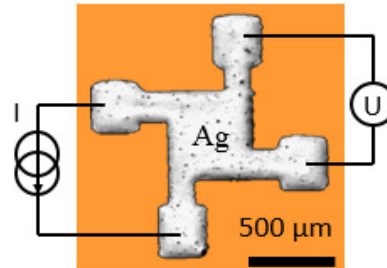
→ Etude comparative nécessaire

Corroboration par d'autres grandeurs
1 → Epaisseur 2 → Module d'Young

Conductivité électrique σ

Motif Van der Pauw imprimés (encre Ag)

$$\sigma = \frac{I \ln 2}{U \pi t}$$

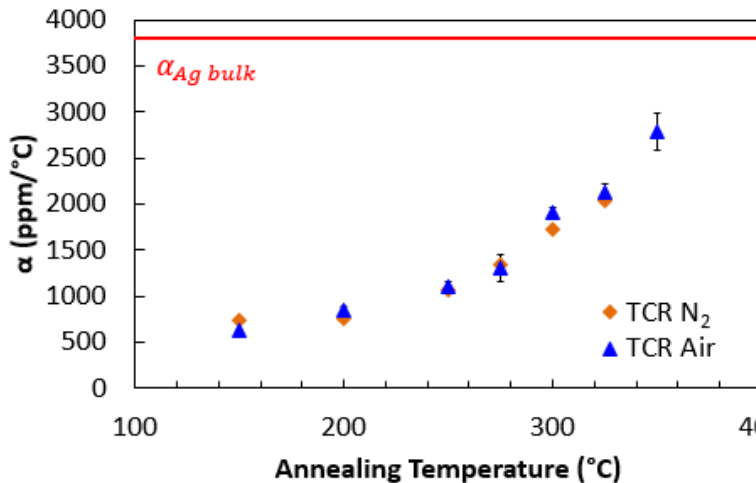
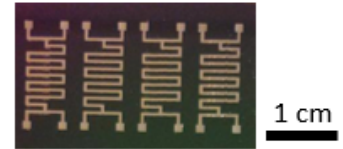


Augmentation de la conductivité jusqu'à 30% de la conductivité de l'argent massif

Coefficient de température α

Définition: α relie la résistance R d'un matériau conducteur à sa température T

$$R(T) = R_0(1 + \alpha(T - T_0)) \text{ for } -50^\circ\text{C} < T < 200^\circ\text{C}$$



- Mesure sous azote
- Gamme étendue de -25°C à $+75^\circ\text{C}$
- Affranchissement de l'influence de l'humidité
- α augmente avec la température de traitement thermique
- Valeurs similaires sous air et azote
- Ecart type < 10%

Résumé

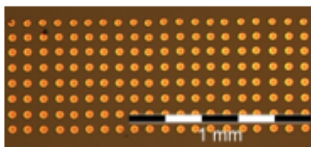
Argent Massif

$$\sigma_{Ag.M} = 6 \cdot 10^7 \text{ S} \cdot \text{m}^{-1} \quad E_{Ag.M} = 83 \text{ GPa}$$

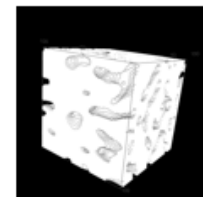
$$\alpha_{Ag.M} = 3800 \text{ ppm} \cdot ^\circ\text{C}^{-1} \quad H_{Ag.M} = 0.3 - 0.7 \text{ GPa}$$

- Etude de l'influence des conditions de traitement thermique sur les propriétés de couches d'argent imprimées
Gamme de température étudiée : 100-300°C → Substrats flexibles
- Propriétés étudiées

Microstructure



- Grains: taille, distribution, forme
- Rugosité
- Porosité: 2D, 3D, forme



↔ **Corrélation des propriétés fonctionnelles des couches imprimées à leur microstructure grâce à des modèles de la littérature** ↔

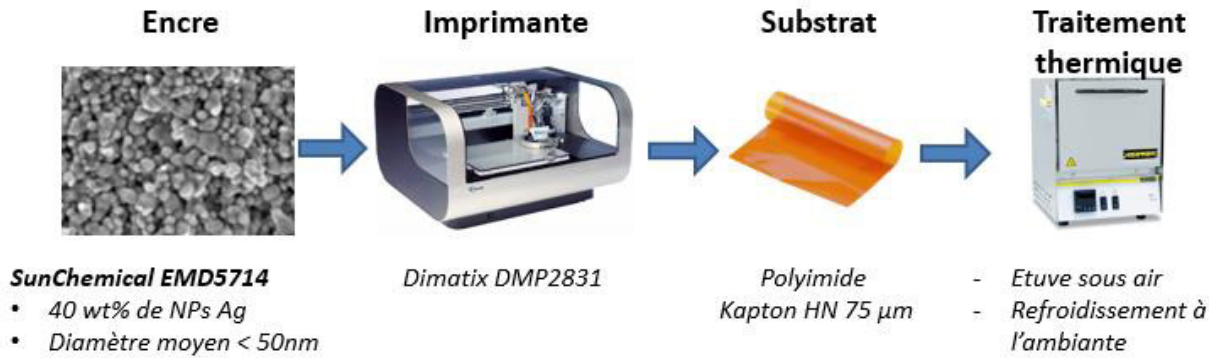
Propriétés électriques

- Conductivité électrique : 1-30% of $\sigma_{Ag.M}$
- Coeff. de température α : 10-70% of $\alpha_{Ag.M}$

Propriétés mécaniques

- Module d'Young : 30-40% de $E_{Ag.M}$
- Dureté: dépend de la taille de grain

Prototypage de composants électroniques imprimés

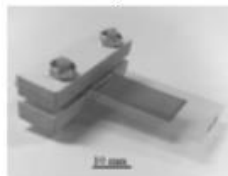


Quels types de composants?

Radio fréquence
 Filtre passe-bande à 2.4 GHz
 Yang, 2007



Capteurs
 Jauge de contrainte
 Andò, 2013



Electronique orga.
 OLEDs
 Mauthner, 2008



Les prototypes réalisés

Jauge Pirani



Filtre PB à 17 GHz



Membrane switch



Capa. M-I-M



Capteur de pression (vide) imprimé Micro-jauge Pirani

Transducers 2013 & Eurosensors XXVII (Barcelona, Spain)

Micro Pirani pressure sensor fabricated by inkjet printing, D. Sette, D. Mercier, P. Brunet-M., C. Poulain, A. Blayo

leti

Prototypage

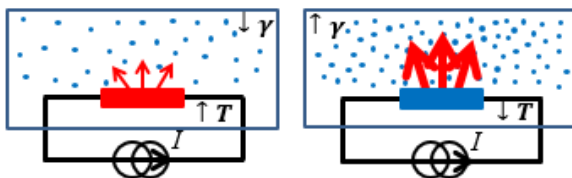
Functional printing – 11/12/2014 | Daniele Sette | 25/34

© CEA. All rights reserved

Capteur de vide – Micro-jauge Pirani

Principe de fonctionnement

Mesurer la variation de résistance d'un élément conducteur chauffé par effet Joule et placé dans l'environnement à contrôler.



$$R(T) = R_0 * [1 + \alpha * (T - T_0)]$$

MEMS devices

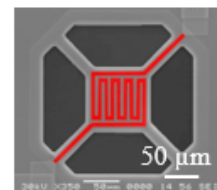
Micro-pont suspendu

Zhang, 2006



Micro-plaque suspendue

Wang, 2008



➔ Procédé de fabrication complexe:

- Nombreuses étapes
- Gravure profonde du silicium



Design – Fabrication – Caractérisation
d'une micro-jauge Pirani entièrement imprimée

leti

Prototypage

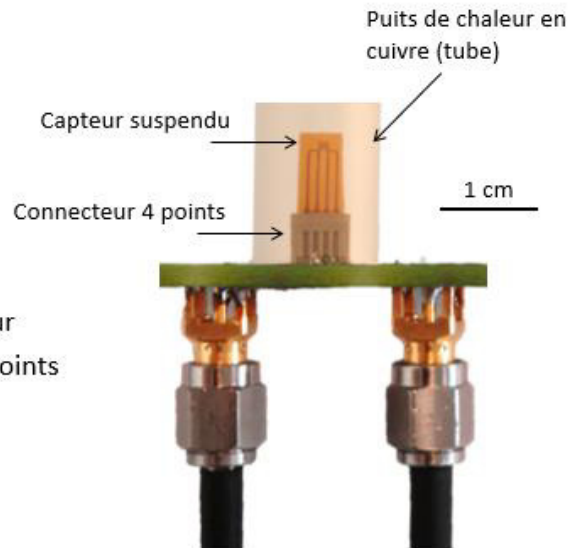
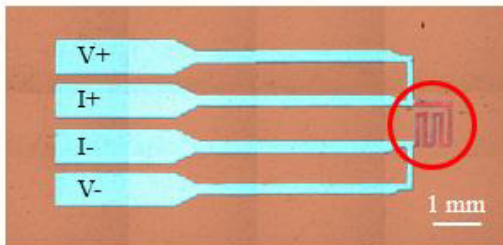
Functional printing – 11/12/2014 | Daniele Sette | 26/34

© CEA. All rights reserved

Micro-jauge Pirani imprimée

■ Élément sensible

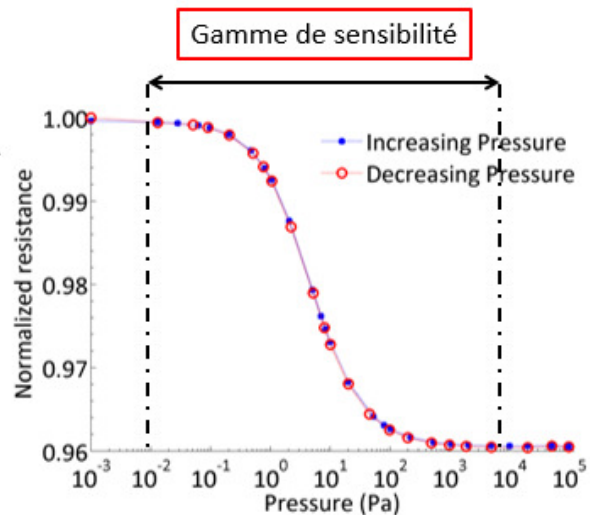
- Résistance en serpentín planaire
- Surface occupée < 1mm²
- Résistance à pression et température ambiante: $R_0 = 3.8 \Omega$
- Traitement thermique: 150°C, 5h
- Substrat: Kapton HN, 75 μm d'épaisseur
- Mesure sous courant DC, méthode 4 points



Montage de la micro-jauge Pirani imprimée

Réponse du capteur

- Point de fonctionnement: 40 mA
- Gamme de sensibilité 10^{-2} à 10^4 Pa
- Correspond à une variation de 4% de la résistance totale
- Faible hystérésis
- Puissance maximum : 6.2 mW à faible pression



Variation de la résistance normalisée de la micro-jauge en fonction de la pression résiduelle dans la chambre



Les caractéristiques de la jauge imprimée sont du même ordre de grandeur que les jauges MEMS du commerce

Filtre Passe-bande centré à 17 GHz imprimé par jet d'encre

International Microwave Symposium 2013 IEEE (Seattle – USA)

Silver Nanoparticles Inkjet Printed 17 GHz Filter, D. Sette, D. Mercier, C. Poulain, A. Blayo

leti

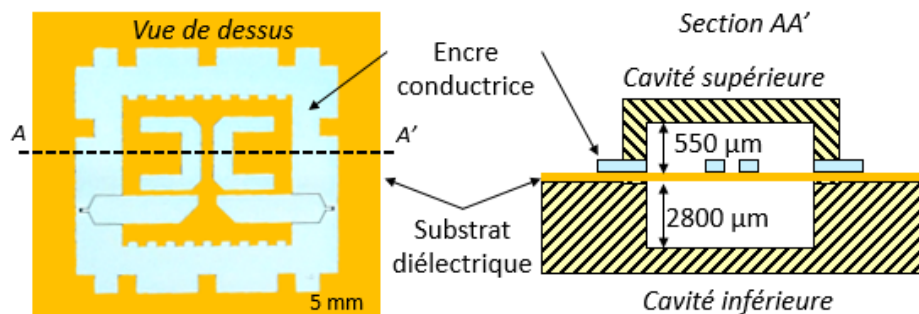
Prototypage

Functional printing – 11/12/2014 | Daniele Sette | 29/34

© IFA, All rights reserved

Filtre imprimé

- Filtre passe-bande à deux pôles, centré à 17 GHz, avec une bande passante de 4%, sur un substrat flexible (Kapton HN, 75 μm)
- Design: suspend entre deux cavités en laiton:
 - Simulation et design réalisés avec la méthode des moments (Agilent Momentum)
- Principe de fonctionnement
 - Couplage électromagnétique entre le motif imprimé et la cavité supérieure
 - Milieu diélectrique \rightarrow Air (très faibles pertes dans le GHz par rapport au substrat)



leti

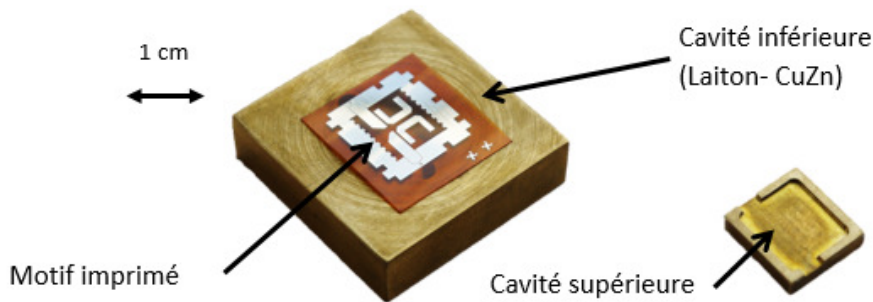
Prototypage

Functional printing – 11/12/2014 | Daniele Sette | 30/34

© IFA, All rights reserved

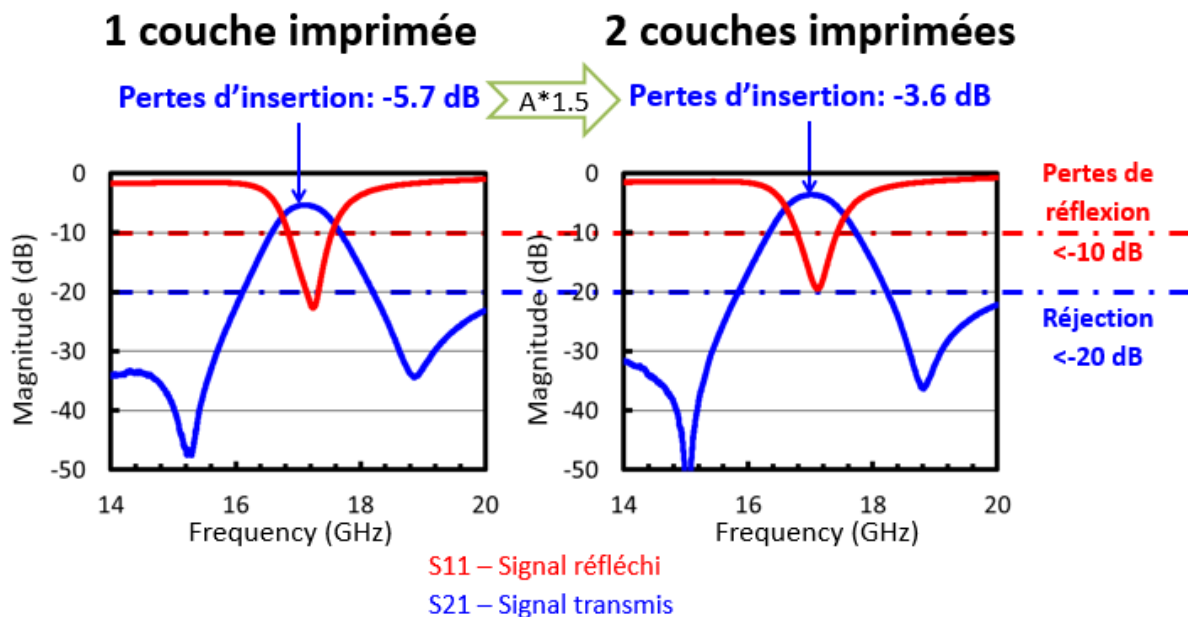
Réalisation du filtre

- Motif imprimé
 - Traitement thermique à 220°C pendant 1 h: $\sigma = 1.5 \cdot 10^7 \text{ S.m}^{-1}$ (25% de $\sigma_{Ag.M}$)
 - Motif collé avec une colle isolante sur la cavité inférieure pour la tenue mécanique
- Cavité supérieure
 - Collée avec laque d'argent (conductrice) sur le plan de masser du motif imprimé et reliée électriquement à la cavité inférieure
 - Alignement manuel sous microscope (erreur de +/- 50 μm)



Réponse du filtre

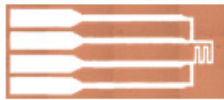
- Mesure : Analyseur de spectre Agilent avec calibration SOLT



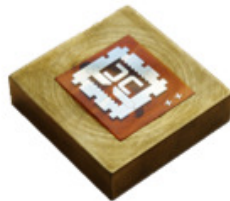
Résumé

Prototypage rapide de composants électroniques fonctionnels présentant des caractéristiques proches de l'état de l'art

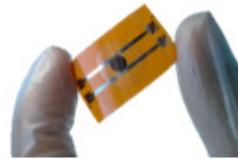
Jauge Pirani



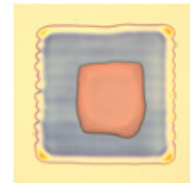
Filtre PB à 17GHz



Membrane switch



Capa M-I-M



Marge d'amélioration des composants réalisés



Sensibilité
TCR



Pertes de transmission
Épaisseur du substrat



Fiabilité
Résistance de contact



Tension de claquage
Constante diélectrique

Références

- Park, B.K. et al., 2007. Direct writing of copper conductive patterns by ink-jet printing. *Thin Solid Films* 515.
- Kaydanova, T., et al., 2007. Direct-write inkjet printing for fabrication of barium strontium titanate-based tunable circuits. *Thin Solid Films* 515, 3820–3824.
- Denneulin, A., et al., 2009. The influence of carbon nanotubes in inkjet printing of conductive polymer suspensions. *Nanotechnology* 20.
- Park, H., et al., 2003. Single drop impactation on a solid surface. *AIChE journal* 49.
- Deegan, R.D., et al., 1997. Capillary flow as the cause of ring stains from dried liquid drops. *Nature* 389.
- Sommer, A.P., 2004. Suffocation of Nerve Fibers by Living Nanovesicles: A Model Simulation—Part II. *Journal of Proteome Research* 3. www.core.materials.ac.uk
- Roberts, A.P., et al., 2000. Elastic Properties of Model Porous Ceramics. *Journal of the American Ceramic Society* 83.
- Yang, L., et al., 2007. Design and characterization of novel paper-based inkjet-printed RFID and microwave structures for telecommunication and sensing applications, in: *Microwave Symposium, 2007*.
- Ando, B., et al., 2013. All-Inkjet Printed Strain Sensors. *IEEE Sensors Journal* 13.
- Mauthner, G., et al., 2008. Inkjet printed surface cell light-emitting devices from a water-based polymer dispersion. *Organic Electronics* 9.
- Zhang, F.T et al., 2006. Thermal Analysis of a Constant Temperature Pirani Gauge Based on Micro-hotplate. *Nano/Micro Engineered and Molecular Systems*.
- Wang, J. et al., 2008. Effect of microscale gaseous thermal conduction on the thermal behavior of a buckled microbridge. *Smart Mater. Struct.* 17 015036.

Conclusion

L'objectif principal de ce travail de thèse a été de contribuer au développement de l'impression fonctionnelle en consolidant les relations interdisciplinaires entre l'impression et la science des matériaux. Dans le cadre des activités de recherche du Leti et du LGP2, les connaissances et savoir-faire en design de composants, caractérisation des matériaux et techniques d'impression ont été mises en commun pour développer des nouvelles compétences.

L'impression par jet d'encre est une technique de fabrication additive sans contact, qui promet des opportunités innovantes pour la fabrication de composants électroniques. Elle peut être adaptée à des substrats rigides, flexibles et même en trois dimensions et la source numérique des motifs en fait une technique totalement adaptable aux besoins de l'application. De nouvelles opportunités ne cessent d'apparaître grâce à l'augmentation et la diversité des matériaux imprimables. Enfin, cette technique rapide à mettre en œuvre et extrêmement flexible est parfaitement adaptée à la fabrication de petite séries, au prototypage et à l'utilisation conjointe avec d'autres techniques comme l'impression 3D et la personnalisation de motifs à la demande.

Parmi les matériaux imprimables, les encres argent sont les plus utilisées; elles ont donc été choisies pour cette thèse et ont fait l'objet d'une étude approfondie. La réalisation de motifs conducteurs passe par un traitement thermique des couches imprimées. Cette étape induit une évolution de leur microstructure (Figure C.1) et affecte fortement leurs propriétés intrinsèques.

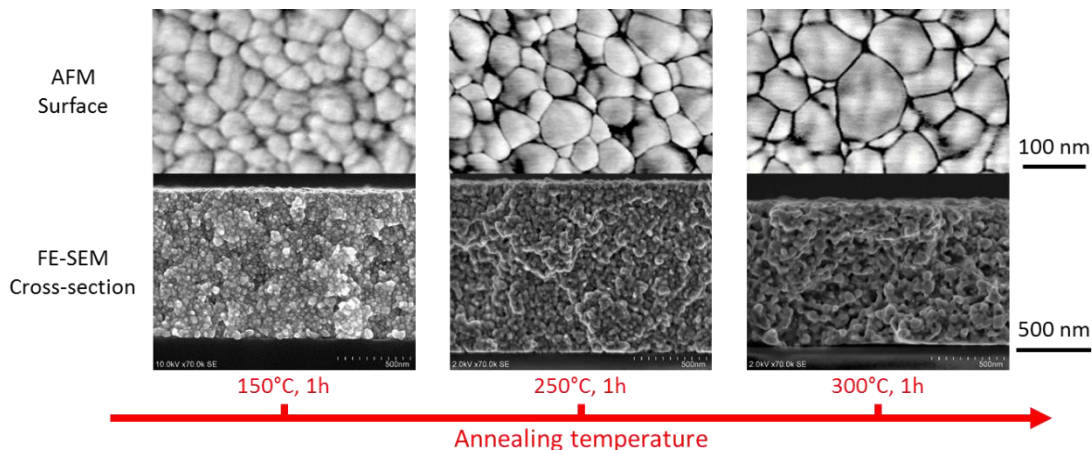


Figure C.1. Evolution de la microstructure de couches d'argent imprimées par jet d'encre.

Cette évolution a fait l'objet d'une étude approfondie dans la gamme de température 100-300°C. Nos équipements et protocoles de caractérisation ont dû être adaptés aux particularités des couches imprimées. Les résultats des observations microscopiques ont montré l'augmentation de la taille de grain et de la rugosité avec la température de traitement et ont mis en évidence différents modes de croissance de grains. De plus, l'observation au microscope électronique de la section des couches imprimées a révélé une structure poreuse avec des dimensions inférieures à 100 nm. La mesure des taux de porosité à ces échelles dans des matériaux métalliques a été un vrai défi, relevé par l'utilisation de techniques d'imagerie en deux et trois dimensions couplant les coupes ioniques (FIB) et la microscopie électronique à balayage (MEB).

Plus récemment, nous avons observé la microstructure des couches d'argent imprimées par tomographie électronique sur des cylindres de 300 nm de diamètre usinés par FIB (Figure C.2). Cette technique permet une observation plus résolue des échantillons et ouvre à de nouvelles pistes dans l'étude des joints de grains en trois dimensions.

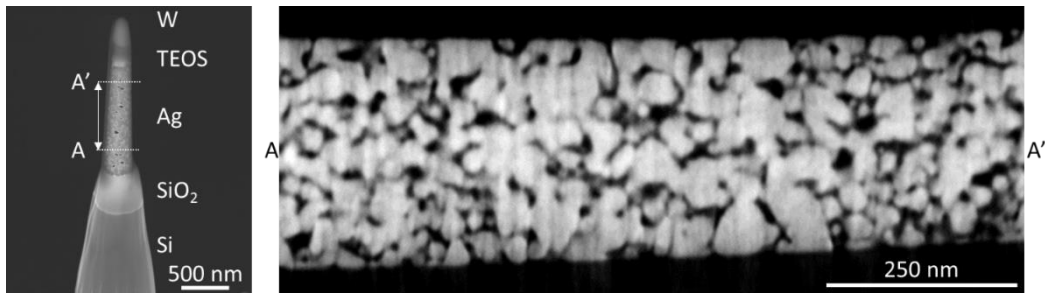


Figure C.2. Tomographie électronique d'une couche d'argent imprimée et traitée en étuve 150°C pendant 1 h.

Les propriétés électriques et mécaniques des couches imprimées ont été étudiées en fonction de la température de traitement. En particulier, la résistivité électrique, le coefficient de température, le module d'Young et la dureté ont été mesurés. Nos équipements de mesure ainsi que les méthodes d'analyse ont dû être adaptés à la microstructure poreuse et polycristalline des couches. Pour assurer la fiabilité et la justesse de ces nouveaux résultats, les grandeurs mesurées ont été corrélées entre elle ou bien à des modèles de la littérature.

Les résultats de caractérisation des couches d'argent ont été obtenus sur une seule encre. Il serait d'un grand intérêt d'employer les protocoles expérimentaux mis au point pour qualifier et caractériser d'autres encres métalliques. De plus, notre étude s'est concentrée principalement sur un traitement thermique en étuve four sous air. En utilisant d'autres méthodes, une évolution différente des nanoparticules d'argent est à prévoir. Nous avons réalisés des essais d'irradiation par laser UV à 192 nm. Cette méthode s'est révélée peu efficace en raison du faible taux d'absorption de l'argent dans les ultraviolets. Aussi, nous avons eu l'occasion de tester des traitements par flash au xénon de Polytec PI sur des couches d'argent imprimées sur des substrats polyimide et silicium. Ces essais ont souligné l'influence des propriétés thermiques du substrat lors de l'exposition des échantillons à des flashes de lumière: deux flashes sur le polyimide ont explosé les motifs argent imprimés alors qu'au moins vingt flashes ont été nécessaires pour faire disparaître la couleur bleutée caractéristique d'une encre non sèche sur le substrat silicium.

La maîtrise du procédé d'impression et la connaissance des propriétés des couches d'argent imprimées nous ont menés à la conception, la fabrication et la qualification de différents prototypes de composants électroniques.

- i. **Un filtre passe-bande centré à 17 GHz imprimé avec 1 et 2 couches.** En premier, nous avons conçu et imprimé un filtre passe-bande centré à 17 GHz sur un substrat polyimide, dont le coût est au moins deux ordres de grandeur inférieur aux substrats utilisés dans ces gammes de fréquence (quartz et saphir). Les dimensions minimales du motif du filtre sont proches des limites de résolution de l'imprimante Dimatix DMP2831. Par conséquent, l'impression du motif avec l'encre argent sur le polyimide a requis l'optimisation des paramètres d'impression pour obtenir des conditions de dépôt stable, répétable et conformes aux dimensions désirées. Ces conditions ont ensuite été réutilisées pour la réalisation des autres composants.

Les pertes de transmission mesurées sur le filtre imprimé avec deux couches sur un substrat Kapton HN, 75 μm sont de 3.6 dB. Des simulations de ce composant montrent que ces pertes sont dues à hauteur de 63 % aux pertes diélectriques dans le substrat. Celles-ci pourraient être encore diminuées en réduisant l'épaisseur du polyimide. Des essais réalisés sur un Kapton HN, 25 μm n'ont pas été concluants à cause d'une délamination de la couche imprimée au moment du traitement thermique en étuve (contraintes thermiques). Une méthode de traitement

sélectif comme les traitements par irradiation ou microondes devrait permettre de limiter ces modes de défaillance du procédé de fabrication.

- ii. **Une micro-jauge Pirani sensible entre 10^{-4} et 100 mbar.** La sensibilité de ce capteur de vide dépend principalement du coefficient de température de l'élément sensible (900 ppm/°C pour cette jauge) et des pertes par conduction dans le substrat. L'augmentation de la température du traitement thermique permet d'augmenter la valeur du TCR et donc la sensibilité du capteur aux variations de pression. Cependant, cela a également pour effet d'augmenter la conductivité électrique du matériau imprimé, ce qui induit des valeurs de résistances plus faibles et donc plus difficiles à mesurer. Des montages électroniques comme une configuration en pont de Wheatstone permettent de s'affranchir de mesures de tensions délicates (de l'ordre du microvolt).
- iii. **Des condensateurs MIM accordables imprimés sur platine pour des applications basse-fréquence et radio-fréquence.** La structure MIM est réalisée en imprimant un sol-gel de BST (couche diélectrique) sur une électrode en platine. L'électrode supérieure est enfin déposée avec l'encre argent. Le motif et la dimension de cette électrode vont définir les caractéristiques du condensateur. L'impression du sol-gel initialement prévu pour des dépôts en "spin-coating" montre la flexibilité et l'adaptabilité du de l'impression par jet d'encre. De plus, cette preuve de concept ouvre des perspectives intéressantes en termes de consommation du produit brut (réduite d'un facteur 40) et en termes de simplification du procédé (gravure des céramiques cristallisées complexe).

Le dernier prototype réalisé est un interrupteur de type "**membrane switch**" dont l'épaisseur est de 250 μm . Ce composant a été fabriqué dans le cadre du projet I2Flex sur un prototype d'imprimante industrielle *JetPac*, au Centre de Microélectronique de Provence. Des tests de fatigues réalisés sur un banc d'essais conçu et monté dans notre laboratoire ont permis de mesurer la résistance de contact et la force d'actionnement sur plus de 100 000 cycles. Ce démonstrateur montre que l'impression jet d'encre peut être utilisée pour des applications de type contact électrique, habituellement réalisée par sérigraphie.

Au cours de cette thèse, d'autres problématiques liées à l'utilisation des techniques d'impression conjointement aux techniques du silicium ont été abordées.

➤ Remplissage d'interconnexions verticales: *Through Polymer Vias* (TPV)

Les TPV sont des lignes de connexion électrique verticales entre deux niveaux d'un composant électrique. Ce type de liaison permet d'augmenter la densité par unité de surface en empilant en 3D plusieurs puces électroniques. Des essais de remplissage de TPV de diamètre entre 80 et 100 μm ont été réalisés sur la Dimatix. Les résultats montrent la formation d'un "liner" conducteur déposé sur les flancs et au fond des ouvertures. Le remplissage complet des TPV aurait nécessité des quantités d'encre 10 à 100 fois plus importantes. Cependant, la Dimatix n'est pas un outil adapté à ce genre d'étude car la tête ne peut être utilisée en mode distributeur goutte-à-goutte. Le remplissage de vias dans du silicium (TSV) par jet d'encre a récemment fait l'objet de plusieurs études (Quack, 2013; Khorramdel, 2014).

➤ Fabrication d'étalons pour des mesures de contamination

La capacité du jet d'encre à délivrer des quantités de matière connues et répétables a permis au laboratoire de mesure de contamination de réaliser des nouveaux types d'étalons. L'idée consiste à déposer des gouttes uniques d'encre argent en des positions connues sur un wafer de silicium. Les

quantités exactes de matières déposées sont mesurées par Décomposition en Phase Vapeur (VPD) et par fluorescence X en réflexion totale.

- Fabrication d'électrodes argent sur des substrats polyimide pour des circuits microfluidiques

Dans les récents travaux de Renaudot au Leti (2014) des circuits microfluidiques reconfigurables et programmables ont été réalisés sur des substrats silicium en utilisant des techniques standard de lithographie. Les dimensions typiques de ces composants étant de plusieurs centimètres, le coût des substrats silicium serait prohibitif pour une production industrielle. Des motifs identiques ont pu être réalisés sur un substrat polyimide (Figure C.3). L'impression de ces électrodes permet de réduire d'une dizaine d'étape le procédé de fabrication en salle blanche et démontre clairement l'intérêt des techniques d'impression pour les composants grande surface.

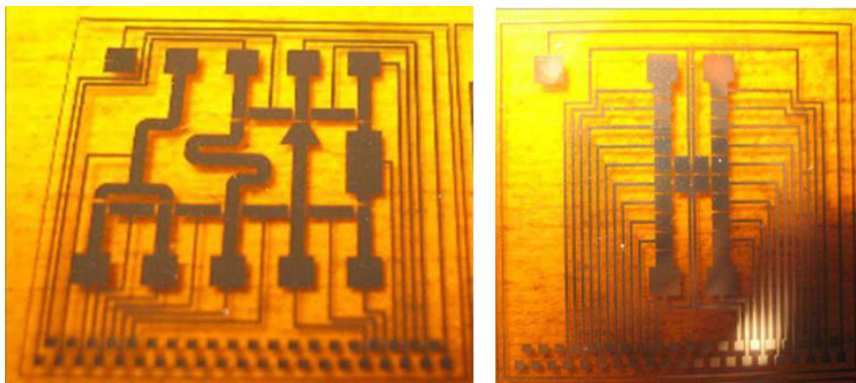


Figure C.3. Electrodes pour des circuits microfluidiques imprimées par jet d'encre sur un substrat polyimide.

En conclusion, cette thèse fournit des résultats originaux concernant les propriétés intrinsèques des couches d'argent imprimées, leur évolution en fonction des conditions de traitement thermique et leur utilisation dans différents types d'applications. Des méthodes et des protocoles expérimentaux ont été développés pour répondre aux contraintes exigeantes des matériaux imprimés (dimensions allant du nanomètre au millimètre, porosité) et les résultats obtenus ont été pondérés et justifiés par des corrélations avec des modèles théoriques et empiriques. Les caractéristiques des prototypes réalisés sont proches de l'état de l'art et le développement des équipements d'impression promet de nouvelles perspectives. On peut citer par exemple le constructeur japonais SIJTechnology (www.sijtechnology.com) qui a réussi à éjecter des gouttes dont le volume est inférieur à 1 femtolitre, permettant d'imprimer des lignes de quelques microns de large.

La problématique de la fiabilité des composants imprimés et flexibles n'a pu être abordée au cours de cette thèse. Cependant des travaux préliminaires dans le cadre d'un stage ingénieur ont permis d'identifier les modes de défaillance des couches d'argent imprimées soumises à des contraintes de traction (fissuration, délamination, flambement). Ces travaux continuent aujourd'hui dans le cadre des travaux de thèse de Marie Le Druillennec au LCFC.

Ces travaux de thèse confirment le potentiel de l'impression par jet d'encre pour la réalisation de motifs dont la fonctionnalité peut aller au-delà de la conduction électrique. Cette thèse, avec une approche fortement expérimentale et multidisciplinaire a été possible grâce au travail collaboratif entre des acteurs académiques et industriels avec des domaines d'expertise en électronique, science des matériaux et technologies d'impression.

Functional printing: From the study of printed layers to the prototyping of flexible devices

Abstract

In the last decade, functional printing has gained a large interest for the manufacturing of electronic components. It stands aside to silicon technologies and specifically targets markets of large area devices (screens, photovoltaics) and flexible electronics (RFID antennas, sensors, smart textiles). In this work, inkjet printed silver layers are characterized depending on the printing conditions and the required post-printing annealing. The evolution of their microstructure, electrical and mechanical properties is investigated as a function of the annealing temperature. The correlation of the measurements with theoretical models supports the experimental methods that were developed. The knowledge of the printed silver layers assets and the optimization of the printing process lead to the design, fabrication and characterization of flexible electronics devices: a 17 GHz band-pass filter printed on polyimide, a flexible vacuum micro-sensor working on the Pirani principle, and a 250 μm thick membrane switch for keyboards. Finally, all-printed RF capacitors were realized by stacking Barium Strontium Titanate (dielectric) and silver printed layers. These prototypes exhibit performances near the state-of-the-art and suggest new opportunities for printing technologies. This thesis offers a thorough study of inkjet printed silver layers and assess their potential for the manufacturing of flexible devices.

Keywords: Inkjet Printing, Silver inks, Nanoparticles, Flexible substrates, Sintering, Characterization, Prototyping

Impression fonctionnelle : de l'étude de couches imprimées au prototypage de composants flexibles

Résumé

Depuis les années 2000, l'impression fonctionnelle connaît un grand succès pour la fabrication de composants électroniques. Elle se positionne de manière complémentaire par rapport aux technologies du silicium et vise principalement les marchés de l'électronique grande surface (écrans, panneaux photovoltaïques) et de l'électronique flexible (RFID, capteurs, textiles intelligents). Dans ce travail, des couches d'argent imprimées par jet d'encre ont été caractérisées en fonction des conditions d'impression et de recuit. L'évolution de leur microstructure, de leurs propriétés électriques et mécaniques a été étudiée. Dans ce cadre, des méthodes expérimentales ont été développées et validées par la bonne corrélation entre les mesures et les modèles. La maîtrise des propriétés de ces couches et l'optimisation de leur procédé de fabrication nous ont conduits à concevoir, fabriquer et caractériser plusieurs composants flexibles: un filtre passe-bande centré à 17 GHz sur un substrat polyimide, un micro-capteur de vide fonctionnant sur le principe de Pirani et un bouton-poussoir d'épaisseur inférieure à 250 μm pour des claviers souples. Enfin, des condensateurs RF ont été réalisés par la superposition de couches imprimées diélectriques (BaSrTi) et conductrices (Ag). Les performances des prototypes réalisés sont proches de l'état de l'art et ouvrent la voie à de nouvelles applications pour les technologies d'impression. Cette étude démontre le potentiel des couches d'argent imprimées par jet d'encre pour la fabrication de dispositifs flexibles.

Mots clés : Impression jet d'encre, Encre argent, Nanoparticules, Substrats flexibles, Frittage, Caractérisation, Prototypage